中国科学技术大学

博士学位论文

RHIC-STAR 实验中轻超核的产生及其寿命的测量

作者姓名：　李秀君
学科专业：　粒子物理与原子核物理
导师姓名：　张一飞 教授　江角晋一 教授
完成时间：　二〇二五年五月二十九日

University of Science and Technology of China
A dissertation for doctor’s degree

Measurements of Hypernuclei Production and Lifetimes from RHIC-STAR Experiment

Author: Li Xiujun

Speciality: Particle Physics and Nuclear Physics

Supervisors: Prof. Yifei Zhang, Prof. ShinIchi Esumi

Finished time: May 29, 2025

中国科学技术大学学位论文原创性声明

本人声明所呈交的学位论文，是本人在导师指导下进行研究工作所取得的成果。除已特别加以标注和致谢的地方外，论文中不包含任何他人已经发表或撰写过的研究成果。与我一同工作的同志对本研究所做的贡献均已在论文中作了明确的说明。

作者签名：________________　　　　签字日期：________________

中国科学技术大学学位论文授权使用声明

作为申请学位的条件之一，学位论文著作权拥有者授权中国科学技术大学拥有学位论文的部分使用权，即：学校有权按有关规定向国家有关部门或机构送交论文的复印件和电子版，允许论文被查阅和借阅，可以将学位论文编入《中国学位论文全文数据库》等有关数据库进行检索，可以采用影印、缩印或扫描等复制手段保存、汇编学位论文。本人提交的电子文档的内容和纸质论文的内容相一致。

控阅的学位论文在解密后也遵守此规定。

☑公开　□控阅（____ 年）

作者签名：________________　　　　导师签名：________________

签字日期：________________　　　　签字日期：________________

摘　要

超核是由包含超子（如 Λ 超子）的核物质组成的特殊核系统，在研究超子–核子（Y–N）相互作用方面具有关键作用。Y–N 相互作用对于理解高重子密度物质（例如中子星内部）的状态方程至关重要。由于超核同时包含核子与超子，它为探索 Y–N 相互作用提供了天然的实验平台。然而，相较于已被深入研究的核子–核子（N–N）相互作用，Y–N 相互作用的实验数据仍然十分有限，导致其理解仍不充分。

本研究的一个核心目标是对超核的内禀性质，尤其是寿命，进行高精度测量。通过将实验测量值与理论预测进行系统比较，可以深入探究 Y–N 相互作用的特性，并进一步了解超核的内部结构。最轻的超核——超氚（${}^{3}_{\Lambda}\mathrm{H}$），由于其 Λ 结合能极低，是一个极弱束缚的系统。理论上，超氚的寿命应与自由 Λ 非常接近。然而，多个实验（包括 STAR）测得的超氚寿命均低于自由 Λ，这一现象被称为“寿命难题”，是当前超核物理的重要研究焦点。本研究旨在通过精密寿命测量为解决这一问题提供新的证据。超核研究的另一重要方面是理解其在重离子碰撞中的产生机制。尽管已有多种理论模型提出，超核的生成过程仍未有统一结论。研究表明，超核产额随能量的演化规律能够为探明其形成机制提供关键线索。

在低碰撞能量下，由于高重子密度环境的存在，轻超核的产额被预测将显著增强。2018 至 2021 年期间，STAR 实验在布鲁克海文国家实验室（BNL）的 RHIC 上开展了束流能量扫描第二期（BES-II），系统采集了多个能量点的金核 + 金核碰撞数据。通过采用固定靶运行模式，将中心质量系的最低能量扩展至 3 GeV，使得实验可达的重子化学势增至约 700 MeV，进入 QCD 相图的高重子密度区域。得益于 BES-II 高统计量数据、低碰撞能量和 STAR 探测器升级，STAR 提供了优越的平台以实现超核的高精度实验研究。

本论文呈现了超氚（${}^{3}_{\Lambda}\mathrm{H}$）、超氢-4（${}^{4}_{\Lambda}\mathrm{H}$）与超氦-4（${}^{4}_{\Lambda}\mathrm{He}$）的寿命测量结果。这些寿命测量都是依据粒子的指数衰减定律来测量的。利用 STAR 在 2018 年于 $\sqrt{s_{NN}} = 7.2$ GeV 采集的数据，测得超氚寿命为 $\tau({}^{3}_{\Lambda}\mathrm{H}) = 219.4 \pm 19.8\ (\mathrm{stat.}) \pm 18.6\ (\mathrm{syst.})$ ps，测得超氢-4 的寿命为 $\tau({}^{4}_{\Lambda}\mathrm{H}) = 217.0 \pm 16.0\ (\mathrm{stat.}) \pm 16.0\ (\mathrm{syst.})$ ps。将该结果与 STAR 在 $\sqrt{s_{NN}} = 3.0$ GeV 的测量联合平均，得到更加精确的寿命结果：$\overline{\tau}({}^{3}_{\Lambda}\mathrm{H}) = 221 \pm 15\ (\mathrm{stat.}) \pm 19\ (\mathrm{syst.})$ ps，$\overline{\tau}({}^{4}_{\Lambda}\mathrm{H}) = 218 \pm 6\ (\mathrm{stat.}) \pm 13\ (\mathrm{syst.})$ ps。两者均为当时最为精确的寿命测量结果。与自由 Λ 的寿命相比，超氚和超氢-4 的寿命分别低约 1.8σ 和 3σ。结合多个实验组的测量数据，其世界平均寿命为自由 Λ 的 $87 \pm 4\%$（超氚）和 $80 \pm 3\%$（超氢-4），显示出超氚和超氢-4 的寿命系统性低于

自由 Λ 寿命。对于超氦-4 (${}^{4}_{\Lambda}\mathrm{He}$)，本文基于 STAR 在 $\sqrt{s_{NN}} = 3.0$、3.2 和 3.5 GeV 的数据进行寿命测量。分别测得寿命为 $\tau({}^{4}_{\Lambda}\mathrm{He}) = 229 \pm 23$ (stat.) $\pm$ 20 (syst.) ps（在 3.0 GeV）和 210 ± 12 (stat.) $\pm$ 11 (syst.) ps（在 3.2–3.5 GeV）。加权平均得到 $\overline{\tau}({}^{4}_{\Lambda}\mathrm{He}) = 214 \pm 10$ (stat.) $\pm$ 10 (syst.) ps，为目前最精确的 ${}^{4}_{\Lambda}\mathrm{He}$ 寿命测量结果。与超氢-4 相似，超氦-4 的寿命也比自由 Λ 的寿命短约 3σ。除了寿命测量，本文还展示了在 $\sqrt{s_{NN}} = 3.2$ GeV 金核 + 金核碰撞中对超氚的不变产额谱、积分产额（dN/dy）以及平均横向动量（$\langle p_T \rangle$）的测量结果。该结果与 RHIC 其他能量点的测量共同构成了首个覆盖高重子密度区域、系统描绘超氚产额随碰撞能量演化关系的完整图景。测量结果显示，随着碰撞能量的降低，dN/dy 呈现出显著上升的趋势，在 $\sqrt{s_{NN}} \approx 3\text{–}4$ GeV 附近达到平台。这一行为反映出高重子密度在增强超氚产额方面的关键作用。与理论模型的比较表明，假设超核与其他轻强子在化学冻出阶段共同形成的热模型，在低能区明显低估了超氚的产额；而包含末态超子和核子并合机制（coalescence）的输运模型则能更好地描述实验数据。此外，$\langle p_T \rangle$ 的测量结果明显低于由轻强子谱拟合得到的 blast-wave 模型预测。这些结果支持超核主要通过末态并合机制形成的观点，并进一步指出，超核与系统的解耦时间不同于轻强子。

综上所述，本文基于 STAR 实验 BES-II 阶段采集的高质量数据，系统测量了轻超核的寿命和产额。这些精确的实验测量数据为超核相关理论模型提供了更为严格的实验约束。实验结果支持了超氚的并合产生机制。

关键词：相对论重离子碰撞，超核，寿命，产生，产额

ABSTRACT

Hypernuclei are special nuclear systems composed of nucleons and hyperons (such as Λ hyperons), and they serve as a crucial platform for studying hyperon–nucleon (Y–N) interactions. These interactions are essential for understanding the equation of state of high-baryon-density matter, such as that found in the cores of neutron stars. However, unlike the well-understood nucleon–nucleon (N–N) interactions, Y–N interactions remain poorly constrained due to limited experimental data.

A primary goal of this work is to perform high-precision measurements of hypernuclear intrinsic properties, especially lifetimes. By systematically comparing experimental results with theoretical predictions, we can better understand Y–N interactions and the internal structure of hypernuclei. The lightest hypernucleus, hypertriton (${}^{3}_{\Lambda}$H), is extremely loosely bound due to its tiny Λ separation energy, and is thus expected to decay with a lifetime close to that of a free Λ. However, several experiments—including STAR—have reported lifetimes shorter than the that of free Λ, a phenomenon referred to as the “lifetime puzzle”. This study aims to shed new light on this issue through precision lifetime measurements. Another focus of hypernuclear research is understanding the production mechanisms of hypernuclei in relativistic heavy-ion collisions. Despite considerable theoretical progress, the exact mechanisms behind hypernuclei production remain unclear. Investigating the production yields of hypernuclei and their energy dependence is vital for uncovering the fundamental processes governing hypernuclei formation in heavy-ion collisions.

The production yield of light hypernuclei is expected to be significantly enhanced at low collision energies due to the high baryon density. The Beam Energy Scan Phase II (BES-II) program, which ran from 2018 to 2021, collected a series of dataset of high statistics in Au+Au collisions at the Relativistic Heavy Ion Collider (RHIC) at Brookhaven National Laboratory (BNL). In particular, the fixed-target mode was utilized to extend the energy range down to $\sqrt{s_{NN}}$ = 3.0 GeV, increasing the baryon chemical potential up to ~700 MeV. Thanks to the high statistics data, low collision energies, and the detector upgrade during BES-II, the STAR BES-II program provides a great opportunity to make precise measurements of hypernuclei production.

In this thesis, the lifetime measurements of ${}^{3}_{\Lambda}$H, ${}^{4}_{\Lambda}$H, and ${}^{4}_{\Lambda}$He are presented. The lifetime is determined by analyzing the exponential decay patterns of the corrected particle yields, in accordance with the exponential decay law. For ${}^{3}_{\Lambda}$H and ${}^{4}_{\Lambda}$H, the lifetimes measured at $\sqrt{s_{NN}}$ = 7.2 GeV are: $\tau(^{3}_{\Lambda}\mathrm{H})$ = 219.4 ± 19.8 (stat.) ± 18.6 (syst.) ps and $\tau(^{4}_{\Lambda}\mathrm{H})$ = 217.0 ± 16.0 (stat.) ± 16.0 (syst.) ps. Combining these with STAR results at $\sqrt{s_{NN}}$ = 3.0 GeV gives the weighted averages: $\overline{\tau}(^{3}_{\Lambda}\mathrm{H})$ = 221 ± 15 (stat.) ± 19 (syst.) ps and $\overline{\tau}(^{4}_{\Lambda}\mathrm{H})$ = 218 ± 6 (stat.) ± 13 (syst.) ps, which are the most precise values to date. Compared to the free Λ lifetime, these values are shorter by about 1.8σ and 3σ, respectively. The world-average values of $^{3}_{\Lambda}\mathrm{H}$ and $^{4}_{\Lambda}\mathrm{H}$ lifetimes from all experiments are 87 ± 4% and 80 ± 3% of the free Λ lifetime, indicating that $^{3}_{\Lambda}\mathrm{H}$ and $^{4}_{\Lambda}\mathrm{H}$ lifetimes are systematically lower than the free Λ lifetime. For $^{4}_{\Lambda}\mathrm{He}$, lifetime measurements at $\sqrt{s_{NN}}$ = 3.0, 3.2, and 3.5 GeV yield: $\tau(^{4}_{\Lambda}\mathrm{He})$ = 229 ± 23 (stat.) ± 20 (syst.) ps at 3.0 GeV and 210 ± 12 (stat.) ± 11 (syst.) ps at 3.2–3.5 GeV. The combined average is $\overline{\tau}(^{4}_{\Lambda}\mathrm{He})$ = 214 ± 10 (stat.) ± 10 (syst.) ps, representing the most precise measurement to date. The $^{4}_{\Lambda}\mathrm{He}$ lifetime, like that of $^{4}_{\Lambda}\mathrm{H}$, is found to be about 3σ shorter than the free Λ lifetime. In addition to lifetime measurements, the differential p_T spectrum, integrated yield (dN/dy), and average transverse momentum ($\langle p_T \rangle$) of $^{3}_{\Lambda}\mathrm{H}$ were measured at $\sqrt{s_{NN}}$ = 3.2 GeV. Combined with data from other RHIC energies, these results provide the first systematic mapping of the energy dependence of $^{3}_{\Lambda}\mathrm{H}$ production across the high baryon density region. The dN/dy rises sharply with decreasing energy and reaches a plateau near $\sqrt{s_{NN}} \approx$ 3–4 GeV, suggesting enhanced production in a high baryon density environment. The observed $\langle p_T \rangle$ values are lower than blast-wave fitted to light hadrons. Thermal model calculations significantly underestimate the hypernuclei yields at low collision energies, whereas transport models incorporating a coalescence mechanism provide a better description of the data. These observations suggest that hypernuclei decouple from the system at a different time compared to light hadrons, and the coalescence formation process is favored.

In summary, this thesis presents precision measurements of lifetimes and yields of light hypernuclei based on STAR BES-II data, providing new constraints on theoretical models and deepening our understanding of Y–N interactions and hypernuclear formation mechanisms in heavy-ion collisions.

Key Words: relativistic heavy-ion collision, hypernucleus, lifetime, production, yield

Contents

List of Figures

List of Tables

Chapter 1 Introduction

1.1 Fundamental Particles in the Standard Model

The four fundamental forces observed in nature are gravity, the electromagnetic force, the strong force, and the weak force. The Standard Model of particle physics is a well-established and extensively tested theoretical framework in modern physics, which describes the fundamental particles and unifies three of the four fundamental interactions, excluding only gravitational interaction.

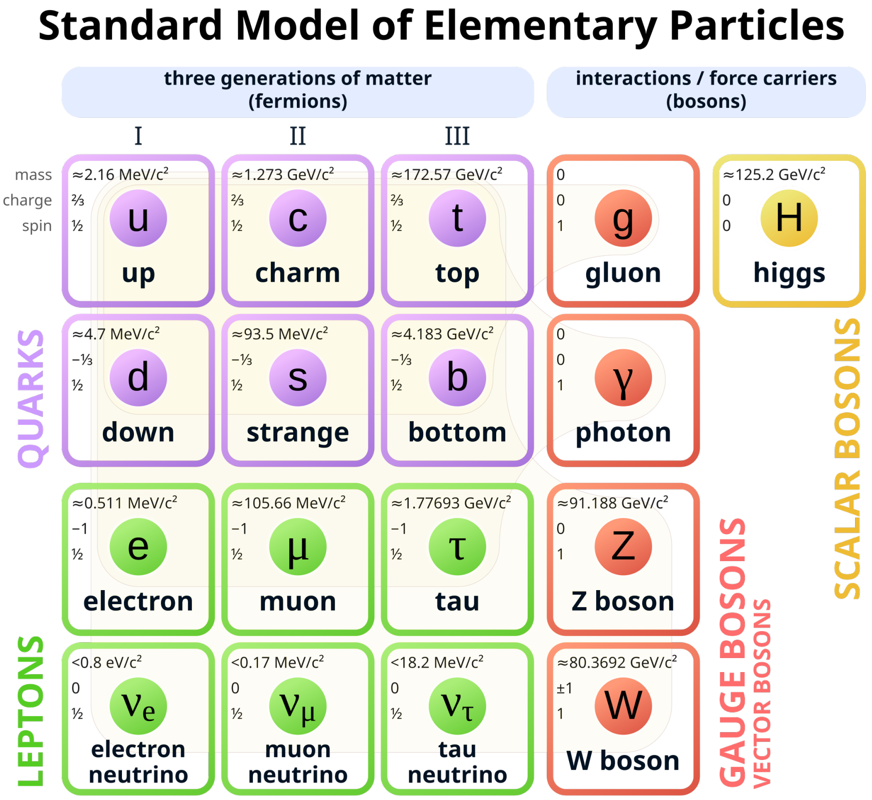

Figure 1.1 The Standard Model of particle physics, illustrating the three generations of matter (quarks and leptons) and the force carrier bosons, including the Higgs boson. This picture is taken from Ref. [1].

In the Standard Model, the fundamental particles that constitute the universe are classified into leptons, quarks, gauge vector bosons, and Higgs boson, as shown in Figure 1.1. The fundamental building blocks of matter are quarks and leptons, while gauge vector bosons and Higgs boson act as the force carriers. Quarks and leptons are both spin-$\frac{1}{2}$ fermions and are organized into three generations (rows) as in Figure 1.1.

There are six flavors of quarks: up (u) and down (d), charm (c) and strange (s), top (t) and bottom (b). Up, charm, and top quarks carry a charge of $+\frac{2}{3}$, while down, strange, and bottom carry a charge of $-\frac{1}{3}$. In addition to electric charge, each quark carries properties known as color charge (red, green, or blue) and weak charge. Quarks participate in the three fundamental interactions: the electromagnetic interaction, governed by electric charge; the strong interaction, governed by color charge; and the weak interaction, governed by weak charge. Quarks combine through the strong interaction to form hadrons, which are further classified into baryons (qqq), such as protons and neutrons, and mesons ($q\bar{q}$), which consist of a quark-antiquark pair.

Similarly, there are six types of leptons: electron (e) and electron neutrino (ν_e), muon (μ) and muon neutrino (ν_μ), tau (τ) and tau neutrino (ν_τ). Among them, the electron, muon, and tau are all charged particles, carrying an electric charge of -1, while their corresponding neutrinos (ν_e, ν_μ, and ν_τ) are neutral and do not carry electric charge. Unlike quarks, leptons do not participate in the strong interaction but do participate in the weak interaction.

Bosons, which mediate fundamental interactions, are classified as vector (spin-1) or scalar (spin-0). The gauge vector bosons, which have spin-1, are the force carriers of the electromagnetic, strong, and weak forces. Gluons (g) mediate the strong interaction between quarks. The photon (γ) mediates the electromagnetic interaction. The weak bosons ($W^\pm$, Z^0) mediate the weak interaction.

The Higgs scalar boson (H) is a fundamental particle associated with the Higgs field, which permeates all of space. The Higgs boson, which has spin-0, is responsible for providing mass to other fundamental particles, such as the $W^\pm$ and Z^0 bosons, leptons, and quarks, through the Higgs mechanism. When particles interact with the Higgs field, they “gain” mass, and this interaction is mediated by the Higgs boson. The discovery of the Higgs boson in 2012 at the Large Hadron Collider (LHC) further confirmed the Higgs mechanism, solidifying the Standard Model’s predictive power [2-3]. This groundbreaking discovery earned François Englert and Peter Higgs the 2013 Nobel Prize in Physics for their theoretical prediction of the Higgs mechanism [4-6].

The Standard Model is one of the most successful and extensively tested theories in modern physics. It has not only provided a comprehensive framework for understanding fundamental particles and their interactions but has also demonstrated remarkable predictive power. Every fundamental particle predicted by the Standard Model, including the Higgs boson, has been experimentally confirmed. Furthermore, it successfully explains a wide range of observed physical phenomena, from particle interactions to the properties of matter at the smallest scales. Despite its success, the Standard Model remains incomplete, as it does not incorporate gravity or explain dark matter, dark energy, and the matter-antimatter asymmetry in the universe. Nevertheless, it stands as a cornerstone of particle physics and continues to be refined through high-energy experiments and theoretical Despite its limitations, the Standard Model underpins explorations of extreme matter states, such as those in heavy-ion collisions.

1.2 Quantum Chromodynamics

Quantum Chromodynamics (QCD) is the theory of the strong interaction, one of the four fundamental forces of nature, governing the behavior of quarks and gluons [7-14]. It is a key component of the Standard Model and is built on the non-Abelian gauge symmetry group $SU(3)_C$, where the subscript C denotes "color," representing the color charge carried by quarks and gluons. Quarks carry one of three color charges: red, green, or blue, while gluons are the mediators of the strong interaction, capable of changing the color of quarks as they interact.

The fundamental dynamics of QCD are encapsulated in the gauge-invariant Lagrangian:

$$\mathcal{L}_{\text{QCD}} = \sum_f \bar{q}_f (i\gamma^\mu D_\mu - m_f) q_f - \frac{1}{4} G^a_{\mu\nu} G^{a,\mu\nu}. \tag{1.1}$$

Here, q_f represents different quark flavors, while D_μ is the covariant derivative, which incorporates interactions between quarks and gluons. The term $G^a_{\mu\nu}$ is the gluon field strength tensor, which describes the self-interactions of gluons and the dynamics of the gauge field. The index $a = 1, 2, \ldots, 8$ denotes the eight independent color states of gluons in the adjoint representation of $SU(3)$.

At short distances, the potential between color charges behaves similarly to a Coulomb-like potential, but instead of the electromagnetic coupling constant α_e, it is governed by the strong interaction coupling constant α_s. The interaction potential between quarks takes the form:

$$V(r) = -\frac{4}{3}\frac{\alpha_s}{r} + \sigma r. \tag{1.2}$$

The first term is analogous to the Coulomb potential in electromagnetism, where α_s is the strong coupling constant, similar to the fine-structure constant α_e in quantum electrodynamics (QED). This term dominates at short distances and is responsible for the attractive interaction between quarks. The second term, σr, represents the linear confinement potential, where σ is the string tension, experimentally determined to be around 0.9 GeV/fm. Unlike QED, where the electromagnetic force weakens with distance, in QCD, the interaction increases as r grows, leading to quark confinement.

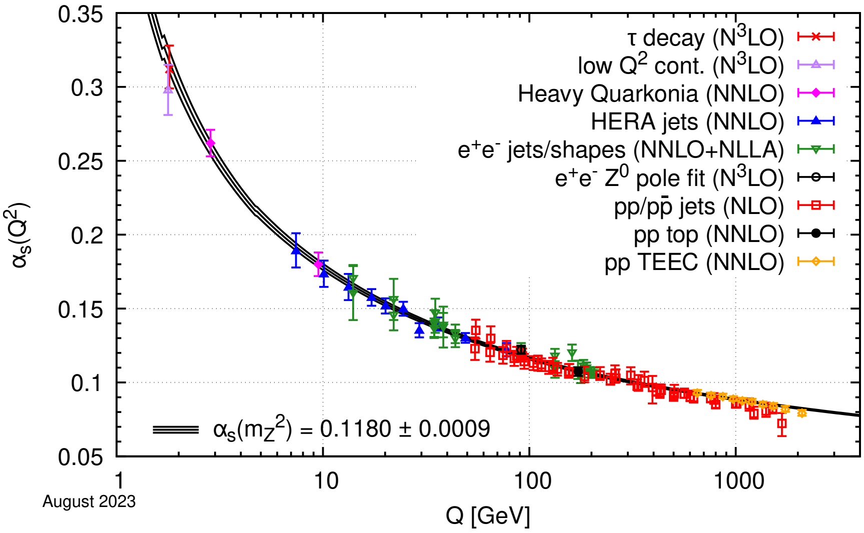

Figure 1.2 Summary of the measurements of the running coupling constant α_s of the strong interaction as a function of the energy scale Q. The measurements can be well described by the black curve from theory prediction. The picture is taken from Ref. [15].

The interaction strength in QCD is energy-dependent and is governed by the running of the strong coupling constant $\alpha_s(Q^2)$. In the 1-loop approximation of perturbative QCD, the evolution of α_s with the energy scale Q^2 is described by the equation [16]:

$$\alpha_s(Q^2) = \frac{1}{\beta_0 \ln(Q^2/\Lambda^2_{QCD})}. \tag{1.3}$$

Here, Q^2 represents the energy scale (or momentum transfer), and Λ_{QCD} is the QCD energy scale parameter, whose value is about 200 MeV, characterizing the transition between perturbative (weakly coupled) and non-perturbative (strongly coupled) regimes of QCD. The coefficient $\beta_0 = \left(11N_c - 2N_f\right)/12\pi$, where $N_c = 3$ is the number of color charges and N_f is the number of active quark flavors, determines the rate at which α_s changes with energy. This equation reflects the fundamental property of asymptotic freedom, where α_s decreases at high energy scales (large Q), allowing quarks and gluons to interact weakly and behave almost as free particles. According to the uncertainty principle, a higher energy scale corresponds to a shorter distance scale. Therefore, at short distances, the interaction between quarks becomes weaker—a phenomenon known as asymptotic freedom. Conversely, at low energy scales (small Q), which correspond to larger distance scales, α_s increases significantly, leading to the phenomenon of confinement, where quarks and gluons are bound within hadrons and cannot exist in isolation.

Figure 1.2 illustrates both the experimental measurements and theoretical predictions for α_s as a function of Q^2. The data points correspond to various experimental determinations of α_s from high-energy processes, while the curve represents the theoretical prediction based on the renormalization group equation. The figure clearly illustrates that as Q^2 increases, α_s decreases and asymptotically approaches zero, confirming the behavior of asymptotic freedom. On the other hand, at lower energy scales, α_s increases significantly, emphasizing the strong interactions that lead to quark confinement. This fundamental behavior underlies many aspects of QCD and plays a crucial role in understanding the structure of hadronic matter.

1.3 QCD Phase Diagram

Due to asymptotic freedom described in the last section, the strong interaction coupling constant, α_s, decreases significantly with increasing energy scale (or decreasing distance), which is referred to as asymptotic freedom. In such extreme conditions, quarks and gluons, normally confined within hadrons, become deconfined, leading to a new phase of strongly interacting matter known as the quark-gluon plasma (QGP) [17-18]. This transition is not only relevant for understanding the early universe but also plays a crucial role in understanding the matter inside neutron stars.

The QCD phase transition can be mapped on a phase diagram in the temperature (T) and baryon chemical potential (μ_B) plane [19-24]. Here, T represents the temperature of the system, which reflects the average kinetic energy of particles and determines the degree of thermal excitation. The baryon chemical potential μ_B quantifies the change in the system's free energy associated with adding one baryon, and it is directly related to the net baryon density. A higher μ_B corresponds to a more baryon-rich environment. Figure 1.3 shows a schematic representation of the QCD phase diagram, highlighting key features such as the hadronic phase, the QGP, the crossover at low μ_B, the first-order phase transition line, and the hypothesized QCD critical point that separates these two regions. This diagram serves as a roadmap for exploring the rich phase structure of matter under extreme conditions.

The high-temperature and low-μ_B region of the QCD phase diagram—corresponding to the QGP phase—is believed to have been exsited in the early Universe, when it was extremely hot and dense. Under these extreme conditions, quarks and gluons were no longer confined within hadrons and could exist as free particles, forming the QGP. Figure 1.4 illustrates the evolution of the Universe. It is believed that the QGP existed in the early Universe, roughly 10^{-6} seconds after the Big Bang. As the Universe continued to expand and cool, quarks and gluons become bound into hadrons. This process marked the QCD phase transition from the QGP phase to hadronic phase and led to the formation of ordinary matter that makes up the visible Universe today.

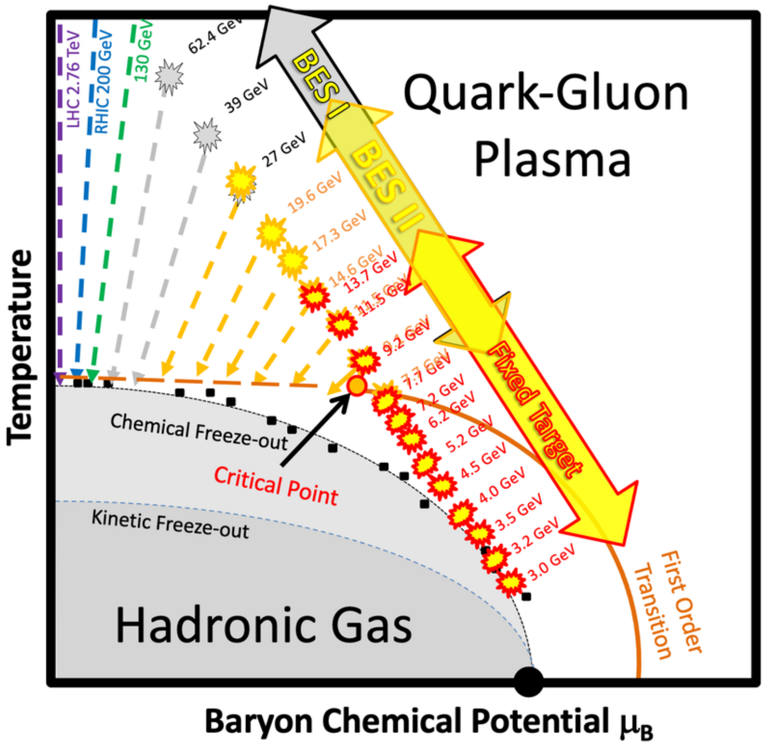

Figure 1.3 A schematic QCD phase diagram in the temperature (T) and baryon chemical potential (μ_B) plane, illustrating the hadronic phase, QGP phase, first-order phase transition, freeze-out, and the QCD critical point. The picture is taken from Ref. [25].

Following the QGP phase, as the system continues to cool and expand, it undergoes a phase transition into the hadronic phase. In this region, quarks and gluons are no longer deconfined but become bound into color-neutral hadrons, marking the onset of confinement. This phase dominates the lower-temperature and lower-μ_B region of the QCD phase diagram.

At high temperature and nearly zero μ_B values, relevant to conditions in the early Universe, lattice QCD calculations predict that the transition from the quark-gluon plasma to hadronic matter occurs smoothly, as a crossover without a sharp phase boundary. The approximate location of the crossover region is indicated by the orange dashed curve in Figure 1.3. In this smooth crossover, hadronic matter and the deconfined state of quarks and gluons gradually and continuously transform into each other. The transition temperature associated with the crossover at $\mu_B \approx 0$ is estimated to be around 155–160 MeV [24, 27-30].

As the system evolves within the hadronic phase, it eventually reaches two important decoupling stages. The first is chemical freeze-out, where inelastic collisions cease and the relative abundances of different particle species are fixed. The second is kinetic freeze-out, when elastic scatterings end and particle momenta are no longer

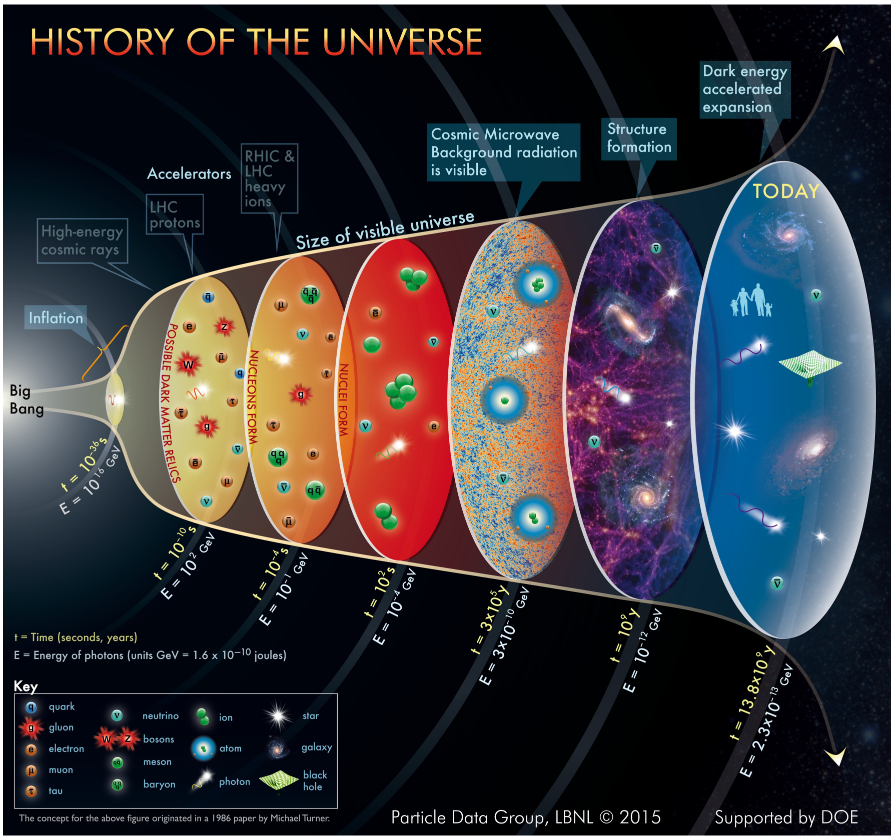

Figure 1.4 Schematic illustration of the evolution of the Universe from the Big Bang to the present day. Figure is taken from Ref. [26].

modified. These freeze-out conditions play a crucial role in determining the final-state particle spectra and correlations observed in experiments, including those of hadrons, light nuclei, and hypernuclei.

As baryon density increases, at higher finite values of μ_B, Lattice QCD predicts that the transition becomes a first-order phase transition, represented by a well-defined boundary line in the temperature versus baryon chemical potential plane, denoted as the solid orange curve in Figure 1.3. The termination of this first-order line is hypothesized to be the QCD critical point, marking the end of the first-order transition and the beginning of the crossover region.

The exact location of the QCD critical point remains an open and actively investigated question. Determining whether this critical point exists, and identifying its precise location, would represent a significant milestone in our understanding of the QCD phase structure [31-33]. Experimentally, the transition from the hadronic phase to the QGP phase can be recreated through relativistic heavy-ion collisions. By varying the collision energies, it is possible to probe different regions of the QCD phase diagram. The Beam Energy Scan (BES) program conducted by the STAR (Solenoidal Tracker at RHIC) experiment at the Relativistic Heavy Ion Collider (RHIC) is specifically designed to explore the high baryon density region and search for signatures of the QCD critical point.

The high-μ_B region of the QCD phase diagram, extensively explored in the BES Phase II program at RHIC, is characterized by strong baryon stopping and high net-baryon density. Such conditions are believed to be realized in the cores of neutron stars, where dense nuclear matter may reach several times nuclear saturation density. The high baryon density in this region create a favorable environment for the formation of exotic nuclear states, such as hypernuclei, which we discuss next.

1.4 Relativistic Heavy-Ion Collisions

In the current universe, which has cooled significantly since the Big Bang, the QGP no longer exists under natural conditions. To experimentally recreate and study the QGP, as well as to explore the phase transitions depicted in the QCD phase diagram, scientists utilize relativistic heavy-ion collisions.

Relativistic heavy-ion collisions, also known as the “Little Bang”, involve accelerating heavy nuclei, such as gold (Au), to relativistic speeds—close to the speed of light—and colliding them. These collisions occur within an extremely small spatial scale of just a few femtometers and generate the extreme temperatures and energy densities similar to those that existed in the early universe. This experimental approach provides a unique opportunity that allow for the formation of QGP and study QGP in laboratory conditions, offering valuable insights into the behavior of strongly interacting matter under extreme conditions.

1.4.1 Collision Geometry

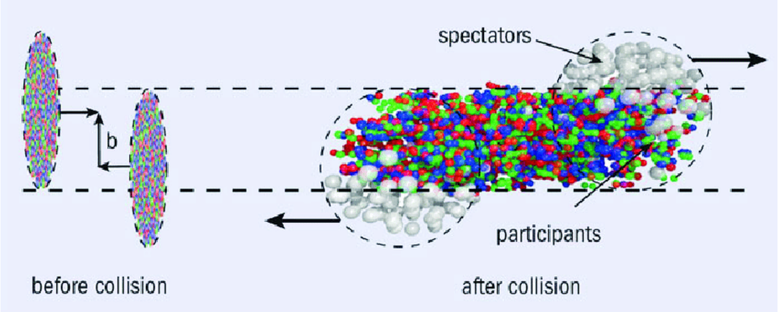

Figure 1.5 Collisions of two heavy nuclei in relativistic heavy ion collisions. This picture is taken from Ref. [34].

In relativistic heavy-ion collisions, understanding the collision geometry is essential for interpreting the dynamics of the interactions. Figure 1.5 schematically illustrates the geometry of a heavy-ion collision. Based on their involvement in the collision, nucleons are classified as participants or spectators. Participant nucleons (depicted in color) are those that undergo at least one inelastic interaction, while spectator nucleons (shown in gray) remain unaffected, passing through the collision zone without interacting. This classification forms the basis of the participant-spectator model, which has successfully described numerous experimental observations in heavy-ion collisions.

Given that the de Broglie wavelength of nucleons is much smaller than the size of the nucleus, the geometry of such collisions can be effectively described using the impact parameter (b), which characterizes the transverse distance between the centers of the two colliding nuclei. Central collisions (small b) result in a large number of participants and minimal spectators, whereas peripheral collisions (large b) exhibit the opposite characteristics. Experimentally, the impact parameter (b) is not directly measurable. Instead, collision centrality is used to quantify the degree of overlap between colliding nuclei and is closely related to b. One commonly used observable is the charged-particle multiplicity (N_{ch}), defined as the total number of charged particles produced in a collision. This can be measured using tracking detectors such as the Time Projection Chamber (TPC). Events are sorted based on these observables, and centrality are defined as percentiles of the distribution. For instance, the $0-5\%$ centrality corresponds to the most central collisions, characterized by the highest N_{ch}. The relationship between observables and geometric quantities like b is calibrated using Monte Carlo Glauber model simulations [35].

1.4.2 Space-time Evolution of Relativistic Heavy-ion Collisions

Relativistic heavy-ion collisions undergo a complex and dynamic evolution through multiple stages. Figure 1.6 shows a schematic representation of the space-time evolution of a heavy-ion collision with QGP formation. The X-axis (z) represents the spatial scale along the beam direction, while the Y-axis (t) represents time. The beams travel at velocities close to the speed of light (c), depicted by black lines. In terms of time, this process can be divided into the following stages.

The small white region under time τ_0 in Figure 1.6 illustrates the pre-equilibrium phase. The process begins with the pre-equilibrium stage, occurring within τ_0 (~ 1 fm/c) after the collision when the two heavy nuclei, such as gold (Au) or lead (Pb), collide at relativistic speeds. This initial interaction creates an overlap zone with extremely high energy density. During this stage, the system is highly non-equilibrium, and thermalization has not yet occurred. Partons (quarks and gluons) interact and redistribute

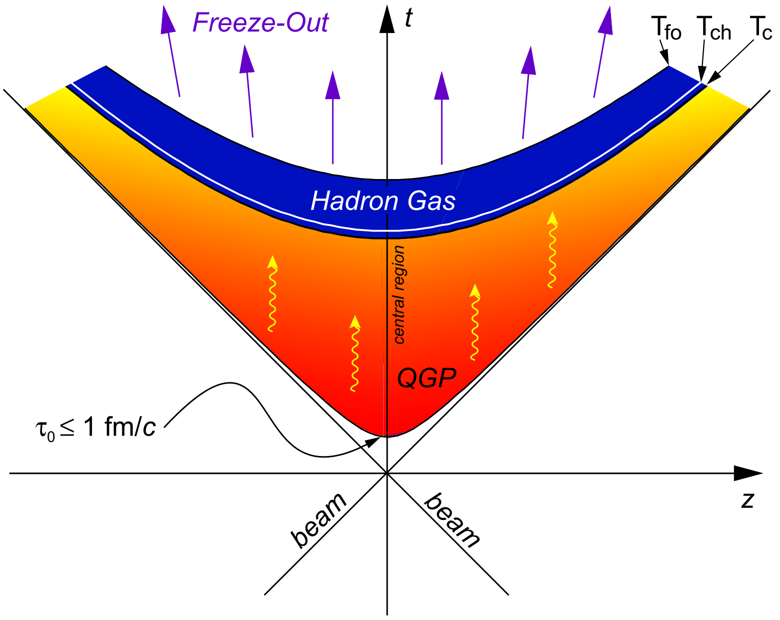

Figure 1.6 Schematic diagram of the evolution of a heavy-ion collision in the light cone, assuming the system passes through a QGP stage. This picture is taken from Ref. [36].

energy and momentum, pushing the system towards local thermal equilibrium.

Once sufficient energy and momentum exchanges occur through cascading reactions, the system achieves local thermal equilibrium at time τ_0. At this stage, the system can be treated as a fluid, and its evolution is described by the equations of relativistic hydrodynamics. The system then enters the QGP phase, shown in orange color in Figure 1.6, where quarks and gluons are deconfined and move freely within the hot and dense medium. The evolution of the QGP is governed by viscous hydrodynamics, with rapid expansion and cooling driven by pressure gradients. A key feature of this phase is the collective flow behavior of particles, and understanding this behavior is crucial for exploring the properties of QGP, such as viscosity and thermalization.

As the system expands and cools further, the energy density decreases, and the characteristic feature of color confinement begins to emerge. This transition is known as hadronization, where quarks and gluons recombine to form hadrons. The deconfined QGP phase transforms into a hadron gas phase dominated by mesons and baryons, depicted in blue in Figure 1.6. During the hadron gas phase, the system consists of interacting hadrons that continue to expand and cool. Both inelastic and elastic collisions occur, altering particle momenta and abundances. This marks the final stage of the evolution towards a state where strong interactions dominate in the form of color-neutral hadrons.

As the system continues to cool and the temperature and density decrease, the average free path of particles eventually exceeds the scale of the system. At this stage, interactions between hadrons become infrequent. First, inelastic collisions cease, marking the chemical freeze-out, during which the composition of particle species becomes fixed, and no new particles are produced or annihilated. As the system cools further, elastic scatterings also stop, leading to the kinetic freeze-out, where the momentum distributions of particles are finalized. These freeze-out particles then propagate freely toward the detectors. By analyzing the yields, momentum distributions, and correlations of these particles, key information about the dynamics, evolution, and thermodynamic properties of the system created in heavy ion collisions can be extracted.

1.5 Hypernuclear Physics

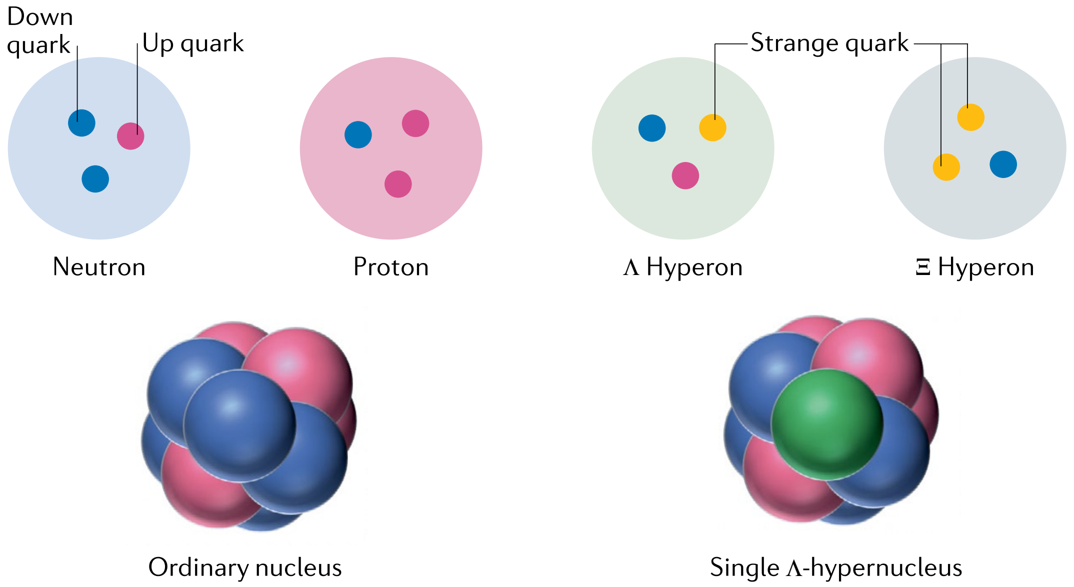

Figure 1.7 Illustration of proton, neutron, and hyperons, and examples of a nucleus and a hypernucleus. This picture is taken from Ref. [37].

As illustrated in Figure 1.7, ordinary nuclei consist of nucleons (protons or neutrons). A neutron is formed by one up quark and two down quarks (udd), while a proton comprises two up quarks and one down quark (uud). Baryons that include at least one strange quark (s) are categorized as hyperons. An example of such a hyperon is the Λ hyperon, consisting of an up, a down, and a strange quark (uds). Other hyperons containing a single strange quark include the Σ hyperons: Σ^+ (uus), Σ^0 (uds), and Σ^- (dds). Hyperons with two strange quarks are the Ξ^0 (uss) and Ξ^- (dss). A Ξ^- hyperon is illustrated in Figure 1.7. The hyperon composed of three strange quarks is the Ω^- (sss).

Hypernuclei are exotic nuclear systems where one or more nucleons are replaced by hyperons [39-41]. This introduces strangeness, a new quantum number, enabling

Figure 1.8 Illustration of nucleons, hyperons, nuclei, and hypernuclei represented in a three-dimensional space defined by charge number, neutron number, and strangeness number. This picture is taken from Ref. [38].

studies of the structure and interactions within atomic nuclei, extending the nuclear chart into a third dimension as shown in Figure 1.8.

The introduction of strangeness into nuclei brings additional degrees of freedom, enriching the field of nuclear physics and offering deeper insights into nuclear structure. Unlike nucleons, hyperons avoid the Pauli exclusion principle in nuclear matter due to their strange quark content. The Pauli exclusion principle states that no two identical fermions can occupy the same quantum state within a quantum system. For nucleons, this restriction arises because they share the same internal quantum numbers—spin, isospin, and flavor—being composed only of up and down quarks. However, hyperons contain at least one strange quark, introducing an additional quantum number known as strangeness. This distinguishes them from nucleons in quantum state classifications. Consequently, hyperons such as Λ, Σ, and Ξ can occupy nuclear states that are already filled by nucleons without violating the Pauli exclusion principle. This unique property allows hyperons to exist in nuclear systems even when lower-energy nucleon states are fully occupied. As a result, hyperons can occupy deeper, more bound nuclear states, providing an essential mechanism for exploring the structure of matter under extreme conditions.

However, the presence of hyperons introduces the so-called “hyperon puzzle” in astrophysics [42-43]. The hyperon puzzle refers to the discrepancy between theoretical predictions and astrophysical observations regarding the presence of hyperons in neutron star inner cores. Theoretically, in the extremely dense cores of neutron stars, where densities exceed 2-3 times the nuclear saturation density, it becomes energetically favorable for nucleons (neutrons and protons) to convert into hyperons. This transition occurs because hyperons can help relieve the Fermi pressure of the nucleons and reduce the system’s overall energy. Hyperons, being exempt from the Pauli ex-

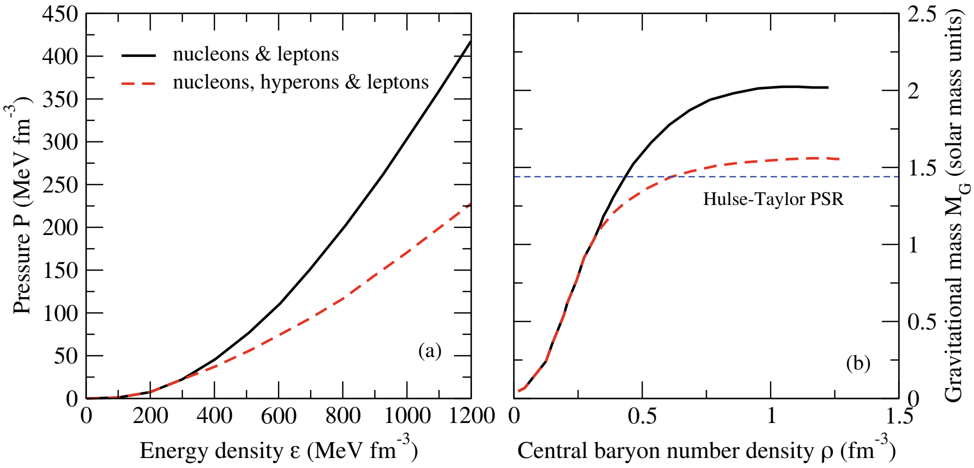

Figure 1.9 Diagram demonstrating the impact of the presence of hyperons on the equation of state (EoS) in panel (a) and on neutron star mass in panel (b). This picture is taken from Ref. [42].

clusion principle with respect to nucleons, provide additional available quantum states, enabling a more energetically favorable configuration. However, the introduction of hyperons also softens the equation of state (EoS)—the relationship between pressure and density in neutron star matter—by reducing the pressure at a given density, as it is illustrated in panel (a) of Figure 1.9. A softer EoS implies that the neutron star is less resistant to gravitational collapse, leading to a lower maximum mass limit for neutron stars, presented in panel (a) of Figure 1.9. This theoretical prediction conflicts with astrophysical observations of neutron stars with masses exceeding two solar masses [44]. This discrepancy forms the core of the hyperon puzzle Resolving this puzzle requires a better understanding of hyperon interactions, particularly the hyperon-nucleon (Y-N) and hyperon-hyperon (Y-Y) interactions.

In hypernuclei, hyperons such as the Λ particle are embedded within ordinary nuclear matter. Therefore, hypernuclei are natural probe to study Y-N and Y-Y interactions, which are much less understood compared to well-established nucleon-nucleon interactions. Unlike the extreme and inaccessible conditions of neutron star interiors, hypernuclei can be produced and studied in experiments, enabling direct measurements of the properties and interactions involving hyperons, which can help build the EoS with hyperons better. Precision measurements on the strength and nature of Y-N interactions through observables like the Λ binding energy (B_Λ), lifetimes, and decay modes of hypernuclei can offer crucial constraints on the theroretical models describing the Y-N interaction. Moreover, the investigation of multi-strange hypernuclei, such as those containing multiple Λ hyperons or even Ξ hyperons, can provide insights into Y-Y interactions. These interactions are even less understood but are essential for modeling the dense core of neutron stars.

1.5.1 Discovery of Hypernuclei

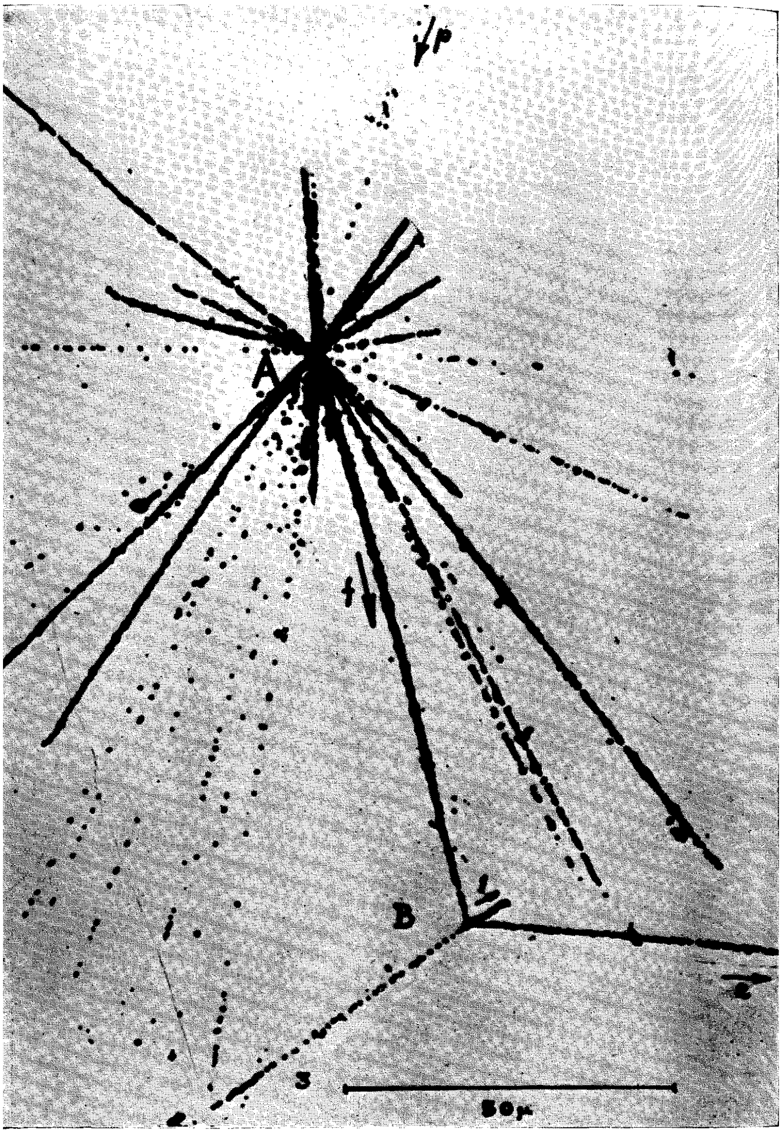

Figure 1.10 The first observation of the decay of a hypernucleus. This picture is taken from Ref. [45].

The first discovery of hypernuclei marks a significant milestone in the field of nuclear physics. In 1952, Polish physicists Marion Danysz and Jerzy Pniewski observed the first hypernuclear event using a 600 µm thick, glass-backed Ilford G5 emulsion plate exposed to cosmic rays at an altitude of 85000 feet in Warsaw [45]. An unusual long-lived multiply charged nuclear fragment, produced from a high-energy cosmic ray, stopped after traveling 90 µm and disintegrated, recorded by a photographic emulsion, as shown in Figure 1.10. The vector from point A to B indicates the track of a potential hypernucleus candidate, while the two lines emanating from point B represent the possible tracks of the two daughter particles resulting from the hypernucleus decay. At first, this observation was met with skepticism. It was suggested that caution should be exercised, as the event might have resulted from the accidental overlap of two unrelated interactions. It was advised to wait for more evidence before publishing the results. However, just after this skepticism, a similar observation was reported independently at Imperial College London [46]. This independent observation strengthened the case for publishing the findings, and both results were later published together in the same journal [45-46].

While early hypernuclear studies using cosmic rays were groundbreaking, they faced significant challenges, particularly low production rates. A major advancement came in the late 1950s with the use of K^- mesons from accelerators, which were captured in nuclear emulsions or helium bubble chambers [47-55]. These photographic detectors allowed direct visualization of hypernuclear events via the strangeness-exchange reaction $K^- + n \rightarrow \Lambda + \pi^-$, where the intrinsic strangeness of the K^- meson enabled conversion of nucleons into hyperons, which is a more effective method for hypernuclei production compared to cosmic rays. In 1963, a significant breakthrough was achieved with the first discovery of a double Λ hypernucleus [56-57]. This event was again observed in Warsaw, with Marion Danysz and Jerzy Pniewski contributing to the discovery. Still using the emulsion detector photographic technique, researchers identified the formation of ${}^{10}_{\Lambda\Lambda}$Be, a beryllium nucleus bound with two Λ hyperons.

Beginning in the 1970s, a technological shift occurred as experimental hypernuclear research transitioned from photographic to electronic detectors. This approach enabled precise studies of hypernuclear structure via the (K^-, π^-) reaction [58-60]. In this reaction, a K^- meson interacts with a nucleon in the target nucleus, and through a strangeness exchange, producing a Λ hyperon. The produced Λ hyperon can be captured by the residual nucleus, leading to the formation of a Λ hypernucleus. Besides the (K^-, π^-) reaction, other reactions, such as (K^-, π^+) [61], (π^+, K^+) [62-63], (π^-, K^+) [64], and (K^-, K^+) [62], were used to produce various hypernuclei, including Λ, Σ, and Ξ hypernuclei. Currently, such reaction-based techniques are still widely employed in modern hypernuclei research, such as the experiments at the Japan Proton Accelerator Research Complex (J-PARC). Equipped with advanced detectors and beamlines, J-PARC has been at the forefront of hypernuclear research, continuously publishing a series of significant studies on hypernuclei [65-67].

Relativistic heavy-ion collisions have emerged as a powerful experimental tool for studying hypernuclei in this century. The extremely high temperatures and densities achieved in heavy-ion collisions create favorable conditions for the abundant production of strange matter, significantly advancing the study of hypernuclei. Particularly, studying the production mechanisms of hypernuclei in relativistic heavy-ion collisions—an environment resembling the conditions of the Big Bang—provides unique insights into their primordial formation in the early universe. The existence and production of hypernuclei in heavy-ion collisions have been well-established over the past decades [68-69]. Recent groundbreaking discoveries, such as the observation of the first antimatter hypernucleus ${}^{3}_{\Lambda}\overline{\mathrm{H}}$ in 2010 [70] and the first ${}^{4}_{\Lambda}\overline{\mathrm{H}}$, recently published in 2024 [71] by the STAR experiment at RHIC, where 15.6 candidates were identified from several billion Au+Au collision events, have further intensified interest in the field of hypernuclear physics. Heavy-ion collisions provide a crucial experimental platform for investigating the intrinsic properties and the production mechanism of hypernuclei.

1.5.2 Λ Binding Energy of Hypernuclei

The Λ binding energy B_Λ, defined as the energy needed to remove the Λ from the hypernucleus, characterizes the Λ -nucleon interaction. The Λ binding energy can be calculated using the invariant masses of the hypernucleus, the Λ hyperon, and the corresponding non-strange core nucleus as follows:

$$B_\Lambda = m_{\mathrm{core}} + m_\Lambda - m_{\mathrm{hypernucleus}}, \tag{1.4}$$

where m_{core} is the invariant mass of the core nucleus (excluding the Λ hyperon), m_Λ is the invariant mass of the Λ hyperon, and $m_{\mathrm{hypernucleus}}$ is the invariant mass of the hypernucleus.

The internal structure of hypernuclei significantly influences the Λ binding energy. Precise measurements of B_Λ provide valuable insights into the underlying Y-N interaction. Since the internal structure of hypernuclei is not yet fully understood, precision experimental measurements of B_Λ, combined with theoretical modeling, are essential for advancing our knowledge of hypernuclear structure.

The hypertriton (${}^{3}_{\Lambda}\mathrm{H}$) is the lightest bound state of hypernuclei with undetermined spin-parity $J^\pi = \frac{1}{2}^+$ or $\frac{3}{2}^+$, consisting of a proton, a neutron, and a Λ hyperon. A recent theoretical study proposes a novel method to probe hypertriton's spin structure via global polarization in heavy-ion collisions [73]. Moreover, the internal structure of hypertriton remains an open question. It is still unclear whether the Λ, neutron, and proton are tightly bound within the hypernucleus, loosely bound as three distinct constituents, or whether the hypertriton is better described as a Λ hyperon weakly bound to a deuteron core. The Λ binding energy of the ${}^{3}_{\Lambda}\mathrm{H}$ is a key observable for understanding the inter-

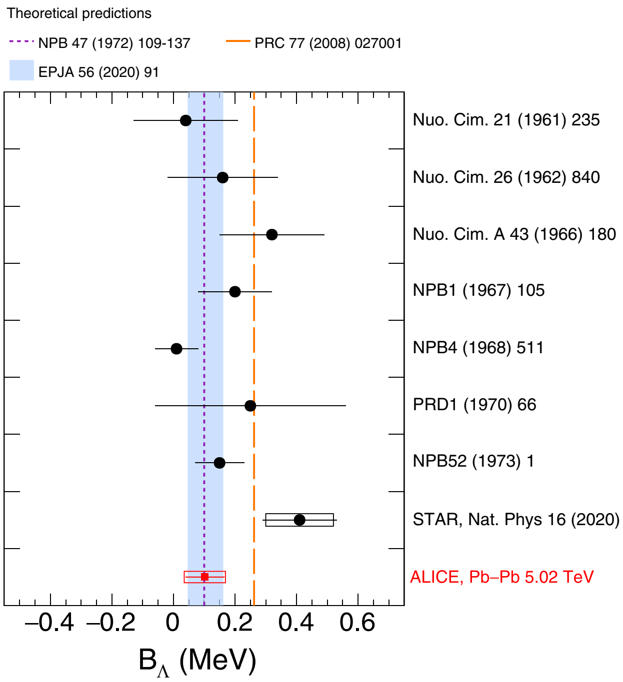

Figure 1.11 Collection of the Λ binding energy measurements for $^{3}_{\Lambda}$H from various experiments, including both historical and recent results. These experimental values are shown in comparison with theoretical predictions from a range of models. The picture is taken from Ref. [72].

nal structure of $^{3}_{\Lambda}$H. Previous experimental measurements, shown in Figure 1.11, have indicated an extremely weak Λ binding energy for $^{3}_{\Lambda}$H. The most recent $^{3}_{\Lambda}$H Λ binding energy measurement from the ALICE (A Large Ion Collider Experiment) Collaboration report a value of $B_\Lambda = 102 \pm 63$ (stat) $\pm$ 67 (syst) keV [72]. This small binding energy is consistent with the hypertriton's large root-mean-square radius (the average distance of the Λ to the deuteron), which is of the order of 10 fm [74-75], confirming that the $^{3}_{\Lambda}$H structure is consistent with a weakly bound system [72].

For the heavier hypernuclei $^{4}_{\Lambda}$H (composed of one Λ hyperon, one proton, and two neutrons) and $^{4}_{\Lambda}$He (composed of one Λ hyperon, two protons, and one neutron), the Λ binding energies are significantly larger, measured in the range of a few MeV, indicating a stronger Y-N interaction. The Λp and Λn interactions are expected to be identical due to the charge symmetry of the strong interaction. The strong force is fundamentally isospin symmetric, meaning it treats protons and neutrons as identical particles, distinguished only by their electric charge. The Λ hyperon, being an isospin singlet (isospin $I = 0$), interacts with nucleons purely through the strong force and does not differentiate between protons and neutrons based on charge. Consequently, in an idealized scenario where electromagnetic effects and mass differences between nucleons are neglected, the Λp and Λn interactions should be identical. Furthermore, according to charge symmetry, the Λ binding energies of mirror hypernuclei, such as ${}^4_\Lambda$H and ${}^4_\Lambda$He, should be equal, as the strong interaction does not distinguish between the interchange of protons and neutrons. However, experimental results show a noticeable difference in the Λ binding energies of these two mirror hypernuclei, indicating the existence of charge symmetry breaking (CSB) effects in the Λ-nucleon interaction.

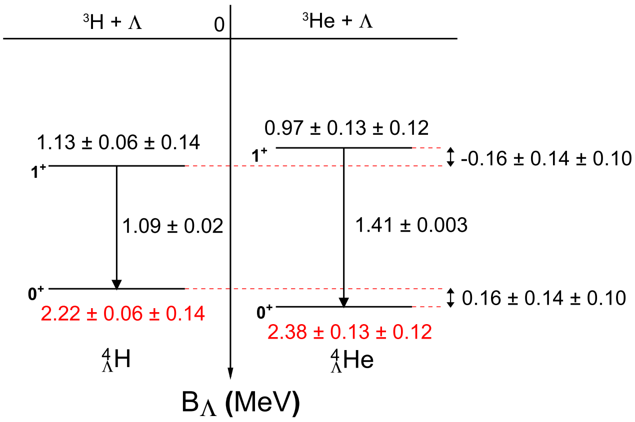

Figure 1.12 The Λ binding energy measurements of ${}^4_\Lambda$H and ${}^4_\Lambda$He from the STAR experiment. The Λ binding energy measurements of ${}^4_\Lambda$H and ${}^4_\Lambda$He in their ground states are obtained by the STAR experiment. The binding energies of the corresponding excited states are derived from γ-ray transition energies measured in previous experiments [76-77]. The picture is taken from Ref. [78].

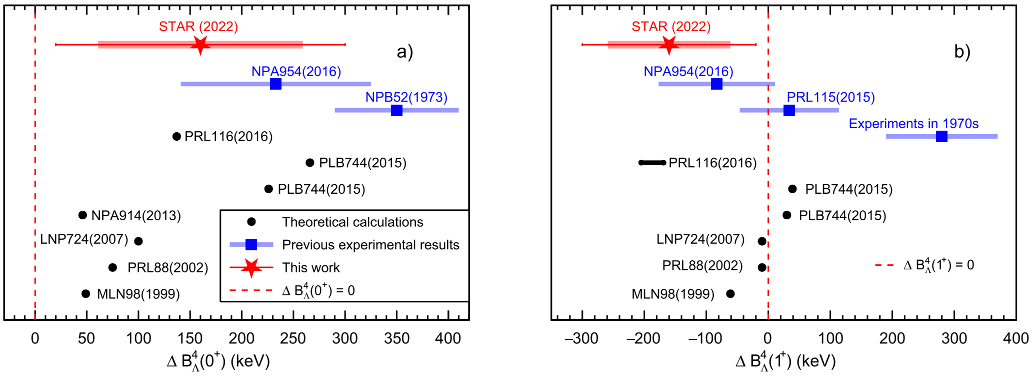

Figure 1.13 The experimental measurements of the Λ binding energy difference between ${}^4_\Lambda$H and ${}^4_\Lambda$He in ground states (panel (a)) and in excited states (panel (b)) compared with theoretical calculations. The picture is taken from Ref. [78].

The STAR Collaboration has measured the Λ binding energies of the mirror hypernuclei, ${}^4_\Lambda$H and ${}^4_\Lambda$He, as illustrated in Figure 1.12 [78]. Compared to the loosely bound ${}^3_\Lambda$H, the significantly stronger Λ binding energies of ${}^4_\Lambda$H and ${}^4_\Lambda$He indicate more compact nuclear structures. The charge symmetry breaking (CSB) effect in hypernuclei with atomic number $A = 4$ is studied through the Λ binding energy differences between ${}^4_\Lambda$H and ${}^4_\Lambda$He. As shown in Figure 1.12 and Figure 1.13, the binding energy differences in both the ground states (0^+) and excited states (1^+) exhibit comparable magnitudes but opposite signs. This distinctive feature is also predicted by the theoretical model denoted as “PRL116(2016)” in Figure 1.12 [79]. This model employs chiral effective field theory (EFT) Y-N potentials combined with a CSB mechanism introduced through Λ–Σ^0 mixing. The measured CSB effect aligns well with various theoretical predictions. It also means that the experimental data do not provide strong discrimination between different models. Further high-precision experimental and theoretical efforts are necessary to fully explore the CSB effect in hypernuclei.

1.5.3 $^{3}_{\Lambda}$H Lifetime

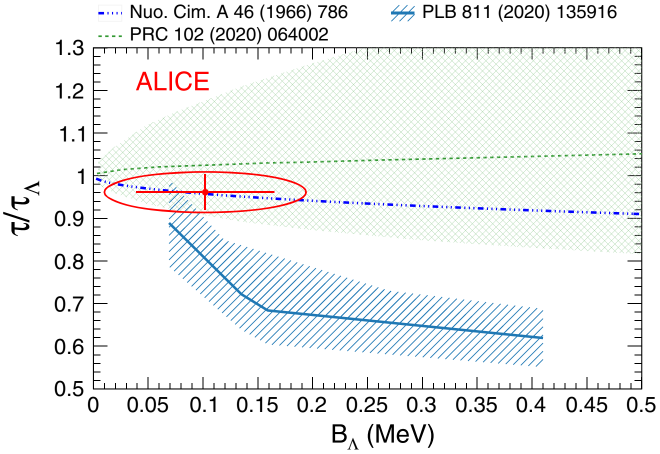

Figure 1.14 The ratio of the $^{3}_{\Lambda}$H lifetime to the free Λ lifetime as a function of the Λ binding energy, based on theoretical predictions. This picture is taken from Ref. [72].

The lifetime of hypernuclei is a fundamental observable for understanding weak decay processes involving hyperons embedded within nuclear matter. In particular, studying the lifetime of $^{3}_{\Lambda}$H provides critical insights, as its comparison with the well-established lifetime of the free Λ hyperon helps to explore the inner structure of $^{3}_{\Lambda}$H. From a theoretical perspective, some models predict a direct correlation, where the Λ binding energy significantly influences the lifetime of $^{3}_{\Lambda}$H. Figure 1.14 presents the ratio of the $^{3}_{\Lambda}$H lifetime to the free Λ lifetime as a function of the Λ binding energy from model calcultaions and experimental measurements from the ALICE Collaboration [72]. In Figure 1.14, theoretical approaches, including pionless EFT with Λ and deuteron degrees of freedom [80] (green), chiral EFT (χEFT) with Λ, proton and neutron degrees of freedom [81] (light blue), and the original pion-exchange calculation [82] (blue), exhibit different degrees of dependence of the hypertriton’s lifetime on its Λ binding energy.

Despite the differences among these models, all models give on a common prediction that when the Λ binding energy is small, the hypertriton’s lifetime is close to that of a free Λ hyperon. This behavior is consistent with the hypertriton’s weakly bound nature, suggests that the decay properties of ${}^{3}_{\Lambda}$H are largely governed by the intrinsic properties of the Λ particle and the Λ decays with minimal influence from the surrounding nuclear environment, behaving almost as if it were a free particle.

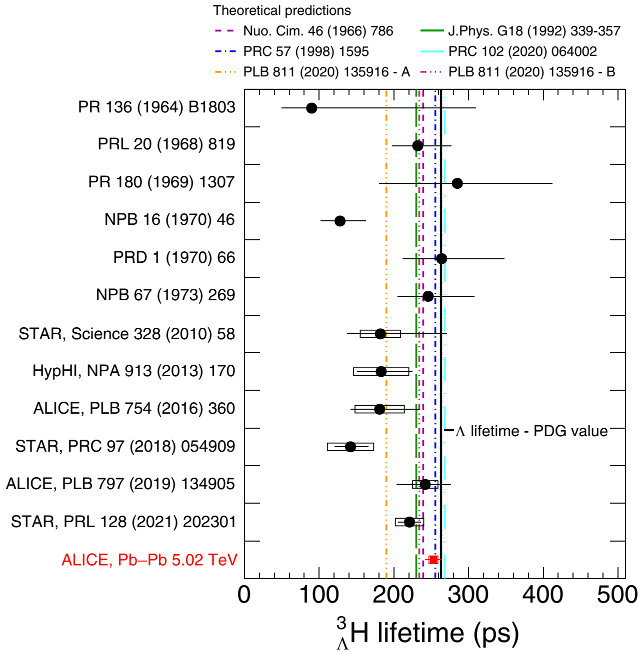

Figure 1.15 The ${}^{3}_{\Lambda}$H lifetime measurements from different experiments compared with theoretical predictions. The ${}^{3}_{\Lambda}$H lifetime measurements from different experiments are presented using markers. The dashed and dash-dotted lines are the theoretical predictions on ${}^{3}_{\Lambda}$H lifetime. The solid black line is the lifetime of the free Λ. This picture is taken from Ref. [72].

In free space, the Λ hyperon decays through weak interactions with a well-established lifetime of approximately 263 ps [83]. As shown in Figure 1.15, a collection of experimental measurements [50-55, 70, 72, 84-88] and theoretical predictions [80-82, 89-90] for the ${}^{3}_{\Lambda}$H lifetime are presented. The horizontal purple line corresponds to a calculation based on the impulse approximation [82], which treats the hypertriton as a loosely bound system with total spin $J = 1/2$, where the deuteron acts as a spectator during the Λ decay. This calculation result uses a Λ binding energy of $B_{\Lambda} = 1$ MeV and includes a correction from final-state pion-nucleon scattering. A second model, denoted as the green line, describes the hypertriton as a Λ hyperon bound to a deuteron core through a ΛN separable potential [89]. In the model, the Λ binding energy is forced to the experimental averaged value $B_{\Lambda} = 0.13 \pm 0.05$ MeV [91]. To simplify the decay dynamics, this calculation adopts the closure approximation. Later, rigorous three-body Faddeev calculations [90] using realistic nucleon-nucleon [92] and hyperon-nucleon potentials [93], shown as the blue line in Figure 1.15, give a hypertriton lifetime about 3% shorter than that of the free Λ. Another theoretical prediction, shown as the blue line, is based on a pionless EFT with Λ and deuteron degrees of freedom [80]. Using the measured $B_\Lambda = 0.13 \pm 0.05$ MeV as input, the model predicts a lifetime slightly higher than the free Λ value. The orange and brown lines in Figure 1.15 represent results from a microscopic three-body calculation based on chiral EFT [81]. The two curves correspond to different assumptions on the Λ separation energy: $B_\Lambda = 135$ keV (orange line) and $B_\Lambda = 69$ keV (brown line), respectively. The earliest hypertriton lifetime measurements were obtained from the absorption of stopped K^- mesons in helium bubble chamber [52-55] and nuclear emulsion [50-51]. More recently, the HypHI [84], STAR [70, 86, 88] and ALICE [72, 85, 87] Collaboration have measured the hypertriton lifetime using heavy-ion collisions. However, as illustrated in Figure 1.15, several experimental results have reported significantly shorter lifetimes for ${}^3_\Lambda$H, leading to what is known as the “hypertriton lifetime puzzle”. Notably, the STAR Collaboration’s 2018 measurement reported a ${}^3_\Lambda$H lifetime significantly shorter than the free Λ lifetime [86]. Although the STAR Collaboration’s most recent result shows an improvement and is closer to the free Λ lifetime compared to the earlier measurement, it still remains considerably lower than the expected free Λ lifetime [88]. In contrast, measurements from the ALICE Collaboration in both 2019 and 2021 consistently reported lifetimes that are in agreement with the free Λ lifetime within experimental uncertainties [72, 87]. This difference in experimental results has created tension over the ${}^3_\Lambda$H lifetime between different experiments and led to many theoretical and experimental studies. Therefore, new and more precise lifetime measurements from STAR experiment are crucial to help resolve the hypertriton lifetime puzzle. These measurements will also improve our understanding of hyperon interactions in nuclear matter and help constrain theoretical models.

1.5.4 Weak Decay Modes of Hypernuclei

To better understand the lifetime of hypernuclei, it is essential to study their weak decay modes. Hypernucleus decays are exclusively governed by the weak interaction. The weak decay of hypernuclei proceeds through two primary modes: mesonic decay (MWD) and non-mesonic decay (NMWD), depending on whether a pion is emitted in the final state.

In mesonic decay, the Λ hyperon inside a hypernucleus decays into a nucleon and a pion, such as:

$$\Lambda \to p + \pi^- \quad \text{(see Figure 1.16 (left))}, \quad \Lambda \to n + \pi^0. \tag{1.5}$$

This process is similar to the free Λ decay but occurs within the nuclear medium, where

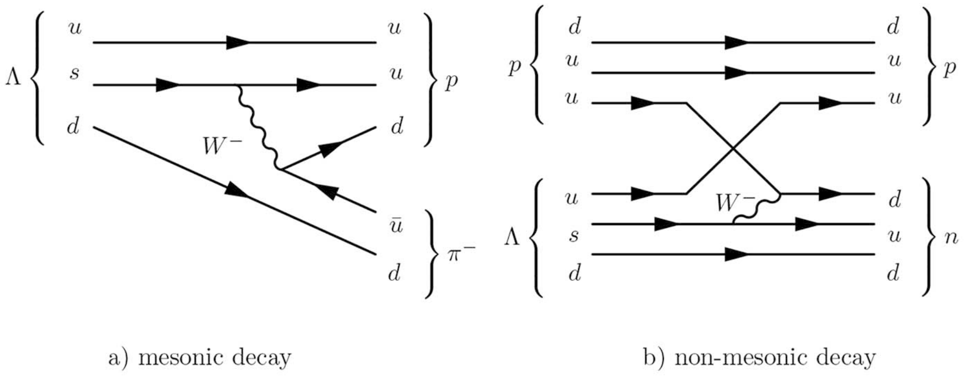

Figure 1.16 Illustration of quark-level processes involved in (a) mesonic and (b) non-mesonic decay modes of a Λ hyperon inside a hypernucleus. The figure is taken from Ref. [94].

surrounding nucleons can modify the decay probability. Mesonic decay in hypernuclei can be suppressed due to the Pauli principle, when the emitted particle momentum falls below the nuclear Fermi momentum. This effect is more pronounced in hypernuclei with larger Λ separation energies, where less energy is available for the emitted particles.

In heavier hypernuclei, where mesonic decays are more suppressed, non-mesonic weak decay becomes more significant. In this mode, the Λ interacts directly with a surrounding nucleon through a weak interaction:

$$\Lambda + p \rightarrow n + p \quad \text{(see Figure 1.16 (right))}, \quad \Lambda + n \rightarrow n + n. \tag{1.6}$$

Unlike mesonic decay, which resembles the free-space decay of a Λ, the non-mesonic channels involve weak interactions between the Λ and the surrounding nucleons within the nuclear medium. These processes can be understood as the weak conversion of a Λ hyperon into a nucleon, mediated by a W boson. Therefore, theoretical models often describe NMWD using meson-exchange frameworks. Moreover, the relatively large Q-value of the NWWD processes ensures that the final-state nucleons are not Pauli blocked, making NMWD more dominant decay mode in heavy-mass hypernuclei. Figure 1.17 presents both theoretical predictions and experimental data for the normalized decay widths of one-proton-induced non-mesonic weak decays as a function of mass number A. A theory using meson exchanges between the Λ hyperon and the nucleon predicts a rising trend with increasing A [95], which is also observed in the experimental measurements.

The total decay width of a hypernucleus is determined by the sum of the partial decay widths of MWD and NMWD channels:

$$\Gamma_{\text{total}} = \Gamma_{\text{MWD}} + \Gamma_{\text{NMWD}}. \tag{1.7}$$

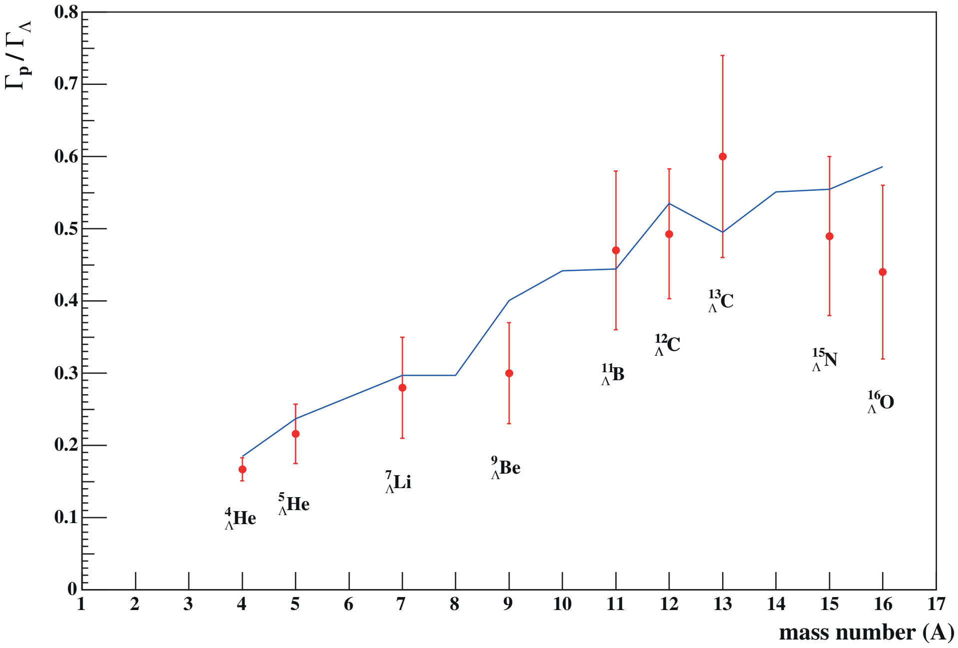

Figure 1.17 Normalized one-proton-induced non-mesonic weak decay widths plotted against mass number *A* of hypernuclei. Experimental data points (red circles) represent experimental measurement results. The blue line represents theory predictions from Ref. [95]. The figure is taken from Ref. [94].

The lifetime of the hypernucleus is then related to the total decay width through the inverse relation

$$\tau = \frac{\hbar}{\Gamma_{\text{total}}}. \tag{1.8}$$

1.5.5 Hypernuclei Production in Heavy-Ion Collisions

The formation of hypernuclei in heavy-ion collisions is not yet fully understood. The production of hypernuclei in heavy-ion collisions is a crucial approach for gaining insights into the fundamental mechanisms underlying hypernuclei formation. Measurements of hypernuclei production spectra and collectivity in heavy-ion collisions offer essential insights into these formation processes.

Theoretical calculations propose two primary mechanisms to explain the production of hypernuclei in heavy-ion collisions: nucleon-hyperon coalescence, where nearby nucleons and hyperons combine in phase space, and thermal emission, where hypernuclei emerge from a chemically equilibrated system during the hadronization phase.

In the coalescence picture, hypernuclei and nuclei are formed when constituent nucleons and hyperons are sufficiently close in both spatial and momentum space. This process occurs when the relative distances and momenta of the constituents fall within specific proximity thresholds, or equivalently, when their wave functions overlap significantly in phase space, allowing them to “coalesce” into a bound state. Given complete phase space information of nucleons and hyperons at a given moment, the formation probability of a bound nucleus from a pair or triplet of baryons can be determined using the coalescence formula [96-97]:

$$\frac{dN}{d^3P} = g \int d^3x_1 d^3x_2 d^3p_1 d^3p_2 f_A(\vec{x}_1, \vec{p}_1) f_B(\vec{x}_2, \vec{p}_2) \rho^W_{AB} \delta^3(\vec{P} - \vec{p}_1 - \vec{p}_2). \tag{1.9}$$

Here, $f_A(\vec{x}_1, \vec{p}_1)$ and $f_B(\vec{x}_2, \vec{p}_2)$ represent the phase-space distributions of the constituent nucleons and hyperons. ρ^W_{AB} is the Wigner phase space density for the bound state formed by particles A and B. This function includes information about both the relative positions and momenta of the constituent particles, effectively characterizing the internal structure of the composite system. It reflects how likely particles A and B are to form a bound state based on their spatial and momentum proximity in phase space.

Two common implementation of coalescence process are:

- Wigner Function based coalescence: This method relies on the quantum mechanical description of particles. The Wigner phase-space density is used to account for the quantum mechanical internal structure of the hypernucleus and nucleus. The coalescence probability is calculated by integrating over the overlap of the Wigner functions of the constituent baryons and the formed hypernucleus. It is a more detailed and accurate method.
- Box coalescence: This is a simplified method where particles are considered to coalesce if they are within predefined boundaries in momentum and coordinate space, represented as a "box" in phase space. It assumes that the ρ^W_{AB} is a product of step functions. The coalescence probability is considered constant within a fixed range of relative positions and momenta and zero outside these boundaries. If the relative momenta and positions of two constituent nucleons fall within these defined boundaries, they are assumed to form a bound state. This approach is simpler and quick to compute but less sensitive to the detailed internal structure of the hypernucleus.

In the box coalescence, the procedure of formation of a three-constituent nucleus or hypernucleus with mass number $A = 3$, follows the following steps:

- Formation of a two-constituent state. The absolute values of the relative distance and momentum of all possible nucleon (or hyperon) pairs at freeze-out from transport models are calculated in their center-of-mass frame. A preliminary two-constituent state is formed if the following conditions are satisfied:

$$\Delta r = |\vec{r}_{n1} - \vec{r}_{n2}| < \Delta r_{max,nn}, \quad \Delta p = |\vec{p}_{n1} - \vec{p}_{n2}| < \Delta p_{max,nn}.$$

The preliminary two-constituent state is then characterized by the combined momentum:

$$\vec{p}_{nn} = \vec{p}_{n1} + \vec{p}_{n2},$$

and the position:

$$\vec{r}_{nn} = \frac{\vec{r}_{n1} + \vec{r}_{n2}}{2}.$$

- Addition of a third constituent. In the local rest frame of this preliminary two-constituent state, the model searches for a third nucleon or hyperon. The third particle is added if it satisfies the proximity conditions:

  $$\Delta r = |\vec{r}_{nn} - \vec{r}_{n3}| < \Delta r_{max,nnn}, \quad \Delta p = |\vec{p}_{12} - \vec{p}_{n3}| < \Delta p_{max,nnn}.$$

  The potential formation of a three-constituent state with $A = 3$ is then characterized by the combined momentum:

  $$\vec{p}_{123} = \vec{p}_{nn} + \vec{p}_{n3},$$

  and the position:

  $$\vec{r}_{123} = \frac{\vec{r}_{n1} + \vec{r}_{n2} + \vec{r}_{n3}}{3}.$$

In the coalescence production mechanism, the invariant momentum spectra of Λ-hypernuclei with mass number A can be described using the invariant momentum spectra of the constituent nucleons and Λ hyperons:

$$E_A \frac{d^3 N_A}{dp_A^3} = B_A \left(E_p \frac{d^3 N_p}{dp_p^3} \right)^Z \left(E_n \frac{d^3 N_n}{dp_n^3} \right)^N \left(E_\Lambda \frac{d^3 N_\Lambda}{dp_\Lambda^3} \right)^L, \tag{1.10}$$

where E_A and p_A are the energy and momentum of the hypernucleus with mass number A. E_p, E_n, and E_Λ are the energies of the proton, neutron, and Λ hyperon, respectively. Z, N, and L represent the number of protons, neutrons, and Λ hyperons in the hypernucleus, respectively. B_A is the invariant coalescence factor, giving the coalescence probability. The coalescence factor B_A plays a crucial role in relating the production yields of hypernuclei to the yields of their constituent particles.

The thermal model is a fundamental framework used in heavy-ion collisions to describe particle production in heavy-ion collisions. The thermal model of particle production in heavy-ion collisions is based on the assumption that, the abundances of produced particles are fixed at the stage of chemical freeze-out. Only feed-down from decays changes the final particle yields. In thermal model, the hardons, nuclei and hypernuclei are treated equally with thermal equilibrium assumption. The hardons, nuclei and hypernuclei are supposed to freeze out simultaneously in thermal model. Consequently, the yields of light nuclei and hypernuclei compared with hardons can provide critical information about the freeze-out of them.

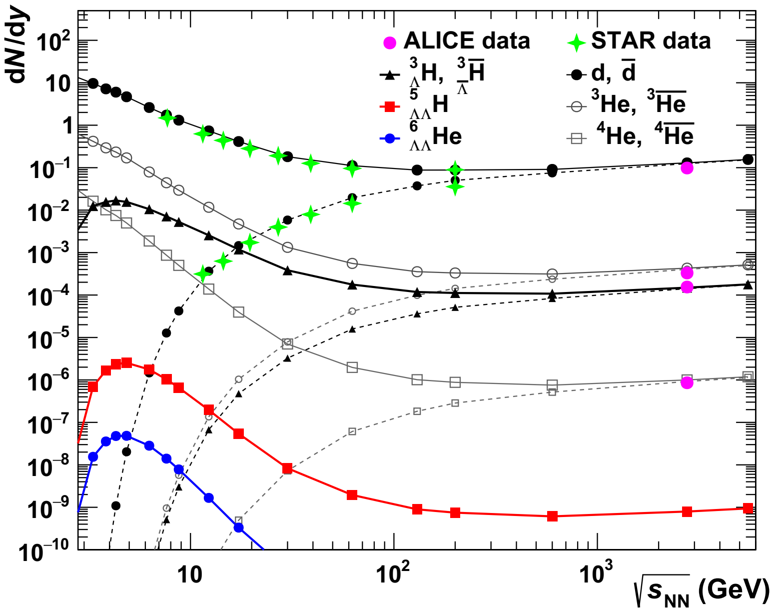

Figure 1.18 Thermal model predictions for light nuclei and hypernuclei production yields, shown as a function of collision energy and compared with experimental results from the ALICE and STAR experiments. This picture is taken from Ref. [98].

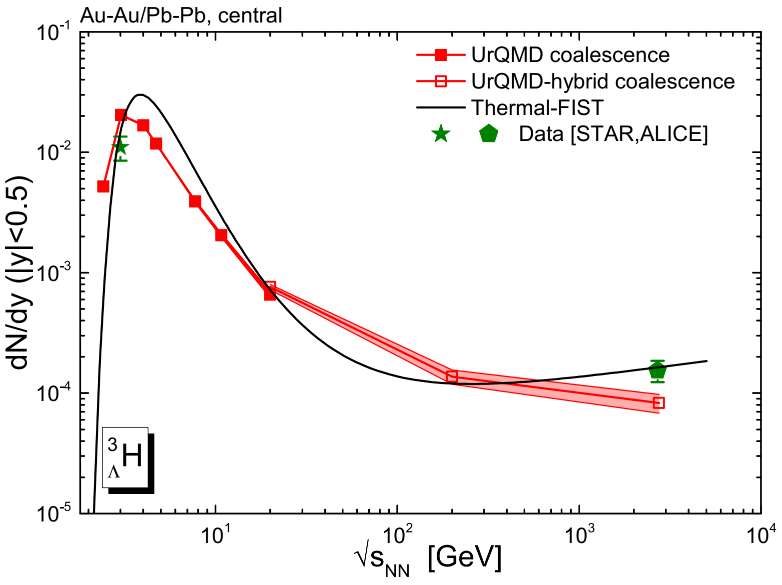

Figure 1.19 Comparison of ${}^3_\Lambda$H production yields as a function of collision energy predicted by the thermal model [99] and the UrQMD model with a coalescence picture. This picture is taken from Ref. [97].

Various experimental observables of hypernuclei are studies through the thermal models and the dynamic models with coalescence applied as an afterburner. In particular, investigating the energy dependence of hypernuclei production yields provides an essential insight. Such studies can distinguish between different formation mechanism models and improve our understanding of the production mechanism.

As shown in Figure 1.18, the thermal model predicts an enhancement in hypernuclei production at lower energies [98]. Similarly, Figure 1.19 demonstrates that the coalescence model also anticipates an increase in the production of ${}^{3}_{\Lambda}\mathrm{H}$ at lower energies, consistent with the thermal model's predictions. The pronounced enhancement in hypernuclei production at lower collision energies can be attributed to the high baryon density of the collision system. These findings highlight the importance of conducting heavy-ion collision experiments in this low energy region to advance hypernuclei research.

However, as seen in Figure 1.19, the current data is limited to only two energy points, making it difficult to decisively differentiate between the thermal and coalescence models. Although both models offer reasonable descriptions of the data, subtle differences exist. For example, the coalescence model predicts a slightly lower peak in hypertriton yields and a more pronounced suppression at higher beam energies compared to the thermal model. Nonetheless, the limited data points restrict the ability to draw strong conclusions. To address this limitation, more hypernuclei yield measurements at a wide range of collision energies are needed to enable a more comprehensive comparison with model predictions and help clarify the underlying mechanisms of hypernuclei production.

The Strangeness Population Factor (S_A) is defined as:

$$S_A = \frac{{}^{A}_{\Lambda}\mathrm{H}}{{}^{A}\mathrm{He} \times \left(\frac{\Lambda}{p}\right)}. \tag{1.11}$$

This double ratio represents the relative suppression of hypernuclei production compared to light nuclei production. The S_A serves as an effective observable for studying the differences in the production mechanisms of light nuclei and hypernuclei. This is because it minimizes the influence of variations in hyperon production, effectively canceling out such effects.

According to the coalescence parameter relation in 1.10, S_A can be expressed in terms of the coalescence parameters B_A of light nuclei and hypernuclei:

$$S_A = \frac{{}^{A}_{\Lambda}\mathrm{H}}{{}^{A}\mathrm{He} \times \left(\frac{\Lambda}{p}\right)} = \frac{B_A\left({}^{A}_{\Lambda}\mathrm{H}\right)(p_T)}{B_A\left({}^{A}\mathrm{He}\right)(p_T)}. \tag{1.12}$$

Model studies suggest that S_3 is sensitive to the onset of deconfinement [100]. The AMPT model, which simulates the dynamics of heavy-ion collisions, has two distinct

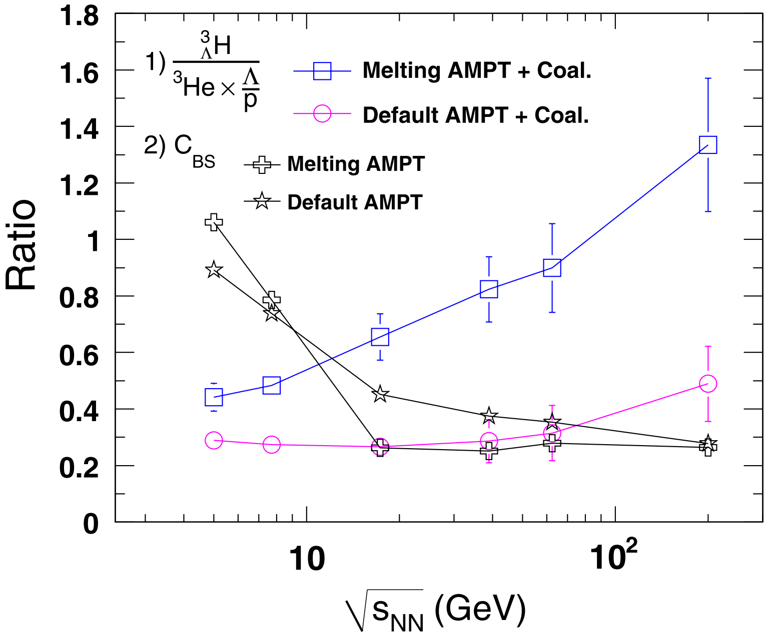

Figure 1.20 Energy dependence of S_3 and C_{BS} are presented. The figure is taken from Ref. [100].

modes: the default AMPT model that incorporates purely hadronic interactions, and the string melting AMPT model that includes a fully partonic phase during the early evolution of the collision system [101]. These two modes can be employed to distinguish between hadronic and partonic effects. As shown in Figure 1.20, the S_3 values obtained from the string melting AMPT are significantly higher than those from the default AMPT, which suggest S_3 is enhanced in a system with the presence of partonic interactions. Furthermore, the increase in S_3 with collision energy is more pronounced than the decrease observed in the global baryon-strangeness correlation coefficient C_{BS}. The C_{BS} is a global observable that quantifies the overall correlation between baryon number and strangeness in the system and is frequently used as an indicator for the onset of deconfinement. This suggests that S_3, which is more sensitive to local baryon-strangeness correlation, could potentially serve as a more effective probe for studying the onset of deconfinement.

Figure 1.21 presents the predictions of S_3 as a function of collision energy [97]. In the coalescence model, two different sets of source radius were employed, corresponding to the box coalescence parameter Δr. The larger source radius, $\Delta r = 9.5$ fm, is consitent with the characteristic large radius of the loosely bound hypertriton. In comparison, the smaller source radius, $\Delta r = 4.3$ fm, chosen to align with the size of triton. The figure clearly illustrates that at lower collision energies ($\sqrt{s_{NN}} \leq 20$ GeV), the coalescence model exhibits strong sensitivity to the choice of source radius. A larger source size notably suppresses the predicted S_3 values. This suppression arises be-

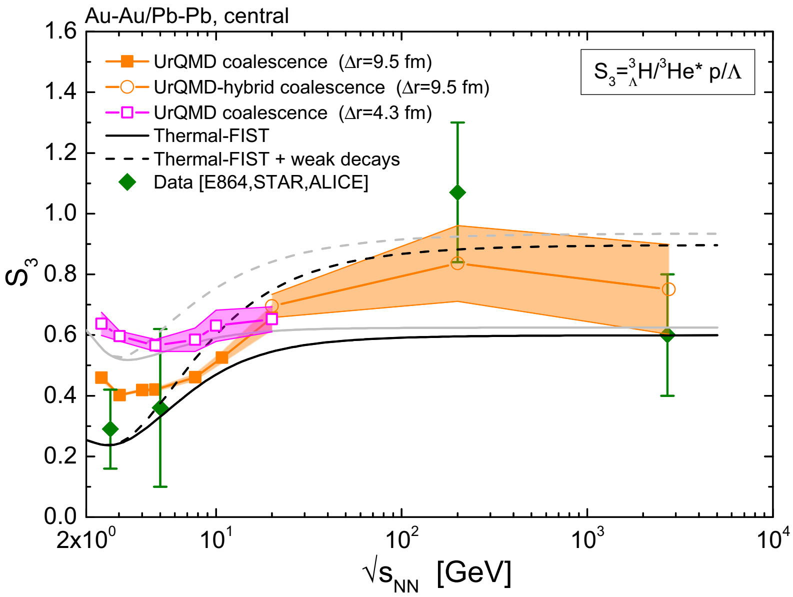

Figure 1.21 The energy dependence of S_3 under various scenarios is presented. The solid black and grey lines represent thermal model predictions that include weak decay feed down from hyperons to protons, while the dashed lines depict results without this correction. Additionally, the black lines account for feed-down contributions from unstable nuclei, whereas the grey lines do not. Results from the coalescence approach with a coalescence radius of $\Delta_r = 9.5$ fm are shown as an orange band. The magenta band corresponds to coalescence results using a smaller coalescence radius of $\Delta_r = 4.3$ fm. Experimental data are indicated by green symbols. The figure is taken from Ref. [97].

cause a larger spatial distance between constituent particles reduces the probability of successful coalescence into hypernuclei. Additionally, the thermal model, particularly when including feed-down contributions from unstable nuclei to stable lighter nuclei (such as p, d, t, ^{3}He, and ^{4}He), also predicts a noticeable suppression of S_3 at lower energies [102]. This is attributed to the decay processes affecting the final observed yields of stable particles, subsequently influencing the calculated S_3. The role of feed-down in thermal models emphasizes the complexity of final yield estimations. Comparing experimental data with coalescence model predictions will provide stronger confirmation of the hypertriton's loosely bound nature and its large radius. To conclusively differentiate between these models, high-precision experimental data across a range of beam energies are essential. Such measurements would not only validate the underlying assumptions and mechanisms within each model but also deepen our understanding of structure and formation dynamics of $^3_\Lambda$H in heavy-ion collisions.

1.6 Motivation of this Thesis

The internal structure and production mechanisms of $^3_\Lambda$H in heavy-ion collisions remain not fully understood. One of the key challenges is the long-standing hypertriton lifetime puzzle, where experimental measurements show discrepancies from theoretical predictions. Understanding the formation mechanisms and intrinsic properties of hypertriton is crucial for advancing knowledge of hypernuclear physics and Y-N interactions.

The RHIC BES phase II (BES II) program provides an excellent opportunity to explore these phenomena [103]. The BES-II program, conducted at the RHIC facility at Brookhaven National Laboratory (BNL), is designed to investigate the QCD phase diagram by varying the collision energies of heavy ions from $\sqrt{s_{NN}}$ = 3 to 54.4 GeV. Theoretical studies have suggested that the production of hypernuclei is significantly enhanced at low collision energies due to high baryon density. This wide energy range includes the low-energy region where hypernuclear production is expected to be significantly enhanced. The STAR experiment previously reported measurements of the ${}^{3}_{\Lambda}\mathrm{H}$ lifetime in 2018 [86], which indicated a significantly shorter lifetime compared to the well-established free Λ hyperon lifetime.

The primary objective of this thesis is to utilize the high-statistics data from the RHIC BES-II program to conduct precise measurements of light hypernuclei lifetimes and production yields. One of the major goals is to reslove the hypertriton lifetime puzzle by performing high-precision measurements of ${}^{3}_{\Lambda}\mathrm{H}$. This work aims to clarify the discrepancies in previous measurements and theroies. In addition, this thesis focuses on improving lifetime measurements of the mirror hypernuclei ${}^{4}_{\Lambda}\mathrm{H}$ and ${}^{4}_{\Lambda}\mathrm{He}$. Enhancing the measurement precision for these hypernuclei, especially the extremely rare ${}^{4}_{\Lambda}\mathrm{He}$, will provide valuable experimental data. All these measurements would provide critical input for theoretical calculations, helping to constrain model parameters and improve the understanding of Y-N interactions.

Furthermore, by measuring the production yields of ${}^{3}_{\Lambda}\mathrm{H}$ in heavy-ion collisions at low energies and comparing the results with model predictions, this research seeks to confirm the formation mechanisms of hypernuclei. The analysis will explore whether the formation of hypertriton is predominantly through coalescence or thermal processes.

In summary, this research aims to advance our understanding of hypernuclei by performing precise experimental measurements of lifetimes and production yields. The outcomes are expected to contribute significantly to the understanding of hypernuclei formation, internal structure, and the fundamental nature of Y-N interactions in extreme nuclear environments. The results from this thesis will also constrain the theoretical model of hypernuclei.

1.7 Thesis Outline

The analysis presented in this thesis utilizes data from Au+Au collisions at $\sqrt{s_{NN}}$ = 3.0, 3.2, 3.5, 3.9, and 7.2 GeV, recorded by the STAR detector at RHIC as part of the BES-II program. This thesis particularly focuses on the measurement of light hypernuclei, including ${}^{3}_{\Lambda}$H, ${}^{4}_{\Lambda}$H and ${}^{4}_{\Lambda}$He, aiming to investigate their properties and production mechanisms. Hypernuclei are of special interest due to the introduction of strange quarks into the nuclear system, offering a unique avenue to explore the behavior of strange matter and the underlying hyperon-nucleon interactions.

The thesis is organized as follows:

The first chapter provides a brief overview of the necessary physical background for the analysis. It introduces the fundamental theories of the Standard Model, QCD, the QCD phase structure, the general process of relativistic heavy-ion collisions, and hypernuclei.

The second chapter describes the experimental setup used for data collection. It includes an introduction to RHIC complex, the STAR detector system, and the BES-II program.

The third chapter details the analysis procedures, including the selection of experimental data sets, particle identification, hypernuclei signal reconstruction, efficiency corrections, and systematic uncertainty estimations.

The fourth chapter presents and discusses the experimental measurement results, including lifetime and production yield analyses.

The fifth chapter provides the summary of the analysis and an outlook on future research in the study of hypernuclei.

Chapter 2 Experimental Setup

The exploration of strongly interacting matter, particularly the QGP, requires recreating extreme conditions akin to those present microseconds after the Big Bang. To systematically investigate the properties and evolution of QGP and to map the QCD phase diagram, advanced experimental facilities have been developed. Among these, the RHIC at Brookhaven National Laboratory stands out as a leading platform. Notably, the BES-II program at RHIC is specifically designed to explore regions of high baryon chemical potential, critical for probing the high-density portion of the QCD phase diagram and identifying the potential QCD critical point. This region is also particularly valuable for hypernuclei research, providing insights into hyperon-nucleon interactions and hypernuclei production mechanisms under extreme baryon density conditions. In the following chapter, the RHIC facility, the STAR experiment and the BES-II program are introduced.

2.1 The Relativistic Heavy Ion Collider

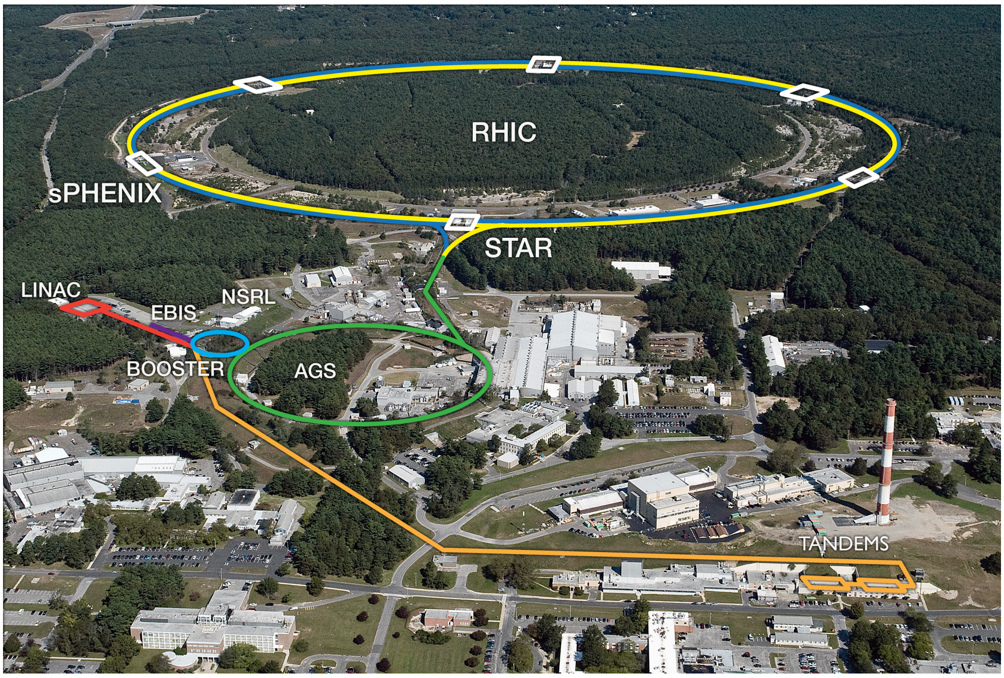

Figure 2.1 An overhead view of the RHIC facility. This picture is taken from Ref. [104].

The Relativistic Heavy Ion Collider [105-107], located at Brookhaven National Laboratory in Upton, New York, is a forefront experimental facility dedicated to investigating nuclear matter under extreme conditions of temperature and density, similar to those present shortly after the Big Bang, as shown in Figure 2.1. Proposed in 1983 as part of a long-term plan for nuclear science [108], the construction of RHIC began in 1991 [109]. It commenced operations in 2000, collecting its first experimental data, establishing itself as the world's first and highest-energy heavy-ion collider [105, 110].

The RHIC consists of two intersecting superconducting storage rings, referred to as the "Blue Ring" and the "Yellow Ring", where particles circulate in clockwise and counter-clockwise directions, respectively. Each ring has a circumference of 3.8 km and intersects at six designated collision points where various experimental detectors are located. Since its operation began in 2000, RHIC has hosted multiple experiments at six intersection points along its 3.8 km circumference. The initial major experiments included STAR at 6 o'clock, PHENIX at 8 o'clock, PHOBOS at 10 o'clock, and BRAHMS at 2 o'clock. The PHOBOS, BRAHMS, and PHENIX experiments ended their operations in 2005, 2006, and 2016, respectively. In 2023, the sPHENIX experiment was newly commissioned at the former PHENIX location. Currently, the STAR experiment continues to operate and contribute valuable data and is the longest running experiment at RHIC.

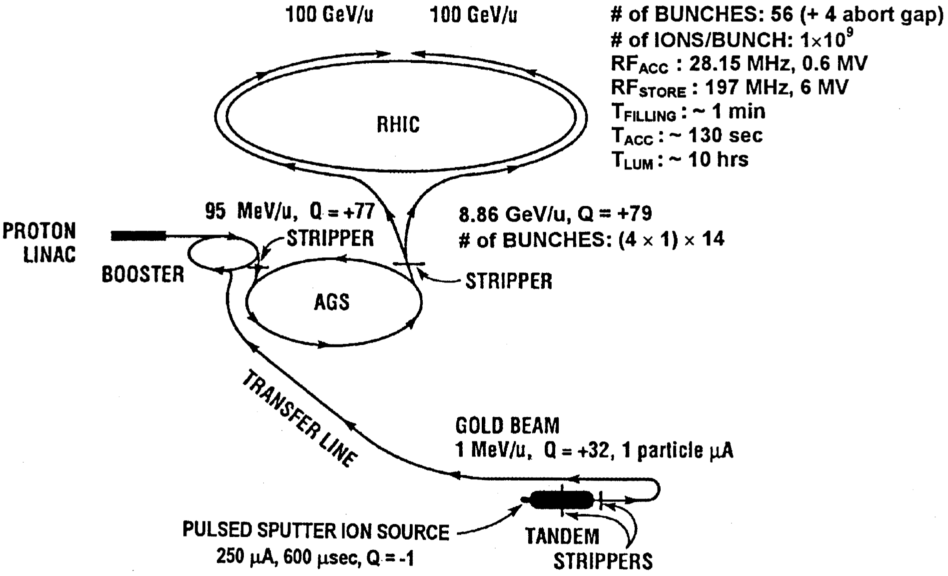

Figure 2.2 Overall schematic diagram of RHIC accelerator complex and acceleration scenario for gold beam. This picture is taken from Ref. [106].

RHIC can accelerate and collide a wide variety of ion species, including protons, deuterons, helium, copper, gold, zirconium, ruthenium, and uranium nuclei [111-116]. The highest energy achieved at RHIC for heavy-ion beams, such as $^{197}_{79}\mathrm{Au}$ ions, is 100 GeV/nucleon [117]. The top collision energy is 510 GeV for p+p collisions [118]. Taking gold ions as an example, as shown in Figure 2.2, acceleration process at RHIC involves several stages to prepare and accelerate the ions for high-energy collisions [106].

Gold ions are initially produced with a negative charge state ($Q = -1e$) by a pulsed sputter ion source and injected into the Tandem Van de Graaff accelerator. Within this accelerator, the ions undergo partial electron stripping and are accelerated to an energy of 1 MeV/nucleon. Upon exiting the Tandem, the ions have a charge state of $Q = +32e$ and are subsequently directed to the Booster Synchrotron for further acceleration and processing. In the Booster Synchrotron ring, additional electrons are stripped, resulting in a charge state of $Q = +77e$, and the ions are accelerated to an energy of 95 MeV/nucleon. Following the Booster, the ions enter the Alternating Gradient Synchrotron (AGS), where they are accelerate further to 8.86 GeV/nucleon, achieving up to 99.7% of the speed of light. At the exit of the AGS, the ions undergo final electron stripping to achieve a fully ionized state with a charge of $Q = +79e$. The completely stripped ions are then transferred via the AGS-to-RHIC beam transfer line, where they are injected into the RHIC rings and accelerated to energies up to 100 GeV/nucleon. The transfer line terminates at a junction where the ions are steered into one of RHIC's two superconducting storage rings. Depending on the magnetic configuration, ions can be injected into either the clockwise-traveling or the counter-clockwise within the RHIC rings. Finally, at the designated collision points within the RHIC rings, the bunches are further compressed and brought into collision. The Tandem Van de Graaff generator was used as the ion source for this acceleration chain. However, since 2012, the Electron Beam Ion Source (EBIS) has replaced it, offering improved performance and reliability as the pulsed sputter ion source. It resides in the proton Linac area as shown in Figure 2.3, and is capable of producing high charge states of heavy ion species from helium to uranium in short pulses [119-120]. The EBIS+linac-based pre-injector system can accelerates these ions to a final energy of 2 MeV/nucleon [119-120]. These ions are then injected into the following synchrotron ring.

In 2020, the U.S. Department of Energy announced plans to upgrade RHIC into an Electron-Ion Collider (EIC), which is expected to start operating in the 2030s [119, 122]. RHIC may have its final run in 2025 to prepare for the construction of the EIC. The upgrade to the EIC will mark an important step forward, offering new opportunities for exploring the inner microcosm dominated by gluons, to reveal the arrangement of the quarks and gluons.

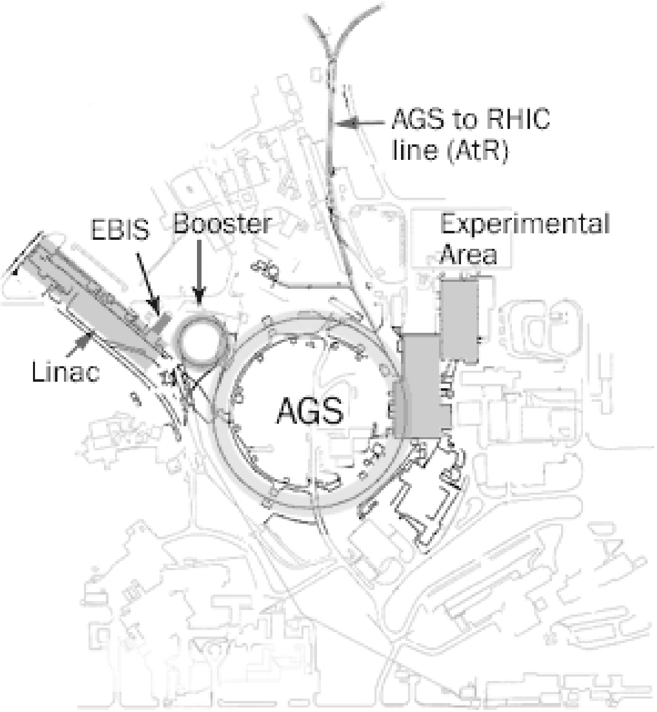

Figure 2.3 Schematic diagram of RHIC accelerator complex with the new pre-injector system, which is called EBIS. This picture is taken from Ref. [121].

2.2 STAR Detector System

The STAR detector is one of the primary experimental detectors at RHIC, designed with the initial aim to study the properties and behavior of strongly interacting nuclear matter under extreme energy densities and to search for signatures of QGP formation [123-124]. In order to achieve these goals, STAR was designed to record the tracks of the aftermath of the relativistic heavy-ion collisions. The STAR detector is a large, massive and complex system, weighing approximately 1200 tons and comparable in size to a house. It offers excellent capabilities in tracking, momentum measurement, and particle identification.

The STAR detector system is centered around the beamline and consists of multiple subsystems. The STAR coordinate system is defined with its origin point at the geometric center of the detector. The x-axis points towards the south, the y-axis extends vertically upward, and the z-axis is aligned along the beam pipe, with its positive direction oriented towards the west. In the schematic Figure 2.4, the side closer to the viewer, where the people are located, corresponds to the east side, while the side farther away represents the west.

The central cylindrical structure of the STAR detector, illustrated in Figure 2.4, consists of multiple subsystems. At its core, the main Time Projection Chamber (TPC) [126] serves as the primary tracking detector, measuring 4.2 meters in length

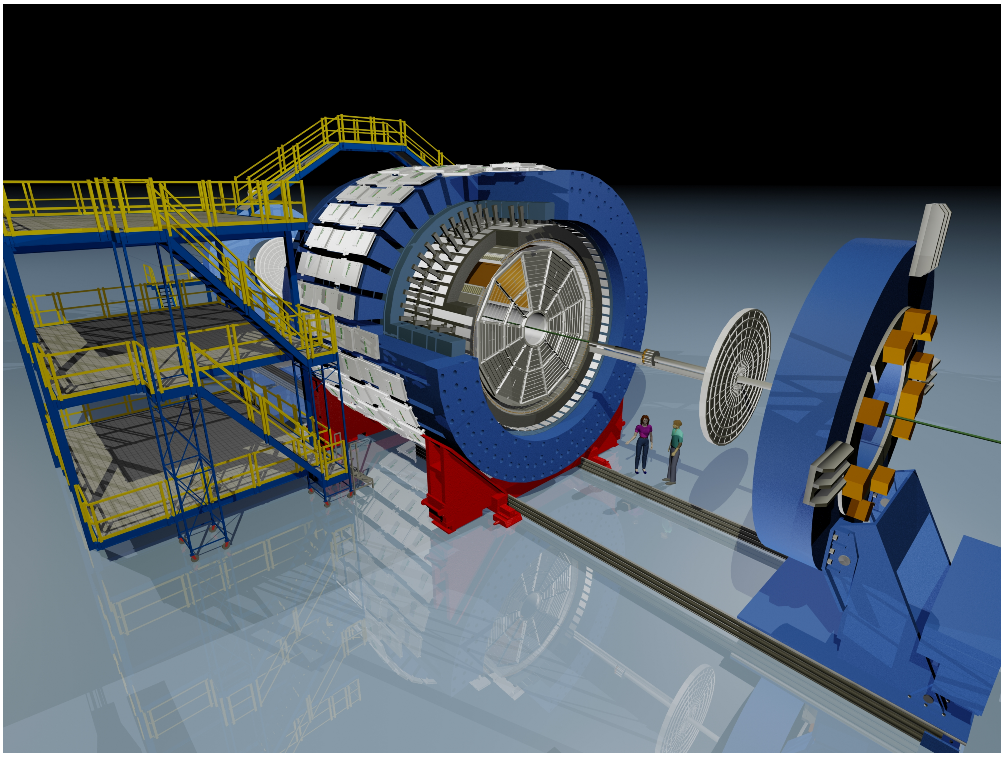

Figure 2.4 The schematic diagram of the STAR detector system. This picture is taken from Ref. [125].

along the beam axis and spanning radially from 50 cm to 200 cm from the beamline. It provides full azimuthal coverage ($0 < \phi < 2\pi$) and a pseudorapidity range of $|\eta| \leq 1.0$ in the center-of-mass frame. The TPC records charged particle tracks, measures their momentum, and identifies particles by measuring their ionization energy loss (dE/dx). As part of the STAR detector upgrade under the BES-II program, the inner sectors of the TPC were rebuilt as the inner Time Projection Chamber (iTPC) [127] upgrade. The iTPC was fully installed in 2019. This upgrade significantly enhanced tracking at small angles relative to the beamline, extending the pseudorapidity coverage from $|\eta| \leq 1.0$ to $|\eta| \leq 1.5$. Futhermore, it improved acceptance for low-momentum tracks and enhanced both momentum and dE/dx resolution. These enhanced detector performance are crucial for BES-II.

Installed around the outside of the TPC, the barrel Time-Of-Flight detector (bTOF, commonly referred to as TOF) [128-129] consists of 120 MRPC (Multi-gap Resistive Plate Chambers) TOF trays, each containing 32 MRPC modules. The TOF system provides full azimuthal coverage ($0 < \phi < 2\pi$) and a pseudorapidity coverage of $|\eta| \lesssim 0.9$. The TOF measures the flight time of charged particles, playing a crucial role in particle identification by distinguishing different particles by mass (strictly speaking, the square of the mass-to-charge ratio). Placed beyond the TOF, the Barrel Electromagnetic Calorimeter (BEMC) [130] plays a crucial role in triggering and studying high-p_T processes. It provides full azimuthal coverage ($0 < \phi < 2\pi$) and extends over a pseudorapidity range of $|\eta| < 1$. By measuring energy deposition and the spatial distribution of electromagnetic showers, the BEMC distinguishes single photons from photon pairs originating from π^0 and η meson decays, as well as differentiates electrons from hadrons. Surrounding the BEMC, the STAR magnet system [131] is a solenoidal magnet with an inner diameter of 5.27 meters, an outer diameter of 7.32 meters, and a length of 6.85 meters. The magnet generates a nearly uniform magnetic field parallel to the beam pipe, with an operational field range of $0.25 < |B_z| < 0.5$ T. All barrel region sub-detectors, except for the MTD, are enclosed within this magnetic field. The Muon Telescope Detector (MTD) [132], installed in 2014 at the outermost layer of the STAR detector system, is specialized for in muon identification and triggering. It provides approximately 45% azimuthal coverage within the pseudorapidity range of $|\eta| < 0.5$. The outermost placement of the MTD ensures that most hadrons are absorbed before reaching the detector, thereby enhancing its capability to distinguish muons from hadrons. On the west side of the STAR detector, an End-cap Electromagnetic Calorimeter (EEMC) [133] is installed, extending the coverage of the BEMC with a pseudorapidity range of $1.086 \leq \eta \leq 2.00$. On the east side of the STAR detector, an End-cap Time-Of-Flight detector (eTOF) [134] is employed, providing a pseudorapidity coverage of $1.05 < \eta < 1.5$. Fully installed in 2019 as part of the STAR detector upgrade for BES-II program, the eTOF enhances the detector's particle identification capabilities, extending the momentum range over which different particle species can be distinguished.

In addition to these sub-detectors, the Event Plane Detector (EPD), Vertex Position Detector (VPD), and Zero-Degree Calorimeter (ZDC) are positioned along the beamline on either side of the STAR detector. The Vertex Position Detector (VPD) [135] is symmetrically positioned at a distance of 5.7 meters from the center of STAR and is designed to measure the primary collision vertex location and determine the event "start time", which is crucial for time-of-flight-based particle identification. Further along the beamline, at a distance of 18 meters from the detector's center, the Zero-Degree Calorimeter (ZDC) [136] is positioned at small forward angles. It detects neutral spectator fragments, primarily neutrons, emitted along the beam directions in heavy-ion collisions, playing a crucial role in collision centrality determination and luminosity monitoring. The two EPD wheels [137-138] are designed to measure charged particles emitted in the forward and backward directions and have been fully operational since 2018 as part of the BES-II program detector upgrades. Positioned 3.75 meters from the center of the STAR detector, they are positioned at the same location of Beam-Beam Counter (BBC) [139]. While the BBC covered a pseudorapidity range of $3.3 < |\eta| < 5.0$, the EPD extends this range to $2.1 < |\eta| < 5.1$. Compared to the BBC, the EPD provides significantly improved resolution of event plane reconstruction and enhances centrality determination.

2.2.1 Time Projection Chamber

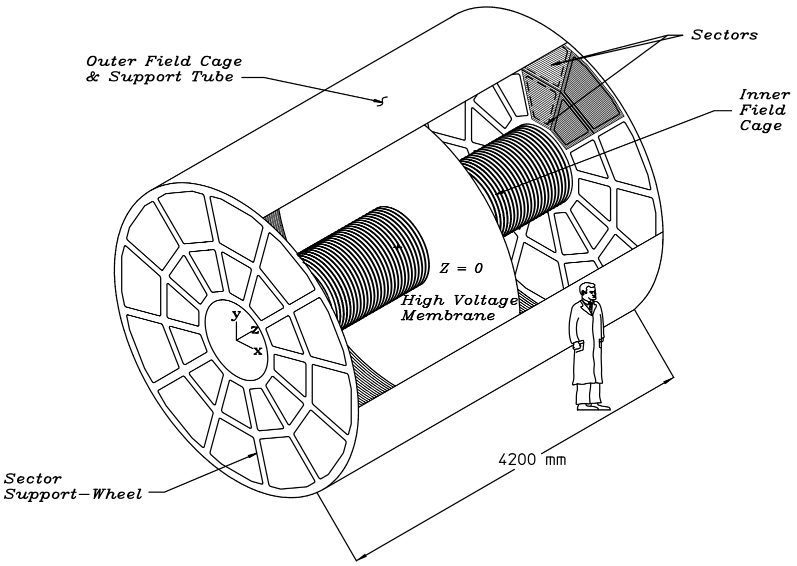

Figure 2.5 The schematic diagram of the STAR TPC. This picture is taken from Ref. [126].

The Time Projection Chamber (TPC) serves as the primary tracking detector of the STAR experiment at RHIC [126]. It enables three-dimensional tracking and particle identification across a large acceptance range, playing a vital role in reconstructing particle trajectories, measuring momentum, and distinguishing between different particle species.

As depicted in Figure 2.5, the STAR TPC is a cylindrical detector with a length of 4.2 meters and a diameter of 4.0 meters. It consists of two concentric field cage cylinders, with the Inner Field Cage having a radius of 0.5 meters and the Outer Field Cage having a radius of 2.0 meters. It covers full azimuth within pseudorapidity range of $|\eta| < 1.8$ by the geometry. The drift volume between these two field cages cylinders is divided into two equal sections, each 2.1 meters in length, by a thin conductive Central Membrane (CM) at the center of the TPC. The drift chamber is filled with P10 gas, composed of 90% argon (Ar) and 10% methane (CH_4), at 2 mbar above atmospheric pressure. This gas mixture is chosen for its high electron drift velocity, which reaches a stable peak at relatively low electric fields, reducing sensitivity to temperature and pressure fluctuations. The ability to operate at lower electric fields or voltages also simplifies the design of the field cage. Argon, as a high-Z noble gas, provides excellent dE/dx resolution by generating approximately 28 free electron-ion pairs per centimeter of track length, enhancing particle identification capabilities. Methane, on the other hand, acts as a quenching gas, absorbing ultraviolet photons that are emitted simultaneously with the electron-ion pairs. By preventing these photons from triggering additional secondary electron production via the photoelectric effect on the TPC surfaces, methane helps maintain a controlled ionization environment, reducing unwanted charge buildup and improving detector stability. The uniform electric field inside the TPC is established through the central membrane, the end caps, and the concentric field cage cylinders. The central membrane is operated at high voltage 28 kV. The end caps are held at ground potential. The field cage consists of a series of equi-potential rings that segment the space between the central membrane and the anode planes into 182 divisions. The central membrane is attached to the central ring. To maintain a uniform electric field, the rings are biased using resistor chains, creating a consistent voltage gradient between the central membrane and the grounded end caps. This uniform electric field is essential for the controlled drift of ionization electrons, enabling precise particle tracking and identification. As a result, a well-defined and uniform electric field of approximately 135 V/cm is generated along the beamline, achieving an electron drift velocity of 5.45 cm/μs. Additionally, the magnetic field maintained by the magnet subsystem is also aligned with the beamline, with a strength of 0.5 T in this analysis.

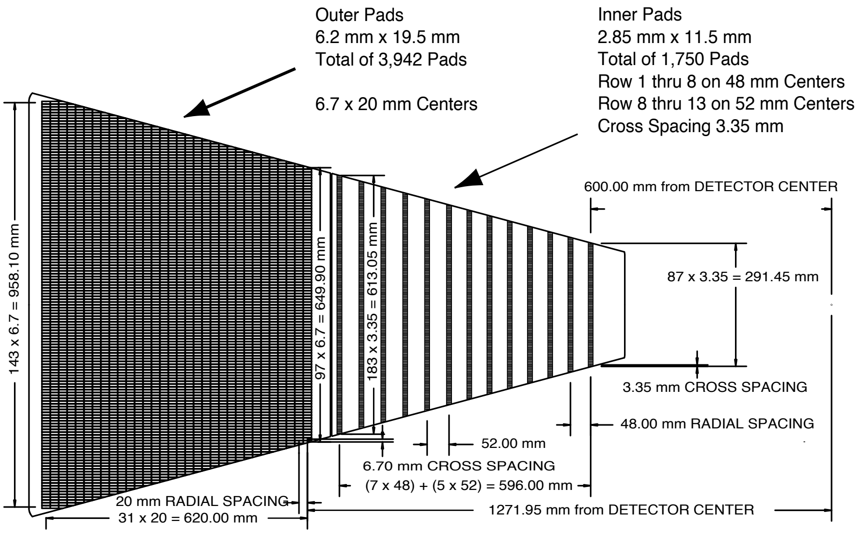

Figure 2.6 The schematic diagram of a full readout sector. The inner subsector, positioned on the right, consists of smaller pads arranged in rows with wider spacing. In contrast, the outer subsector, located on the left, features larger pads that are more densely packed. This picture is taken from Ref. [126].

The readout system of the TPC is based on Multi-Wire Proportional Chambers (MWPC) with readout pads. It is structured into modular units supported by aluminum wheels, forming an array of 12 sectors arranged in a circular pattern, resembling a clock face. This configuration ensures minimal spacing of 3 mm between sectors, creating a compact and efficient readout system. As shown in Figure 2.5, the 12 readout sectors are symmetrically positioned on both end-cap planes. The modular sector-based design simplifies both construction and maintenance. Each readout sector is further divided into inner and outer subsector. Figure 2.6 illustrate a full sector in the pad plane of TPC end-cap before the iTPC upgrade. The inner subsector contains 13 pad rows, while the outer subsector consists of 32 pad rows. With a total of 45 pad rows per sector, the system enables up to 45 hits per track, ensuring comprehensive track reconstruction. The outer subsectors feature continuous pad coverage with larger pads of size 6.2 mm × 19.5 mm, eliminating gaps between pad rows to enhance dE/dx resolution. This configuration ensures full collection of the ionization signals along the track, increasing the number of detected ionization electrons and improving the statistical accuracy of dE/dx measurements. Additionally, the seamless pad arrangement contributes to better tracking resolution by reducing position measurement errors through anti-correlation effects between adjacent pad rows. The inner subsector was designed with smaller pad size 2.85 mm × 11.5 mm, which helps relieve track merging at small radii in region of high track density. This smaller pad size enhances two-hit resolution, making the inner subsector highly effective for reconstructing tracks in regions with high particle multiplicity. However, the use of smaller pads necessitated a design trade-off, resulting in separated pad rows instead of continuous pad coverage. This constraint was imposed by cost considerations and the available packing density of front-end electronics channels. As a result, while the inner subsectors significantly extend position measurements towards smaller radii, its contribution to dE/dx resolution is somewhat limited. With the iTPC upgrade in 2019, the inner subsectors are rebuilt with 40 new pad rows, while the outer subsectors remain unchanged, increasing the total number of pad rows per sector from 45 to 72. This expansion enables up to 72 hits per track, significantly enhancing tracking capabilities. The additional pad rows in the inner subsector minimize gaps between them, resulting in continuous pad coverage, leading to improvement on dE/dx resolution.

The TPC plays a crucial role in reconstructing charged particle trajectories and performing particle identification (PID) by measuring ionization energy loss. The entire process of obtaining track and particle information involves multiple stages, including drift electron detection, track reconstruction, momentum determination, and energy loss-based PID.

As charged particles traverse the TPC, they ionize the working gas, producing ion-electron pairs along their paths. The resulting ionization electrons drift towards one of the readout end caps under a uniform electric field, moving at a drift velocity of approximately 5.45 cm/μs. To ensure accurate tracking, the TPC is equipped with a laser calibration system that independently measures the drift velocity every few hours using artificial tracks generated by laser beams [140-141]. These drifting electrons serve as the primary means of reconstructing the trajectory of the ionizing particle.

Upon reaching the MWPCs near the readout planes, the electrons encounter a grid of anode wires. In the high-field region surrounding these wires, avalanche multiplication occurs, amplifying the charge signal by a factor of 1000–3000. The positive ions generated during the avalanche induce a measurable image charge on the segmented readout pads. The signal of the charge induced from an avalanche is distributed across multiple adjacent readout pads. The electronics system collects these signals, and the hit position in the x-y plane is determined using a charge centroid reconstruction method. By analyzing the distribution of induced charge over neighboring pads, this method achieves a spatial resolution finer than the width of an individual pad. Additionally, the MWPC measures the arrival time of the ionization electrons as they travel from their ionization point to the anode plane. Using the event start time, which is established by external detectors such as the VPD, the drift time can be determined. By combining the measured drift time with the known electron drift velocity, the z-position of the ionization point is accurately reconstructed. Given the (x, y, z) positions of the ionization points, the full trajectory of the ionizing particle can be determined.

Since the TPC operates within a solenoidal magnetic field of 0.5 T along the longitudinal direction, charged particles follow helical trajectories due to the Lorentz force acting perpendicular to both the magnetic field and their velocity. This results in circular motion in the plane transverse to the magnetic field (the x-y plane) and uniform motion along the field direction (z-axis), producing a helix-shaped trajectory. The full momentum vector of the particle can be extracted from the reconstructed helical path. In the presence of a magnetic field $\vec{B} = B\hat{z}$, the momentum decomposes into a component perpendicular to $\vec{B}$ (transverse) and one parallel to it (longitudinal):

$$\vec{p} = \vec{p}_T + \vec{p}_L = (p_x\hat{x} + p_y\hat{y}) + p_z\hat{z}, \quad p_T = \sqrt{p_x^2 + p_y^2}, \tag{2.1}$$

where $\vec{p}_T = p_x\hat{x} + p_y\hat{y}$ is the transverse momentum (perpendicular to the magnetic field direction), and $\vec{p}_L = p_z\hat{z}$ is the longitudinal momentum (parallel to the magnetic field direction). The Lorentz force only affects the transverse motion, causing the trajectory to bend with radius R. To derive the transverse momentum from the observed curvature of the trajectory in the magnetic field, we begin with the Lorentz force experienced by a charged particle moving through a magnetic field:

$$\vec{F}_{\text{Lorentz}} = q\vec{v} \times \vec{B}. \tag{2.2}$$

This force is always perpendicular to both $\vec{v}$ and $\vec{B}$, which causes the particle to undergo circular motion in the plane perpendicular to the field, i.e., the transverse x-y plane. The radius R of this circular motion reflects the curvature of the track and depends on the particle's transverse velocity v_T and the magnetic field strength. The magnitude of the Lorentz force acting as the centripetal force for the circular motion is:

$$F = |q|v_T B, \tag{2.3}$$

where $|q|$ is the absolute value of the particle's electric charge and v_T is the transverse speed (the component of $\vec{v}$ perpendicular to $\vec{B}$). Meanwhile, the required centripetal force to maintain circular motion is given by:

$$F = \frac{mv_T^2}{R}, \tag{2.4}$$

where m is the particle's mass and R is the curvature radius of its circular path in the x-y plane. Equating the Lorentz force and the centripetal force:

$$|q|v_T B = \frac{mv_T^2}{R}. \tag{2.5}$$

Recognizing that the transverse momentum is $p_T = mv_T$, we finally obtain:

$$p_T = |q|BR. \tag{2.6}$$

This expression shows that the transverse momentum is directly proportional to the magnetic field strength and the radius of curvature. Thus, by measuring R from the track curvature and knowing B, the transverse momentum p_T of the particle can be accurately extracted from its trajectory. The total momentum of the particle can be extracted from the curvature radius and the pitch angle of the helix, which is determined from the geometrical shape of the reconstructed trajectory and reflects the ratio between longitudinal and transverse motion. In addition, the sign of the particle's electric charge is determined from the direction of curvature: positively and negatively charged particles bend in opposite directions under the magnetic field, resulting in helices with opposite handedness. Together, these features allow the TPC to determine the momentum over charge and the charge sign of a particle with high precision. This provides essential information for tracking and event reconstruction, contributing to accurate particle identification and kinematic analysis in high-energy collision events.

The energy loss of a charged particle as it traverses the TPC gas is a valuable quantity for particle identification (PID). Theoretically, the dE/dx of a charged particle as a function of its momentum p is described by the Bethe-Bloch equation:

$$\frac{dE}{dx} = Kz^2 \frac{Z}{A} \frac{1}{\beta^2} \left[\frac{1}{2} \ln \frac{2m_e c^2 \beta^2 \gamma^2 T_{\max}}{I^2} - \beta^2 - \frac{\delta(\beta\gamma)}{2} \right], \tag{2.7}$$

where $K = 4\pi N_A r_e^2 m_e c^2 \approx 0.307075$ MeV$\cdot$ mol$^{-1}\cdot$cm^2 is a proportionality constant, z is the charge of the incident particle, and Z and A represent the charge number and atomic mass of the medium, respectively. $T_{\max}$ refers to the highest possible kinetic energy transferred in a single collision, I is the mean excitation potential characteristic of the material, and δ accounts for density-dependent effects. This equation describes how charged particles lose energy through ionization as they move through a medium, depending on their velocity and charge. Since different particles follow distinct energy loss curves at a given momentum, the Bethe-Bloch equation provides a foundation for PID by distinguishing various particle species based on their measured dE/dx values.

In the STAR TPC, as a charged particle traverses the working gas, it undergoes collisions with gas molecules, causing atomic ionization and releasing ionization electrons. The deposited energy of a charged particle is estimated by summing the charge signals collected across multiple pad rows along its track. However, due to granularity in the ionization process and statistical fluctuations described by Landau distribution, the energy loss varies significantly across different track segments. In most ionization process, only a few tens of eV are released, while in rare collisions, hundreds of eV are lost, resulting in the production of more ionization electrons [142]. As a result, rare high-energy losses can lead to the formation of large ionization clusters in certain short track segments, causing unusually high energy deposition. This distorts the calculated dE/dx and introduces significant statistical fluctuations, ultimately limiting the accuracy of measurements. Due to these fluctuations, measurement of dE/dx over short track segments fails to provide a reliable representation of the actual energy loss. To obtain a more reliable measurement of dE/dx, the truncated mean method is applied. This approach removes the top 30% of the largest ionization clusters and averages the remaining 70% of the collected energy loss samples. By excluding these high-energy outliers, the truncated mean method effectively mitigates the impact of statistical fluctuations, yielding a more stable estimate of the most probable energy loss. Although the truncated mean method significantly improves the accuracy of dE/dx measurements, further studies have shown that directly fitting the entire dE/dx distribution with straggling functions, which characterize statistical fluctuations in energy loss, provides a more representative estimation of the most probable energy loss [143-144]. This approach enhances the calibration of dE/dx by correcting for systematic variations in gas gain, detector response, and path length effects. By incorporating such modeling, detector-dependent biases are reduced, improving particle identification (PID) performance in the STAR TPC.

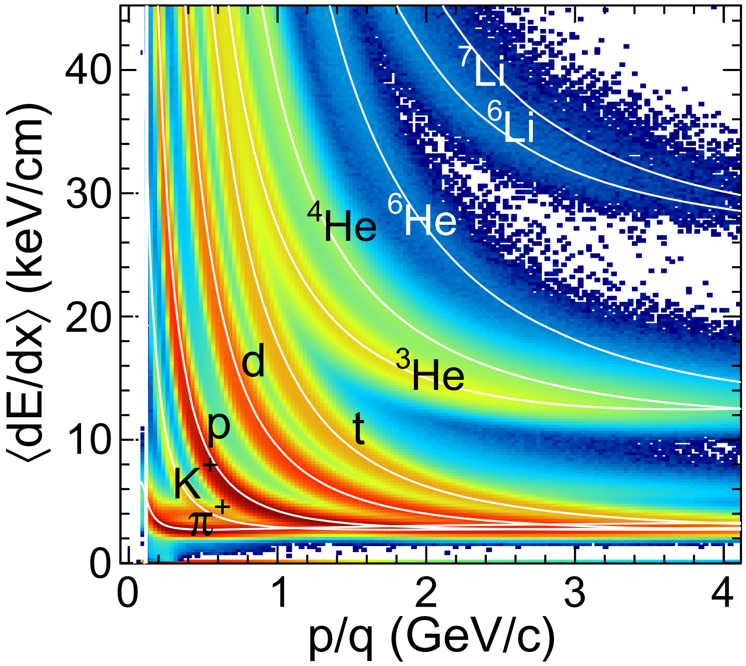

Figure 2.7 Momentum dependence of dE/dx for positively charged particles measured by the TPC. The curves represent the Bichsel expectation for each species [144]. The picture is taken from Ref. [145].

Figure 2.7 illustrates the momentum dependence of dE/dx for charged particles measured by the TPC. The bands corresponding to pions, kaons, protons, deuterons, tritons and other light nuclei are presented in the picture, while the theoretical predictions are depicted as the curves. As momentum increases, the bands gradually overlap due to the convergence of the theoretical dE/dx values for different particle species.

Completed in 2019, the iTPC upgrade introduced a finer segmentation of the inner pad plane and a renewal of the inner sector wire chambers, significantly enhancing the performance of the TPC [127]. With the iTPC upgrade, the lower p_T threshold has been reduced from 125 MeV/c to 60 MeV/c, significantly improving sensitivity to

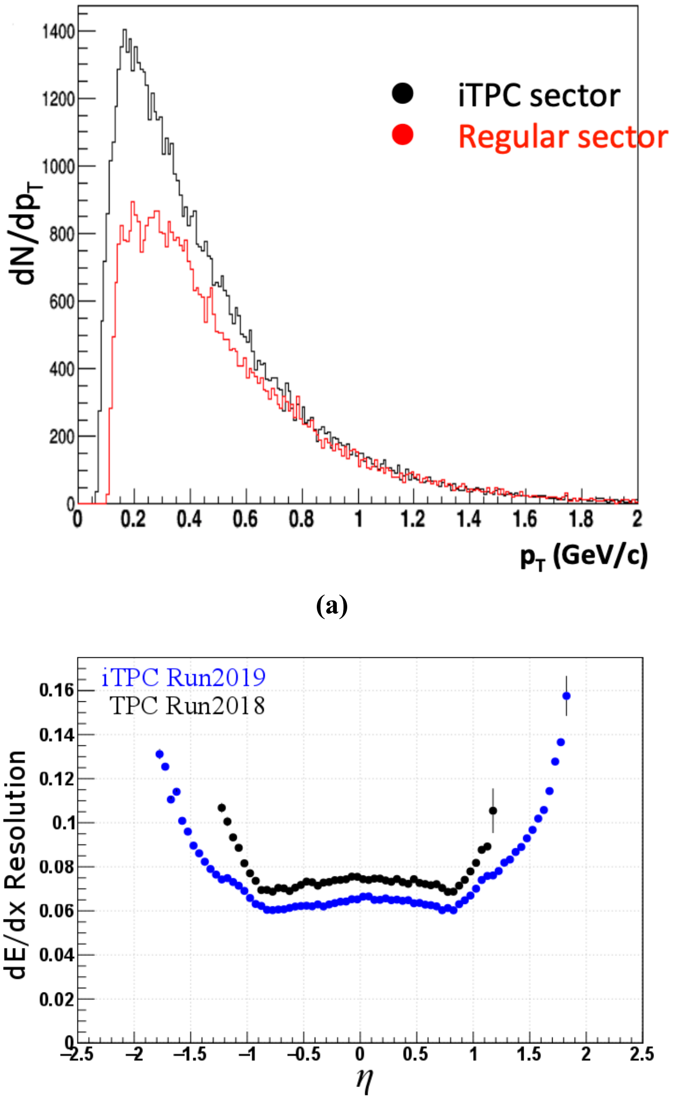

(a)

(b)

Figure 2.8 Performance comparison of the TPC before and after the iTPC upgrade. The improvements achieved with the iTPC include a lower p_T threshold, enhanced tracking efficiency, extended η acceptance, and improved dE/dx resolution. The picture is taken from Ref. [146].

low-momentum tracks compared to the previous TPC configuration. Additionally, the iTPC measurements exhibit enhanced precision in both tracking and energy loss resolution. The pseudorapidity acceptance, previously constrained by tracking performance and detector geometry, has been extended from $|\eta| \leq 1.0$ to $|\eta| \leq 1.5$, allowing for more comprehensive coverage of particle trajectories. Figure 2.8 illustrates the reconstructed p_T distribution and the dE/dx resolution as a function of η, demonstrating the improved performance resulting from the iTPC upgrade [146]. The increased acceptance enables measurements at smaller angles relative to the beamline, enhancing the detector's capability to explore a wider phase space. These advancements are essential for data collection in BES-II, particularly in the fixed-target (FXT) mode, where precise tracking and extended acceptance are crucial.

2.2.2 Time of Flight

The STAR TOF system is desined with the primary goal of enhancing particle identification, particularly in the high-momentum region, where the particle identificition using dE/dx from TPC become less effective. The TOF detector is bulit based on Multigap Resistive Plate Chambers (MRPC) technology [147], The barrel Time of Flight detector was installed in the STAR experiment in 2010. By precisely measuring time intervals along with track momentum and position information from the TPC, the TOF system significantly enhances the particle identification capability.

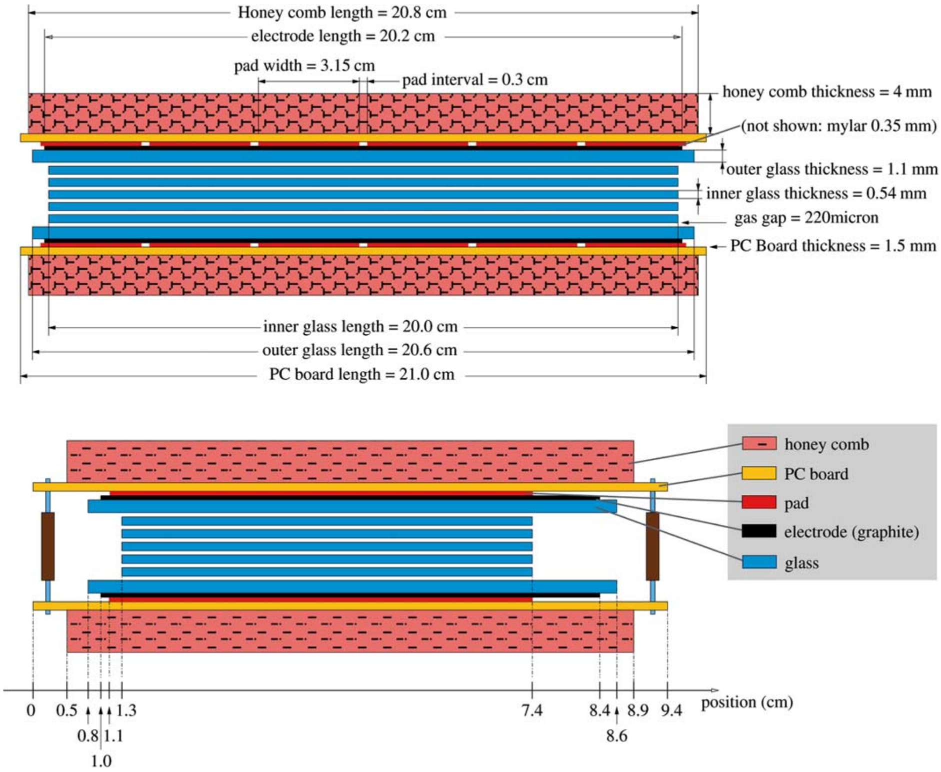

Figure 2.9 Schematic diagram of an MRPC module. The top view represents the long edge, while the bottom view corresponds to the short edge. The figure is taken from Ref. [129].

The TOF system consists of 120 trays, covering the entire cylindrical surface of STAR's TPC, providing full azimuthal acceptance and a pseudorapidity range of $|\eta| \lesssim 0.9$ [128-129]. Each tray contains 32 MRPC modules, with each module having 6 readout channels. Figure 2.9 illustrates the side and end views of an MRPC module. The upper and lower views in the figure correspond to the long and short edges, respectively. Each MRPC module consists of a stack of 7 resistive plates, comprising five 0.54 mm-thick inner glass plates and two 1.1 mm-thick outer glass plates, separated by six

220 μm-wide gas gaps. The gaps are filled with a gas mixture of 95% Freon R-134a and 5% SF_6 at STAR. Isobutane improves the timing resolution, while SF_6 suppresses large avalanches ("streamers"), preventing unwanted signal distortions. Graphite electrodes are applied to the outer surfaces of the wider outer glass plates. When a high voltage is applied across these electrodes, a strong and uniform electric field is generated within the gaps, ensuring efficient charge multiplication and signal detection.

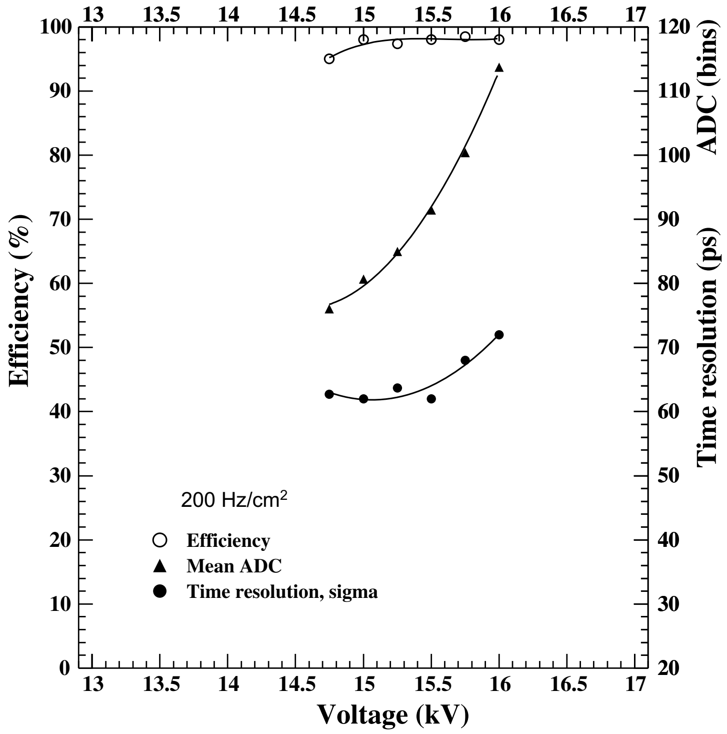

Figure 2.10 Efficiency (open circles), time resolution (solid circles, in ps), and average signal total charge (triangles, in ADC bins with 0.25 pC/bin) as functions of the applied voltage for the STAR MRPCs at an instantaneous beam rate of 200 Hz/cm^2. The figure is taken from Ref. [129]

As a charged particle traverses the MRPC, it ionizes the gas within the gaps, generating primary ionization electrons along its trajectory. The strong electric field inside the gaps induces Townsend avalanche amplification, significantly amplifying the initial ionization signal. Due to the resistive nature of both the electrodes and glass plates (with volume and surface resistivities on the order of 10^{13} Ω/cm and 10^5 Ω, respectively), they are transparent to the induced charge from avalanches. The induced charge from avalanches from all gas gaps are collected on the copper readout pads positioned outside the electrodes. Each readout pad layer contains a row of six pads. Figure 2.10 presents the detection efficiency, time resolution, and average signal charge as functions of the applied voltage, for the STAR MRPCs from CERN test-beam experiments. The results demonstrate a broad voltage plateau, achieving a high detection efficiency

(>95%) and a sub-one hundred picosecound time resolution.

The TOF system determines time intervals using two detectors: an event "start" detector, the VPD, and a charged particle "stop" detector, the barrel of MRPCs. The start time (t_1) is provided by the VPD, while the stop time (t_2) is determined by the MRPC barrel. The time interval for the particle's flight is then given by $\Delta t = t_2 - t_1$. With the path length (L) obtained from the TPC, the inverse velocity ($1/\beta$) of the charged particle is given by:

$$\frac{1}{\beta} = \frac{c\Delta t}{L}, \tag{2.8}$$

where c is the speed of light. The relationship between inverse velocity and particle momentum provides the foundation for the system's particle identification capabilities. The track momentum and the corresponding inverse velocity allow for the determination of the charged particle's mass, given by:

$$m = p\sqrt{\left(\frac{1}{\beta}\right)^2 - 1}. \tag{2.9}$$

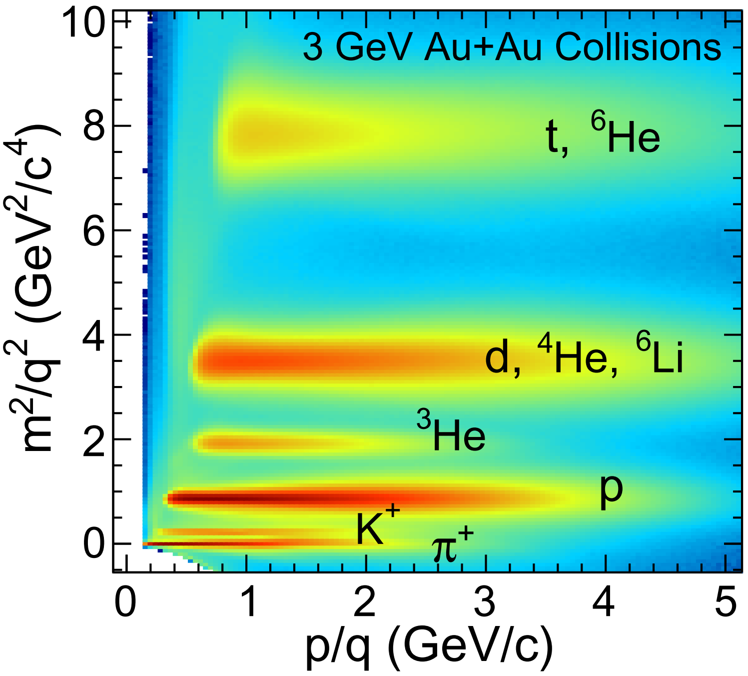

Figure 2.11 Momentum dependence of particle m^2/q^2. The bands of π^+, K^+, p, ^{3}He, d, ^{4}He, ^{6}Li, t, and ^{6}He are presented. ^{4}He and ^{6}Li share the same m^2/q^2 as d, while ^{6}He shares the same m^2/q^2 as t. The figure is adapted from Ref. [145].

Figure 2.11 presents the m^2/q^2 distribution as a function of momentum. As shown, the TOF system provides additional mass information for particle identification (PID). In Figure 2.7, the dE/dx distribution from the TPC illustrates how certain particle species, such as kaons, pions, protons, deuterons, tritons, as well as ^{3}He and ^{4}He, tend to merge at higher momenta, making them indistinguishable using dE/dx alone. However, as demonstrated in Figure 2.11, these overlapping particles can be effectively separated using the measured m^2/q^2 values from the TOF system. The TOF system significantly enhances PID capabilities, especially at higher momentum, where dE/dx alone is insufficient for distinguishing particles.

2.3 Beam Energy Scan Phase II Program

The BES program aims to explore the QCD phase structure by varying the center-of-mass energy of heavy-ion collisions [148]. Conducted from 2010 to 2017, the first phase of the Beam Energy Scan (BES-I) covered Au+Au collisions at $\sqrt{s_{NN}}$ = 7.7 to 200 GeV, corresponding to a baryon chemical potential (μ_B) up to approximately 400 MeV. The results from BES-I provided indications of interesting physics, including the QGP turn-off, ordered phase transition, and QCD critical point at collision energies below 20 GeV [148-152].

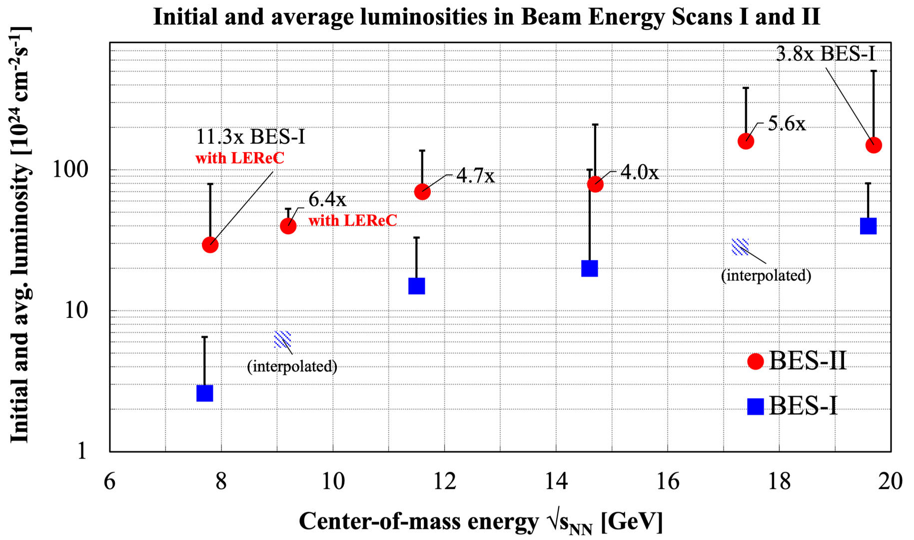

Figure 2.12 Comparision of BES-I (blue) and BES-II (red) luminosity with Au beams at RHIC. Red circles and blue squares represent the average luminosity. A small horizontal bar marks the initial luminosity. The average luminosity at 9.2 GeV during BES-I is interpolated based on data collected at 7.7 and 11.5 GeV. At the two lowest energies LEReC was used. The figure is taken from Ref. [153].

To further investigate the QCD phase diagram, RHIC conducted the BES-II program from 2018 to 2021 [103, 146, 154]. BES-II aimed to extend the exploration to higher baryon chemical potentials with high-statistics data collection, covering a collision energy range of $\sqrt{s_{NN}}$ = 3 to 54.4 GeV in Au+Au collisions. To improve data statistics at low energies, the low-energy electron cooling (LEReC) system [155-156] was implemented to enhance luminosity. As shown in Figure 2.12, both the average luminosity and the initial luminosity in BES-II, presented in blue markers, are increased than that in BES-I ,presented in blue marker for same collision energy. At low collision enwergies, the LEReC To enhance data statistics at low collision energies, the Low Energy RHIC electron Cooler (LEReC) system [155-156] was implemented to significantly boost luminosity. As demonstrated in Figure 2.12, the BES-II program achieved remarkable improvements over BES-I, with blue markers indicating both higher average luminosity (by a factor of approximately 4-11 across different energies) and enhanced initial luminosity at equivalent collision energies. The most substantial gains were observed at the two lowest energies (9.2 and 7.7 GeV/nucleon), where LEReC system is implemented. This upgrade is particularly crucial for exploring the high baryon density region of the QCD phase diagram, where traditional luminosity limitations had previously constrained experimental capabilities. Additionally, several detector upgrades were introduced during BES-II, including the iTPC, eTOF, and EPD, improving particle PID with wider pseudorapidity coverage.

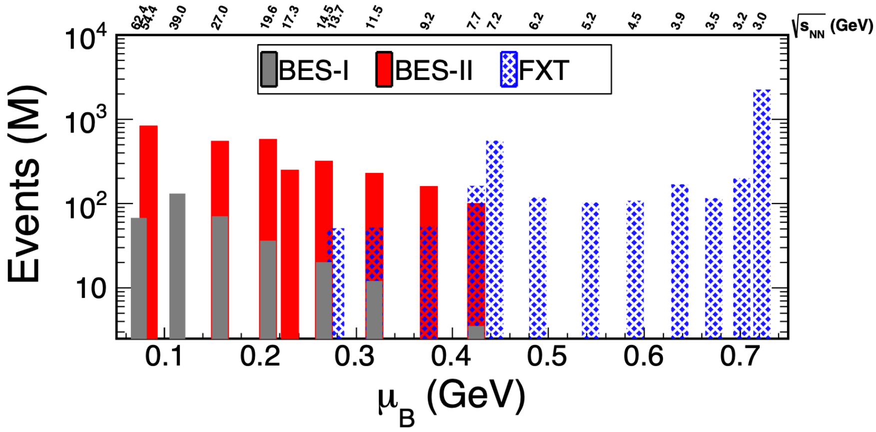

Figure 2.13 BES-I collider (gray), BES-II collider (red), and BES-II fixed target (blue) modes at RHIC. The figure is taken from Ref. [157].

To access even lower collision energies, a fixed-target mode was introduced, allowing for collisions down to $\sqrt{s_{NN}}$ = 3 GeV in Au+Au collisions [103, 146, 154, 158]. The datasets collected at BES-II including both collider and fixed target modes in different collision center-of-mass energies and corresponding μ_B values, compared with BES-I datasets, are shown in Figure 2.13. The BES-II program extends the μ_B range from approximately 400 MeV up to 700 MeV.

The FXT mode setup of STAR detector is illustrated in Figure 2.14. The fixed target, shown in Figure 2.15, is a thin gold foil with a thickness of 250 μm. The target thickness is selected to minimize in-time pileup and beam energy loss associated with a thicker target while preventing excessive heating and potential melting that could occur with a thinner target. The target is positioned at z = 2.01 m on the west side of the

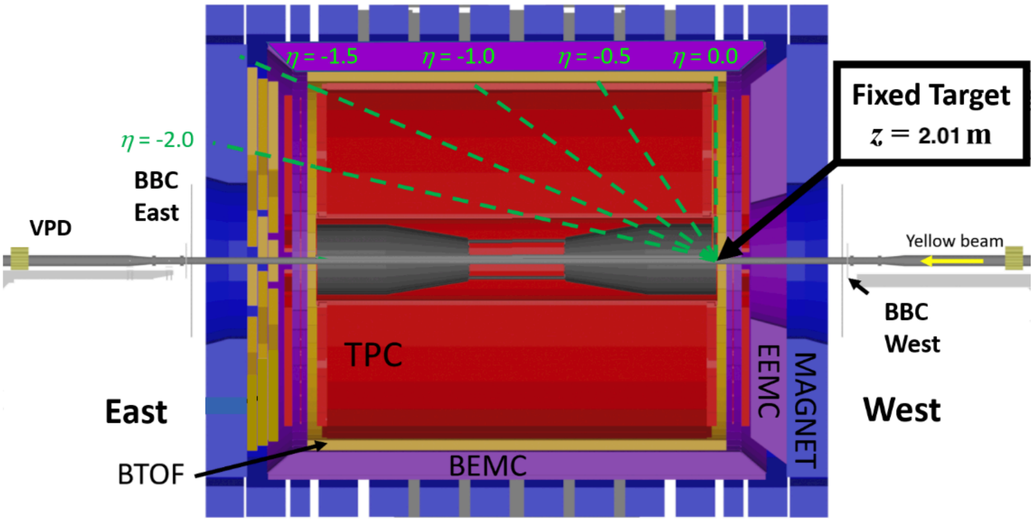

Figure 2.14 The fixed target setup of the STAR detector.

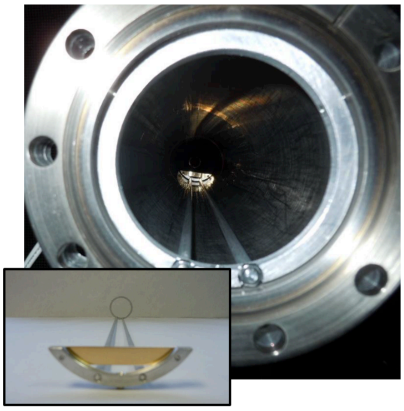

Figure 2.15 The gold target foil used in the fixed target mode. The picture is taken from Ref. [158].

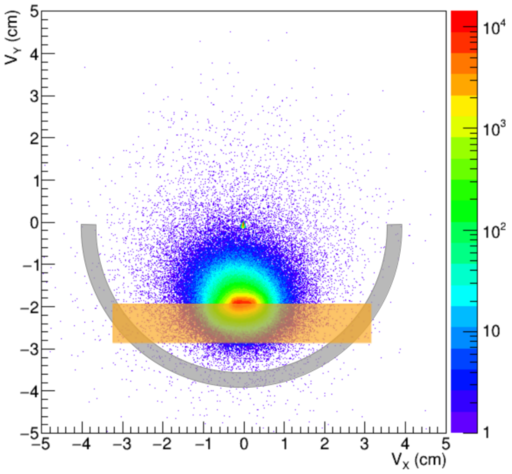

Figure 2.16 The position of the gold target foil (orange band) in the fixed target mode in the x-y plane.

STAR detector and is placed 2 cm below the beam axis. The x–y position of the target foil is indicated by the orange band in Figure 2.16. The beam, traveling from east to west, collides with the fixed target to generate the collision events.

Chapter 3 Experimental Analysis Details and Techniques

3.1 Dataset and Event Selection

3.1.1 Dataset and Trigger

The dataset used in this analysis comes from Au+Au collisions conducted in fixed target mode at center-of-mass energies $\sqrt{s_{NN}}$ = 3.0, 3.2, 3.5, and 7.2 GeV. These collisions were recorded during the years 2018, 2019, and 2020. Table 3.1 provides a detailed summary of the dataset, including the corresponding beam energies, the mid rapidity in lab frame that corresponds to mid-rapidity value 0 in the center-of-mass frame (y_{mid}), trigger IDs, and production tags.

Table 3.1 Summary of data with fixed target mode used in this analysis

System	$\sqrt{s_{NN}}$ (GeV)	E_{beam} (GeV)	y_{mid}	Year	Trigger ID	Production Tag
Au+Au	3.0	3.85	-1.045	2018	620052	P19ie
Au+Au	7.2	26.5	-2.03	2018	630052	P19ie
Au+Au	3.2	4.59	-1.14	2019	680001	P21id
Au+Au	3.5	5.75	-1.25	2020	720000	P21id

The beam energy per nucleon, E_{beam}, corresponds to the center-of-mass energy per nucleon pair, $\sqrt{s_{NN}}$, listed in Table 3.1. The relation between E_{beam} and $\sqrt{s_{NN}}$ in fixed-target mode is given by:

$$\sqrt{s_{NN}} = \sqrt{2m_n^2 + 2m_n E_{\text{beam}}}, \tag{3.1}$$

where $m_n = 0.9311\,\text{GeV}/c^2$ is the rest mass of a nucleon.

The beam-going direction (the yellow beam from west towards east) is defined as the negative z-axis in the laboratory frame in this analysis. However, in the center-of-mass frame of fixed-target mode, the beam-going direction is defined as the positive direction. Therefore, a sign flip is required to match the conventions between the lab and center-of-mass frames. This value, y_{mid}, is used to shift rapidities from the lab frame into the center-of-mass frame via:

$$y_{\text{CM}} = -\left(y_{\text{lab}} - y_{\text{mid}}\right). \tag{3.2}$$

Here, y_{mid} represents the rapidity of the center-of-mass frame with respect to the laboratory frame. In other words, it is the rapidity in the laboratory frame that corresponds to mid-rapidity ($y = 0$) in the center-of-mass frame, or the rapidity in the center-of-mass frame that corresponds to mid-rapidity ($y = 0$) in the laboratory frame.

This analysis utilizes data collected with a minimum bias trigger, designed to minimize selection bias by avoiding strict criteria during data collection [159-160]. Trigger IDs 620052 and 630052 correspond to the 'bbce_tofmult1' trigger, which requires a valid signal from the BBC on the east side and at least one particle detected by the TOF detector. Trigger IDs 680001 and 720000 correspond to the more inclusive 'epde-or-bbce-or-vpde-tof1' trigger. This trigger activates if any one of the EPD, BBC, or VPD on the east side detects a signal, along with at least one particle identified by the TOF detector.

3.1.2 Bad Run Selection

A run refers to a continuous period of data collection during which the detector system operates under fixed experimental conditions. Each run typically lasts from a few minutes to about half an hour and contains a large number of recorded collision events. The full datasets used in this analysis consist of thousands of such runs. To ensure reliable physics results, it is necessary to exclude runs with significant detector or DAQ (data acquisition) issues. These bad runs can introduce systematic biases and degrade data quality.

For the $\sqrt{s_{NN}}$ = 3.0, 3.2, and 3.5 GeV datasets, official bad run lists provided by previous STAR analyses were used. These are based on established detector quality criteria [161-163].

However, no official bad run list was available for the $\sqrt{s_{NN}}$ = 7.2 GeV dataset at the time of this analysis. Therefore, a custom bad run selection procedure was performed, based on both event-level and track-level quantities. Here, we explain some key variables used for run quality assessment.

1. Event-Level

- Position of the primary vertex (PV): V_x, V_y, V_z (coordinates of reconstructed PV)
- Radial vertex offset: $V_r = \sqrt{(V_x - x_0)^2 + (V_y - y_0)^2}$ (relative to collision center in the transverse plane (x_0, y_0))
- Multiplicity measures:
  - RefMult: multiplicity of primary charged particles within $|\eta| < 0.5$
  - gRefMult: RefMult by global tracks

2. Track-Level

- nHitsFit: number of TPC hits used in track fitting
- DCA: distance of closest approach to primary vertex
- η: pseudorapidity

- ϕ: azimuthal angle

The steps are as follows:

1. For each variable of interest, the mean value $\langle v \rangle$ is calculated as a function of run index.
2. The overall mean $\overline{\langle v \rangle}$ and standard deviation σ of the $\langle v \rangle$ distribution are calculated.
3. A run is rejected if $|\langle v \rangle - \overline{\langle v \rangle}| > 3\sigma$.
4. The procedure is repeated once after removing the initially rejected runs.

This statistical filtering approach identifies runs that deviate significantly from the norm, ensuring consistent data quality. The runs rejected in this process are listed in Table 3.2, and rejection results are visualized in Figure 3.1.

Table 3.2 Bad runs identified in the $\sqrt{s_{NN}} = 7.2\,\text{GeV}$ FXT dataset.

Bad Run IDs							
19159043	19159046	19160032	19160033	19160034	19160035	19160036	19160037
19160038	19160039	19160040	19160041	19160042	19160043	19160044	19161001
19161020	19161021	19161022	19161023	19161024	19161025	19161026	19161027
19161028	19161029	19161030	19161034	19161035	19161036	19161037	19164001
19164022	19164023	19164024	19164025	19167053	19168041	–	–

3.1.3 Event Level Selection

In relativistic heavy-ion collisions, the position of the primary vertex is typically described by a set of coordinates (V_x, V_y, V_z). After track reconstruction in the Time Projection Chamber, the primary vertex position can be determined. To ensure that selected events fall within a reasonable detector acceptance, a vertex cut of V_z is applied. Furthermore, to suppress background events from beam-pipe interactions, a radial vertex $|V_r|$ cut is applied based on the transverse distance of the vertex from the collision center in the transverse (x–y) plane (x_0, y_0). The (x_0, y_0) are determined by the (V_x, V_y) distributions from all the collision events, differ slightly in different collision energies. An example of the determination of (x_0, y_0) for the $\sqrt{s_{NN}} = 3.2\,\text{GeV}$ dataset is shown in Figure 3.2. The V_z distribution for the $\sqrt{s_{NN}} = 3.2\,\text{GeV}$ dataset is also presented in Figure 3.3. The specific vertex selection criteria applied in different datasets are summarized in Table 3.3.

The total number of minimum bias events used in this analysis is approximately 251×10^6 at $\sqrt{s_{NN}} = 3.0\,\text{GeV}$, 148×10^6 at $\sqrt{s_{NN}} = 7.2\,\text{GeV}$, 192×10^6 at $\sqrt{s_{NN}} = 3.2\,\text{GeV}$, and 113×10^6 at $\sqrt{s_{NN}} = 3.5\,\text{GeV}$.

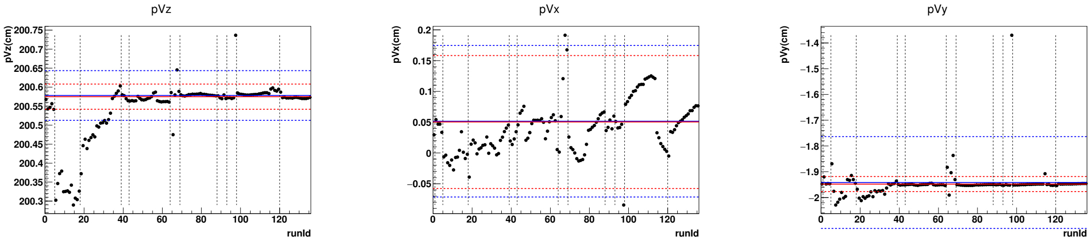

(a) V_z **(b)** V_x **(c)** V_y

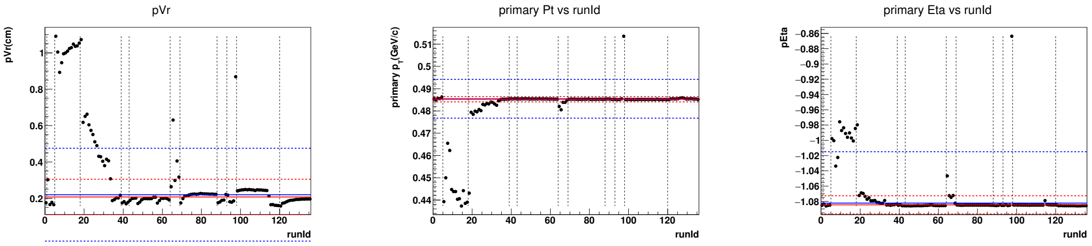

(d) $V_r(0, -2)$ **(e)** p_T **(f)** η

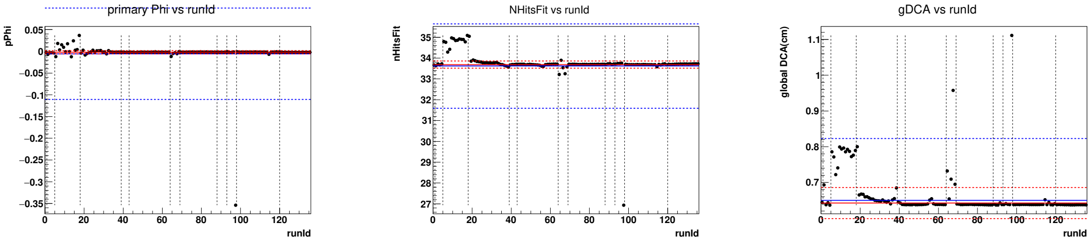

(g) ϕ **(h) NHitsFit** **(i) DCA**

(j) Refmult **(k) gRefmult**

Figure 3.1 Run-by-run distributions of selected quality variables for $\sqrt{s_{NN}} = 7.2\,\mathrm{GeV}$ events. Rejection windows are shown as dashed lines: the first round is shown with blue dashed lines; the second round rejection window is indicated with red dashed lines. The solid black line shows the overall mean value.

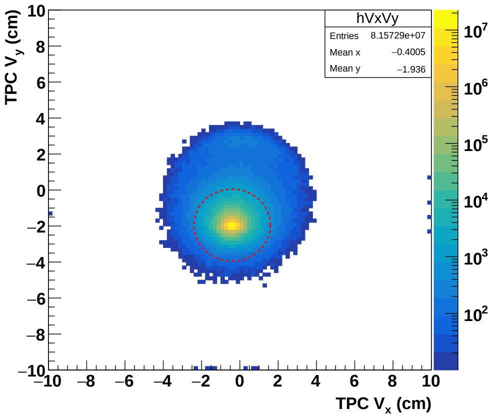

Figure 3.2 Determination of the vertex center position (x_0, y_0) in the transverse plane for $\sqrt{s_{NN}} = 3.2\,$GeV collisions. The center is slightly shifted from the nominal position at $(0, -2)$ cm to approximately $(-0.4, -1.95)$ cm.

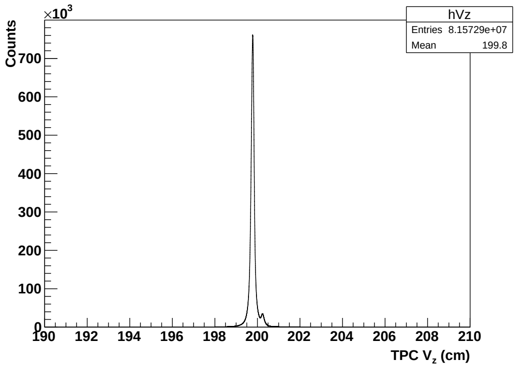

Figure 3.3 Distribution of the longitudinal primary vertex position V_z for $\sqrt{s_{NN}} = 3.2\,$GeV collisions.

Table 3.3 Vertex selection criteria for different datasets.

$\sqrt{s_{NN}}$ **(GeV)**	**Year**	V_z **Cut**	V_r **Cut**
3.0	2018	$198\,\text{cm} < V_z < 202\,\text{cm}$	$\sqrt{V_x^2 + (V_y + 2)^2} < 1.5\,\text{cm}$
7.2	2018	$198\,\text{cm} < V_z < 202\,\text{cm}$	$\sqrt{V_x^2 + (V_y + 2)^2} < 1.5\,\text{cm}$
3.2	2019	$198\,\text{cm} < V_z < 202\,\text{cm}$	$\sqrt{(V_x + 0.4)^2 + (V_y + 1.95)^2} < 2\,\text{cm}$
3.5	2020	$198\,\text{cm} < V_z < 202\,\text{cm}$	$\sqrt{(V_x + 0.3)^2 + (V_y + 1.98)^2} < 2\,\text{cm}$

3.1.4 Centrality Determination

For fixed-target experiments, the FXT multiplicity (FXTRefmult) is defined as the number of primary tracks in a single event after event-level cuts have been applied. Collision centrality classes are then determined by fitting the charged-particle multiplicity distribution with a Monte Carlo Glauber model [35].

For each energy, the centrality definitions follow those established in STAR official studies [161-164]. Table 3.4 summarizes the FXTRefmult cut ranges used to define collision centrality classes at each beam energy.

3.2 Particle Signal Extraction

3.2.1 Track Quality Cuts

In this analysis, signal reconstruction is mainly performed using tracking and ionization energy loss information from the TPC. To ensure good tracking quality and reliable momentum reconstruction, a minimum of 15 TPC hits (nHitsFit $\geq$ 15) is required

Table 3.4 FXTRefmult cuts for centrality definition at various collision energies.

Centrality	3.0 GeV	7.2 GeV	3.2 GeV	3.5 GeV
0–5%	142–195	191–240	≥200	≥217
5–10%	119–141	154–190	169–199	181–216
10–15%	101–118	124–153	144–168	152–180
15–20%	86–100	100–123	122–143	128–151
20–25%	72–85	80–99	104–121	108–127
25–30%	60–71	64–79	87–103	89–107
30–35%	50–59	50–63	72–86	73–88
35–40%	41–49	39–49	59–71	59–72
40–45%	33–40	30–38	48–58	47–58
45–50%	26–32	22–29	38–47	37–46
50–55%	21–25	16–21	30–37	28–36
55–60%	16–20	12–15	23–29	22–27
60–65%	12–15	9–11	17–22	16–21
65–70%	9–11	6–8	13–16	12–15
70–75%	7–8	4–5	9–12	8–11
75–80%	5–6	2–3	6–8	6–7

for each track in all lifetime measurements at $\sqrt{s_{NN}}$ = 3.0, 3.2, 3.5, and 7.2 GeV. For the yield measurement at $\sqrt{s_{NN}}$ = 3.2 GeV, a stricter requirement of nHitsFit ≥ 20 is applied.

To suppress contributions from split tracks—where a single particle may be reconstructed as multiple tracks due to spurious hits in different TPC sectors—a requirement on the hit ratio is also applied. The ratio of fitted hits to maximum possible hits, nHitsFit/nHitsPoss, is required to be greater than 0.52 for each tarck. This ensures that the number of fitted points exceeds 52% of the maximum expected hits for a given track, thus effectively rejecting poorly reconstructed or duplicated tracks.

Furthermore, a cut on the TPC dEdxError (Error of dE/dx) is applied at $\sqrt{s_{NN}}$ = 3.0 and 7.2 GeV, requiring $0.04 <$ dEdxError < 0.12, which is effective in eliminating split tracks due to poor ionization measurement quality. However, in the 3.2 and 3.5 GeV datasets, a significant fraction of tracks have dEdxError values of zero due to data quality issues in those productions. Therefore, instead of applying a dEdxError cut, a minimum requirement of nHitsDedx $\geq$ 5 is used at 3.2 and 3.5 GeV to ensure sufficient hits for dE/dx.

3.2.2 Particle Identification Recalibration

The daughter particles in this analysis are identified using the ionization energy loss ($\mathrm{d}E/\mathrm{d}x$) information from the TPC. Two variables are utilized for PID: $\mathrm{d}E/\mathrm{d}x$ and the derived quantity dEdxPuLL (or n_σ), both plotted as a function of particle rigidity (p/q, where q is the particle charge). The dEdxPuLL is defined as:

$$\mathrm{dEdxPuLL} = \frac{1}{\sigma_{\mathrm{d}E/\mathrm{d}x}} \ln\left(\frac{\langle \mathrm{d}E/\mathrm{d}x\rangle}{(\mathrm{d}E/\mathrm{d}x)_{\mathrm{Bichsel}}}\right), \tag{3.3}$$

where $\langle \mathrm{d}E/\mathrm{d}x\rangle$ is the measured energy loss, $(\mathrm{d}E/\mathrm{d}x)_{\mathrm{Bichsel}}$ is the expected value from the Bichsel model, and $\sigma_{\mathrm{d}E/\mathrm{d}x}$ is the corresponding measurement uncertainty. To improve PID accuracy, both dE/dx and dEdxPuLL can be recalibrated using pure particle samples selected via mass-squared (m^2) information from the TOF detector.

Although TOF is not used directly for particle reconstruction in this analysis, the m^2 vs. p/q distribution plays a key role in calibrating the dE/dx-based selections. Figure 3.4a present the m^2 as a function of p/q from TOF and TPC, based on which we can choose m^2 range to get purer particle samples to determine the PID. For pions, we select $-0.1 < m^2 < 0.15$; for protons, we select $0.5 < m^2 < 1.5$; for ^{3}He, we select $1.5 < m^2 < 2.5$ $(\mathrm{GeV}/c^2)^2$; for ^{4}He, we select $2.5 < m^2 < 4.5$ $(\mathrm{GeV}/c^2)^2$. Under narrow p/q bins, the distributions of dEdxPuLL and dE/dx are fit with Gaussian functions to extract the mean and width. This allows recalibration of PID.

The calibrated dE/dx-based PID selections for ^{3}He and ^{4}He at $\sqrt{s_{NN}} = 3.0$ and 7.2 GeV are shown in Figure 3.5. Particle identification is performed within the rigidity range $0.4 < p/q < 6.0\,\mathrm{GeV}/c$, and tracks outside this range are excluded. For ^{3}He, the upper PID band retains 2.5σ of the calibrated distribution. The lower band is defined differently depending on rigidity: for $p/q > 0.85\,\mathrm{GeV}/c$, a 3.0σ band is used, while for $p/q < 0.85\,\mathrm{GeV}/c$, a tighter 1.5σ band is applied to suppress triton contamination. For ^{4}He, both the upper and lower PID bands retain 2.5σ of the distribution calibrated from the 7.2 GeV dataset. At $\sqrt{s_{NN}} = 3.0$ and 7.2 GeV, the n_σ distributions of protons and π^- are symmetric and centered around zero. Therefore, a uniform PID selection of $|n_\sigma| < 3$ is applied to both protons and π^- at these energies.

The calibrated dE/dx and dEdxPuLL distributions for PID at $\sqrt{s_{NN}} = 3.2$ and 3.5 GeV are presented in Figures 3.4 and 3.6. At these energies, the n_σ distributions of protons and π^- are distorted, with their means deviating from zero. To ensure reliable particle identification, dEdxPuLL-based cuts are applied using momentum-dependent selection windows.

At $\sqrt{s_{NN}} = 3.2\,\mathrm{GeV}$, the following PID windows are used: For ^{3}He, a standard $\pm 3\sigma$ band is applied for tracks with $0.4 < p/q < 4\,\mathrm{GeV}/c$, and a window of $2 < \mathrm{dEdxPuLL} < 8$ is used for $p/q > 4\,\mathrm{GeV}/c$. For π^-, a $\pm 3\sigma$ selection is applied for $p/q < 4\,\mathrm{GeV}/c$, and a window $-2 < \mathrm{dEdxPuLL} < 6$ is used for $p/q > 4\,\mathrm{GeV}/c$. For protons, a standard $\pm 3\sigma$ band is applied for $p/q < 1.6\,\mathrm{GeV}/c$; for $p/q > 4\,\mathrm{GeV}/c$, the selection is switched to $-2 < \mathrm{dEdxPuLL} < 5$, and in the intermediate region

$1.6 < p/q < 4\,\mathrm{GeV}/c$, an asymmetric window of -2σ to $+3\sigma$ is applied.

At $\sqrt{s_{NN}} = 3.5\,\mathrm{GeV}$, similar momentum-dependent PID cuts are used with slightly modified boundaries: For ^{3}He, a standard $\pm 3\sigma$ PID selection is applied for $0.4 < p/q < 4\,\mathrm{GeV}/c$, and the window $2 < \mathrm{dEdxPuLL} < 8$ is used for $p/q > 4\,\mathrm{GeV}/c$. For π^-, a standard $\pm 3\sigma$ band is used for $p/q < 3.5\,\mathrm{GeV}/c$, while for $p/q > 4\,\mathrm{GeV}/c$, the window is $-2.5 < \mathrm{dEdxPuLL} < 5.5$. For protons, the selection is again divided: for $p/q < 1.6\,\mathrm{GeV}/c$, a $\pm 3\sigma$ band is used; for $1.6 < p/q < 4\,\mathrm{GeV}/c$, an asymmetric window of -2σ to $+3\sigma$ is applied; and for $p/q > 4\,\mathrm{GeV}/c$, a selection of $-2.5 < \mathrm{dEdxPuLL} < 5$ is applied.

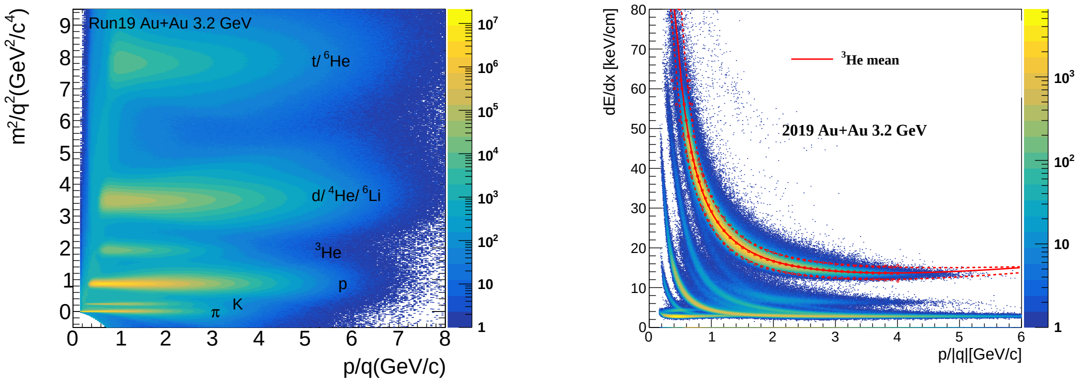

(a) m^2 **vs.** p/q **for TOF-selected particles** **(b) Recalibrated** dE/dx **vs.** p/q **for** ^{3}**He**

Figure 3.4 TOF-based calibration and TPC-based PID distributions in Au+Au collisions at $\sqrt{s_{NN}} = 3.2\,\mathrm{GeV}$**. (Left)** m^2 **distribution used to select pure particle samples for calibration. (Right) Calibrated** $\mathrm{d}E/\mathrm{d}x$ **vs.** p/q **for** ^{3}He**, with red open circles representing the** $\pm 3\sigma$ **PID band.**

3.2.3 Particle Reconstruction Channels and KFParticle Package

In this analysis, ${}^3_\Lambda$H and ${}^4_\Lambda$H are reconstructed through their two-body mesonic weak decay channels:

$$ {}^3_\Lambda\mathrm{H} \rightarrow {}^3\mathrm{He} + \pi^-, \tag{3.4}$$

$$ {}^4_\Lambda\mathrm{H} \rightarrow {}^4\mathrm{He} + \pi^-. \tag{3.5}$$

The ${}^4_\Lambda$He hypernucleus is reconstructed via its three-body decay mode:

$$ {}^4_\Lambda\mathrm{He} \rightarrow {}^3\mathrm{He} + p + \pi^-. \tag{3.6}$$

The daughter particles (π^-, p, ^{3}He, and ^{4}He) are identified using ionization energy loss measurements from the TPC, as described in the previous section.

The KF Particle package [165-166] is employed to reconstruct the hypernuclear candidates in this study. In the KF Particle, each particle is represented by an 8-dimensional state vector that includes the position (x, y, z), momentum (p_x, p_y, p_z), energy (E), and the flight length parameter $(s = l/p)$, where l is the path length and p is

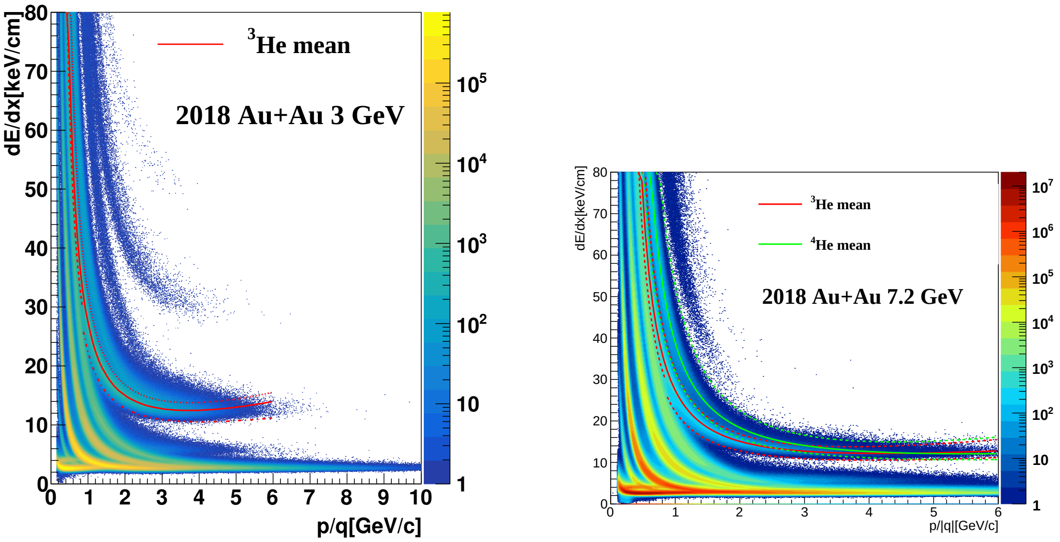

(a) Au+Au collisions at $\sqrt{s_{NN}} = 3.0\,\mathrm{GeV}$ (b) Au+Au collisions at $\sqrt{s_{NN}} = 7.2\,\mathrm{GeV}$

Figure 3.5 TPC energy loss (dE/dx) as a function of particle rigidity (p/q) in Au+Au collisions at $\sqrt{s_{NN}}$ = 3.0 and 7.2 GeV collected in 2018. The red solid lines shows the calibrated means of ^{3}He at 3.0 and 7.2 GeV. The ^{3}He PID bands are indicated by the red dashed lines. Similarly, the green dashed lines represent the ^{4}He PID band, and the green solid line shows the corresponding mean at 7.2 GeV.

the total momentum of the particle. The reconstructed state vector and its associated covariance matrix C contain all the necessary information about the particle, including uncertainties and correlations of its parameters, and the χ^2 quantities during reconstruction, which are essential for assessing the quality of the reconstruction. The estimation of the mother particle (the decay vertex) is iteratively updated through an iterative fitting procedure over all daughter particles using the Kalman filter algorithm. This allows for precision and efficiency reconstruction of short-lived particles.

Figure 3.7 presents schematic illustrations of hypernuclear decay topologies. Panel (a) shows the two-body decay of $^3_\Lambda$H or $^4_\Lambda$H, and panel (b) shows the three-body decay of $^4_\Lambda$He. These diagrams highlight the geometric and statistical variables used in the KFParticle reconstruction framework.

The following is a description of the key topological observables:

- **DCA (Distance of Closest Approach)**: Measures the minimum distance between two particle trajectories (e.g., decay daughters) or between a track and the primary vertex. A small DCA between daughters supports a common origin from a secondary decay, while a large DCA to the primary vertex suggests the particle is not primary.
- **Decay length l**: The distance from the reconstructed decay vertex to the primary vertex, representing the flight path of the mother hypernucleus.

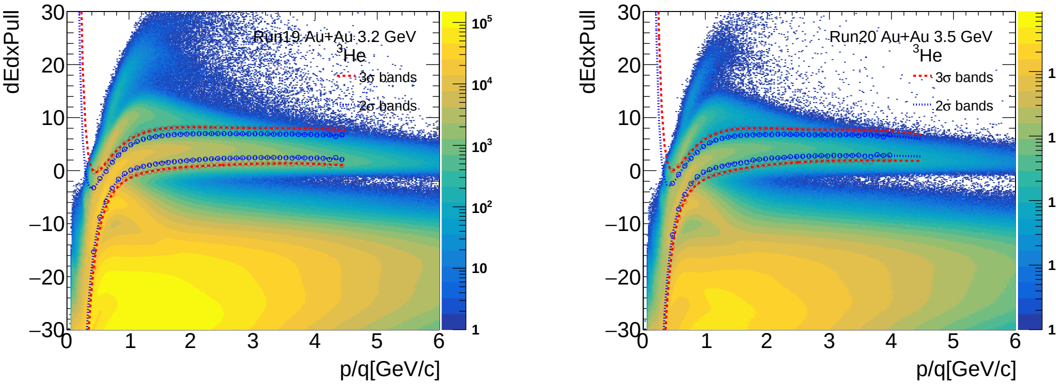

(a) ^{3}**He** dEdxPuLL **vs.** p/q **at** $\sqrt{s_{NN}}$ = 3.2 **GeV** **(b)** ^{3}**He** dEdxPuLL **vs.** p/q **at** $\sqrt{s_{NN}}$ = 3.5 **GeV**

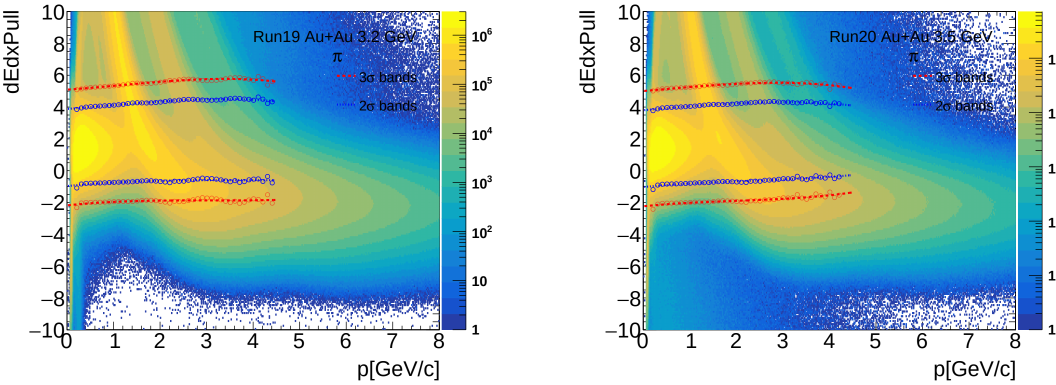

(c) π^- dEdxPuLL **vs.** p/q **at** $\sqrt{s_{NN}}$ = 3.2 **GeV** **(d)** π^- dEdxPuLL **vs.** p/q **at** $\sqrt{s_{NN}}$ = 3.5 **GeV**

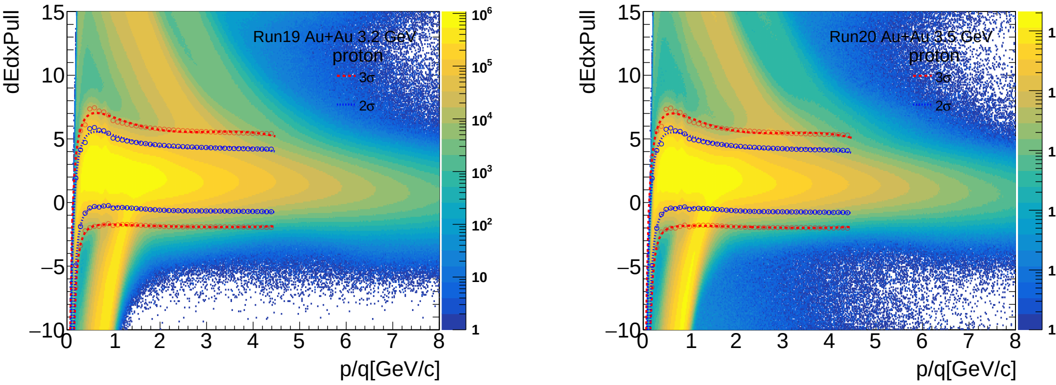

(e) Proton dEdxPuLL **vs.** p/q **at** $\sqrt{s_{NN}}$ = 3.2 **GeV** **(f) Proton** dEdxPuLL **vs.** p/q **at** $\sqrt{s_{NN}}$ = 3.5 **GeV**

Figure 3.6 Recalibrated dEdxPuLL **vs.** p/q **distributions for** ^{3}**He,** π^-**, and proton in Au+Au collisions at** $\sqrt{s_{NN}}$ = 3.2 **and** 3.5 **GeV.**

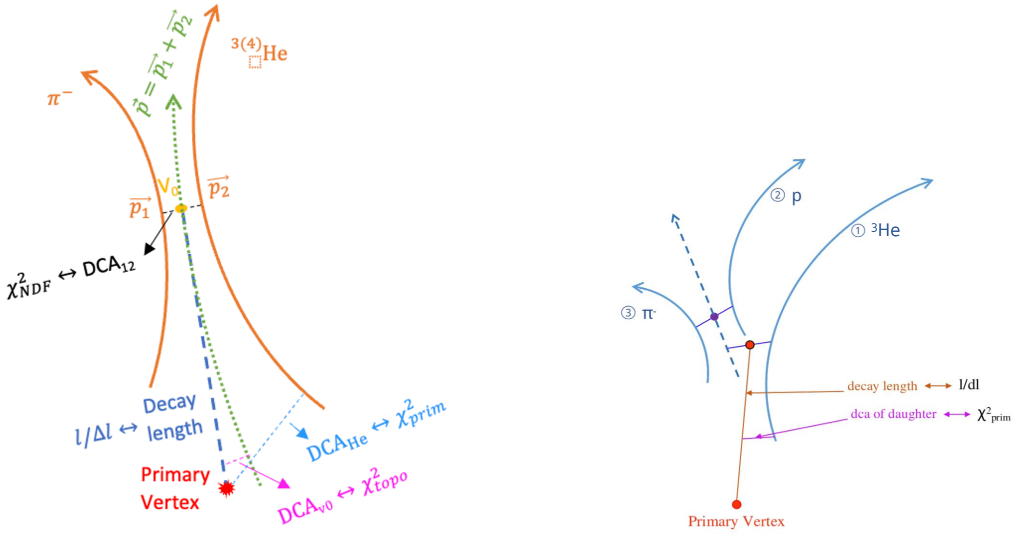

(a) Two-body decay topology of $^{3}_{\Lambda}$H or $^{4}_{\Lambda}$H. **(b) Three-body decay topology of $^{4}_{\Lambda}$He.**

Figure 3.7 Schematic illustrations of weak decay topologies for hypernuclei. Common topological observables, such as the DCA, decay length, and KFParticle-specific statistical quantities (e.g., χ^2-based variables), are annotated.

- **Decay length significance** $l/\Delta l$: The decay length normalized by its uncertainty. A large value implies a well-separated and precisely reconstructed secondary decay vertex.
- $\chi^2_{\mathbf{prim}}$: The χ^2 value representing the deviation of a single daughter track with the primary vertex.A small value suggests that the track is compatible with originating from the primary vertex, whereas a large value indicates that the track is more likely to come from a secondary decay.
- $\chi^2_{\mathbf{topo}}$: The χ^2 between the reconstructed mother particle trajectory and the primary vertex. This variable tests whether the hypernucleus is consistent with originating from the primary vertex. A large value favors a secondary origin.
- $\chi^2_{\mathbf{NDF}}$: The χ^2 for the fit of daughter tracks to a common secondary vertex. A low χ^2_{NDF} indicates a good quality decay vertex; a high value suggests poor vertex compatibility, often associated with background.
- $\chi^2_{\mathbf{prim},p-\pi}$: The χ^2 of the combined proton and pion tracks when constrained to originate from the primary vertex. A large value suggests that the pair is unlikely to be primary and instead likely comes from a secondary decay.

The topological cut selections used for each beam energy and particle type are summarized in the following section.

3.2.4 Analysis Cuts

The topological cuts applied in this analysis for different beam energies ($\sqrt{s_{NN}}$ = 3.0, 3.2, 3.5, and 7.2 GeV) are summarized in Tables 3.5, 3.6, and 3.7.

At $\sqrt{s_{NN}}$ = 7.2 GeV, the topological selections for $^{4}_{\Lambda}$H are listed in Table 3.5. For $^{3}_{\Lambda}$H, the listed cuts correspond to the pre-topological selections applied before the multivariate training.

For the reconstruction of $^{3}_{\Lambda}$H at $\sqrt{s_{NN}}$ = 3.0 GeV, topological selections listed in Table 3.6 are applied. To optimize the signal significance, these selections are adjusted according to different transverse momentum (p_T), rapidity, and centrality intervals.

At $\sqrt{s_{NN}}$ = 3.2 and 3.5 GeV, topological selections for reconstruction of $^{4}_{\Lambda}$He are applied as shown in Table 3.7. In addition to vertex quality and track-level cuts, invariant mass selections are imposed to further suppress combinatorial background. Specifically, the mass windows $1.075 < M(p\pi) < 1.112\,\mathrm{GeV}/c^2$ and $3.74 < M(p\,^3\mathrm{He}) < 3.768\,\mathrm{GeV}/c^2$ are applied. These cuts reduce the background for the three-body decay reconstruction. A looser χ^2_{topo} cut is applied in the 3.2 and 3.5 GeV analyses compared to 3.0 GeV, due to a significant efficiency dip observed in the $-1.5 < \eta_{\mathrm{lab}} < -1$ region. This dip is caused by worsened χ^2_{topo} and χ^2_{prim} of ^{3}He distributions related to possible track splitting of ^{3}He and mis-modeling in embedding after the iTPC upgrade. The looser cut helps reduce this effect and ensures stable efficiency across η.

Table 3.5 Topological cuts for $^{3}_{\Lambda}$H and $^{4}_{\Lambda}$H lifetime analysis at $\sqrt{s_{NN}}$ = 7.2 GeV.

Cut Variable	$^{3}_{\Lambda}$H	$^{4}_{\Lambda}$H
Decay length l [cm]	> 1	> 1
$l/\Delta l$	> 3	> 3
χ^2_{topo}	< 5	< 4
χ^2_{NDF}	< 10	< 4
$\chi^2_{\mathrm{prim},\pi}$	> 1	> 10
$\chi^2_{\mathrm{prim,He}}$	> 1	> 3

3.2.5 TMVA Training

To enhance the purity of the $^{3}_{\Lambda}$H signal at $\sqrt{s_{NN}}$ = 7.2 GeV, a multivariate analysis is performed using the Toolkit for Multivariate Data Analysis (TMVA) [167]. A Boosted Decision Tree (BDT) is trained with rotational background events as the background sample and well-weighted embedded Monte Carlo $^{3}_{\Lambda}$H tracks as the signal sample.

Before applying the BDT training, a set of pre-topological cuts is imposed on $^{3}_{\Lambda}$H candidates, listed in Table 3.5. The BDT model is then trained to distinguish signal from

Table 3.6 Topological cuts for $^{3}_{\Lambda}$H production analysis at $\sqrt{s_{NN}}$ = 3.2 GeV for different centralities.

Cut Variable	0–10% Centrality	10–40% Centrality
χ^2_{topo}	< 12	< 12
χ^2_{He}	> 0	> 0
p_T [GeV/c]	> 2.2	> 2.1
Rapidity range	$-1 < y < -0.5$	$-1 < y < -0.5$
Decay length l [cm]	> 3	> 1
$l/\Delta l$	> 9	> 3
χ^2_{π}	> 2	> 2
χ^2_{NDF}	< 4	< 5
Out of the above p_T and rapidity range		
Decay length l [cm]	> 3	> 5
$l/\Delta l$	> 3	> 3
χ^2_{π}	> 2	> 2
χ^2_{NDF}	< 7	< 7

Table 3.7 Topological cuts for $^{4}_{\Lambda}$H lifetime analysis at $\sqrt{s_{NN}}$ = 3.0, 3.2, and 3.5 GeV.

Cut Variable	3.0 GeV	3.2/3.5 GeV
Decay length l [cm]	> 7	> 7
$l/\Delta l$	> 8	> 8
χ^2_{topo}	< 2.5	< 10
χ^2_{NDF}	< 4	< 5
$\chi^2_{\text{prim},\pi}$	> 15	> 20
$\chi^2_{\text{prim},p}$	> 15	> 10
$\chi^2_{\text{prim,He}}$	> 3	> 2
$\chi^2_{\text{prim},p-\pi}$	> 10	> 4
DCA(He, p, π) [cm]	< 1	< 1
DCA hierarchy	–	DCA(He) $<$ DCA(p) $<$ DCA(π)

background based on topological variables. Figure 3.8 shows the training performance, including the overtraining check (left) and the cut efficiency curve (right). The optimal BDT response threshold is selected by scanning for the point of maximum $^{3}_{\Lambda}$H signal significance. The default BDT selection used in this analysis corresponds to a BDT response value greater than 0.0602.

3.2.6 Hypernuclei Signal Reconstruction

To suppress edge effects and minimize possible mismatches between data and simulation, fiducial acceptance cuts are applied consistently to both real and embedded events in lifetime analysis. These cuts help reduce effects from imperfect detector geometry descriptions in simulations, particularly where acceptance may differ significantly due to geometry mismatches.

Figure 3.9 and 3.10 show the distributions of transverse momentum versus center-of-mass rapidity (p_T vs. y_{CM}) for reconstructed $^{3}_{\Lambda}$H and $^{4}_{\Lambda}$H candidates at $\sqrt{s_{NN}}$ = 7.2 GeV. The corresponding acceptance distributions for $^{4}_{\Lambda}$He at $\sqrt{s_{NN}}$ = 3.0, 3.2,

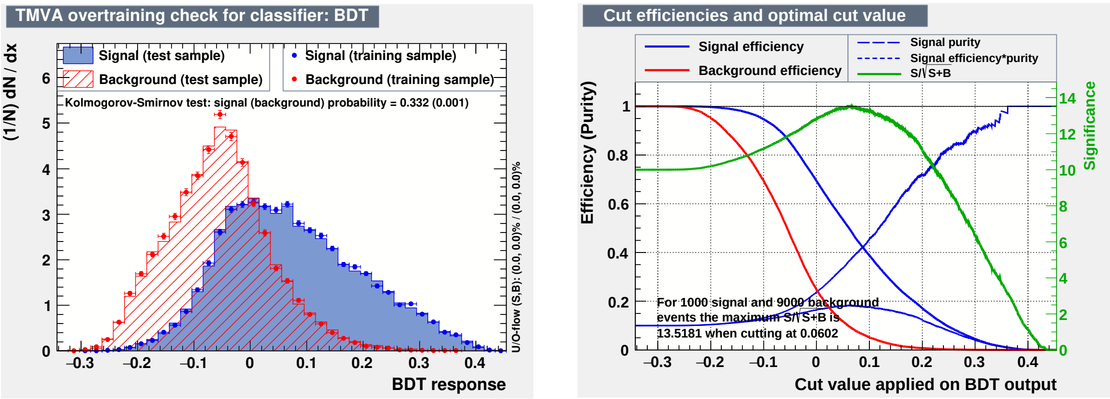

(a) TMVA-BDT Overtraining Check **(b) BDT Cut Efficiency**

Figure 3.8 TMVA-BDT training results for $^3_\Lambda$H at $\sqrt{s_{NN}}$ = 7.2 GeV: (a) overtraining check comparing signal and background distributions in training and test samples, and (b) significance scan for optimal BDT response cut.

and 3.5 GeV are shown in Figures 3.11–3.13. In all plots, the fiducial cut regions are indicated by solid red boundaries. The target rapidity boundary in the center-of-mass frame, $y_{\text{CM,target}}$, varies with the beam energy: $y_{\text{CM,target}} = -2.03$ at $\sqrt{s_{NN}} = 7.2$ GeV, $y_{\text{CM,target}} = -1.045$ at $\sqrt{s_{NN}} = 3.0$ GeV, $y_{\text{CM,target}} = -1.14$ at $\sqrt{s_{NN}} = 3.2$ GeV, and $y_{\text{CM,target}} = -1.25$ at $\sqrt{s_{NN}} = 3.5$ GeV.

The reconstructed signals, corresponding background estimates, extracted signal, and acceptance distributions are presented in Figures 3.9–3.13. Clear signal peaks are observed for all channels above the estimated combinatorial backgrounds. The background estimation methods vary across beam energies:

- At $\sqrt{s_{NN}}$ = 7.2 GeV, for both $^3_\Lambda$H and $^4_\Lambda$H, the background is constructed by rotating all π^- tracks in the transverse plane at eight fixed angles: $45^\circ, 90^\circ, 135^\circ, 180^\circ, 225^\circ, 270^\circ$, and 315°, generating uncorrelated combinations.
- At $\sqrt{s_{NN}}$ = 3.0 GeV, for $^4_\Lambda$He, the background is estimated using an event-mixing technique. In this method, uncorrelated background are constructed by combining ^{3}He tracks from one event with (p, π^-) pairs taken from an another similar events within the same centrality.
- At $\sqrt{s_{NN}}$ = 3.2 and 3.5 GeV, the background for $^4_\Lambda$He is estimated using a track rotation method. Specifically, the ^{3}He tracks are rotated in the transverse plane by random angles uniformly distributed between 10° and 350°, repeated 20 times for ^{3}He.

These estimated combinatorial backgrounds reproduce the true background shapes reasonably well, as shown in Figures 3.9–3.13.

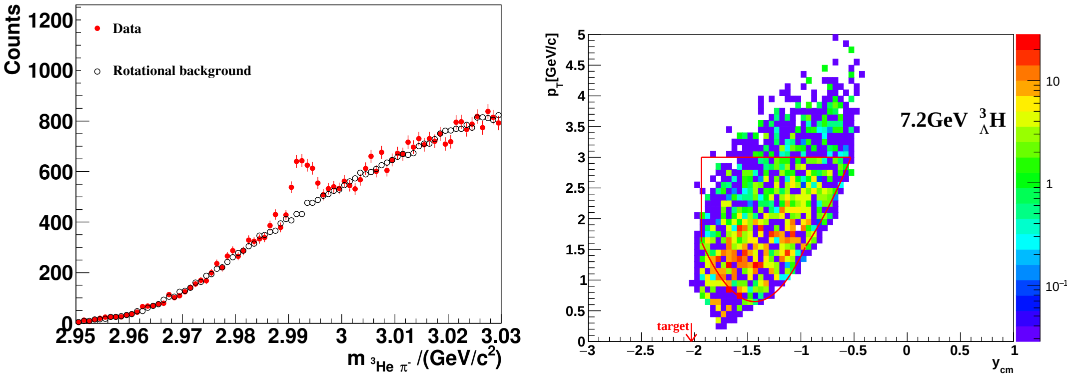

Figure 3.9 $^{3}_{\Lambda}$H signal reconstruction at $\sqrt{s_{NN}}$ = 7.2 GeV. Left: invariant mass distribution of ^{3}He–π with rotational background; right: p_T vs. $y_{\rm CM}$ acceptance with fiducial cuts shown in red.

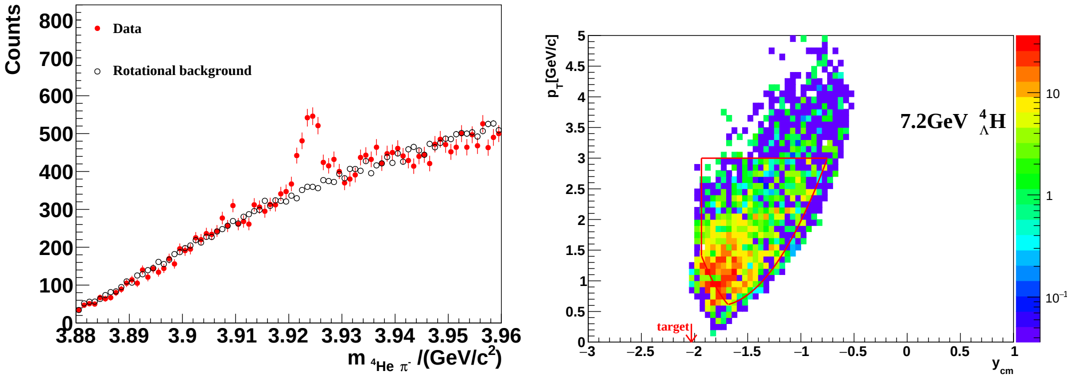

Figure 3.10 $^{4}_{\Lambda}$H signal reconstruction at $\sqrt{s_{NN}}$ = 7.2 GeV. Left: invariant mass distribution of ^{4}He–π with rotational background; right: p_T vs. $y_{\rm CM}$ acceptance with fiducial cuts shown in red.

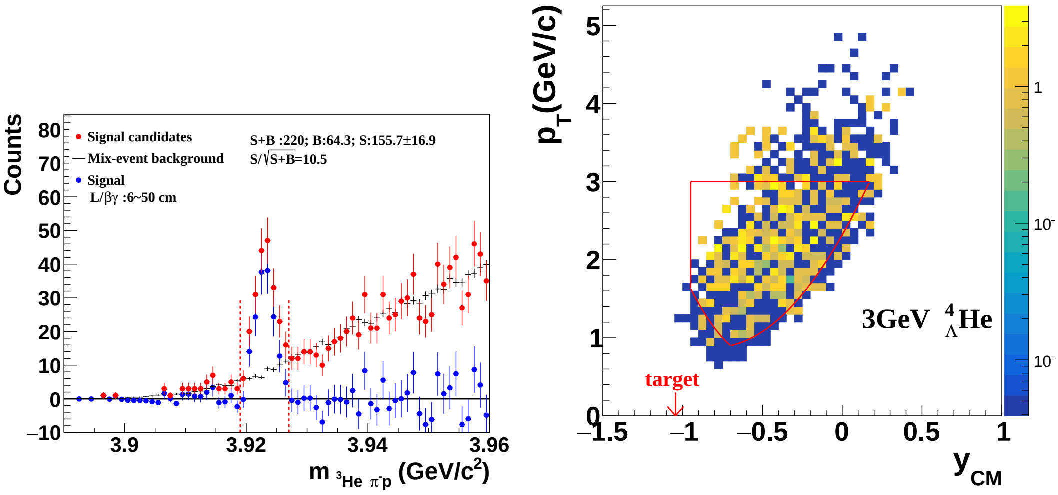

Figure 3.11 $^{4}_{\Lambda}$He signal reconstruction at $\sqrt{s_{NN}}$ = 3.0 GeV. Left: foreground (red), background (black), and extracted signal (blue); right: p_T vs. $y_{\rm CM}$ acceptance with fiducial cuts shown in red.

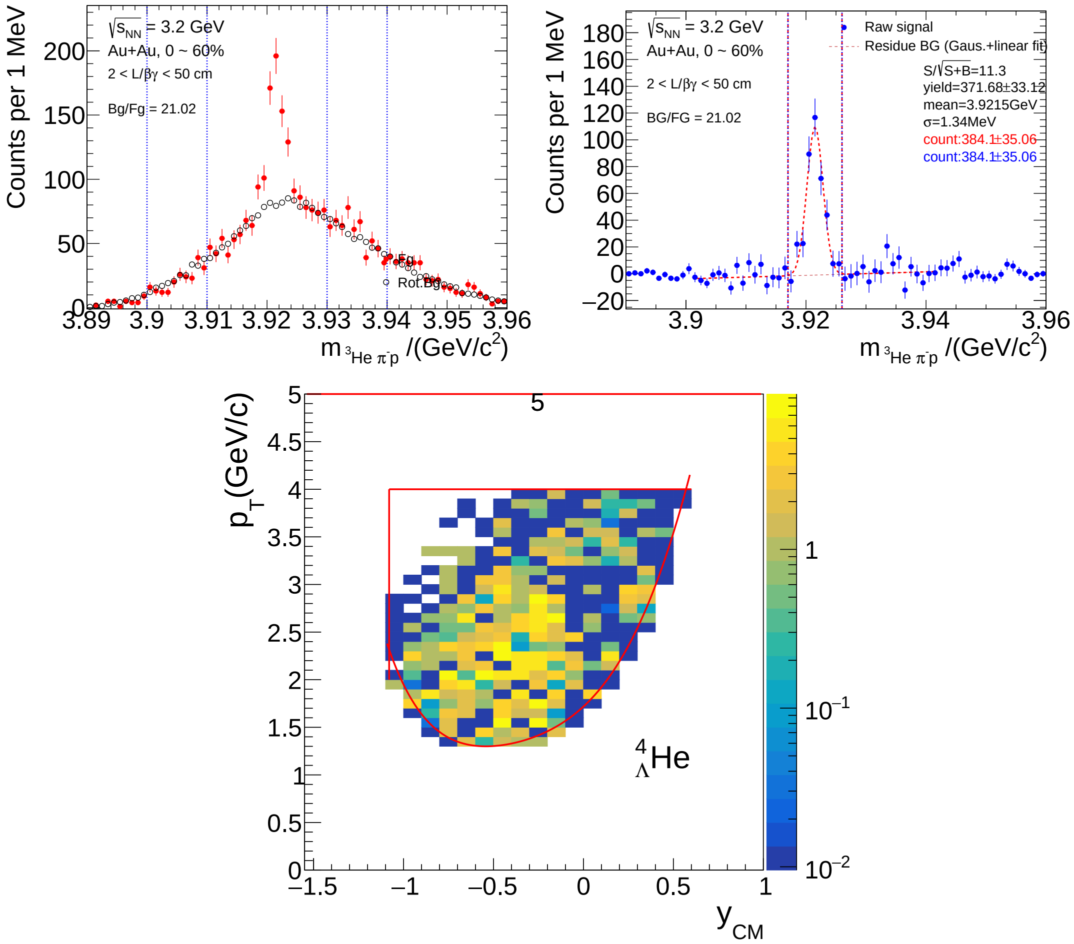

Figure 3.12 $^4_\Lambda$He signal reconstruction at $\sqrt{s_{NN}}$ = 3.2 GeV. Top-left: foreground and scaled rotational background; top-right: extracted signal fit; bottom: p_T vs. $y_{\rm CM}$ acceptance with fiducial cuts shown in red.

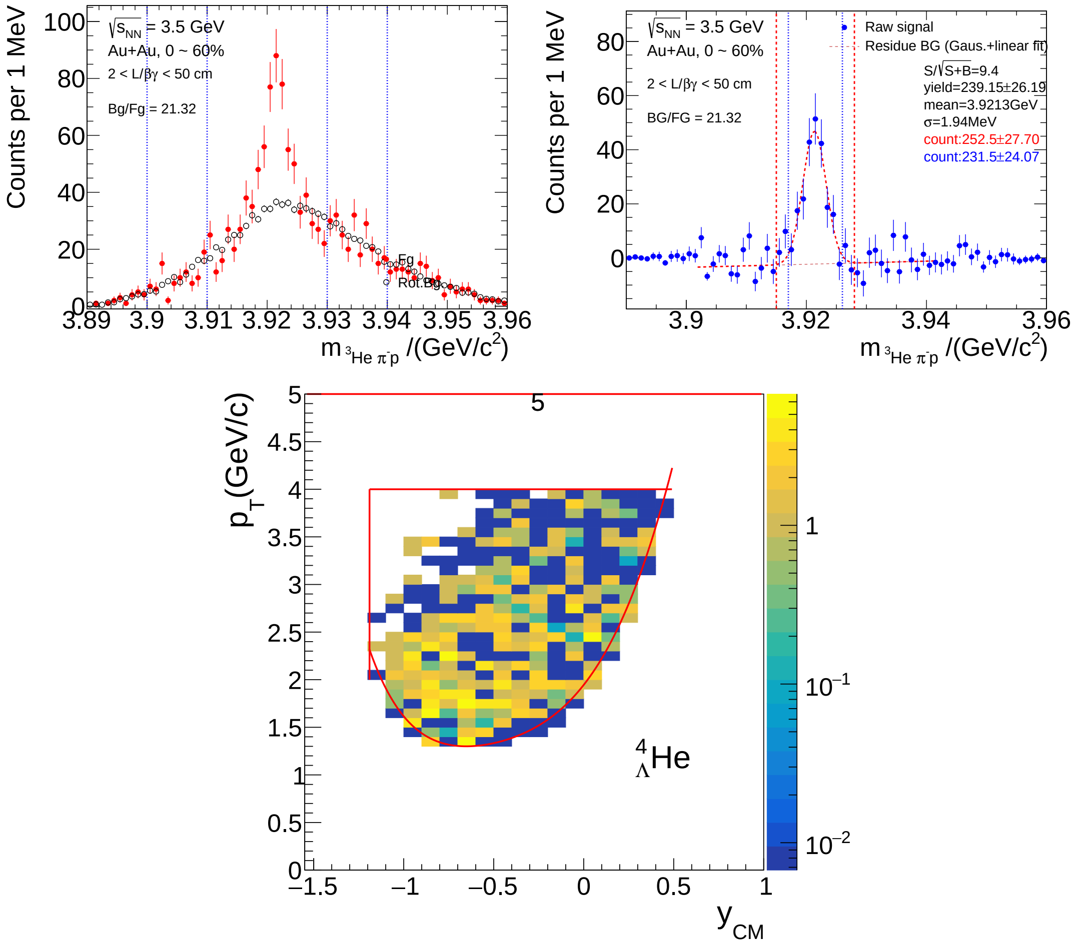

Figure 3.13 **$^{4}_{\Lambda}$He signal reconstruction at $\sqrt{s_{NN}}$ = 3.5 GeV. Top-left: foreground and scaled rotational background; top-right: extracted signal fit; bottom: p_T vs. y_{CM} acceptance with fiducial cuts shown in red.**

3.3 Lifetime Analysis

The lifetime extraction procedure follows the method used in Ref. [86]. We begin by extracting the raw signal counts in bins of proper length $L/\beta\gamma$, from which the binned yield $\Delta N_{\mathrm{raw}}/\Delta(L/\beta\gamma)$ is obtained. These raw yields are then corrected by the reconstruction efficiency as a function of $L/\beta\gamma$ using the formula:

$$\frac{\Delta N}{\Delta(L/\beta\gamma)} = \frac{1}{\epsilon(L/\beta\gamma)} \times \frac{\Delta N_{\mathrm{raw}}}{\Delta(L/\beta\gamma)}. \tag{3.7}$$

To obtain the continuous $dN/d(L/\beta\gamma)$ distribution, a bin-shifting correction is applied to the efficiency-corrected yields. The lifetime τ is extracted by fitting an exponential function to the corrected distribution of signal counts as a function of $L/\beta\gamma$, where L is the decay length. The functional form used in the fit is:

$$N(L/\beta\gamma) = N_0 \exp\left(-\frac{L}{\beta\gamma c\tau}\right), \tag{3.8}$$

where N_0 is the normalization constant, $\beta\gamma$ is the Lorentz factor, and c is the speed of light. The inverse of the negative slope of the fitted function, multiplied by c, yields the measured lifetime τ.

3.3.1 Raw Signal Extraction in $L/\beta\gamma$ Bins

1. ${}^{3}_{\Lambda}\mathrm{H}$ and ${}^{4}_{\Lambda}\mathrm{H}$ at $\sqrt{s_{NN}} = 7.2$ GeV

The signal yields of ${}^{3}_{\Lambda}\mathrm{H}$ and ${}^{4}_{\Lambda}\mathrm{H}$ are extracted using a bin-counting method applied within several $L/\beta\gamma$ intervals. A fixed mass window is used in each bin: $2.988 < M(^{3}\mathrm{He}\pi^{-}) < 2.997$ GeV/c^2 for ${}^{3}_{\Lambda}\mathrm{H}$, and $3.919 < M(^{4}\mathrm{He}\pi^{-}) < 3.929$ GeV/c^2 for ${}^{4}_{\Lambda}\mathrm{H}$, corresponding to three times the width of the mass peak. The following five $L/\beta\gamma$ intervals are used:

[2, 8, 12, 16, 22, 40] cm.

Invariant mass distributions for the 2-body decays ${}^{3}_{\Lambda}\mathrm{H} \rightarrow {}^{3}\mathrm{He}+\pi^{-}$ and ${}^{4}_{\Lambda}\mathrm{H} \rightarrow {}^{4}\mathrm{He}+\pi^{-}$ in each $L/\beta\gamma$ bin are shown in Figures 3.14 and 3.15, respectively.

The combinatorial background is estimated using a rotational method, where daughter π^{-} tracks are rotated in the transverse plane by 8 fixed angles to generate statistically uncorrelated background candidates. These backgrounds are then scaled according to the ratio of yields in the sideband regions between data and background distributions. The sideband regions are defined as follows: for ${}^{3}_{\Lambda}\mathrm{H}$, $3.006 < M(^{3}\mathrm{He}\pi^{-}) < 3.028$ GeV/c^2; for ${}^{4}_{\Lambda}\mathrm{H}$, $3.938 < M(^{4}\mathrm{He}\pi^{-}) < 3.950$ GeV/c^2. These regions are located approximately 8 to 15 or 20 mass widths away from the respective mass peaks, and are marked with dotted lines in Figure 3.14 and 3.15.

After subtracting the scaled background from the raw spectra, the residual distributions are fitted with a linear function in the residual-fit ranges: $2.950 < M(^3\mathrm{He}\pi^-) < 2.984$ and $3.005 < M(^3\mathrm{He}\pi^-) < 3.040$ GeV/c^2 for $^3_\Lambda$H; $3.893 < M(^4\mathrm{He}\pi^-) < 3.908$ and $3.940 < M(^4\mathrm{He}\pi^-) < 3.955$ GeV/c^2 for $^4_\Lambda$H. The resulting fits, shown as red lines in Figures 3.14 and 3.15, are found to be close to zero, confirming the robustness of the background subtraction.

2. $^4_\Lambda$He at $\sqrt{s_{NN}} = 3.0$ GeV

The signal yields of $^4_\Lambda$He at $\sqrt{s_{NN}} = 3.0$ GeV are extracted using a bin-counting method applied in several $L/\beta\gamma$ intervals. A fixed 3σ mass window, $3.919 < M(p\pi^{-3}\mathrm{He}) < 3.927$ GeV/c^2, is used as the counting window in each bin. The following four $L/\beta\gamma$ intervals are used:

$$[6,\ 14,\ 18,\ 30,\ 50]\ \mathrm{cm}.$$

Invariant mass distributions for the 3-body decay $^4_\Lambda\mathrm{He} \to {}^3\mathrm{He} + p + \pi^-$ in each $L/\beta\gamma$ bin are shown in Figure 3.16.

The combinatorial background is estimated using an event-mixing method, where a mixed-event candidate is constructed from a ^{3}He track and a $(p-\pi^-)$ pair from different events. The mixed background is normalized by matching the integral in the sideband region $3.930 < M(p\pi^{-3}\mathrm{He}) < 3.946$ GeV/c^2 between the same-event and mixed-event distributions.

After subtracting the scaled background, the residual distributions are fitted with a linear function in the regions $3.890 < M(p\pi^{-3}\mathrm{He}) < 3.915$ and $3.931 < M(p\pi^{-3}\mathrm{He}) < 3.960$ GeV/c^2, which are outside of about $\pm 6\sigma$ from the peak center. The resulting fits, shown as black lines in Figure 3.16, lie close to zero.

3. $^4_\Lambda$He at $\sqrt{s_{NN}} = 3.2$ and 3.5 GeV

The signal extraction for $^4_\Lambda$He at $\sqrt{s_{NN}} = 3.2$ and 3.5 GeV uses the same bin-counting technique with the following $L/\beta\gamma$ bin boundaries:

$$[6,\ 14,\ 18,\ 25,\ 40]\ \mathrm{cm}.$$

Invariant mass distributions for the 3-body decay $^4_\Lambda\mathrm{He} \to {}^3\mathrm{He} + p + \pi^-$ in each $L/\beta\gamma$ bin are shown in Figures 3.17 and 3.18.

The combinatorial background is estimated using a rotation method, where the ^{3}He track is randomly rotated 20 times in the transverse plane between 10° and 350° to form

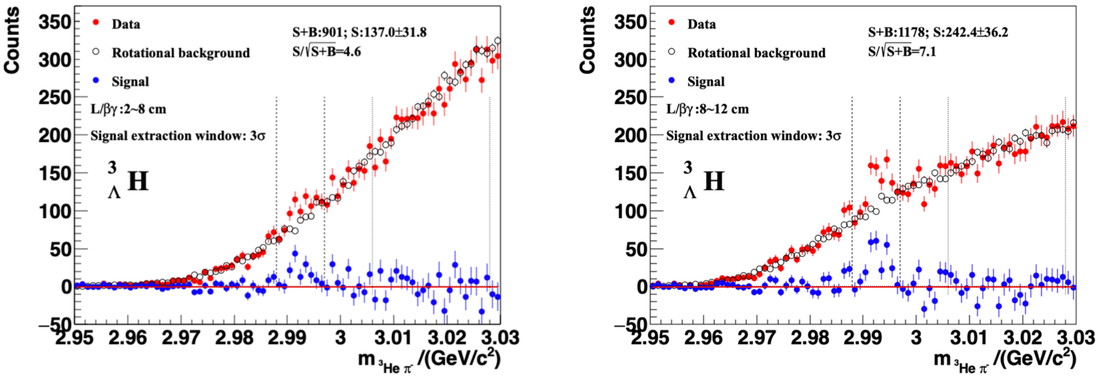

(a) $L/\beta\gamma$ Bin 1: 2–8 cm **(b) $L/\beta\gamma$ Bin 2: 8–12 cm**

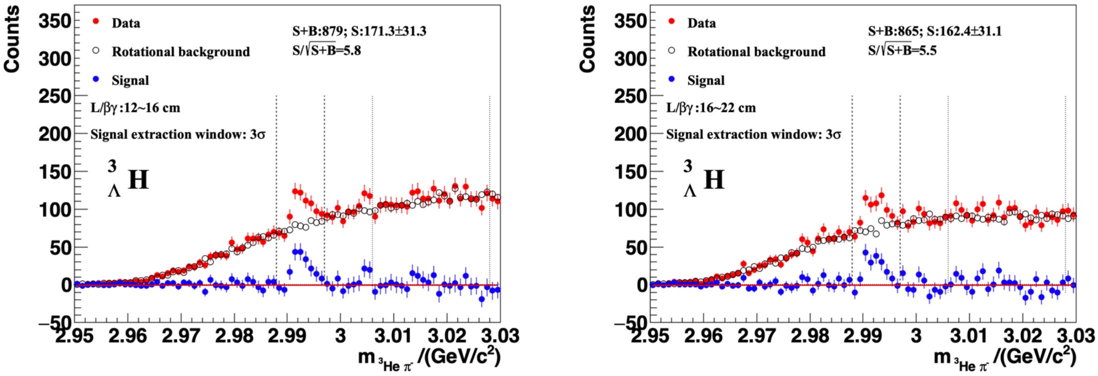

(c) $L/\beta\gamma$ Bin 3: 12–16 cm **(d) $L/\beta\gamma$ Bin 4: 16–22 cm**

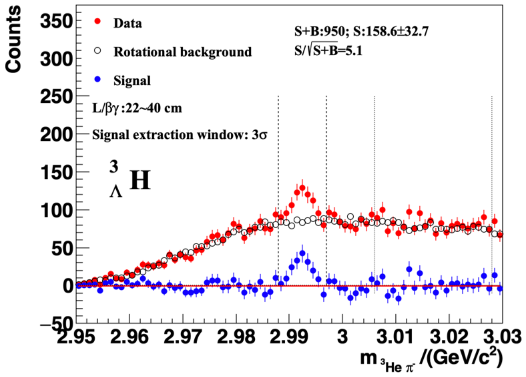

(e) $L/\beta\gamma$ Bin 5: 22–40 cm

Figure 3.14 Invariant mass distributions of $^{3}_{\Lambda}$H candidates in different $L/\beta\gamma$ bins at $\sqrt{s_{NN}}$ = 7.2 GeV(0–80% centrality). Red circles: foreground; black circles: rotational background; blue circles: background-subtracted signal; red line: residual background fit. The dashed vertical lines near the signal peak indicate the counting window, and the dotted lines mark the sideband regions.

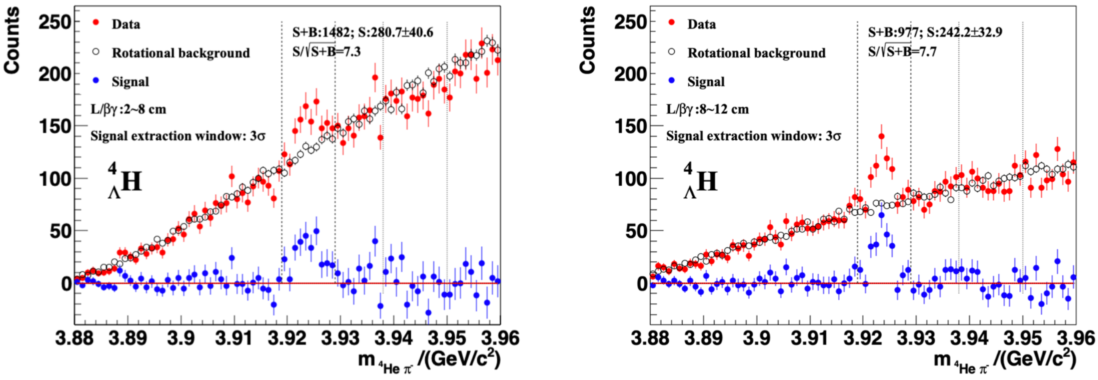

(a) $L/\beta\gamma$ Bin 1: 2–8 cm **(b) $L/\beta\gamma$ Bin 2: 8–12 cm**

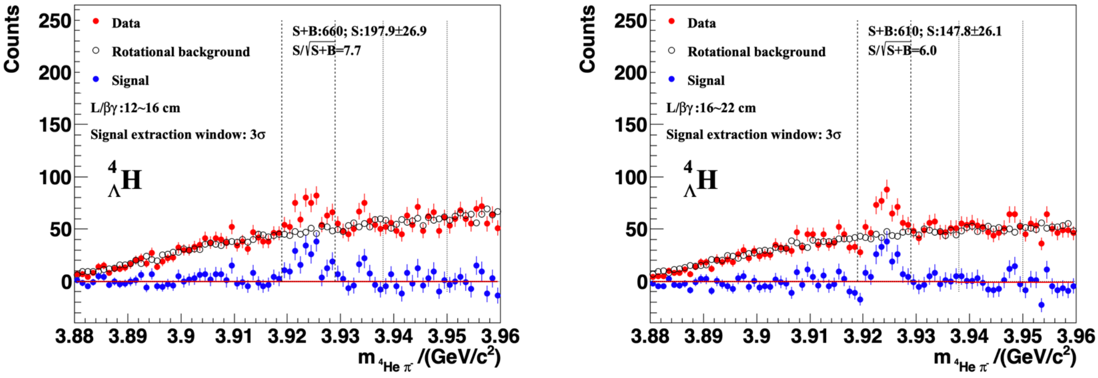

(c) $L/\beta\gamma$ Bin 3: 12–16 cm **(d) $L/\beta\gamma$ Bin 4: 16–22 cm**

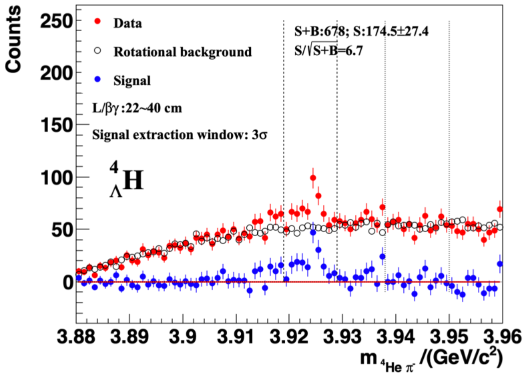

(e) $L/\beta\gamma$ Bin 5: 22–40 cm

Figure 3.15 Invariant mass distributions of $^4_\Lambda$H candidates in different $L/\beta\gamma$ bins at $\sqrt{s_{NN}}$ = 7.2 GeV(0–80% centrality). Red circles: foreground; black circles: rotational background; blue circles: background-subtracted signal; red line: residual background fit. The dashed vertical lines near the signal peak indicate the counting window, and the dotted lines mark the sideband regions.

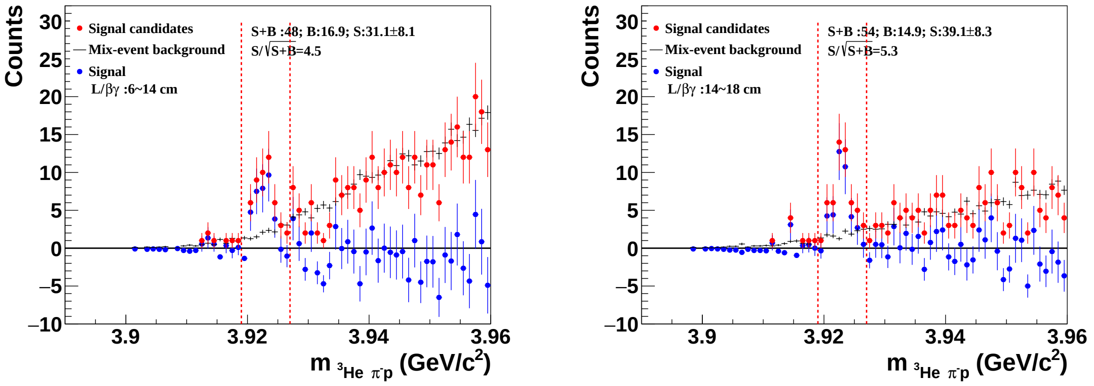

(a) $L/\beta\gamma$ Bin 1: 6–14 cm **(b) $L/\beta\gamma$ Bin 2: 14–18 cm**

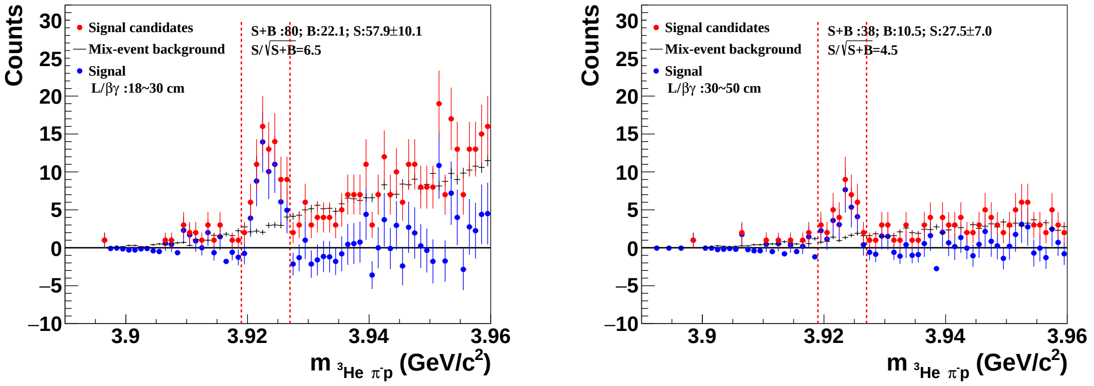

(c) $L/\beta\gamma$ Bin 3: 18–30 cm **(d) $L/\beta\gamma$ Bin 4: 30–50 cm**

Figure 3.16 Invariant mass distributions of ${}^{4}_{\Lambda}$He candidates in different $L/\beta\gamma$ bins (0–60% centrality) at $\sqrt{s_{NN}} = 3.0$ GeV.

uncorrelated combinations. The background is scaled by matching the integral in the sideband regions $3.900 < M(p\pi^{-3}\text{He}) < 3.910$ GeV/c^2 and $3.930 < M(p\pi^{-3}\text{He}) < 3.940$ GeV/c^2 for foreground and background.

After background subtraction, the remaining signal is fitted together with a linear function for the residual background and a Gaussian for the peak in the range $3.9017 < M(p\pi^{-3}\text{He}) < 3.9416$ GeV/c^2 in each $L/\beta\gamma$ bin. The mass resolution extracted from the Gaussian component determines the signal extraction window, defined as $\pm 3\sigma$ around the peak position. This signal extraction region is indicated by the red vertical dashed lines in the invariant mass plots of signal candidates, as shown in the right plots in Figures 3.17 and 3.18.

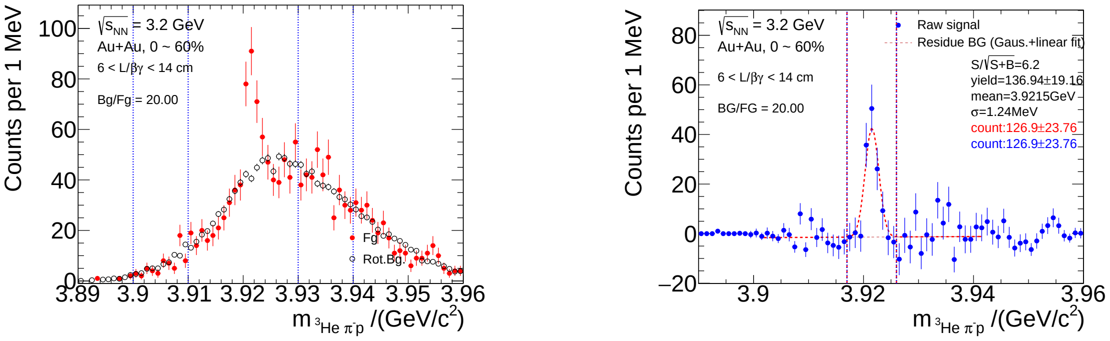

(a) Foreground + background (Bin 1) **(b) Signal fit (Bin 1)**

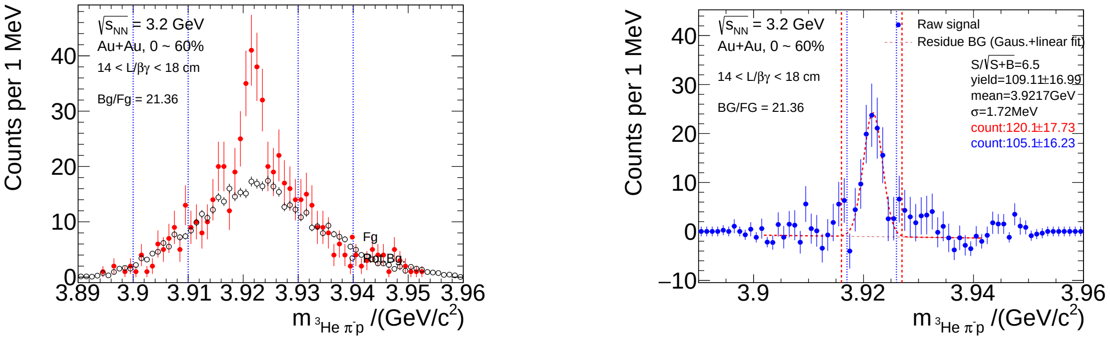

(c) Foreground + background (Bin 2) **(d) Signal fit (Bin 2)**

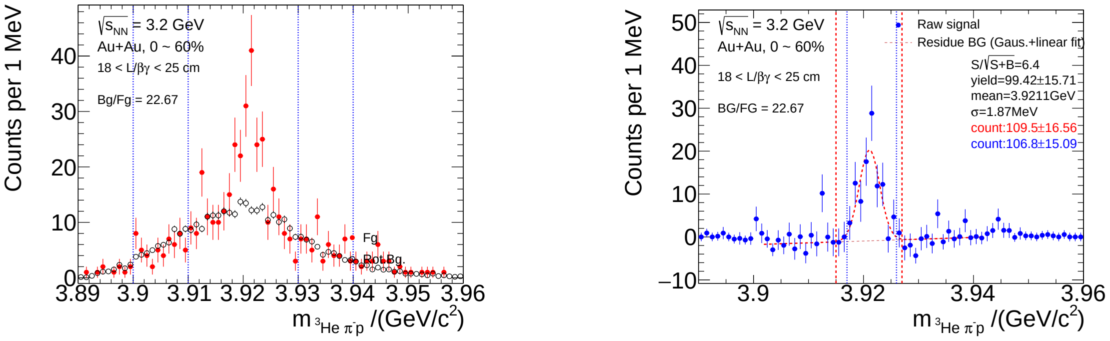

(e) Foreground + background (Bin 3) **(f) Signal fit (Bin 3)**

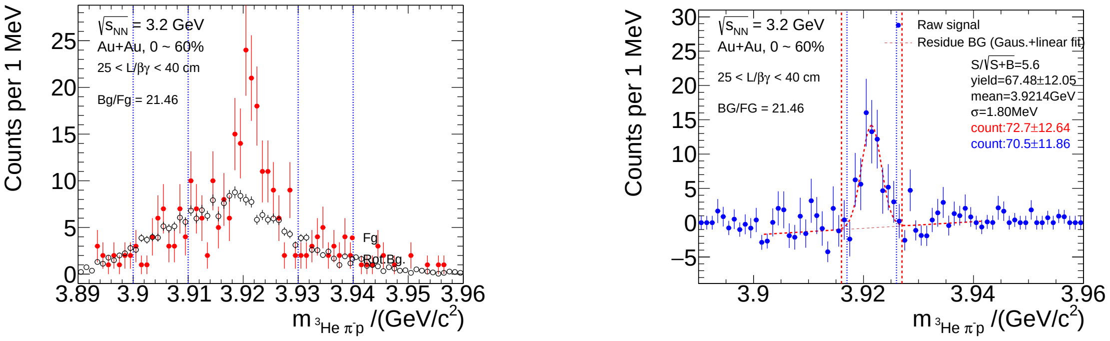

(g) Foreground + background (Bin 4) **(h) Signal fit (Bin 4)**

Figure 3.17 ${}^{4}_{\Lambda}$**He signal extraction in different** $L/\beta\gamma$ **bins in 0–60% centrality at** $\sqrt{s_{NN}}$ **= 3.2 GeV.**

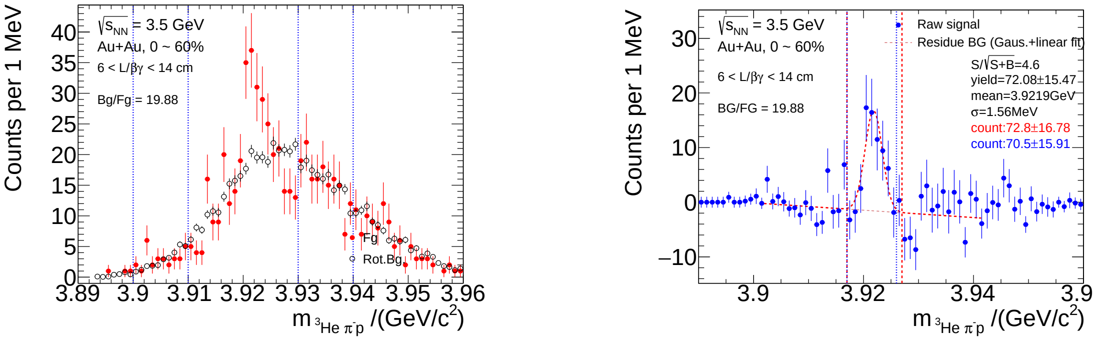

(a) Foreground + background (Bin 1) **(b) Signal fit (Bin 1)**

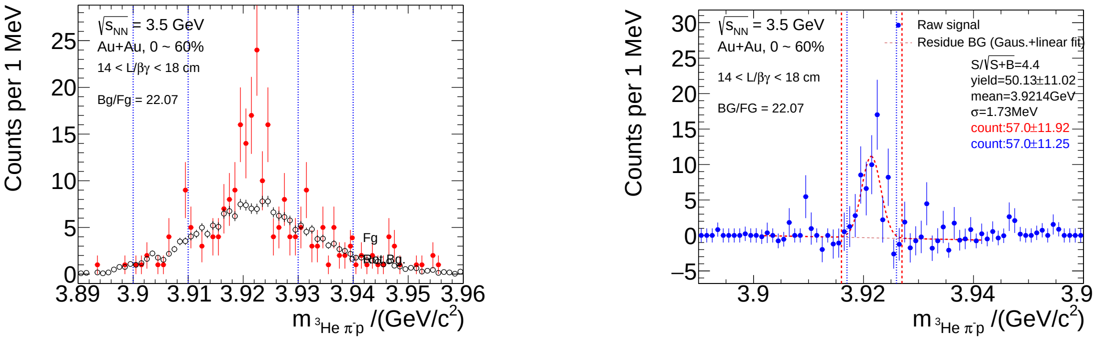

(c) Foreground + background (Bin 2) **(d) Signal fit (Bin 2)**

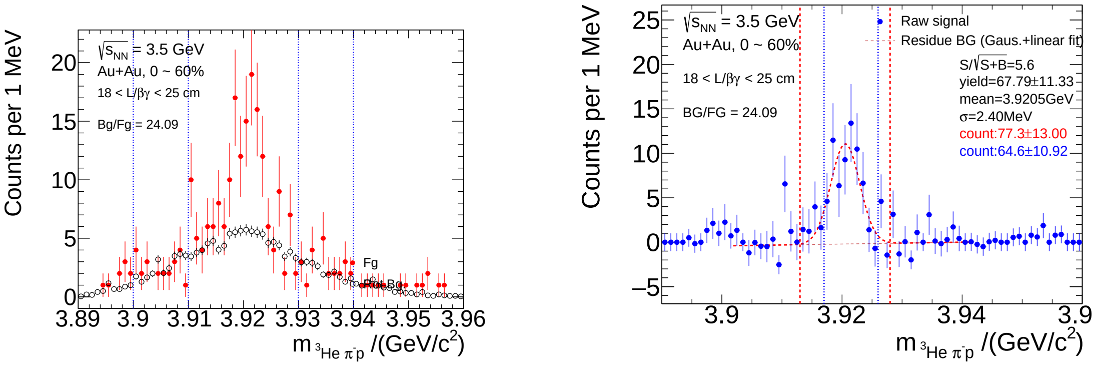

(e) Foreground + background (Bin 3) **(f) Signal fit (Bin 3)**

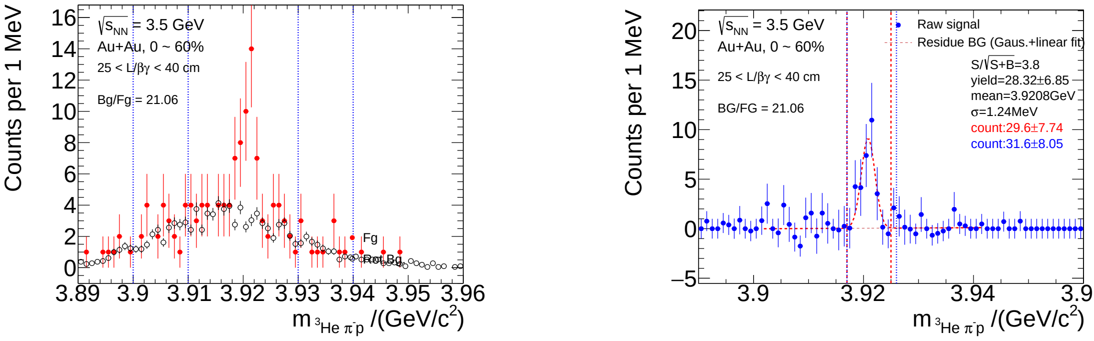

(g) Foreground + background (Bin 4) **(h) Signal fit (Bin 4)**

Figure 3.18 $^{4}_{\Lambda}$He signal extraction in different $L/\beta\gamma$ bins in 0–60% centrality at $\sqrt{s_{NN}}$ = 3.5 GeV.

3.3.2 Reconstruction Efficiency

The reconstruction efficiency is estimated using the standard STAR embedding technique [168-169]. In this approach, Monte Carlo (MC) tracks of hypernuclei and their daughter particles are first generated and propagated through the STAR detector using the full detector simulation framework based on GEANT3. These simulated tracks are then embedded into real minimum-bias events at the raw data level. Subsequently, the combined events (MC + real data) undergo the same reconstruction chain as the real data, including track finding, vertexing, and particle identification. This ensures that the detector effects, background conditions, and reconstruction inefficiencies are realistically accounted for in the efficiency determination.

1. Embedding Re-weighting

Before calculating the reconstruction efficiency, we apply re-weighting procedures to ensure that the MC simulations can reflect the distributions observed in data correctly.

（1） Phase-Space Re-weighting

The original MC embedding samples are usually generated with a flat p_T spectrum and a uniform distribution in rapidity or pseudorapidity. However, in real data, the p_T spectrum is typically exponential. To ensure consistency between the phase-space distributions of the embedded MC samples and the experimental data, the MC events are re-weighted as functions of rapidity and p_T.

Specifically, a quadratic function is applied to reproduce the rapidity distribution, after either a Boltzmann function or an m_T-exponential function is used in the p_T direction to match the observed raw spectra from data. For example, assuming a Boltzmann distribution for the hypernuclear yields, the transverse mass distribution follows the form:

$$\frac{dN}{m_T\,dm_T} \sim m_T e^{-m_T/T_\mathrm{B}}, \tag{3.9}$$

where T_B is the inverse slope parameter (or effective temperature). To express this in terms of p_T, we use the transformation:

$$\frac{dp_T}{dm_T} = \frac{d\sqrt{m_T^2 - m_0^2}}{dm_T} = \frac{m_T}{p_T}, \tag{3.10}$$

which leads to the p_T distribution:

$$\frac{dN}{dp_T} \sim p_T m_T e^{-m_T/T_\mathrm{B}}. \tag{3.11}$$

This function is then used to assign phase-space weights in the p_T direction, ensuring that the MC sample roughly reproduces the shape of the measured spectra.

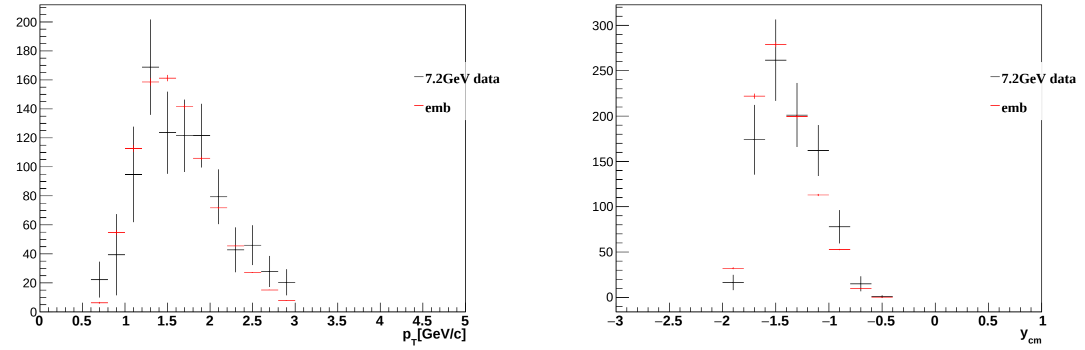

(a) p_T distribution for ${}^3_\Lambda$H **(b) Rapidity distribution for ${}^3_\Lambda$H**

Figure 3.19 Comparison of p_T and rapidity distributions of data and weighted embedding for ${}^3_\Lambda$H at $\sqrt{s_{NN}}$ = 7.2 GeV.

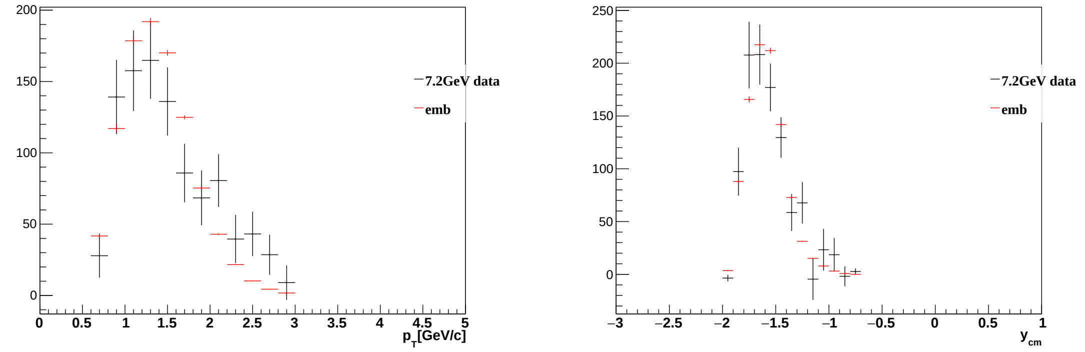

(a) p_T distribution for ${}^4_\Lambda$H **(b) Rapidity distribution for ${}^4_\Lambda$H**

Figure 3.20 Comparison of p_T and rapidity distributions of data and weighted embedding for ${}^4_\Lambda$H at $\sqrt{s_{NN}}$ = 7.2 GeV.

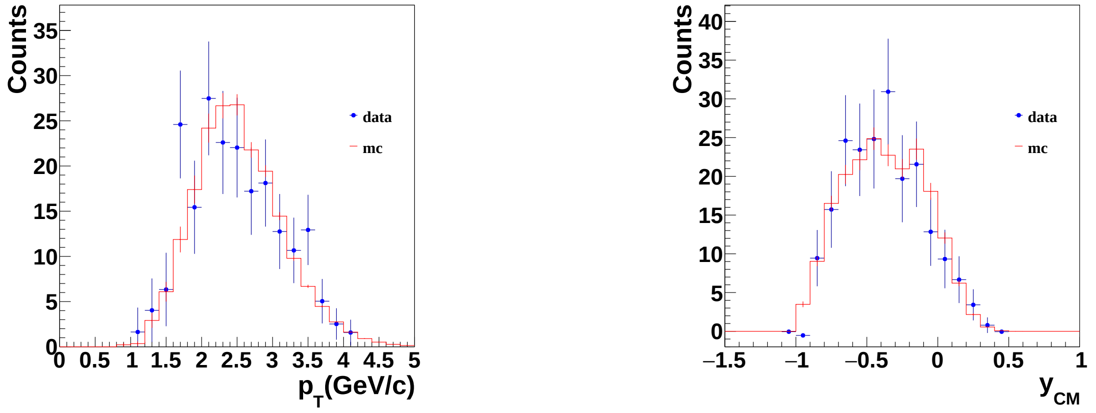

(a) p_T distribution **(b) Rapidity distribution**

Figure 3.21 Comparison of p_T and rapidity distributions of data and weighted embedding for ${}^4_\Lambda$He at $\sqrt{s_{NN}}$ = 3.0 GeV.

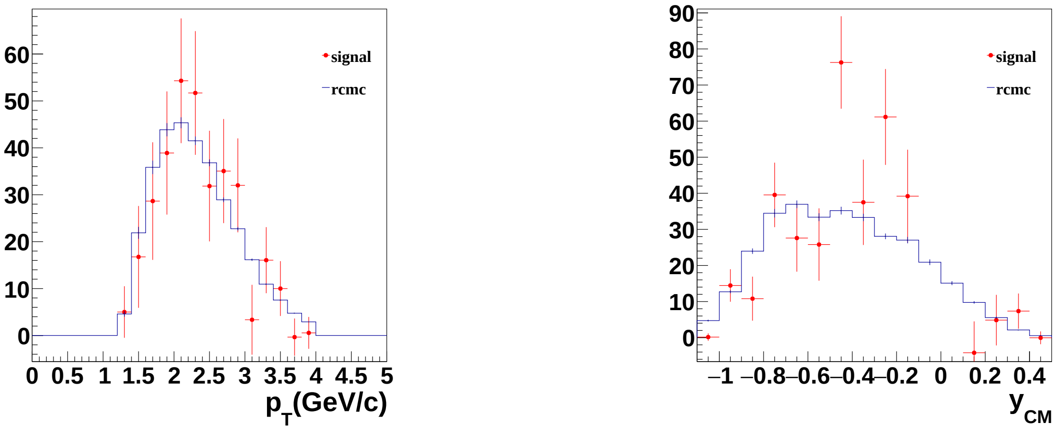

(a) p_T distribution **(b) Rapidity distribution**

Figure 3.22 Comparison of p_T and rapidity distributions of data and weighted embedding for ${}^{4}_{\Lambda}\mathrm{He}$ at $\sqrt{s_{NN}} = 3.2$ GeV.

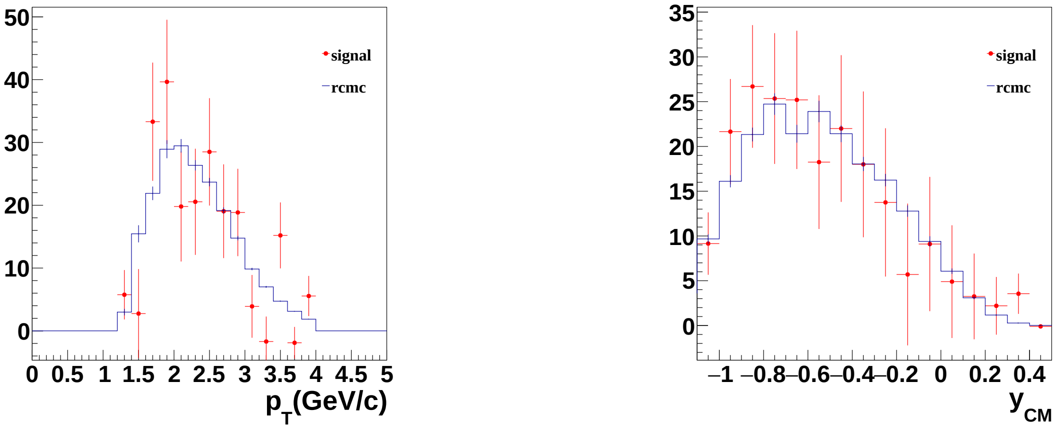

(a) p_T distribution **(b) Rapidity distribution**

Figure 3.23 Comparison of p_T and rapidity distributions of data and weighted embedding for ${}^{4}_{\Lambda}\mathrm{He}$ at $\sqrt{s_{NN}} = 3.5$ GeV.

For the $\sqrt{s_{NN}}$ = 7.2 GeV dataset, the ${}^{3}_{\Lambda}\mathrm{H}$ embedding is weighted using a Boltzmann distribution with temperature T_B = 150 MeV, while for ${}^{4}_{\Lambda}\mathrm{H}$, a temperature T_B = 100 MeV is used. The comparison of weighted MC to data is shown in Figures 3.19 and 3.20. For the ${}^{4}_{\Lambda}\mathrm{He}$ embedding at $\sqrt{s_{NN}}$ = 3.0 GeV, a Boltzmann distribution with temperature T_B = 200 MeV is used. At $\sqrt{s_{NN}}$ = 3.2 and 3.5 GeV, T_B = 210 MeV is applied. The comparisons between the weighted embedding and data distributions at $\sqrt{s_{NN}}$ = 3.0, 3.2 and 3.5 GeV are shown in Figures 3.21, 3.22, and 3.23, respectively.

(2) Dalitz Plot Re-weighting

For ${}^{4}_{\Lambda}\mathrm{He}$, obvious discrepancies are observed between the invariant mass distributions of daughter particle pairs of the reconstructed signals from the experimental data and the reconstructed MC signals from the embedding simulation. As shown in Fig-

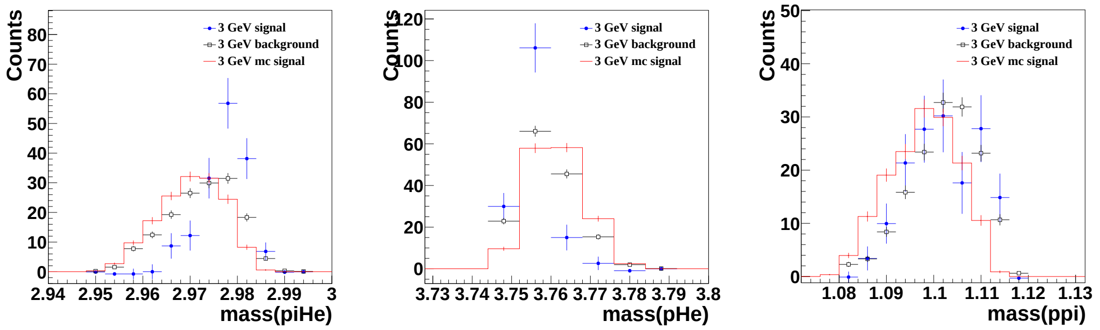

(a) $m(^3\mathrm{He}, \pi^-)$ **(b)** $m(^3\mathrm{He}, p)$ **(c)** $m(p, \pi^-)$

Figure 3.24 Invariant mass distributions of daughter particle pairs without Dalitz re-weighting for $^4_\Lambda$He at $\sqrt{s_{NN}}$ = 3.0 GeV. The reconstructed MC signals are compared with data signals. Shape mismatches are observed between MC and data.

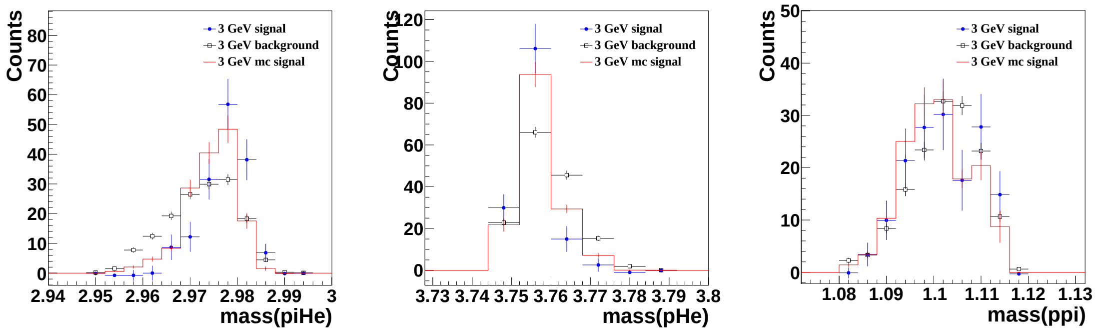

(a) $m(^3\mathrm{He}, \pi^-)$ **(b)** $m(^3\mathrm{He}, p)$ **(c)** $m(p, \pi^-)$

Figure 3.25 Invariant mass distributions of daughter particle pairs after Dalitz re-weighting in embedding for $^4_\Lambda$He at $\sqrt{s_{NN}}$ = 3.0 GeV. The reconstructed MC signals are compared with data signals. The agreement between simulation and data is significantly improved.

ure 3.24, the embedding—assuming a uniform (phase-space) three-body decay—does not fully reproduce the observed shapes in the invariant mass spectra of $m(^3\mathrm{He}, \pi^-)$, $m(^3\mathrm{He}, p)$, and $m(p, \pi^-)$ for $^4_\Lambda$He at at $\sqrt{s_{NN}}$ = 3.0 GeV. The reconstructed MC signals depicted in red can't describe the signals from experimental data denoted in blue well. Obvious mismatch of the peak position in$m(^3\mathrm{He}, \pi^-)$ and $m(^3\mathrm{He}, p)$ are observed.

In order to account for potential decay dynamics and final-state interactions, a Dalitz plot re-weighting is applied to correct for the observed mismatches. This involves constructing a two-dimensional re-weighting histogram in the Dalitz plane, defined as the ratio of experimental data to reconstructed MC signals in each bin. Once the Dalitz weight is applied, the invariant mass distributions of the daughter pairs of $^4_\Lambda$He reconstructed from the embedding match those from the data much better at $\sqrt{s_{NN}}$ = 3.0 GeV, as illustrated in Figure 3.25.

The $^4_\Lambda$He lifetime analyses at $\sqrt{s_{NN}}$ = 3.2 and 3.5 GeV are also performed with the Dalitz weight applied to match reconstructed MC to data, similar to those used in $^4_\Lambda$He analysis at $\sqrt{s_{NN}}$ = 3.0 GeV. The comparisons before and after applying the Dalitz

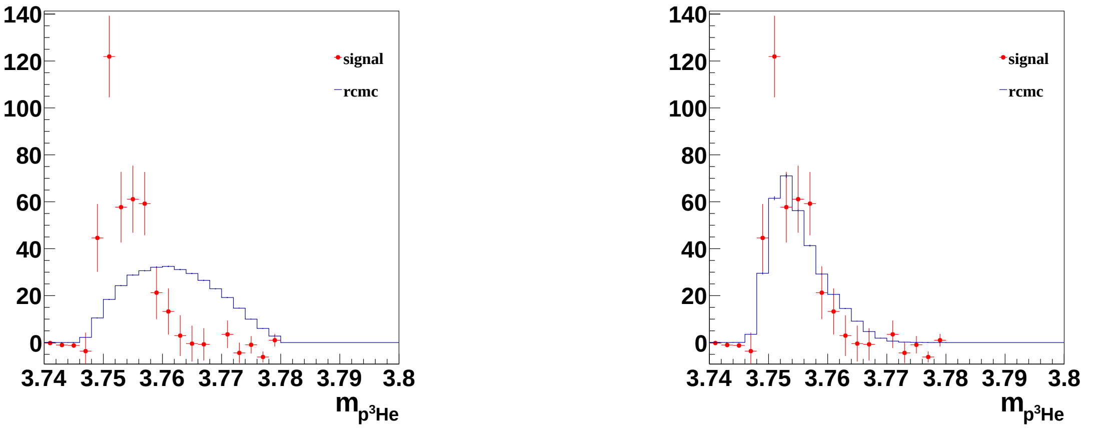

(a) 3.2 GeV: $m(^3\text{He}, p)$ before (b) 3.2 GeV: $m(^3\text{He}, p)$ after

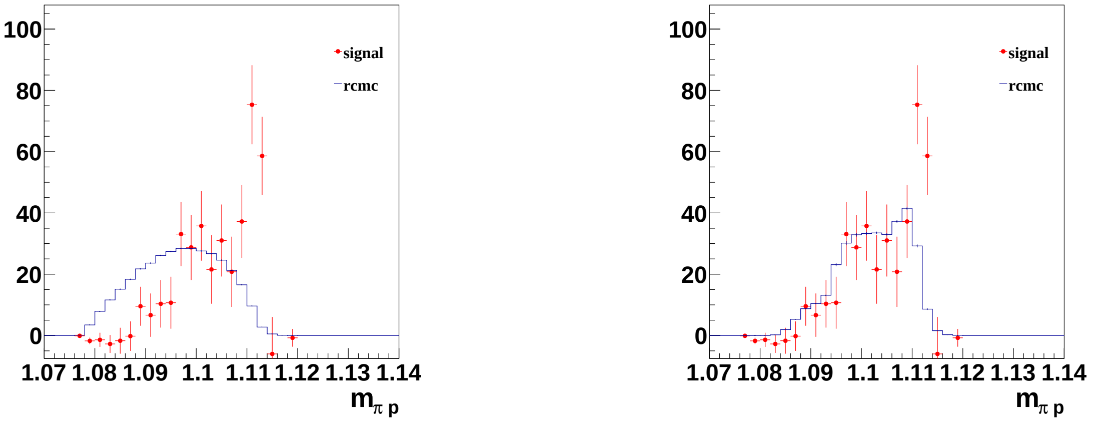

(c) 3.2 GeV: $m(p, \pi^-)$ before (d) 3.2 GeV: $m(p, \pi^-)$ after

Figure 3.26 Comparison of invariant mass distributions of daughter particle pairs before and after applying Dalitz weights for $^4_\Lambda$He at $\sqrt{s_{NN}}$ = 3.2 GeV. Shape mismatches are observed between MC and data without Dalitz re-weighting (left).

weight at $\sqrt{s_{NN}}$ = 3.2 and 3.5 GeV are shown in Figures 3.26 and 3.27. This procedure improves the agreement between MC and data, ensuring a more accurate evaluation of efficiency and systematic uncertainties.

(3) Lifetime Re-weighting

To ensure consistency between the decay length distributions or the lifetimes in data and simulation, an additional lifetime re-weighting is applied to the embedded MC $^4_\Lambda$He particles based on their proper decay length, defined as $pl = L/(\beta\gamma)$. In the embedding of $\sqrt{s_{NN}}$ = 3.0 GeV, the lifetime of MC $^4_\Lambda$He is set equal to that of a free Λ, τ = 263.2 ps. However, the world-average measured value for $^4_\Lambda$He is $\tau_{\text{aim}} = 250 \pm 18$ ps [170-171].

After applying phase-space weights in p_T and rapidity as well as Dalitz-plot weights, the effective lifetime of the MC $^4_\Lambda$He sample at $\sqrt{s_{NN}}$ = 3.0 GeV is found to be reduced to approximately 258 ps, as shown in the left panel of Figure 3.28, which

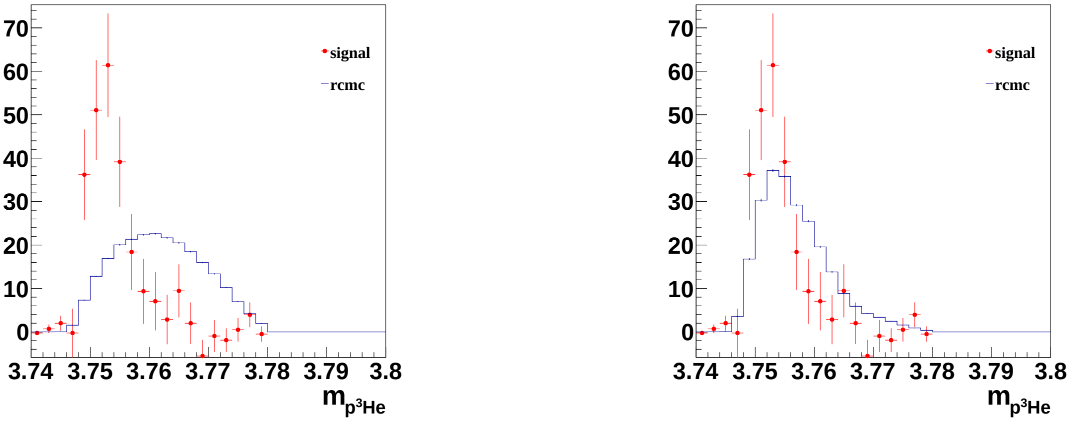

(a) 3.5 GeV: $m(^3\text{He}, p)$ before **(b) 3.5 GeV: $m(^3\text{He}, p)$ after**

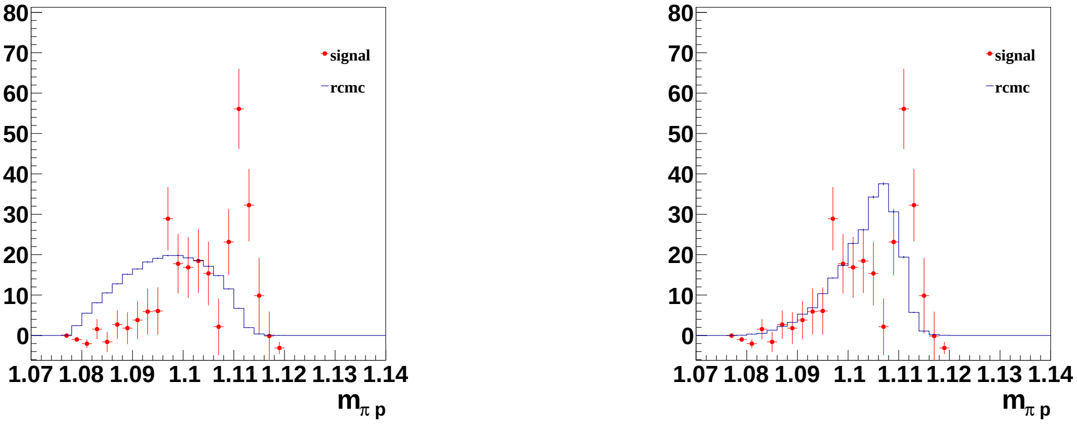

(c) 3.5 GeV: $m(p, \pi^-)$ before **(d) 3.5 GeV: $m(p, \pi^-)$ after**

Figure 3.27 Comparison of invariant mass distributions of daughter particle pairs before and after applying Dalitz weights for $^4_\Lambda$He at $\sqrt{s_{NN}} = 3.5$ GeV. Shape mismatches are observed between MC and data without Dalitz re-weighting (left).

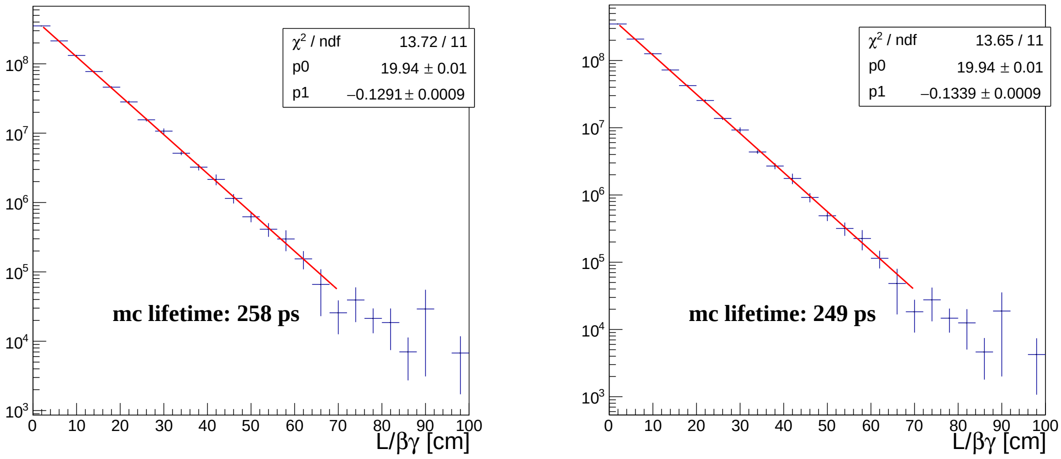

(a) Without lifetime re-weighting **(b) With lifetime re-weighting**

Figure 3.28 Proper decay length distribution of embedded MC $^4_\Lambda$He at $\sqrt{s_{NN}}$ = 3.0 GeV, before and after lifetime re-weighting. The lifetime is extracted from the slope.

still deviates slightly from the target world average value.

To correct for this mismatch, we apply a lifetime weight on proper decay length to mc particles using the ratio of two exponential decay distributions:

$$w(pl) = \exp\left[\frac{1}{c}\left(\frac{1}{\tau_0} - \frac{1}{\tau_{\text{aim}}}\right) \cdot pl\right], \tag{3.12}$$

where c is the speed of light, τ_0 is the initial lifetime, and τ_{aim} is the desired (target) lifetime. This procedure effectively reshapes the decay length distribution in the simulation to better match the world average lifetime. As shown in the right panel of Figure 3.28, after applying this lifetime re-weighting, the MC sample is effectively corrected to a lifetime of approximately 249 ps, which is in close agreement with the world average.

In the $\sqrt{s_{NN}}$ = 3.0 GeV analysis, this re-weighting process is performed iteratively: the measured ${}^4_\Lambda$He lifetime is used as the new τ_{aim} to define the MC weighting, which then yields a more accurate measurement in the next iteration. This procedure is repeated iteratively until convergence is reached. The final MC sample used for efficiency correction corresponds to a lifetime of 230 ps, which matches the measured lifetime value. No systematic uncertainty from lifetime re-weighting is considered for the ${}^4_\Lambda$He lifetime analysis at $\sqrt{s_{NN}}$ = 3.0 GeV.

In contrast, for the $\sqrt{s_{NN}}$ = 3.2 and 3.5 GeV analyses, the input MC lifetime of of ${}^4_\Lambda$He in embedding is set as the world-average lifetime. However, we apply lifetime re-weighting to vary the effective MC lifetime to 210 ps, 230 ps, and 270 ps. The 230 ps and 270 ps values approximately correspond to the $\pm 1\sigma$ range of the world-average lifetime. The 210 ps variation is introduced to account for the lower central value of ${}^4_\Lambda$He lifetime measured at $\sqrt{s_{NN}}$ = 3.0 GeV compared to the world-average value, representing -2σ of the world average and within about -0.7σ relative to the ${}^4_\Lambda$He lifetime measured at $\sqrt{s_{NN}}$ = 3.0 GeV. This variation is used to estimate the systematic uncertainty associated with the imperfect knowledge of the true ${}^4_\Lambda$He lifetime.

2. Efficiency as a Function of $L/\beta\gamma$

After applying the same reconstruction method and the same analysis cuts, and re-weighting the embedding sample to match data, the ratio of the reconstructed MC signals to the input MC signals gives the reconstruction efficiency.

For ${}^3_\Lambda$H and ${}^4_\Lambda$H at $\sqrt{s_{NN}}$ = 7.2 GeV, the reconstruction efficiencies as a function of $L/\beta\gamma$ are shown in Figure 3.29. These are calculated using MC samples with phase-space re-weighting.

For ${}^4_\Lambda$He at $\sqrt{s_{NN}}$ = 3.0 GeV, the efficiency is first evaluated using MC samples that are re-weighted to an effective lifetime of 249 ps. The resulting efficiency

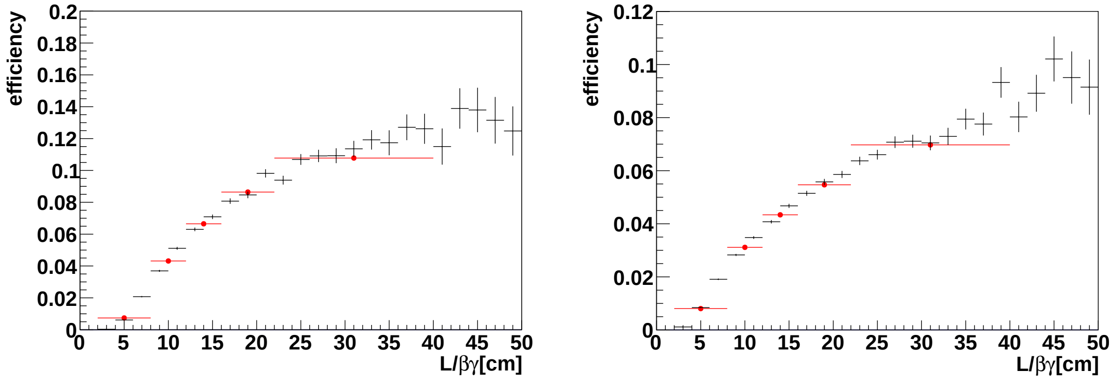

(a) $^{3}_{\Lambda}$H **(b) $^{4}_{\Lambda}$H**

Figure 3.29 Reconstruction efficiency as a function of $L/\beta\gamma$ for $^{3}_{\Lambda}$H (left) and $^{4}_{\Lambda}$H (right) at $\sqrt{s_{NN}}$ = 7.2 GeV.

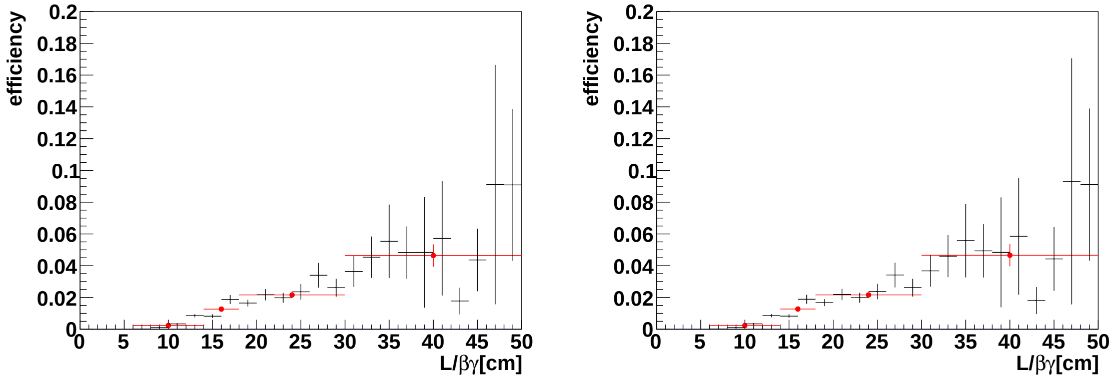

(a) $^{4}_{\Lambda}$He MC lifetime 249 ps **(b) $^{4}_{\Lambda}$He MC lifetime 230 ps (convergence)**

Figure 3.30 Reconstruction efficiency as a function of $L/\beta\gamma$ for $^{4}_{\Lambda}$He at $\sqrt{s_{NN}}$ = 3.0 GeV.

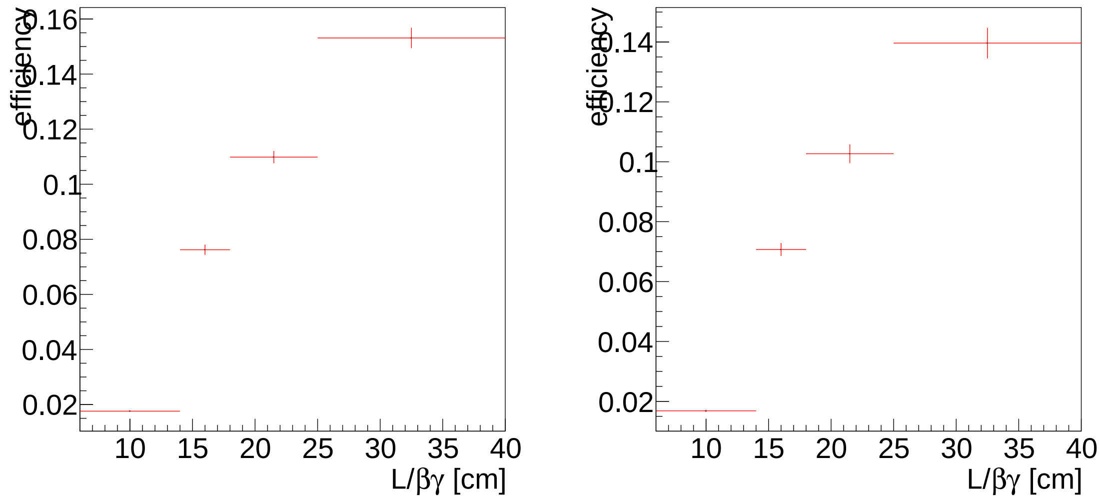

(a) $^{4}_{\Lambda}$He at 3.2 GeV **(b) $^{4}_{\Lambda}$He at 3.5 GeV**

Figure 3.31 Reconstruction efficiency as a function of $L/\beta\gamma$ for $^{4}_{\Lambda}$He at $\sqrt{s_{NN}}$ = 3.2 and 3.5 GeV.

distribution is shown in Figure 3.30 (left). In the subsequent iteration, the efficiency is calculated using a MC lifetime re-weighting to 230 ps, as shown in Figure 3.30 (right), where convergence is achieved. These are calculated using MC samples re-weighted with phase-space, Dalitz plot, and MC lifetime weights.

For $^4_\Lambda$He at $\sqrt{s_{NN}}$ = 3.2 and 3.5 GeV, the reconstruction efficiencies as functions of $L/\beta\gamma$ are presented in Figure 3.31. These are calculated using MC samples with phase-space and Dalitz plot re-weighting.

3.3.3 Lifetime Extraction

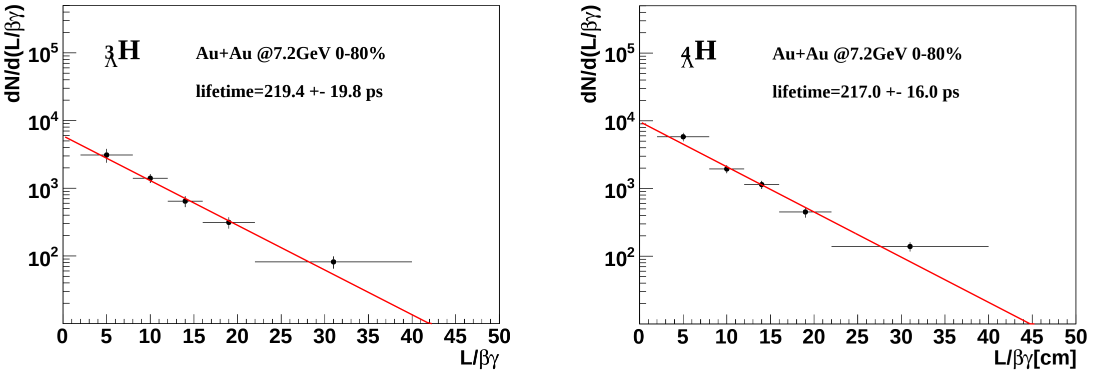

(a) $^3_\Lambda$H corrected yield **(b) $^4_\Lambda$H corrected yield**

Figure 3.32 Corrected yields and exponential fits as a function of $L/\beta\gamma$ for $^3_\Lambda$H (left) and $^4_\Lambda$H (right) at $\sqrt{s_{NN}}$ = 7.2 GeV.

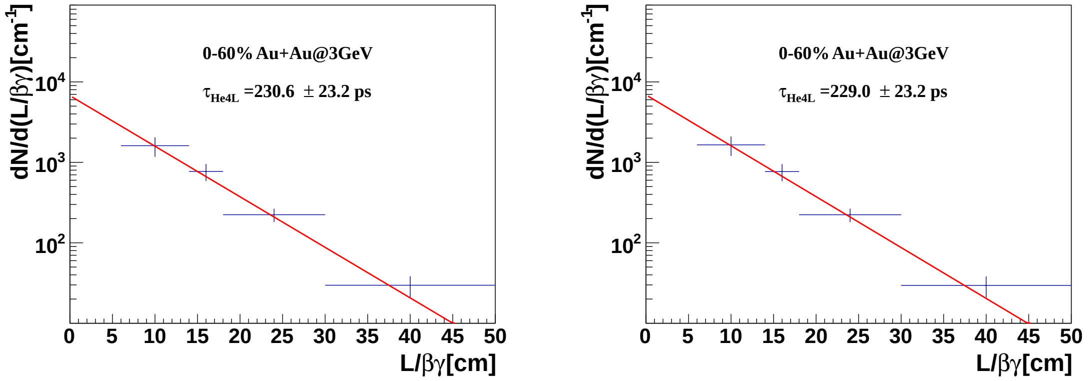

(a) $^4_\Lambda$He MC lifetime 249 ps **(b) $^4_\Lambda$He MC lifetime 230 ps (convergence)**

Figure 3.33 Corrected yields and exponential fits as a function of $L/\beta\gamma$ for $^4_\Lambda$He at $\sqrt{s_{NN}}$ = 3.0 GeV using different MC lifetimes.

Following the exponential decay law given in Eq. (3.8), the lifetime τ is extracted by fitting the efficiency-corrected yields as a function of $L/\beta\gamma$ with an exponential function. The corrected yields are obtained by dividing the raw signal counts in each $L/\beta\gamma$ bin by the corresponding reconstruction efficiency.

Figure 3.32 shows the lifetime results for $^3_\Lambda$H and $^4_\Lambda$H at $\sqrt{s_{NN}}$ = 7.2 GeV, along

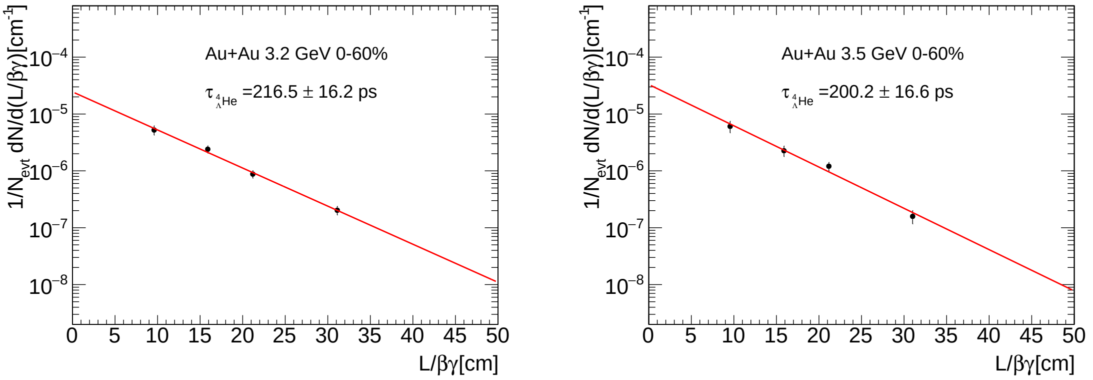

(a) $\sqrt{s_{NN}}$ = 3.2 GeV **(b)** $\sqrt{s_{NN}}$ = 3.5 GeV

Figure 3.34 Corrected yields and exponential fits as a function of $L/\beta\gamma$ for $^{4}_{\Lambda}$He at $\sqrt{s_{NN}}$ = 3.2 and 3.5 GeV.

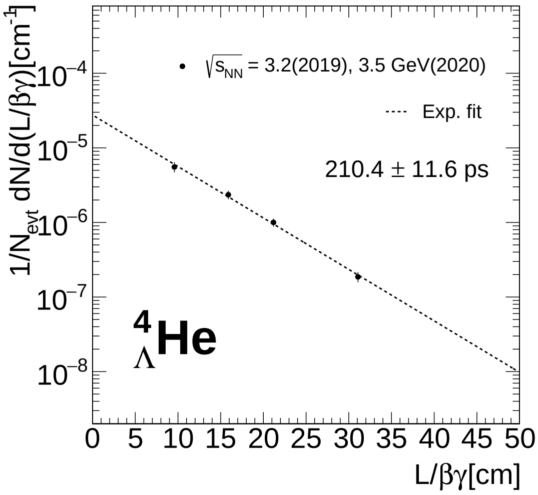

Figure 3.35 Combined corrected yield and exponential fit as a function of $L/\beta\gamma$ for $^{4}_{\Lambda}$He, based on data from $\sqrt{s_{NN}}$ = 3.2 and 3.5 GeV.

with the fitted exponential decay curves. The extracted lifetimes and their corresponding statistical uncertainties are shown in the figures. Similar lifetime analyses are performed for other collision energies.

For $^{4}_{\Lambda}$He at $\sqrt{s_{NN}}$ = 3.0 GeV, the corrected yield as a function of $L/\beta\gamma$ is extracted to perform the lifetime analysis. Figure 3.33 shows the corresponding exponential fits for two scenarios: the left panel shows the fit with a re-weighted MC lifetime of 249 ps, while the right panel displays the result using MC lifetime 230ps from the first iteration result. The measured lifetime in the right panel is found to be in good agreement with the 230 ps MC input, indicating that the iteration has reached convergence.

For $^{4}_{\Lambda}$He at $\sqrt{s_{NN}}$ = 3.2 and 3.5 GeV, the corrected yields and their exponential fits are shown in Figure 3.34. To improve statistical precision, the corrected yields from both energies are combined to perform a joint lifetime extraction, with the fit result presented in Figure 3.35. The extracted $^{4}_{\Lambda}$He lifetime is lower than the MC input lifetime; however, variations in the MC lifetime are accounted for in the systematic uncertainty, which will be discussed in the next section.

3.4 Systematic Uncertainty Estimation of Lifetime Analysis

3.4.1 Sources of Systematic Uncertainty

The following sources of systematic uncertainty are considered in the lifetime measurements:

1. **Topological Variables.** The topological variables used in the analysis may not be perfectly reproduced by simulations, leading to systematic uncertainties in reconstruction efficiency. To estimate the associated uncertainty, variations in the selection cuts on the topological variables are applied.
2. **Single Track Efficiency.** The tracking efficiency is not perfectly reproduced by simulations. We estimate the uncertainty by varying the nHitsFit required for tracks. At $\sqrt{s_{NN}}$ = 7.2 and 3.0 GeV, nHitsFit is varied from 15 to 20 and 25. At $\sqrt{s_{NN}}$ = 3.2 and 3.5 GeV, it is varied from 15 to 17 and 20.
3. **Raw Yield Extraction.** The raw signal extraction procedure may not be perfect. Uncertainties in the raw signal extraction method are evaluated by varying the signal counting window or counting method. At $\sqrt{s_{NN}}$ = 3.0 and 7.2 GeV, the window is expanded from 3σ to 4σ and 5σ. At $\sqrt{s_{NN}}$ = 3.2 and 3.5 GeV, we evaluate different methods for extracting the corrected yields: (i) integrating the signal from a Gaussian fit, (ii) bin-by-bin counting within a fixed 3σ mass window, and (iii) bin-by-bin counting using a 3σ mass window determined from Gaussian fits in each $L/\beta\gamma$ interval.
4. **Input MC Distributions.** Although MC simulations are re-weighted to match the experimental data, they do not perfectly reproduce the observed distributions. To estimate the associated uncertainty, we vary the applied re-weighting and evaluate its impact on the results. The re-weighting strategies used at different energies are summarized below:
   - $\sqrt{s_{NN}}$ = 7.2 GeV: phase-space re-weighting;
   - $\sqrt{s_{NN}}$ = 3.0 GeV: phase-space and Dalitz-plot re-weighting;
   - $\sqrt{s_{NN}}$ = 3.2 and 3.5 GeV: phase-space, Dalitz-plot, and MC lifetime re-weighting.

These four sources are included in the evaluation of the systematic uncertainty on the lifetime measurement.

3.4.2 Systematic Uncertainty Estimation Method

1. Direct Variation Method

If two or more variations are available for a given source, the systematic uncertainty is calculated as:

$$\Delta_i^{\text{sys}} = \frac{1}{2}\left|Y_{\text{Max}} - Y_{\text{Min}}\right|, \tag{3.13}$$

where Y_{Max} and Y_{Min} are the maximum and minimum yields obtained with the variations.

If only one variation is considered, the uncertainty is given by:

$$\Delta_i^{\text{sys}} = \left|Y_{\text{Vary}} - Y_{\text{Def}}\right|, \tag{3.14}$$

where Y_{Vary} and Y_{Def} are the yields from the varied and default settings, respectively.

Total systematic uncertainty is computed by adding individual contributions in quadrature:

$$\Delta_{\text{Total}}^{\text{sys}} = \sqrt{\sum_{i=1}^{n}\left(\Delta_i^{\text{sys}}\right)^2}. \tag{3.15}$$

For the ${}^{3}_{\Lambda}\text{H}$ and ${}^{4}_{\Lambda}\text{H}$ lifetime analyses at $\sqrt{s_{NN}} = 7.2$ GeV, this method is applied to estimate the systematic uncertainties.

2. Barlow Test Method

For the ${}^{4}_{\Lambda}\text{He}$ lifetime analyses at $\sqrt{s_{NN}} = 3.0$, 3.2, and 3.5 GeV, the Barlow test method [172] is applied to avoid overestimating systematic uncertainties due to statistical fluctuations.

The difference between the default yield Y_{Def} and the varied yield Y_{Vary} is:

$$\Delta = \left|Y_{\text{Vary}} - Y_{\text{Def}}\right|. \tag{3.16}$$

The uncertainty on this difference is:

$$\sigma_\Delta = \sqrt{\left|\sigma_{\text{Vary}}^2 - \sigma_{\text{Def}}^2\right|}, \tag{3.17}$$

where σ_{Vary} and σ_{Def} are the statistical uncertainties associated with the varied and default yield extractions, respectively.

If $\Delta < \sigma_\Delta$, then the variation is regarded as arising from statistical fluctuations and is not included in the systematic uncertainty.

If $\Delta > \sigma_\Delta$, the systematic uncertainty associated with that variation is computed as:

$$\sigma_{\text{sys}} = \sqrt{\Delta^2 - \sigma_\Delta^2}. \tag{3.18}$$

For multiple variations of the same source, the total systematic uncertainty from this source is calculated as the root-mean-square of the individual contributions:

$$\sigma_{\text{sys, var}} = \sqrt{\frac{1}{n}\sum_{k=1}^{n}\left(\sigma_{\text{sys}}^{\text{cut}_k}\right)^2}, \tag{3.19}$$

where n is the number of variations, and $\sigma_{\text{sys}}^{\text{cut}_k}$ denotes the systematic uncertainty from the k-th variation.

The total systematic uncertainty from all significant sources is calculated by summing their contributions in quadrature:

$$\sigma_{\text{sys}}^{\text{tot}} = \sqrt{\sum_{j}\left(\sigma_{\text{sys, var}_j}\right)^2}, \tag{3.20}$$

where $\sigma_{\text{sys, var}_j}$ represents the systematic uncertainty from the j-th source.

3.4.3 ${}^{3}_{\Lambda}$H and ${}^{4}_{\Lambda}$H lifetime systematic uncertainties at $\sqrt{s_{NN}} = 7.2$ GeV

1. Topological cuts

Table 3.8 Topological cut variations for systematic study of ${}^{3}_{\Lambda}$H lifetime analysis at $\sqrt{s_{NN}}$ = 7.2 GeV. The default value is shown in bold.

Cut Variable	${}^{3}_{\Lambda}$H
BDT response	> (−0.01, **0.0602**, 0.14)

Table 3.9 Topological cut variations for systematic study of ${}^{4}_{\Lambda}$H lifetime analysis at $\sqrt{s_{NN}}$ = 7.2 GeV. The default values are shown in bold.

	χ^2_{topo}	χ^2_{ndf}	$\chi^2_{\text{prim},\pi}$	$\chi^2_{\text{prim,He}}$
${}^{4}_{\Lambda}$H	< (3, **4**, 5)	< (3, **4**, 5)	> (3, **10**, 20)	> (1.5, **3**, 10)

The topological selections used for the systematic uncertainty estimation are summarized in Tables 3.8 and 3.9. For ${}^{3}_{\Lambda}$H, variations in the BDT response cut lead to a relative efficiency change of approximately ±50%.

The extracted lifetimes using these different cut settings are shown in Figures 3.36 and 3.37. The resulting systematic uncertainties due to topological cuts are estimated to be 6.49% for ${}^{3}_{\Lambda}$H and 4.42% for ${}^{4}_{\Lambda}$H, respectively.

2. Single Track Efficiency

The nHitsFit selection is varied from the default value of 15 to 20 and 25. The corresponding lifetime results are shown in Figure 3.38. The systematic uncertainties associated with these variations are estimated to be 2.10% for ${}^{3}_{\Lambda}$H and 1.80% for ${}^{4}_{\Lambda}$H, respectively.

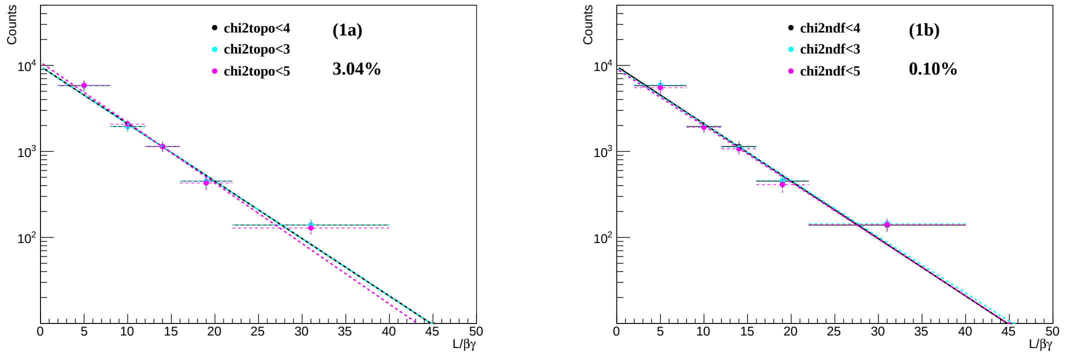

(a) χ^2_{topo} (b) χ^2_{NDF}

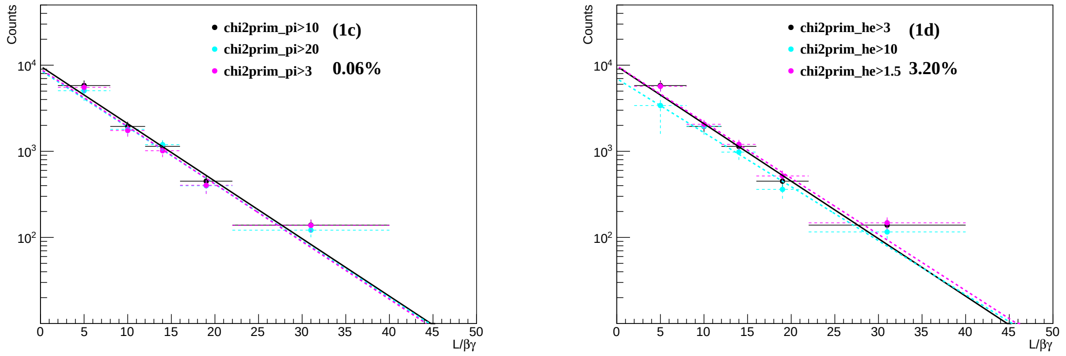

(c) $\chi^2_{\text{prim},\pi}$ (d) $\chi^2_{\text{prim},{}^3He}$

Figure 3.36 Lifetime fits for ${}^4_\Lambda$H at $\sqrt{s_{NN}}$ = 7.2 GeV under different topological cut variations. Each panel shows the result obtained by varying a specific cut parameter from its default setting, including the result for the default configuration.

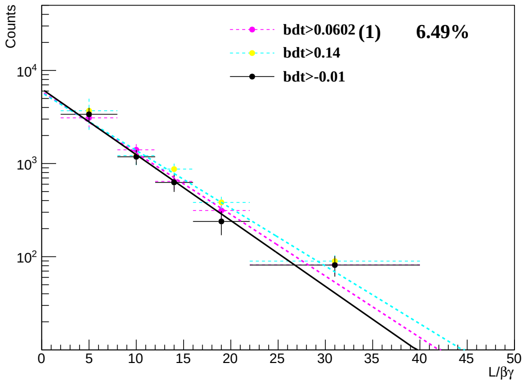

Figure 3.37 Lifetime fit for ${}^3_\Lambda$H at $\sqrt{s_{NN}}$ = 7.2 GeV under variations of the BDT response cut, including the result for the default configuration.

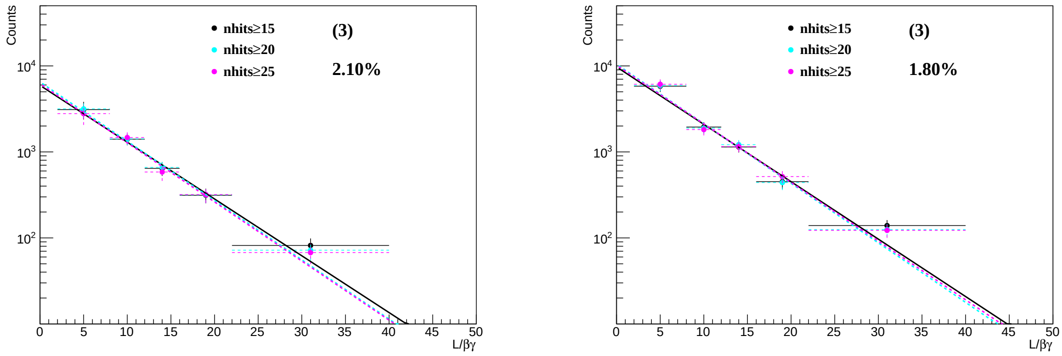

Figure 3.38 Lifetime fits for ${}^{3}_{\Lambda}$H (left) and ${}^{4}_{\Lambda}$H (right) at $\sqrt{s_{NN}}$ = 7.2 GeV under variations of the `nHitsFit` track quality cut.

3. Raw Yield Extraction

To assess the systematic uncertainty associated with raw yield extraction, the invariant mass counting window is varied from the default 3σ to 4σ and 5σ. The corresponding lifetime results are shown in Figure 3.39. The resulting systematic uncertainties are estimated to be 3.76% for ${}^{3}_{\Lambda}$H and 5.41% for ${}^{4}_{\Lambda}$H, respectively.

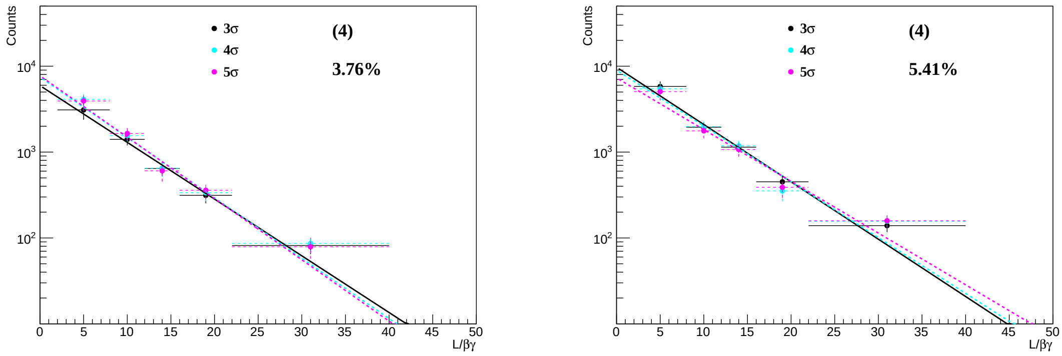

Figure 3.39 Lifetime fits for ${}^{3}_{\Lambda}$H (left) and ${}^{4}_{\Lambda}$H (right) at $\sqrt{s_{NN}}$ = 7.2 GeV under variations of the raw yield extraction window (3σ, 4σ, and 5σ).

4. Input MC Distributions

To evaluate the systematic uncertainty related to the input MC distributions, the phase-space re-weighting temperature T_B is varied. For ${}^{3}_{\Lambda}$H, the default value of 150 MeV is changed to 130 MeV and 170 MeV, as shown in the right panel of Figure 3.40. For ${}^{4}_{\Lambda}$H, the default temperature of 100 MeV is varied to 80 MeV and 120 MeV, as shown in the left panel of Figure 3.40. The resulting systematic uncertainties are estimated to be 3.37% for ${}^{3}_{\Lambda}$H and 1.18% for ${}^{4}_{\Lambda}$H.

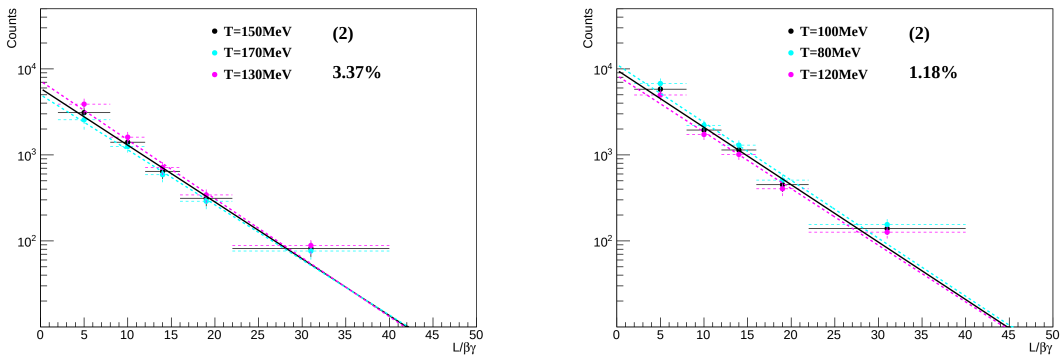

Figure 3.40 Lifetime fits for ${}^{3}_{\Lambda}$H (left) and ${}^{4}_{\Lambda}$H (right) at $\sqrt{s_{NN}}$ = 7.2 GeV under different input MC distributions via phase-space re-weighting.

Table 3.10 Summary of systematic uncertainties for the lifetime analysis of ${}^{3}_{\Lambda}$H and ${}^{4}_{\Lambda}$H at $\sqrt{s_{NN}}$ = 7.2 GeV.

Systematic uncertainty source	${}^{3}_{\Lambda}$H	${}^{4}_{\Lambda}$H
Topological cuts	6.49%	4.42%
Input MC distributions	3.37%	1.18%
Single track efficiency	2.10%	1.80%
Raw yield extraction	3.76%	5.41%
Total	8.50%	7.31%

5. Total Systematic Uncertainties for ${}^{3}_{\Lambda}$H and ${}^{4}_{\Lambda}$H at $\sqrt{s_{NN}}$ = 7.2 GeV

All sources of systematic uncertainties for the ${}^{3}_{\Lambda}$H and ${}^{4}_{\Lambda}$H lifetime measurements at $\sqrt{s_{NN}}$ = 7.2 GeV are summarized in Table 3.10. For ${}^{3}_{\Lambda}$H, the dominant contribution arises from variations in topological selections (6.49%), followed by uncertainties from raw yield extraction (3.76%), input MC modeling (3.37%), and single track efficiency (2.10%). The total systematic uncertainty is estimated to be 8.50%. For ${}^{4}_{\Lambda}$H, the largest contributions are from raw yield extraction (5.41%) and topological cuts (4.42%), with additional contributions from input MC distributions (1.18%) and single track efficiency (1.80%). The total systematic uncertainty is estimated to be 7.31%.

The extracted ${}^{3}_{\Lambda}$H and ${}^{4}_{\Lambda}$H lifetimes at $\sqrt{s_{NN}}$ = 7.2 GeV, including statistical and systematic uncertainties, are:

$$\tau({}^{3}_{\Lambda}\mathrm{H}) = 219.4 \pm 19.8\ (\mathrm{stat.}) \pm 18.6\ (\mathrm{syst.})\ \mathrm{ps}, \tag{3.21}$$

$$\tau({}^{4}_{\Lambda}\mathrm{H}) = 217.0 \pm 16.0\ (\mathrm{stat.}) \pm 16.0\ (\mathrm{syst.})\ \mathrm{ps}. \tag{3.22}$$

3.4.4 ${}^{4}_{\Lambda}$He lifetime systematic uncertainties at $\sqrt{s_{NN}}$ = 3.0 GeV

The variations used for the systematic study of the ${}^{4}_{\Lambda}$He lifetime at $\sqrt{s_{NN}}$ = 3.0 GeV are summarized in Table 3.11. Variations related to Dalitz plot re-weighting are not included in this table. To evaluate the corresponding systematic uncertainty, 1000 alternative re-weighting histograms are generated by fluctuating the bin contents of the default two-dimensional distribution of Dalitz plot re-weighting. For each bin, a new value is sampled using the expression:

$$\texttt{newBinContent} = \texttt{gRandom->Gaus(binContent, binError)}, \tag{3.23}$$

where `binContent` and `binError` denote the value and its statistical uncertainty of each bin, respectively.

Table 3.11 Systematic variations used in the ${}^{4}_{\Lambda}$He lifetime analysis at $\sqrt{s_{NN}}$ = 3.0 GeV. The default configuration and variations are shown. Each variation is applied individually.

Category	ID	Setting
	Default	$\chi^2_{\text{topo}} < 2.5$, $\chi^2_{\text{NDF}} < 4$, $\chi^2_{\text{prim},{}^3He} > 3$, $\chi^2_{\text{prim},p} > 15$, $\chi^2_{\text{prim},\pi} > 15$, $l/\Delta l > 8$, $l > 7\ cm$, $\chi^2_{\text{prim},p-\pi} > 10$, input p_T spectrum with T_B = 200 MeV, $nHitsFit \geq 15$, 3σ signal window
Topological variables	1	$\chi^2_{\text{topo}} < 2$
	2	$\chi^2_{\text{topo}} < 3$
	3	$\chi^2_{\text{NDF}} < 3$
	4	$\chi^2_{\text{NDF}} < 5$
	5	$\chi^2_{\text{prim},{}^3He} > 5$
	6	$\chi^2_{\text{prim},{}^3He} > 4$
	7	$\chi^2_{\text{prim},\pi} > 5$
	8	$\chi^2_{\text{prim},\pi} > 25$
	9	$\chi^2_{\text{prim}\,p} > 10$
	10	$\chi^2_{\text{prim},,p} > 20$
	11	$l/\Delta l > 9$
	12	$l/\Delta l > 7$
	13	$l > 6cm$
	14	$l > 8cm$
	15	$\chi^2_{\text{prim},p-\pi} > 9$
	16	$\chi^2_{\text{prim},p-\pi} > 11$
MC p_{T} input	17	T_B = 230 MeV
	18	T_B = 170 MeV
Signal track efficiency	19	$nHitsFit \geq 20$
	20	$nHitsFit \geq 25$
Raw yield extraction	21	4σ signal window
	22	5σ signal window

The lifetime results obtained from the systematic variations listed in Table 3.11 are shown in Figure 3.41. In the figure, the red solid circle on the far left represents the default result. Black open circles indicate variations that fail the Barlow test and are thus attributed to statistical fluctuations and excluded from the systematic uncertainty. Black solid circles represent variations that pass the Barlow test and are included in the final systematic estimation.

The results from the Dalitz plot re-weighting variations are shown in Figure 3.42, following the same symbol convention. A horizontal red line denotes the central value

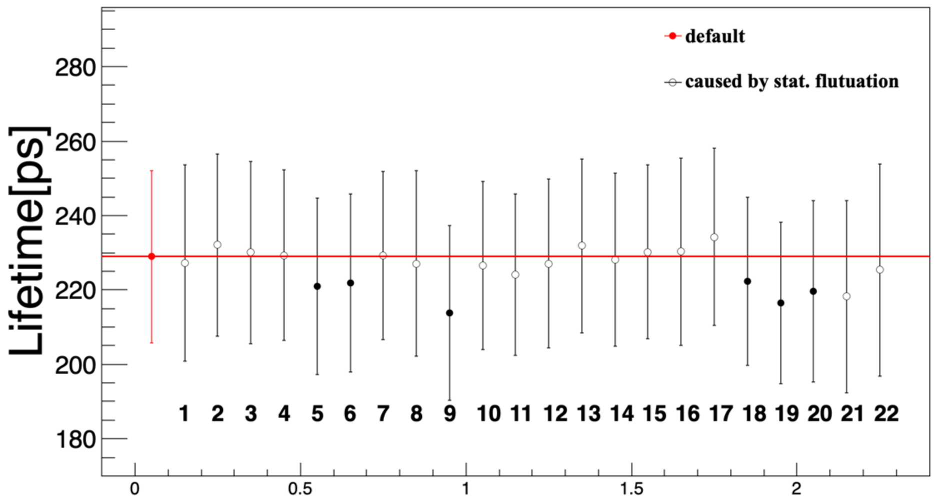

Figure 3.41 **$^{4}_{\Lambda}$He lifetime results from the variations listed in Table 3.11 at $\sqrt{s_{NN}}$ = 3.0 GeV. Each data point corresponds to a specific variation ID. The red solid circle on the left indicates the default result. Black open (solid) circles represent variations excluded from (included in) the systematic uncertainty estimation based on the Barlow test.**

of the default result. Due to the large number of variations (N = 1000), the points appear densely clustered around this central value. The corresponding systematic uncertainty from Dalitz re-weighting is estimated to be 3.73% for $^{4}_{\Lambda}$He.

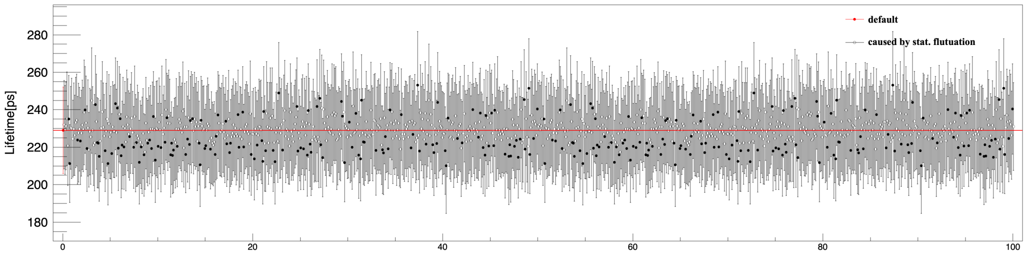

Figure 3.42 **$^{4}_{\Lambda}$He lifetime results from Dalitz plot re-weighting variations at $\sqrt{s_{NN}}$ = 3.0 GeV. The red solid circle indicates the default result, and the horizontal red line marks its central value. Black open (solid) circles represent variations excluded from (included in) the systematic uncertainty estimation based on the Barlow test.**

Table 3.12 Summary of systematic uncertainties for the $^{4}_{\Lambda}$He lifetime analysis at $\sqrt{s_{NN}}$ = 3.0 GeV.

Systematic uncertainty source	Uncertainty [ps]	Relative uncertainty
Topological cuts	15.6	6.81%
Input MC		4.11%
- Phase-space re-weighting	3.98	1.74%
- Dalitz Plot re-weighting	8.54	3.73%
Single Track Efficiency	7.73	3.38%
Raw Yield Extraction	–	<1%
Total	**19.80**	**8.64%**

All sources of systematic uncertainty in the $^{4}_{\Lambda}$He lifetime analysis at $\sqrt{s_{NN}}$ = 3.0 GeV are summarized in Table 3.12. These include contributions from topological cuts, input MC variations—comprising both phase-space and Dalitz plot re-weighting—single track efficiency, and raw yield extraction. The dominant contribution arises from topological cut variations, which corresponds to 15.6 ps or 6.81%. The total contribution from input MC variations is 4.11%, consisting of 1.74% from phase-space re-weighting (3.98 ps) and 3.73% from Dalitz re-weighting (8.54 ps). Single track efficiency contributes 7.73 ps (3.38%). No significant systematic uncertainty is observed from raw yield extraction. The total systematic uncertainty is estimated to be 19.80 ps, corresponding to 8.64%.

The measured lifetime of ${}^4_\Lambda$He at $\sqrt{s_{NN}}$ = 3.0 GeV is:

$$\tau({}^4_\Lambda\text{He}) = 229 \pm 23\ (\text{stat.}) \pm 20\ (\text{syst.})\ \text{ps}. \tag{3.24}$$

The total uncertainty, calculated by adding the statistical and systematic uncertainties in quadrature, is approximately 30.5 ps.

3.4.5 ${}^4_\Lambda$He lifetime systematic uncertainties at $\sqrt{s_{NN}}$ = 3.2 and 3.5 GeV

Table 3.13 Systematic variations used in the ${}^4_\Lambda$He lifetime analysis at $\sqrt{s_{NN}}$ = 3.2 and 3.5 GeV. Each variation is applied individually, except for topological cuts where all combinations are scanned.

Category	Subcategory	Default	Variations
Topological cuts	χ^2_{topo}	< 10	< 12, < 8
	χ^2_{NDF}	< 5	< 6, < 4
	$\chi^2_{\text{prim},{}^3\text{He}}$	> 2	> 0, > 4
	$\chi^2_{\text{prim},\pi}$	> 20	> 15, > 25
	$\chi^2_{\text{prim},p}$	> 10	> 8, > 12
	l [cm]	> 7	> 6, > 8
	$\chi^2_{\text{prim},p-\pi}$	> 4	> 3, > 5
MC Input	p_T spectrum T_B	210 MeV	180 MeV, 240 MeV
	MC lifetime τ_{MC}	~250 ps	210 ps, 230 ps, 270 ps
Signal track efficiency	$nHitsFit$	≥ 15	≥ 17, ≥ 20

The variations used for the systematic study of the ${}^4_\Lambda$He lifetime from the combined yields at $\sqrt{s_{NN}}$ = 3.2 and 3.5 GeV are summarized in Table 3.13. The systematic uncertainty associated with topological cuts is estimated by combinations of seven key topological variables: χ^2_{topo}, χ^2_{NDF}, $\chi^2_{\text{prim},{}^3\text{He}}$, $\chi^2_{\text{prim},p}$, $\chi^2_{\text{prim},\pi}$, l, and $\chi^2_{\text{prim},p\text{-}\pi}$. Each variable is varied over three values (the default plus two variations), leading to a total of $3^7 = 2187$ topological cut combinations.

Variations related to Dalitz plot re-weighting and raw signal extraction are not included in this table. To evaluate the systematic uncertainty from Dalitz re-weighting, 100 new re-weighting histograms are generated by fluctuating the bin contents of the default Dalitz 2D distribution, following the same procedure as used for $\sqrt{s_{NN}}$ = 3.0 GeV.

For the estimation of the systematic uncertainty associated with raw signal extraction, different methods are applied. The default method performs bin-by-bin counting of signal candidates within a 3σ mass window, where the window width is obtained from a Gaussian fit applied in each $L/\beta\gamma$ interval. In one variation, the signal yield is extracted using the integral of the Gaussian fit instead of direct counting. One variation uses the integral of the Gaussian fit result instead of direct counting. In another, bin-by-bin counting is also used, but with a fixed 3σ mass window applied uniformly across all $L/\beta\gamma$ intervals. This fixed window is determined from a Gaussian fit performed without applying an $L/\beta\gamma$ selection.

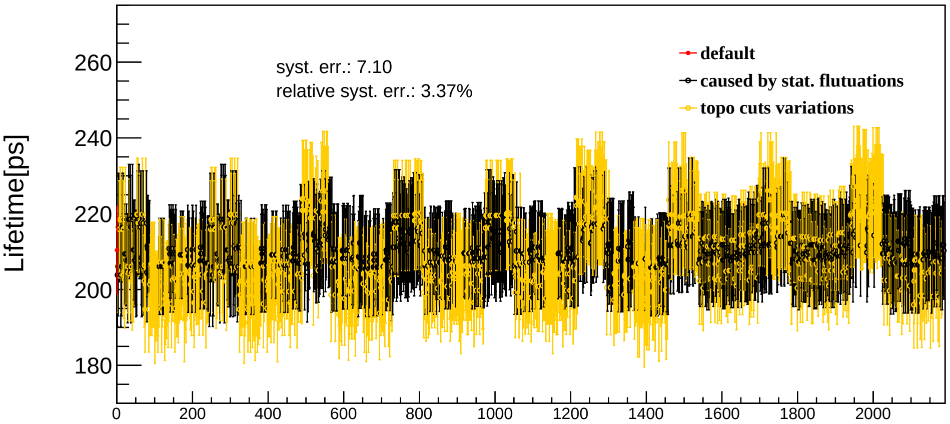

Figure 3.43 **${}^{4}_{\Lambda}$He lifetime results from 2187 topological cut combinations, each varying seven variables over three values. The red solid circle shows the default case. Orange points pass the Barlow test and are included in the systematic uncertainty estimation, while black open circles are excluded as statistically flutuations.**

The lifetime results obtained from different combinations of topological cuts are shown in Figure 3.43. In the following figures illustrating the systematic uncertainty estimation, the red solid circle indicates the default result. Orange circles correspond to variations that pass the Barlow test and are included in the evaluation of the systematic uncertainty. Black circles represent variations that fail the Barlow test and are considered to arise from statistical fluctuations.

Figure 3.44 shows the lifetime results from Dalitz plot re-weighting variations. One default and 100 varied re-weighting histograms are generated by applying Gaussian smearing to the bin contents of the default 2D distribution of Dalitz plot re-weighting, following the same method used at $\sqrt{s_{NN}} = 3.0$ GeV.

The effect of phase-space re-weighting on the MC input is shown in Figure 3.45, where re-weighting temperatures of $T_B = 210$ MeV (default), 180 MeV, and 240 MeV are applied to evaluate the impact on the extracted lifetime.

Figure 3.46 presents the extracted lifetime results under different MC lifetime re-

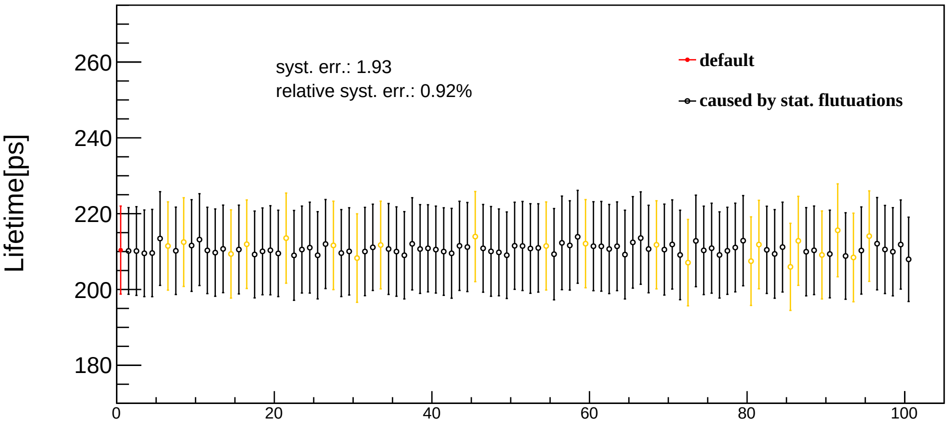

Figure 3.44 ${}^{4}_{\Lambda}$**He lifetime results from Dalitz plot re-weighting variations. The leftmost red point shows the default result, while the remaining 100 are obtained by Gaussian fluctuations of the default 2D Dalitz distribution bins.**

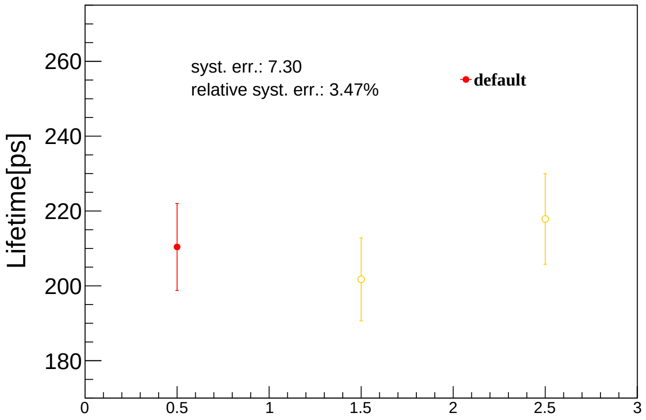

Figure 3.45 ${}^{4}_{\Lambda}$**He lifetime results obtained via different phase-space re-weighting using** T_B = 210 **MeV (default), 180 MeV, and 240 MeV (from left to right) at** $\sqrt{s_{NN}}$ **= 3.2 and 3.5 GeV.**

weighting. Four input values are tested: the default lifetime of approximately 250 ps (default), 210 ps, 230 ps, and 270 ps, to evaluate the associated systematic uncertainty.

The impact of track quality selection on the extracted lifetime is shown in Figure 3.47, where the minimum number of TPC hits (nHitsFit) is varied from the default value of 15 to 17 and 20.

Figure 3.48 illustrates the impact of different raw signal extraction methods on the extracted lifetime. The default approach performs bin-by-bin counting within a 3σ mass window, where the window is determined individually for each $L/\beta\gamma$ interval. The two alternative methods are: (1) extracting the signal using the integral of the Gaussian fit, and (2) applying a fixed 3σ mass window uniformly across all $L/\beta\gamma$ intervals.

All sources of systematic uncertainties for the combined ${}^{4}_{\Lambda}$He lifetime analysis at

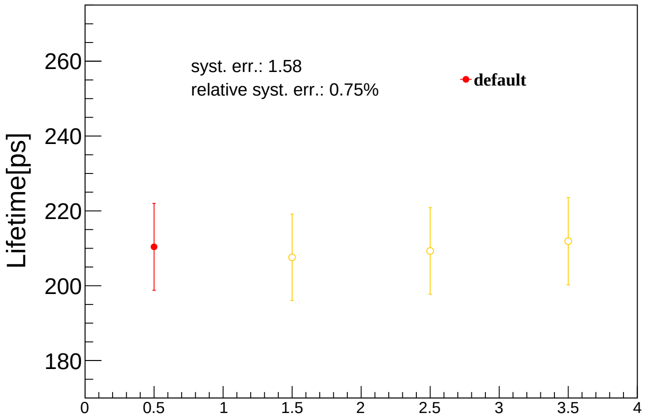

Figure 3.46 ${}^{4}_{\Lambda}$He lifetime results under MC lifetime re-weighting with MC lifetime values of approximately 250 ps (default), 210 ps, 230 ps, and 270 ps (from left to right) at $\sqrt{s_{NN}}$ = 3.2 and 3.5 GeV.

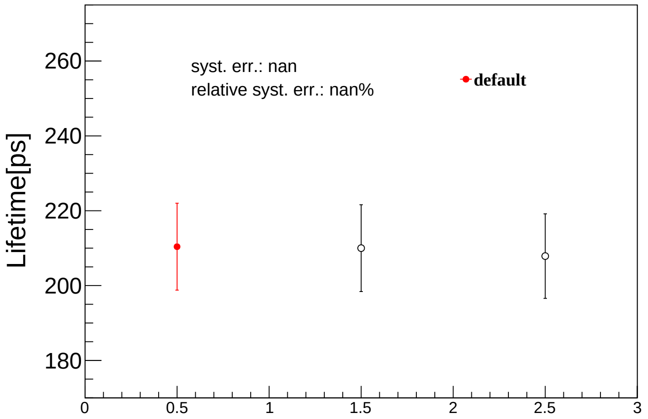

Figure 3.47 ${}^{4}_{\Lambda}$He lifetime results from varying the nHitsFit requirement: ≥15 (default), ≥17, and ≥20 (from left to right) at $\sqrt{s_{NN}}$ = 3.2 and 3.5 GeV.

Table 3.14 Summary of systematic uncertainties for the ${}^{4}_{\Lambda}$He lifetime analysis at $\sqrt{s_{NN}}$ = 3.2 and 3.5 GeV.

Systematic uncertainty source	Uncertainty [ps]	Relative uncertainty
Topological cuts	7.1	3.4%
Input MC		3.7%
- Phase-space re-weighting	7.3	3.5%
- Dalitz plot re-weighting	1.9	0.9%
- MC lifetime re-weighting	1.6	0.8%
Single Track Efficiency	–	<1%
Raw Yield Extraction	3.9	1.8%
Total	**11.2**	**5.3%**

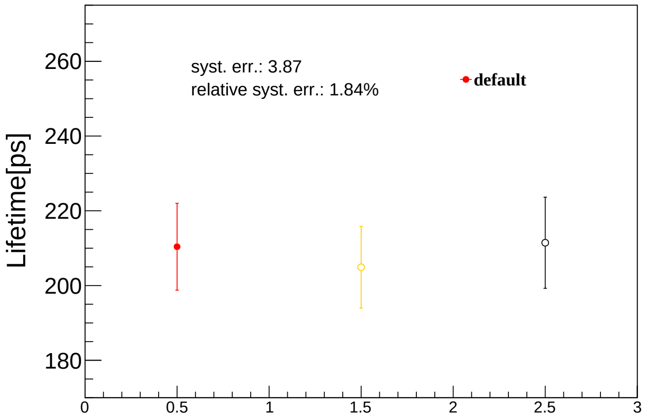

Figure 3.48 **$^{4}_{\Lambda}$He lifetime results from different raw signal extraction methods at $\sqrt{s_{NN}} = 3.2$ and 3.5 GeV. The default method (solid circle, left) uses bin-by-bin counting within a 3σ mass window determined in each $L/\beta\gamma$ interval. Variations include: (1) Gaussian integral method (open circle, middle), and (2) fixed 3σ window counting across all intervals (open circle, right).**

$\sqrt{s_{NN}} = 3.2$ and 3.5 GeV are summarized in Table 3.14. The contributions are categorized into four main sources: topological cut variations, input MC distributions, single track efficiency, and raw yield extraction. The largest contributions arise from input MC and topological cuts, contributing 3.7% and 3.4% relative uncertainty, respectively. The MC-related uncertainty is further decomposed into phase-space re-weighting (3.5%), Dalitz plot re-weighting (0.9%), and MC lifetime re-weighting (0.8%). No significant systematic uncertainty is observed from from single track efficiency. The raw yield extraction contributes 1.8%. The total systematic uncertainty is estimated to be 11.2 ps, corresponding to a relative uncertainty of 5.3%.

The measured lifetime of $^{4}_{\Lambda}$He at $\sqrt{s_{NN}} = 3.2$ and 3.5 GeV is:

$$\tau(^{4}_{\Lambda}\text{He}) = 210 \pm 12\ (\text{stat.}) \pm 11\ (\text{syst.})\ \text{ps}. \tag{3.25}$$

The total uncertainty, obtained by adding the statistical and systematic uncertainties in quadrature, is approximately 16 ps.

3.5 Yield Analysis of $^{3}_{\Lambda}$H at $\sqrt{s_{NN}} = 3.2$ GeV

The yield analysis of $^{3}_{\Lambda}$H begins with raw signal extraction performed in bins of transverse momentum (p_T) within different rapidity intervals. The raw yields are then corrected for the reconstruction efficiency using the following relation:

$$\frac{\Delta N}{\Delta p_T \Delta y} = \frac{1}{\epsilon^{\text{reco}}} \times \frac{\Delta N_{\text{raw}}}{\Delta p_T \Delta y}. \tag{3.26}$$

The efficiency-corrected yields are subsequently used in further analyses, such as the invariant p_T spectra, the integrated yield dN/dy and the mean transverse momentum $\langle p_{\mathrm{T}} \rangle$.

3.5.1 Raw Signal Extraction

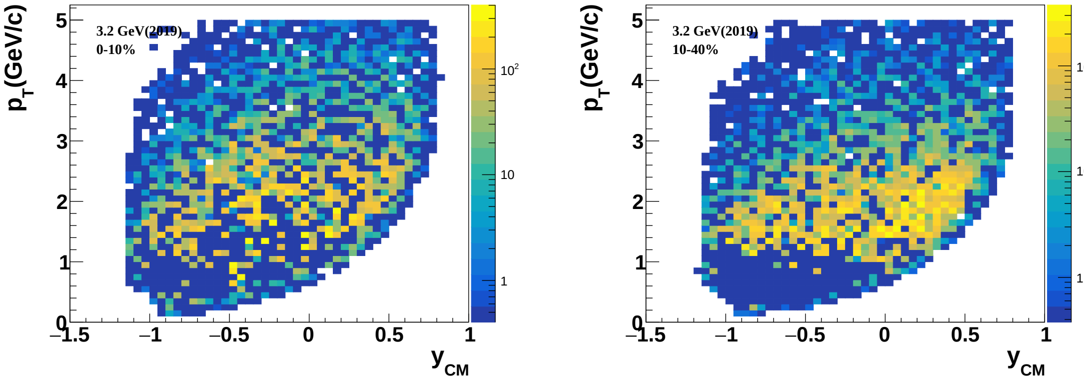

(a) 0–10% centrality

(b) 10–40% centrality

Figure 3.49 Acceptance distributions of reconstructed ${}^{3}_{\Lambda}$H signal candidates in Au+Au collisions at $\sqrt{s_{NN}}$ = 3.2 GeV in 0–10% and 10–40% centralities.

Cuts on topological variables are optimized to enhance the signal significance across different p_T and rapidity intervals. The selection criteria are summarized in Table 3.6.

Figure 3.49 presents the acceptance distribution of reconstructed ${}^{3}_{\Lambda}$H signal candidates in Au+Au collisions at $\sqrt{s_{NN}}$ = 3.2 GeV. The reconstructed invariant mass distributions in various p_T bins and rapidity intervals, for centralities 0–10% and 10–40%, are presented in Figures 3.50, 3.51, 3.52, and 3.53.

In each figure, the red solid circles denote the raw invariant mass distributions of ${}^{3}_{\Lambda}$H candidates. Combinatorial backgrounds, constructed using a mixed-event technique within the same centrality class, are shown as black open circles. These backgrounds are normalized in the mass range $3.008 < M({}^{3}\mathrm{He}\pi^{-}) < 3.018$ GeV/c^2, corresponding to the region approximately $+8\sigma$ to $+13\sigma$ above the signal peak, where no signal contribution is expected.

After subtracting the scaled background, the resulting distributions (blue solid circles) are fitted with a Gaussian function plus a linear background (red dashed line). The Gaussian describes the ${}^{3}_{\Lambda}$H signal, while the linear term accounts for the remaining background. The fits are performed within the mass window $2.970 < M({}^{3}\mathrm{He}\pi^{-}) <$ 3.020 GeV/c^2. The raw yields in each bin are then obtained from the integral of the Gaussian component.

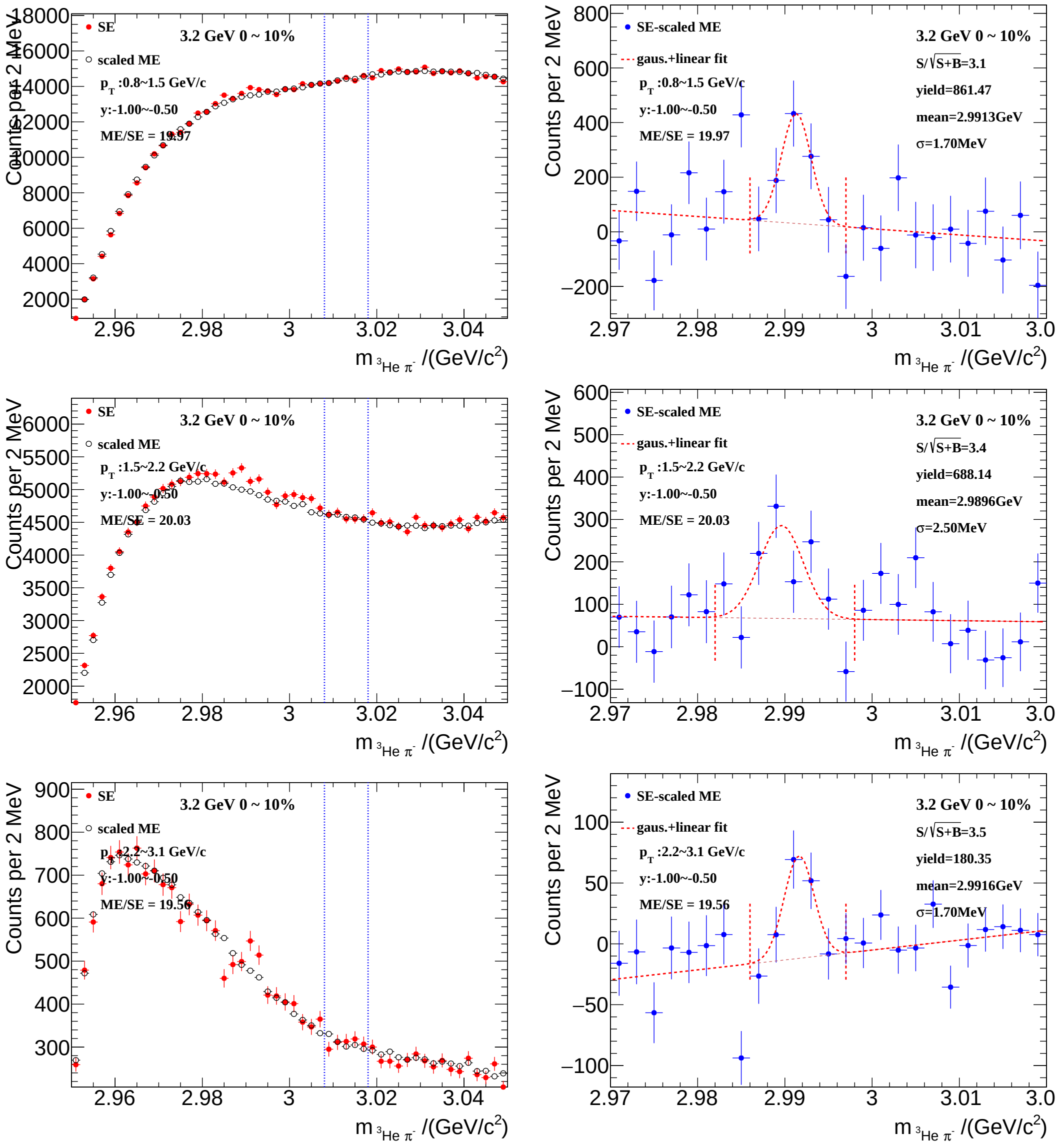

Figure 3.50 Reconstructed ${}^{3}_{\Lambda}$H candidates in $-1 < y < -0.5$ from 0–10% central Au+Au collisions at $\sqrt{s_{NN}} = 3.2$ GeV.

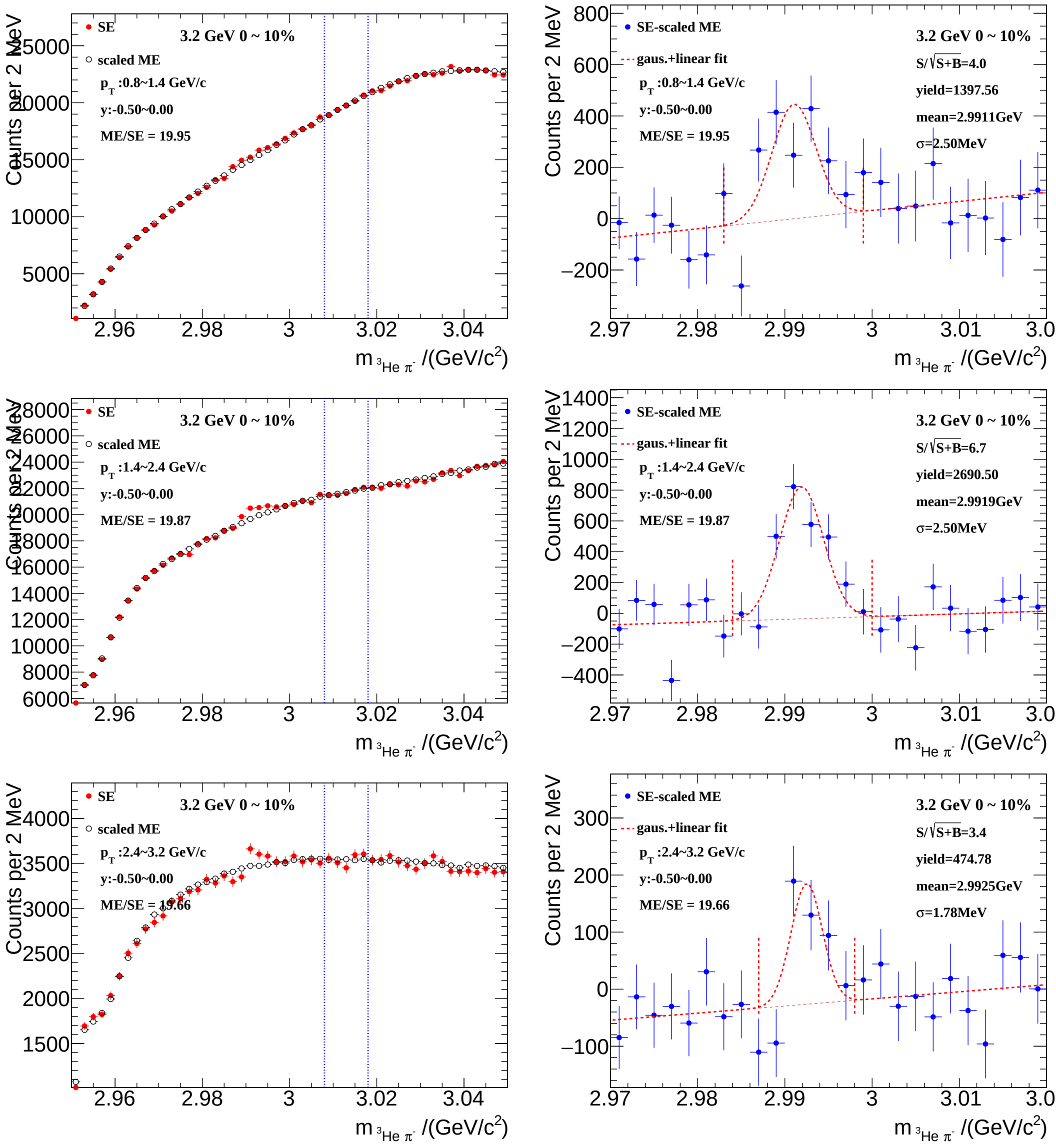

Figure 3.51 Reconstructed $^{3}_{\Lambda}$H candidates in $-0.5 < y < 0$ from 0–10% central Au+Au collisions at $\sqrt{s_{NN}}$ = 3.2 GeV.

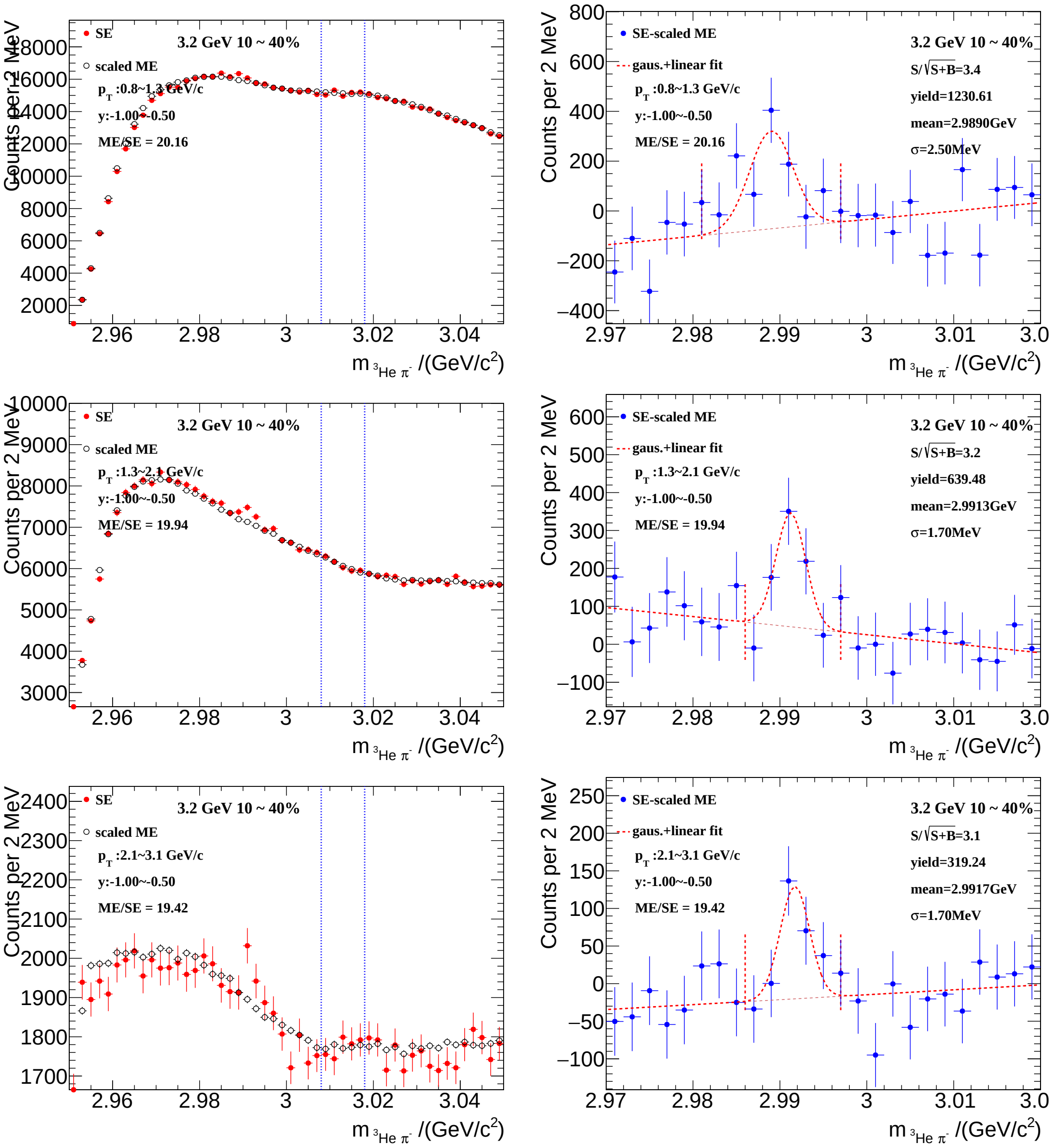

Figure 3.52   Reconstructed $^{3}_{\Lambda}$H candidates in $-1 < y < -0.5$ from 10–40% central Au+Au collisions at $\sqrt{s_{NN}} = 3.2$ GeV.

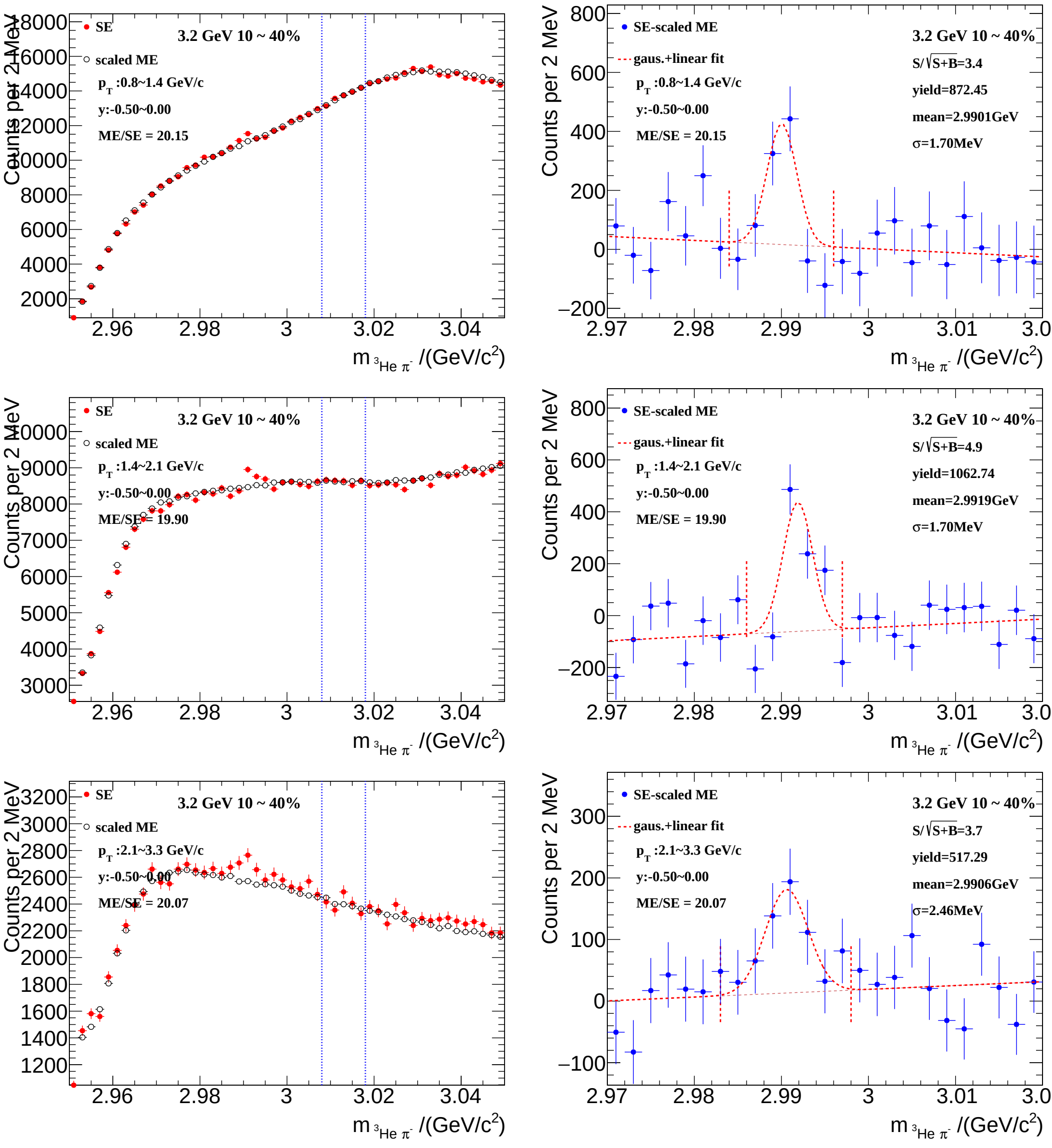

Figure 3.53 Reconstructed $^{3}_{\Lambda}$H candidates in $-0.5 < y < 0$ from 10–40% central Au+Au collisions at $\sqrt{s_{NN}} = 3.2$ GeV.

3.5.2 Reconstruction Efficiency

The reconstruction efficiency is estimated using the standard STAR embedding method, as described in Section 3.3.2. To ensure reliable comparisons with experimental data, MC simulations are re-weighted to match the observed distributions from experimental data before the efficiency calculation.

After re-weighting, the ${}^{3}_{\Lambda}\mathrm{H}$ signal is reconstructed from the embedding sample using the same analysis procedure and topological selection criteria as applied to the real data.

1. Embedding Re-weighting

As mentioned in Section （1） of 3.3.2, the default p_{T} and rapidity distributions of the MC particles in the embedding sample do not fully reproduce those observed in data. To correct for this discrepancy, re-weighting is applied to the MC sample based on the kinematic properties of the real signal. In this yield analysis, the re-weighting in p_{T} is performed using an exponential function in transverse mass m_T, rather than a simple Boltzmann distribution. The m_T-exponential distribution takes the form:

$$\frac{dN}{m_T dm_T} \sim e^{-m_T/T}. \tag{3.27}$$

Using the transformation described in Eq. (3.10), this can be rewritten in terms of p_T as:

$$\frac{dN}{dp_T} \sim p_T\, e^{-m_T/T}. \tag{3.28}$$

This functional form is used to assign weights to MC particles as a function of p_T, ensuring consistency with the spectral shape observed in data.

To determine a reasonable starting point for the reconstruction efficiency evaluation, several m_T-exponential functions with different inverse slope parameters (T_{m_T}) are tried to compare with the experimental data. The function that best describes the data is chosen as the initial weighting function. The reconstruction efficiency is then recalculated, and the procedure is iterated: updated spectra measurements are used to refine the weighting function until convergence is achieved. Since this iterative phase-space re-weighting procedure is designed to closely match the experimental data, it is not included in the estimation of systematic uncertainty.

The p_T and rapidity distributions of the reconstructed MC ${}^{3}_{\Lambda}\mathrm{H}$ from embedding sample and ${}^{3}_{\Lambda}\mathrm{H}$ signals reconstructed from experimental data are compared in Figure 3.54.

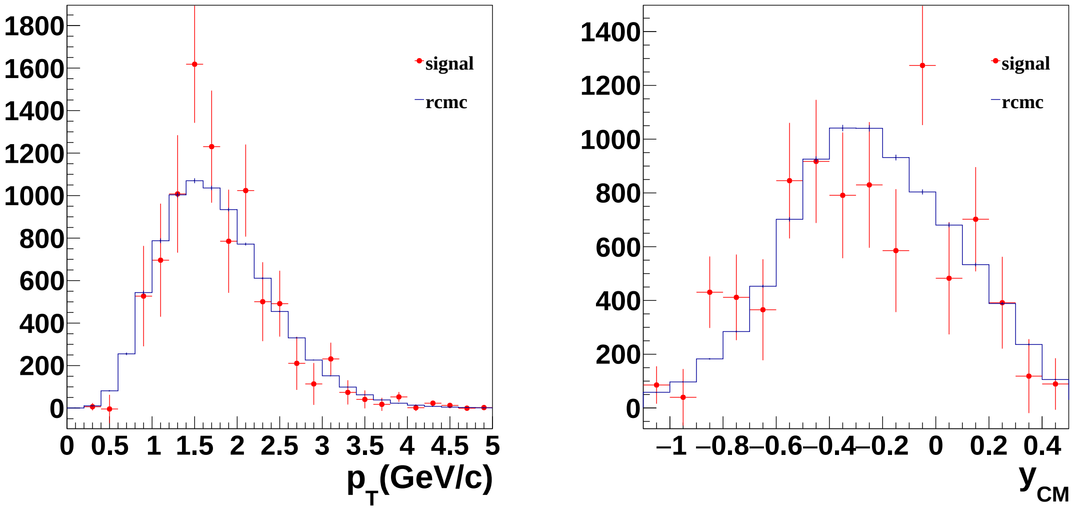

(a) p_T comparison (0–10% centrality) **(b) Rapidity comparison (0–10% centrality)**

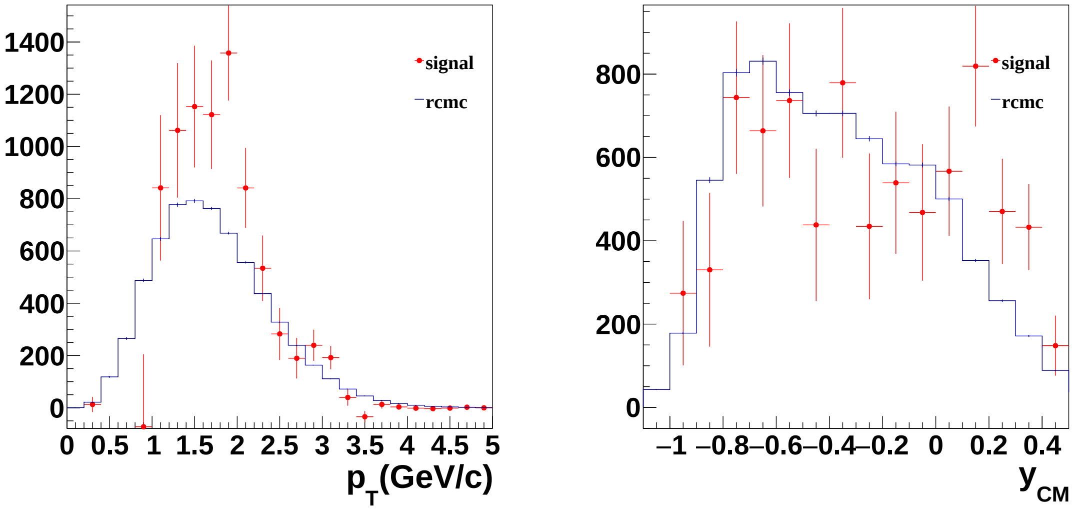

(c) p_T comparison (10–40% centrality) **(d) Rapidity comparison (10–40% centrality)**

Figure 3.54 Comparison of kinematic distributions between data and weighted embedding for ${}^{3}_{\Lambda}$H in Au+Au collisions at $\sqrt{s_{NN}}$ = 3.2 GeV. Distributions are shown for p_T (left) and rapidity (right) in 0–10% (top) and 10–40% (bottom) centrality bins.

The lifetime of ${}^{3}_{\Lambda}\mathrm{H}$ in the MC simulation is further re-weighted to match the world average value of 229 ps. This ensures consistency between the embedding sample and the expected decay of ${}^{3}_{\Lambda}\mathrm{H}$. The distributions after lifetime re-weighting are shown in Figure 3.55 for both 0–10% and 10–40% centrality.

With all phase-space and MC lifetime re-weighting corrections applied, the reconstruction efficiency can be reliably estimated, as discussed in the following section.

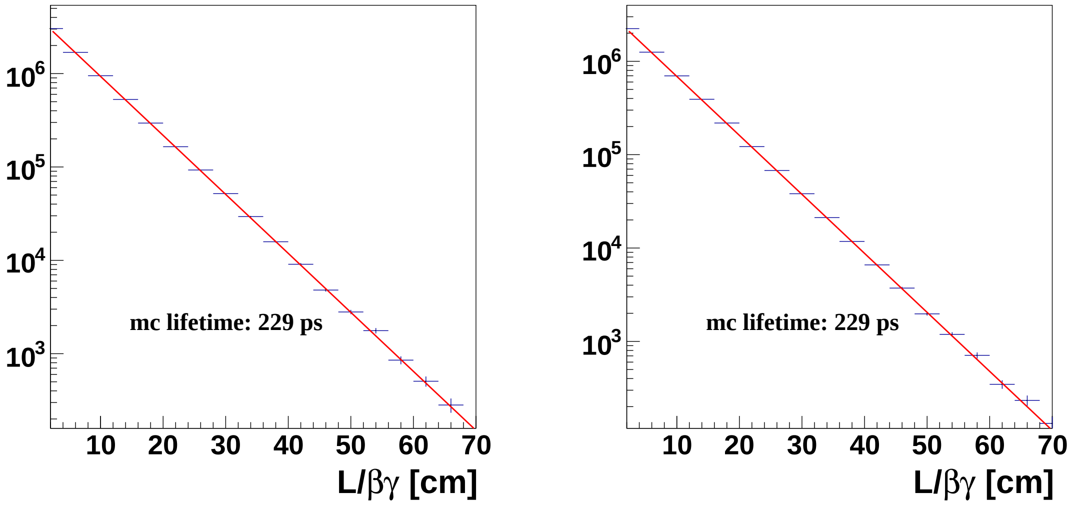

(a) 0–10% centrality **(b) 10–40% centrality**

Figure 3.55 Distributions of the embedded ${}^{3}_{\Lambda}\mathrm{H}$ sample after applying lifetime re-weighting to the world average value of 229 ps in Au+Au collisions at $\sqrt{s_{NN}} = 3.2$ GeV.

2. Efficiency Result

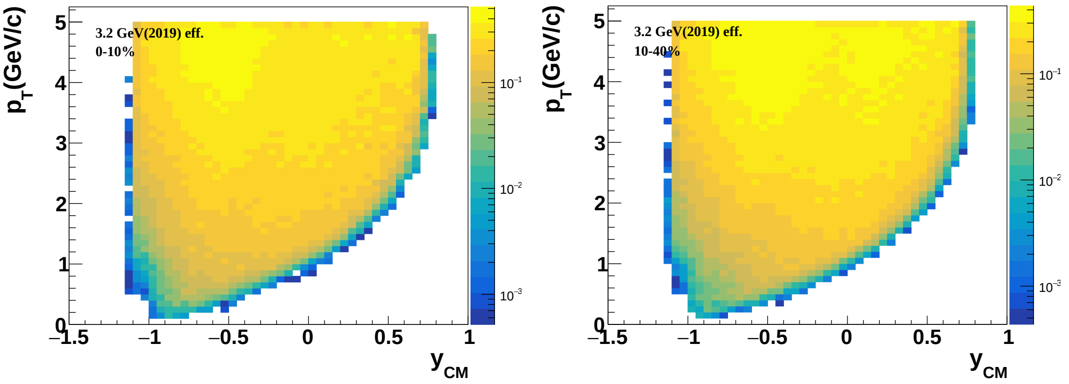

Figure 3.56 The reconstruction efficiency of ${}^{3}_{\Lambda}\mathrm{H}$ in Au+Au collisions at $\sqrt{s_{NN}} = 3.2$ GeV in 0–10% and 10–40% centralities.

The reconstruction efficiency is defined as the ratio between the number of reconstructed ${}^{3}_{\Lambda}\mathrm{H}$ candidates that pass all track quality cut and topological selections, and the number of input MC ${}^{3}_{\Lambda}\mathrm{H}$ particles:

$$\epsilon^{\mathrm{reco}} = \frac{\text{Reconstructed MC } {}^{3}_{\Lambda}\mathrm{H} \text{ (after track QA and topological cuts)}}{\text{MC } {}^{3}_{\Lambda}\mathrm{H}}. \tag{3.29}$$

This efficiency quantifies the overall detector acceptance and analysis selection effects.

It is evaluated in two dimensions as a function of transverse momentum and rapidity.

The resulting two-dimensional reconstruction efficiencies are presented in Figure 3.56 for 0–10% and 10–40% centralities.

3.5.3 Differential p_T Spectra Measurement

The invariant transverse momentum (p_T) spectra of ${}^3_\Lambda$H, corrected for reconstruction efficiency, are calculated in each p_T and rapidity interval using the following equation:

$$\frac{d^2N}{2\pi p_\mathrm{T} dp_\mathrm{T} dy} \cdot B.R. = \frac{1}{2\pi \cdot N^\mathrm{evt} \cdot \epsilon^\mathrm{reco}} \cdot \frac{\Delta N^\mathrm{raw}}{p_\mathrm{T} \Delta p_\mathrm{T} \Delta y}. \tag{3.30}$$

Here, N^evt is the total number of analyzed events, Δp_T and Δy are the bin widths in transverse momentum and rapidity, respectively. The $B.R.$ denotes the decay branching ratio of the channel ${}^3_\Lambda\mathrm{H} \rightarrow {}^3\mathrm{He} + \pi^-$. The efficiency ϵ^reco represents the reconstruction efficiency of ${}^3_\Lambda$H as determined from embedding studies.

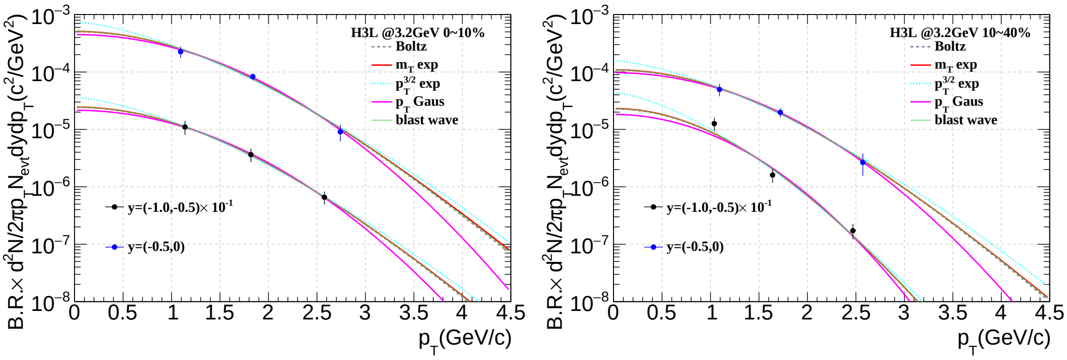

Figure 3.57 The corrected p_T spectra of ${}^3_\Lambda$H with statistical uncertainties in Au+Au collisions at $\sqrt{s_{NN}}$ = 3.2 GeV in 0–10% and 10–40% centralities.

The efficiency-corrected p_T spectra of ${}^3_\Lambda$H in Au+Au collisions at $\sqrt{s_{NN}}$ = 3.2 GeV for 0–10% and 10–40% centralities are shown in Figure 3.57. In these two plots, only statistical uncertainties are included.

3.5.4 Method for dN/dy and $\langle p_T \rangle$ Measurements

Due to limited detector acceptance and statistics, the ${}^3_\Lambda$H yields cannot be measured down to $p_T = 0$. To account for the unmeasured low-p_T region, extrapolation is performed using empirical functions that describe the shape of the measured spectra.

By default, the m_T-exponential function,

$$\frac{d^2N}{2\pi p_T dp_T dy} = C \cdot \exp\left(-\frac{m_T}{T}\right), \tag{3.31}$$

is used to describe the ${}^3_\Lambda$H spectra. In practice, however, the fit is performed to the $\frac{d^2N}{dp_T dy}$

distribution, instead of the invariant yield form $\frac{d^2N}{2\pi p_T dp_T dy}$, in order to reduce bias from the determination of bin center.

When carrying out the fitting, the integral of the function over each bin (rather than the value at the bin center) is used—corresponding to the "I" option in the ROOT histogram fit. We can get the fraction of the total yields in the measured p_T region from the fit function over the integrated yields at $p_{\mathrm{T}} > 0$. The fraction is computed as:

$$\text{Frac} = \frac{\int_{\text{measured } p_T} \text{Fun}(p_T)\, dp_T}{\int_0^\infty \text{Fun}(p_T)\, dp_T}, \tag{3.32}$$

where Fun denotes the function used for fitting. The total integrated yield is then given by:

$$\frac{dN}{dy} = \frac{\sum \text{Measured } {}^3_\Lambda\text{H yields}}{\text{Frac}}. \tag{3.33}$$

In the default m_T-exponential function case, Fun is defined as:

$$\text{Fun}(p_T) = 2\pi p_T \cdot C \cdot \exp\left(-\frac{m_T}{T}\right). \tag{3.34}$$

The statistical uncertainty on the yield is propagated as:

$$\Delta^{\text{stat}} = \frac{\Delta^{\text{stat}}_{\text{measured}}}{\text{Frac}}. \tag{3.35}$$

The mean transverse momentum, $\langle p_T \rangle$, is also extracted from the fit function:

$$\langle p_T \rangle = \frac{\int p_T \cdot \frac{d^2N}{dp_T dy}\, dp_T}{\int \frac{d^2N}{dp_T dy}\, dp_T}. \tag{3.36}$$

The integration range used in this analysis is $p_T \in [0, 10]$ GeV/c.

The statistical uncertainty on $\langle p_T \rangle$ is evaluated by varying the inverse slope parameter T_{eff} of the default fitting function $C \cdot \exp(-m_T/T_{\text{eff}})$ by $\pm 1\sigma$. The uncertainty is then taken as half of the difference between the maximum and minimum $\langle p_T \rangle$ values obtained from this variation. The half of the difference between maximum and minimum is the statistical error.

3.5.5 Branch Ratio of ${}^3_\Lambda\text{H} \rightarrow {}^3\text{He} + \pi^-$

The branching ratio of the two-body decay channel ${}^3_\Lambda\text{H} \rightarrow {}^3\text{He} + \pi^-$ is a necessary input for determining the absolute yield. Since this decay mode accounts for only part of all possible hypertriton decays, we rely on indirect measurements and isospin considerations to estimate its value.

A precision measurement from the STAR experiment reports the following ratio [173]:

$$R_3 = \frac{\mathrm{B.R.}(^3\mathrm{He} + \pi^-)}{\mathrm{B.R.}(^3\mathrm{He} + \pi^-) + \mathrm{B.R.}(d + p + \pi^-)} = 0.357 \pm^{0.028}_{0.027} . \tag{3.37}$$

This represents the fraction of the two-body decay mode among all π^--decay modes of $^3_\Lambda\mathrm{H}$, i.e., both the two-body and three-body decays with π^-.

However, π^- modes are not the only mesonic decay channels of the hypertriton. There are also neutral pion (π^0) modes. In total, the weak decay modes of $^3_\Lambda\mathrm{H}$ are:

- Two-body mesonic decays:

$$^3_\Lambda\mathrm{H} \to {}^3\mathrm{He} + \pi^-,$$
$$^3_\Lambda\mathrm{H} \to {}^3\mathrm{H} + \pi^0.$$

- Three-body mesonic decays:

$$^3_\Lambda\mathrm{H} \to d + p + \pi^-,$$
$$^3_\Lambda\mathrm{H} \to d + n + \pi^0.$$

- Four-body mesonic decays:

$$^3_\Lambda\mathrm{H} \to p + p + n + \pi^-,$$
$$^3_\Lambda\mathrm{H} \to p + n + n + \pi^0.$$

- Non-mesonic decays:

$$^3_\Lambda\mathrm{H} \to p + p + n,$$
$$^3_\Lambda\mathrm{H} \to d + p.$$

Among the weak decay modes of $^3_\Lambda\mathrm{H}$, those involving a neutral pion (π^0) in the final state are experimentally difficult to detect due to the extremely short lifetime of the π^0 and its immediate electromagnetic decay into two photons. As a result, most experimental measurements focus on decay channels with charged pions (π^-). To account for the unobserved π^0 contributions when estimating the total decay width or lifetime, an isospin symmetry argument is typically invoked. In particular, for the two-body and three-body mesonic decay modes, it is commonly assumed that the branching ratio to π^- is twice that to π^0 [174-175]:

$$\frac{\Gamma_{\pi^-}}{\Gamma_{\pi^-} + \Gamma_{\pi^0}} = \frac{2}{3}. \tag{3.38}$$

In addition to the two- and three-body mesonic decays, four-body mesonic decays contribute a small amount, with an estimated branching ratio of 0.9% [90]. For the non-mesonic decay branching ratio, a value of 1.7% is predicted [176]. Combining these considerations, the branching ratio of the dominant two-body decay channel

${}^{3}_{\Lambda}\mathrm{H} \rightarrow {}^{3}\mathrm{He} + \pi^{-}$ can be estimated as:

$$\mathrm{B.R.}({}^{3}_{\Lambda}\mathrm{H} \rightarrow {}^{3}\mathrm{He} + \pi^{-}) = R_3 \times (1 - \mathrm{B.R.}_{\text{4-body}} - \mathrm{B.R.}_{\text{non-mesonic}}) \times \frac{2}{3}. \tag{3.39}$$

Then we get an estimated branching ratio of 23 ± 3 % for the ${}^{3}_{\Lambda}\mathrm{H} \rightarrow {}^{3}\mathrm{He} + \pi^{-}$ channel.

3.6 Systematic Uncertainty Estimation of Yield Analysis

3.6.1 Sources of Systematic Uncertainty

Table 3.15 Cut variations for systematic uncertainty estimation in Au+Au collisions at $\sqrt{s_{NN}}$ = 3.2 GeV for 0–10% centrality.

Category	Subcategory	Default	Variation
Region: $p_T > 2.2$ GeV/c, $-1 < y < -0.5$	l [cm]	> 3	$> 1, > 5$
	$\chi^2_{\mathrm{prim},\pi}$	> 2	> 5
	χ^2_{NDF}	< 4	< 5
Else region	l [cm]	> 3	$> 1, > 5$
	$\chi^2_{\mathrm{prim},\pi}$	> 7	> 10
	χ^2_{NDF}	< 2	< 4
Common topo cuts	χ^2_{Topo}	< 12	< 10
Single track efficiency	$nHitsFit$	≥ 20	$\geq 15, \geq 25$

Table 3.16 Cut variations for systematic uncertainty estimation in Au+Au collisions at $\sqrt{s_{NN}}$ = 3.2 GeV for 10–40% centrality.

Category	Subcategory	Default	Variation
Region: $p_T > 2.1$ GeV/c, $-1 < y < -0.5$	l [cm]	> 1	> 3
	$\chi^2_{\mathrm{prim},\pi}$	> 2	> 5
	χ^2_{NDF}	< 5	< 6
Else region	l [cm]	> 5	> 6.5
	$\chi^2_{\mathrm{prim},\pi}$	> 7	> 10
	χ^2_{NDF}	< 2	< 4
Common topo cuts	χ^2_{Topo}	< 12	< 10
Single track efficiency	$nHitsFit$	≥ 20	$\geq 15, \geq 25$

The systematic uncertainty estimation for the ${}^{3}_{\Lambda}\mathrm{H}$ yield analysis includes the four main sources discussed in Section 3.4.1, with new source specific to the yield measurements. Each source and its implementation in this analysis are briefly summarized below.

1. **Topological variables:** Variations of topological cuts are applied to estimate their impact on the yield measurement. The cut values used in the systematic study are summarized in Tables 3.15 and 3.16 for 0–10% and 10–40% centralities, respectively.
2. **Single track efficiency:** Two types of variations are considered. First, the nHitsFit cut is varied to evaluate its impact on the reconstruction efficiency. Second, an additional 5% uncertainty per track is assigned due to the absence of a dedicated

TPC tracking efficiency evaluation for the FXT datasets by the STAR tracking efficiency group. This results in a total of 10% systematic uncertainty for ${}^{3}_{\Lambda}$H reconstruction via the two-body decay channel. This source of uncertainty, including both the nHitsFit variation and the global tracking efficiency uncertainty, affects observables that depend on absolute yield normalization, such as invariant p_T spectra and dN/dy. However, since $\langle p_T \rangle$ depends on the shape of the p_T distribution, the effect of overall efficiency scaling cancels out.

3. **Raw yield extraction:** The systematic uncertainty from raw yield extraction is evaluated by varying the background normalization region. By default, the combinatorial background is scaled using the sideband range $3.008 < M(^{3}\mathrm{He}\pi^{-}) < 3.018\ \mathrm{GeV}/c^2$, which corresponds to approximately +8 to +13 standard deviations from the signal peak. Two alternative sideband regions are used for comparison:
    - $3.006 < M(^{3}\mathrm{He}\pi^{-}) < 3.016\ \mathrm{GeV}/c^2$ ($+12$ to $+17\sigma$),
    - $3.016 < M(^{3}\mathrm{He}\pi^{-}) < 3.026\ \mathrm{GeV}/c^2$ ($+7$ to $+12\sigma$).

    The extracted raw yields obtained using these different background scaling windows are compared, and the observed variations are assigned as the systematic uncertainty.
4. **Input MC distributions:** The worldwide measurement on ${}^{3}_{\Lambda}$H lifetime τ has uncertainties. By default, the mean value of τ is used. For systematic estimation, the embedded hypertriton lifetime is varied within its world-average uncertainty ($\tau \pm \sigma$).
5. **Extrapolation uncertainty:** Since the measurement does not cover the full p_T range, yields outside the measured region must be extrapolated using fits to the p_T spectra. Five empirical functions [88, 168, 177] are used for this purpose:
    - Blast-Wave function [168, 178]
    - Boltzmann: $C \cdot m_T \exp(-m_T/T)$
    - Exponential in m_T: $C \cdot \exp(-m_T/T)$
    - Exponential in p_T: $C \cdot \exp(-p_T/\mu)$
    - Power-law exponential: $C \cdot \exp(-p_T^{3/2}/\mu)$

    The central values of dN/dy and $\langle p_T \rangle$ are obtained from the default fit method described in Section 3.5.4. The maximum deviations of the integrated yields dN/dy and mean p_T obtained using the five fit functions are assigned as the systematic uncertainties due to extrapolation. Example fits are shown in Figure 3.57.

The systematic uncertainty sources included for each observable are summarized below:

- Differential p_T spectra: Sources 1–4 are included.
- dN/dy: Sources 1–5 are included.
- $\langle p_T \rangle$: Sources 1 and 3–5 are included.

The systematic uncertainty in yield analysis is estimated through the direct variation method described in Section 3.4.2.

3.6.2 Differential p_{T} Spectra, dN/dy and $\langle p_{\mathrm{T}} \rangle$ Results

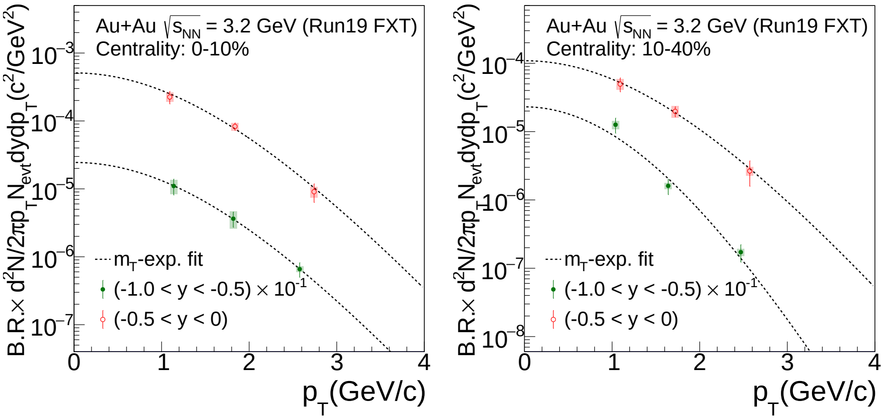

Figure 3.58 The corrected differential p_{T} spectra of $^{3}_{\Lambda}$H in Au+Au collisions at $\sqrt{s_{NN}}$ = 3.2 GeV in 0-10% and 10-40% centrality classes, including both statistical and systematic uncertainties. The boxes represent systematic uncertainties and the vertical lines represent statistical uncertainties.

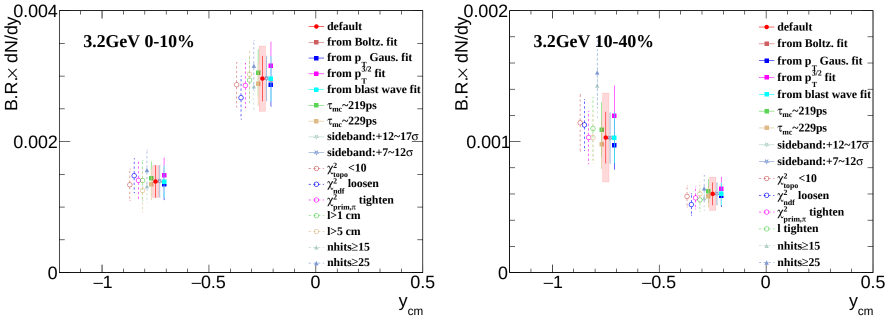

Figure 3.59 The integrated yield dN/dy of $^{3}_{\Lambda}$H measured with different variations for the systematic uncertainty study in Au+Au collisions at $\sqrt{s_{NN}}$ = 3.2 GeV for 0–10% and 10–40% centralities.

The differential p_{T} spectra with systematic uncertainties are shown in Figure 3.58.

The measured dN/dy of $^{3}_{\Lambda}$H resulting from each variation can be found in Figure 3.59. The final $^{3}_{\Lambda}$H dN/dy, corrected for reconstruction efficiency and including the systematic uncertainty estimation, is presented in Figure 3.60. A summary of the relative systematic uncertainties from different sources is provided in Table 3.17. These uncertainties arise from various sources, including raw yield extraction, tracking, topo-

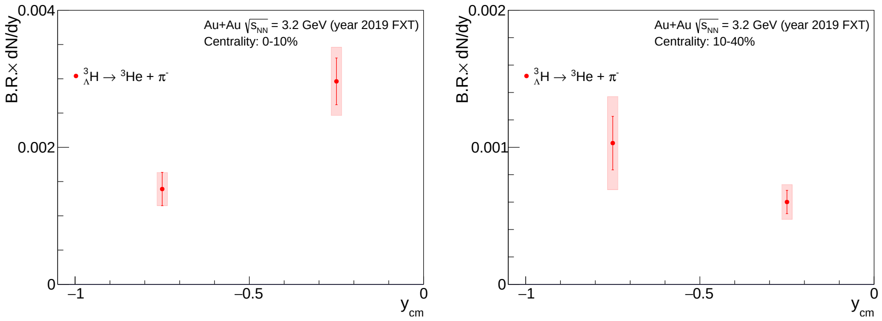

Figure 3.60 The integrated yield dN/dy of $^{3}_{\Lambda}$H, including both statistical and systematic uncertainties, in Au+Au collisions at $\sqrt{s_{NN}}$ = 3.2 GeV for 0–10% and 10–40% centrality classes. The boxes represent systematic uncertainties and the vertical lines represent statistical uncertainties.

Table 3.17 Summary of relative systematic uncertainties on dN/dy for $^{3}_{\Lambda}$H in Au+Au collisions at $\sqrt{s_{NN}}$ = 3.2 GeV.

Source	0–10%		10–40%	
	$[-1, -0.5)$	$[-0.5, 0)$	$[-1, -0.5)$	$[-0.5, 0)$
Raw yield extraction	0.4%	0.2%	0.4%	0.05%
Tracking efficiency	8.8%	5.3%	24.1%	6.1%
Tracking uncertainty (assigned)	10%	10%	10%	10%
$^{3}_{\Lambda}$H MC lifetime	3.4%	2.9%	5.5%	3.4%
Topological cuts	9.2%	11.1%	15.9%	16.7%
Extrapolation	5.1%	4.9%	11.0%	4.4%
Total	**17.4%**	**16.8%**	**32.9%**	**21.2%**

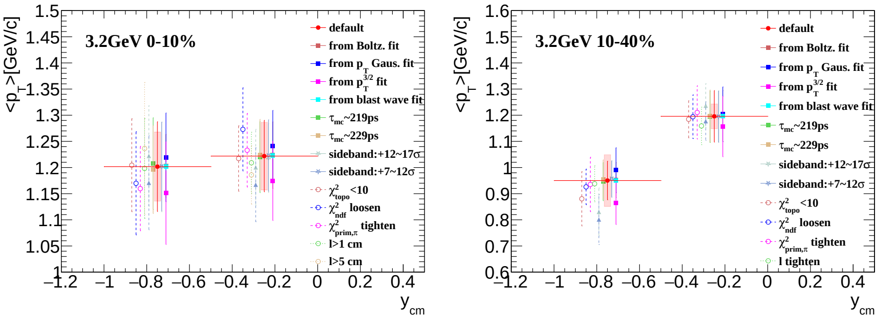

Figure 3.61 The measured $\langle p_T \rangle$ as a function of rapidity in Au+Au collisions at $\sqrt{s_{NN}}$ = 3.2 GeV, obtained under different variations for the systematic uncertainty study.

logical selection cuts, and the choice of input lifetime in the Monte Carlo simulations. Among these, tracking, topological cuts, and the functional form used for extrapolation contribute the main uncertainties.

The measured $^{3}_{\Lambda}$H $\langle p_T \rangle$ resulting from each variation can be found in Figure 3.61. The $^{3}_{\Lambda}$H $\langle p_T \rangle$, corrected for reconstruction efficiency and including the systematic uncertainty estimation, is presented in Figure 3.62. The corresponding relative systematic uncertainties from different sources are summarized in Table 3.18. All sources of systematic uncertainty in the $^{4}_{\Lambda}$He lifetime analysis at $\sqrt{s_{NN}}$ = 3.0 GeV are summarized in Table 3.12. These systematic uncertainties arise from several sources, including raw

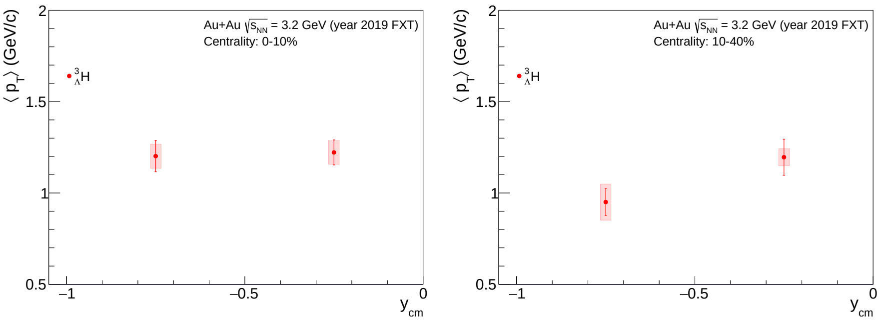

Figure 3.62 The measured $\langle p_T \rangle$ as a function of rapidity in Au+Au collisions at $\sqrt{s_{NN}}$ = 3.2 GeV, including both statistical and systematic uncertainties. The boxes represent systematic uncertainties and the vertical lines represent statistical uncertainties.

Table 3.18 Summary of relative systematic uncertainties on $\langle p_T \rangle$ for ${}^{3}_{\Lambda}$H in Au+Au collisions at $\sqrt{s_{NN}}$ = 3.2 GeV.

Source	**0–10%**		**10–40%**	
	$[-1, -0.5)$	$[-0.5, 0)$	$[-1, -0.5)$	$[-0.5, 0)$
Raw yield extraction	0.05%	0.2%	0.4%	0.06%
${}^{3}_{\Lambda}$H MC lifetime	0.5%	0.2%	0.4%	0.1%
Topological cuts	4.7%	4.5%	8.0%	3.4%
Extrapolation	2.8%	2.7%	6.5%	2.0%
Total	**5.5%**	**5.3%**	**10.4%**	**4.0%**

yield extraction, topological selection cuts, the choice of fit functions used in the extraction, and the choice of input lifetime in the Monte Carlo simulations. The dominant contribution arises from variations in the topological cuts. The second most significant source is the extraction fit functions, consistent with the different p_{T} spectra shapes observed between various fitting functions as illustrated in Figure 3.57.

Chapter 4 Results and Discussions

4.1 ${}^{3}_{\Lambda}$H, ${}^{4}_{\Lambda}$H and ${}^{4}_{\Lambda}$He Lifetimes

The measured lifetimes of ${}^{3}_{\Lambda}$H and ${}^{4}_{\Lambda}$H in Au+Au collisions at $\sqrt{s_{NN}} = 7.2$ GeV from the STAR experiment are:

$$\tau({}^{3}_{\Lambda}\mathrm{H}) = 219.4 \pm 19.8\ (\mathrm{stat.}) \pm 18.6\ (\mathrm{syst.})\ \mathrm{ps}, \quad \sigma_{\mathrm{total}} = 27.1\ \mathrm{ps}, \tag{4.1}$$

$$\tau({}^{4}_{\Lambda}\mathrm{H}) = 217.0 \pm 16.0\ (\mathrm{stat.}) \pm 16.0\ (\mathrm{syst.})\ \mathrm{ps}, \quad \sigma_{\mathrm{total}} = 22.6\ \mathrm{ps}. \tag{4.2}$$

Here, the total uncertainty is define as:

$$\sigma_{\mathrm{total}} = \sqrt{\sigma^2_{\mathrm{stat.}} + \sigma^2_{\mathrm{syst.}}}. \tag{4.3}$$

STAR has also reported lifetime measurements at $\sqrt{s_{NN}} = 3.0$ GeV [179]. The results are:

$$\tau({}^{3}_{\Lambda}\mathrm{H}) = 222.8 \pm 22.9\ (\mathrm{stat.}) \pm 18.3\ (\mathrm{syst.})\ \mathrm{ps}, \quad \sigma_{\mathrm{total}} = 29.4\ \mathrm{ps}, \tag{4.4}$$

$$\tau({}^{4}_{\Lambda}\mathrm{H}) = 218.4 \pm 6.8\ (\mathrm{stat.}) \pm 13.0\ (\mathrm{syst.})\ \mathrm{ps}, \quad \sigma_{\mathrm{total}} = 14.8\ \mathrm{ps}. \tag{4.5}$$

The lifetime measurements at $\sqrt{s_{NN}} = 7.2$ and 3.0 GeV, both collected by the STAR experiment in 2018, are in good agreement with each other.

To improve statistical precision, we combine these measurements at $\sqrt{s_{NN}} = 7.2$ and 3.0 GeV. Since both measurements are from the STAR experiment with similar experimental setups and analysis methods, in this averaging procedure, statistical uncertainties from the two measurements are treated as independent, while systematic uncertainties are assumed to be fully correlated. The weighted average and associated uncertainties are calculated as follows:

$$\overline{\tau} = \frac{\sum_i w_i \tau_i}{\sum_i w_i}, \tag{4.6}$$

$$\sigma_{\overline{\tau},\mathrm{stat.}} = \frac{1}{\sqrt{\sum_i w_i}}, \tag{4.7}$$

$$\sigma_{\overline{\tau},\mathrm{syst.}} = \frac{\sum_i w_i \sigma_{i,\mathrm{syst.}}}{\sum_i w_i}, \tag{4.8}$$

where the weight is defined as $w_i = 1/\sigma^2_{i,\mathrm{stat.}}$. The resulting average lifetimes of ${}^{3}_{\Lambda}$H and ${}^{4}_{\Lambda}$H of $\sqrt{s_{NN}} = 7.2$ and 3.0 GeV are:

$$\overline{\tau}({}^{3}_{\Lambda}\mathrm{H}) = 221 \pm 15\ (\mathrm{stat.}) \pm 19\ (\mathrm{syst.})\ \mathrm{ps}, \quad \sigma_{\mathrm{total}} = 24\ \mathrm{ps}, \tag{4.9}$$

$$\overline{\tau}({}^{4}_{\Lambda}\mathrm{H}) = 218 \pm 6\ (\mathrm{stat.}) \pm 13\ (\mathrm{syst.})\ \mathrm{ps}, \quad \sigma_{\mathrm{total}} = 15\ \mathrm{ps}. \tag{4.10}$$

These average values represented the most precision measurements at the time of publication [88].

The measured lifetime of ${}^{4}_{\Lambda}\mathrm{He}$ in Au+Au collisions at $\sqrt{s_{NN}} = 3.0$ GeV from the STAR experiment is:

$$\tau({}^{4}_{\Lambda}\mathrm{He}) = 229 \pm 23\,(\mathrm{stat.}) \pm 20\,(\mathrm{syst.})\ \mathrm{ps}, \quad \sigma_{\mathrm{total}} = 31\ \mathrm{ps}. \tag{4.11}$$

The measured lifetime of ${}^{4}_{\Lambda}\mathrm{He}$ in Au+Au collisions at $\sqrt{s_{NN}} = 3.2$ and 3.5 GeV from the STAR experiment is:

$$\tau({}^{4}_{\Lambda}\mathrm{He}) = 210 \pm 12\,(\mathrm{stat.}) \pm 11\,(\mathrm{syst.})\ \mathrm{ps}, \quad \sigma_{\mathrm{total}} = 16\ \mathrm{ps}. \tag{4.12}$$

These results are consistent within uncertainties. The measurement at $\sqrt{s_{NN}} = 3.2$ and 3.5 GeV achieves significantly improved precision in both statistical and systematic uncertainties. This improvement is largely attributed to enhanced detector performance following the iTPC upgrade. The average lifetime of ${}^{4}_{\Lambda}\mathrm{He}$ from measurements at $\sqrt{s_{NN}} = 3.0$, 3.2, and 3.5 GeV is:

$$\overline{\tau}({}^{4}_{\Lambda}\mathrm{He}) = 214 \pm 10\,(\mathrm{stat.}) \pm 10\,(\mathrm{syst.})\ \mathrm{ps}, \quad \sigma_{\mathrm{total}} = 15\ \mathrm{ps}. \tag{4.13}$$

This result represents the most precise measurement of the ${}^{4}_{\Lambda}\mathrm{He}$ lifetime to date.

Figure 4.1 summarizes the lifetime measurements for ${}^{3}_{\Lambda}\mathrm{H}$, ${}^{4}_{\Lambda}\mathrm{H}$, and ${}^{4}_{\Lambda}\mathrm{He}$. The measured lifetimes of ${}^{3}_{\Lambda}\mathrm{H}$ and ${}^{4}_{\Lambda}\mathrm{H}$, obtained from the average of results at $\sqrt{s_{NN}} = 7.2$ GeV (presented in this thesis) and 3.0 GeV from the STAR experiment, are shown as red solid markers [88]. The measurements of ${}^{4}_{\Lambda}\mathrm{He}$ from $\sqrt{s_{NN}} = 3.0$, 3.2, and 3.5 GeV collisions, also from STAR and presented in this thesis, are shown as red open markers. These results are compared with both earlier and more recent experimental measurements [50-55, 67, 70, 72, 84-86, 180-187], as well as with theoretical predictions [74, 81-82, 89-90, 188] and the free Λ lifetime [83]. Published experimental lifetimes are indicated by solid circles, while preliminary measurements are represented by open circles. Theoretical estimations are displayed as colorful lines for ${}^{3}_{\Lambda}\mathrm{H}$, and as an orange band for both ${}^{4}_{\Lambda}\mathrm{H}$ and ${}^{4}_{\Lambda}\mathrm{He}$. The global averages of all experimental measurements and their uncertainties are illustrated by light blue bands. The free Λ lifetime, $\tau_{\Lambda} = 263.2 \pm 0.2$ ps [83], is shown as a thin black band.

The global averages are shown as light blue vertical bands in Figure 4.1. Based on

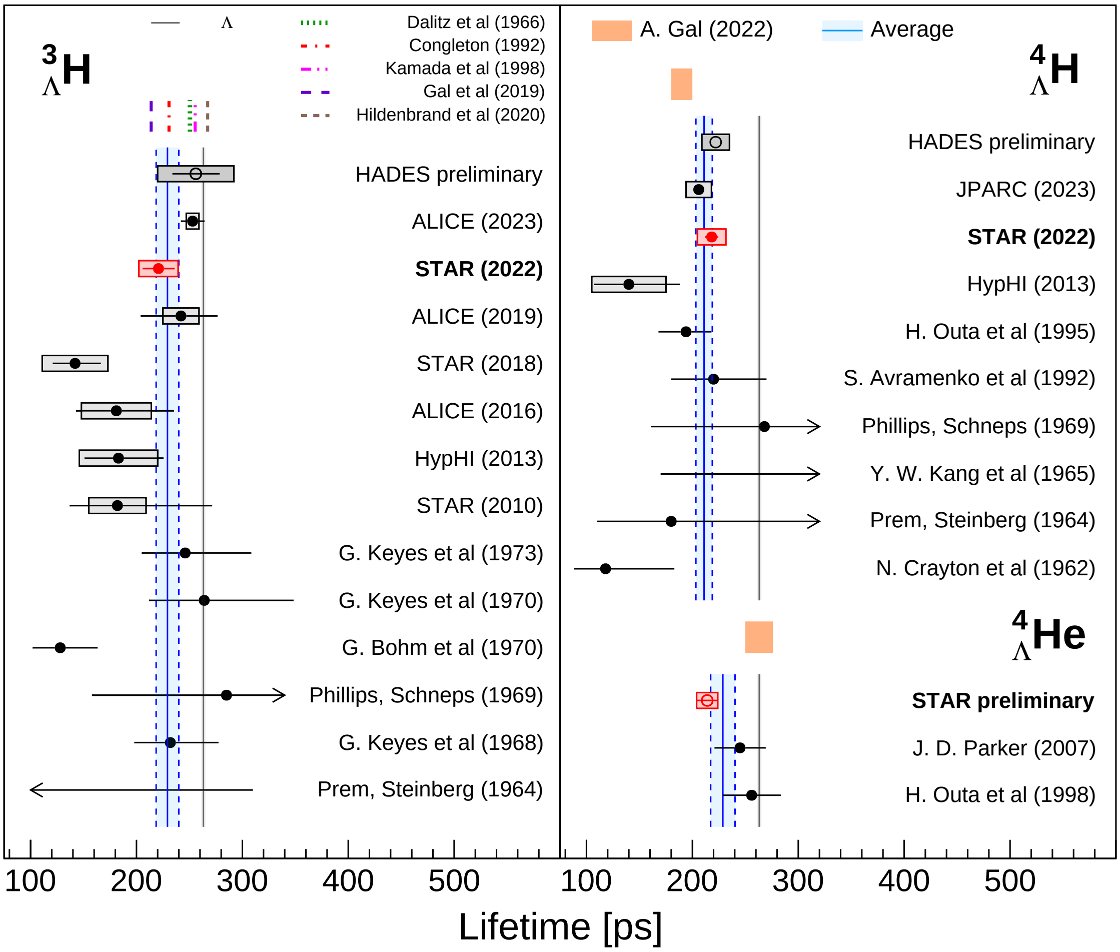

Figure 4.1 Lifetime measurements of $^{3}_{\Lambda}$H (left), $^{4}_{\Lambda}$H (right top), and $^{4}_{\Lambda}$He (right bottom). Experimental measurements, theoretical predictions, and the free Λ lifetime are compared in this figure. The averaged STAR results, including the measurements presented in this thesis, are shown as red circles. The measurements from various experiments are presented with black circles. The global average values are indicated by light blue bands.

all available experimental results, the global averaged lifetimes are:

$$\tau_{\text{avg}}(^{3}_{\Lambda}\text{H}) = 229 \pm 11 \text{ ps}, \tag{4.14}$$

$$\tau_{\text{avg}}(^{4}_{\Lambda}\text{H}) = 211 \pm 8 \text{ ps}, \tag{4.15}$$

$$\tau_{\text{avg}}(^{4}_{\Lambda}\text{He}) = 229 \pm 12 \text{ ps}. \tag{4.16}$$

For comparison, the free Λ lifetime is $\tau_{\Lambda} = 263.2 \pm 0.2$ ps [83], indicated by the thin black lines in Figure 4.1. The global average lifetime ratios relative to the free Λ are:

$$\tau_{\text{avg}}(^{3}_{\Lambda}\text{H})/\tau_{\Lambda} = 87 \pm 4\%, \tag{4.17}$$

$$\tau_{\text{avg}}(^{4}_{\Lambda}\text{H})/\tau_{\Lambda} = 80 \pm 3\%, \tag{4.18}$$

$$\tau_{\text{avg}}(^{4}_{\Lambda}\text{He})/\tau_{\Lambda} = 87 \pm 5\%. \tag{4.19}$$

These results indicate that the lifetimes of $^{3}_{\Lambda}$H, $^{4}_{\Lambda}$H and $^{4}_{\Lambda}$He are systematically shorter than that of free Λ.

The ${}^{3}_{\Lambda}$H lifetime, indicated by the red marker—including the measurement presented in this thesis—is consistent within 2.5σ with results from ALICE [72, 85, 180], previous STAR measurements [70, 86], as well as results from HypHI [84], HADES [181], and early emulsion and bubble chamber experiments [50-55]. The STAR 2010 [70], HypHI 2013 [84], ALICE 2016 [85], and the average result from this analysis [88] all lie below the global average but within 1σ. In contrast, the ALICE 2019 result [180] lies slightly above the global average (by approximately 0.5σ), while the STAR 2018 result [86] lies more than 2σ below it. The ${}^{3}_{\Lambda}$H lifetime obtained in this analysis is shorter than the free Λ lifetime by approximately 1.8σ. However, the most recent ALICE measurement reported in 2023 [72], with significantly reduced uncertainties, yields a value above the global average and is consistent with the free Λ lifetime within about 0.8σ. The result from this analysis is also consistent with the ALICE measurement within approximately 1.2σ. Similarly, the latest preliminary result from HADES lies above the global average and within 1σ, yielding a lifetime in good agreement with that of the free Λ, though with a relatively large uncertainty. Both of these recent results—ALICE and HADES—are more consistent with the free Λ lifetime than the ${}^{3}_{\Lambda}$H measurement reported in this analysis.

A comparison of results from different facilities yields the following average lifetimes relative to the free Λ lifetime:

- GSI-based experiments (HypHI and HADES): $(89 \pm 15)\%$, consistent with the free Λ lifetime within 1σ;
- LHC (ALICE): $(95 \pm 6)\%$, consistent within 1σ;
- RHIC (STAR): $(75 \pm 9)\%$, consistent within 2.7σ.

These comparisons suggest a discrepancy between STAR and ALICE measurements. The STAR results consistently indicate a shorter ${}^{3}_{\Lambda}$H lifetime, while ALICE measurements align more closely with the free Λ lifetime. This tension underscores the need for further high-precision lifetime measurements, particularly at RHIC, to resolve the current inconsistency.

Early theoretical predictions for the ${}^{3}_{\Lambda}$H lifetime generally lie within 15% of the free Λ lifetime [82, 89-90], primarily due to the extremely weak binding of the Λ hyperon in the hypertriton. Ref. [74] that includes attractive pion final-state interactions (FSI) predicts a reduced ${}^{3}_{\Lambda}$H lifetime to $(81 \pm 2)\%$ of τ_{Λ}. In contrast, more recent calculations based on pionless effective field theory (EFT), which model the system using Λd degrees of freedom and assume a binding energy of $B_{\Lambda} = 0.13$ MeV, predict a lifetime approximately 1–2% longer than τ_{Λ} [80]. Despite differences in the underlying assumptions and treatment of decay dynamics, both the model including pion FSI [74] and the one treating ${}^{3}_{\Lambda}\mathrm{H}$ as a loosely bound two-body Λd system [89] yield lifetime predictions that are in good agreement with the world-average experimental value and, in particular, with the measurement reported in this thesis. In contrast, the recent ALICE result from 2023 favors predictions from three-body calculations without pion FSI [90] and closure-approximation estimates [82], and is also consistent with the pionless EFT result [80] within 1.2σ.

For ${}^{4}_{\Lambda}\mathrm{H}$, the measured lifetime shown as the red marker—including the result presented in this thesis—is consistent with all previous experimental measurements [50, 52, 67, 84, 181-185] within 2.5σ, and agrees with the theoretical estimation of 195 ± 10 ps [188] within 1.3σ. The ${}^{4}_{\Lambda}\mathrm{H}$ lifetime result obtained in this analysis is shorter than the free Λ lifetime by about 3σ.

Similarly, the measured lifetime of ${}^{4}_{\Lambda}\mathrm{He}$ presented in this thesis(indicated by the red marker) is consistent with the two existing experimental measurements [186-187] within 1.5σ, and agrees with the theoretical estimation from Ref. [188] within 2.6σ. The ${}^{4}_{\Lambda}\mathrm{He}$ lifetime result obtained in this analysis deviates from the free Λ lifetime by approximately 3σ. This lifetime estimation in Ref. [188], based on the isospin rule ($\Delta I = 1/2$), estimates a shorter lifetime for ${}^{4}_{\Lambda}\mathrm{H}$ compared to ${}^{4}_{\Lambda}\mathrm{He}$, with the ratio $\tau({}^{4}_{\Lambda}\mathrm{H})/\tau({}^{4}_{\Lambda}\mathrm{He}) = 0.74 \pm 0.04$. The ratio of the ${}^{4}_{\Lambda}\mathrm{H}$ to ${}^{4}_{\Lambda}\mathrm{He}$ in this thesis is:

$$\tau({}^{4}_{\Lambda}\mathrm{H})/\tau({}^{4}_{\Lambda}\mathrm{He}) = 1.02 \pm 0.10, \tag{4.20}$$

which is statistically consistent with unity and deviates from the theoretical value by approximately 2.6σ. The ratio of the global average lifetimes extracted from experimental data is:

$$\tau_{\mathrm{avg}}({}^{4}_{\Lambda}\mathrm{H})/\tau_{\mathrm{avg}}({}^{4}_{\Lambda}\mathrm{He}) = 0.92 \pm 0.06, \tag{4.21}$$

which is consistent with unity by approximately 1.3σ, and with the theoretical value within 2.5σ. The precision lifetime measurements of ${}^{4}_{\Lambda}\mathrm{H}$ and ${}^{4}_{\Lambda}\mathrm{He}$ provides valuable constraints on theoretical models of hypernuclear decay, including the underlying Y–N interaction and the internal structure of the hypernucleus. Continued high-precision measurements of isospin mirror hypernuclei ${}^{4}_{\Lambda}\mathrm{H}$ and ${}^{4}_{\Lambda}\mathrm{He}$ will further illuminate the role of isospin in hypernuclear weak decay.

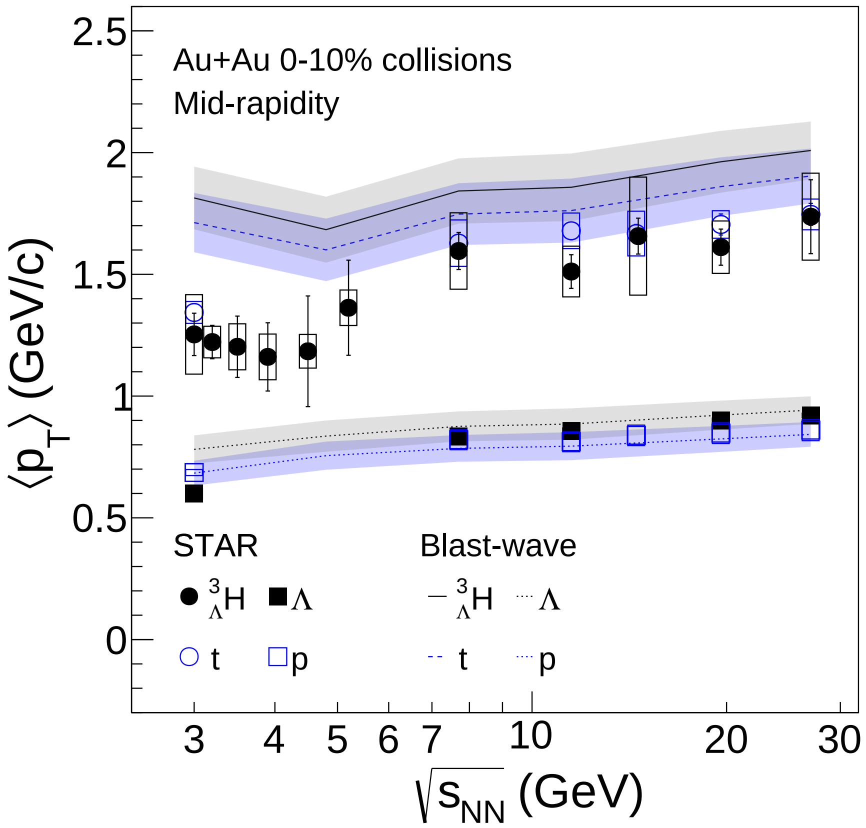

Figure 4.2 Energy dependence of the average transverse momentum $\langle p_T \rangle$ in Au+Au central (0–10%) collisions at mid-rapidity. The measurements of $^{3}_{\Lambda}$H, triton, Λ and proton are compared with a blast-wave parameterized from fits to light hadron (π, K, p) spectra. The boxes represent systematic uncertainties and the vertical lines represent statistical uncertainties.

4.2 Energy Dependence of $\langle p_T \rangle$ of $^{3}_{\Lambda}$H

Figure 4.2 presents the energy dependence of the $\langle p_T \rangle$ for $^{3}_{\Lambda}$H, triton, Λ and proton in central Au+Au collisions at mid-rapidity. The $^{3}_{\Lambda}$H production measurement at $\sqrt{s_{\mathrm{NN}}}$ = 3.2 GeV presented in this thesis is included in this figure. The $^{3}_{\Lambda}$H and triton data points appear close to each other and are represented by circles, while the Λ and proton data points—also close to one another—are represented by squares at lower $\langle p_T \rangle$. These results are compared with theoretical calculations from the blast-wave (BW) model, which describes the collective transverse expansion of the system at kinetic freeze-out. The model assumes a thermalized source with a common radial flow velocity field and a common kinetic freeze-out surface [178]. The BW calculations presented in this figure are based on the kinetic freeze-out parameters extracted from simultaneous fits to the spectra of light hadrons (π, K, p) [168, 189-190]. These parameters characterize the thermodynamic conditions at the point where hadrons decouple kinetically. At $\sqrt{s_{NN}}$ = 3.0 –5.2 GeV, the measured $\langle p_T \rangle$ values of $^{3}_{\Lambda}$H lie below the BW predictions, indicating a suppression relative to the collective flow observed for light hadrons. At $\sqrt{s_{NN}}$ = 3.0 GeV, triton is also overestimated. At higher energies above $\sqrt{s_{NN}}$ = 7.7 GeV, the BW calculations are generally consistent with the data for ${}^{3}_{\Lambda}$H and triton, with only a slight overestimation of the measured $\langle p_T \rangle$. From the blast-wave perspective, a particle's transverse momentum is determined by a combination of thermal motion and radial flow expansion. Heavier particles, such as nuclei, are expected to gain more $\langle p_T \rangle$ from radial flow compared to lighter hadrons under the same freeze-out conditions. We do observe higher $\langle p_T \rangle$ of ${}^{3}_{\Lambda}$H and triton compared with Λ and proton in Figure 4.2. However, the observed suppression of $\langle p_T \rangle$ relative to the BW calculations suggests that light nuclei and hypernuclei, such as ${}^{3}_{\Lambda}$H and triton, may not fully participate in the same collective expansion as light hadrons. It can be interpreted as that ${}^{3}_{\Lambda}$H and triton decouple from the system at different time compared to light hadrons. This softening of the ${}^{3}_{\Lambda}$H spectrum may also be explained by the coalescence model using a Wigner-function formalism, which accounts for the extended spatial structure of the hypertriton [191]. Due to its loosely bound nature and the resulting large spatial size, the Wigner distribution of ${}^{3}_{\Lambda}$H becomes very dilute in phase space, making it less likely for constituent particles to satisfy the coalescence condition, especially at high p_{T}.

4.3 Energy Dependence of dN/dy of ${}^{3}_{\Lambda}$H

The energy dependence of ${}^{3}_{\Lambda}$H production provides important insights into its formation mechanism in heavy-ion collisions. In this thesis, we present the ${}^{3}_{\Lambda}$H production measurements at $\sqrt{s_{\mathrm{NN}}}$ = 3.2 GeV. The dN/dy result, together with measurements at other RHIC energies, constitutes the first systematic and complete mapping of the energy dependence of ${}^{3}_{\Lambda}$H production in the high baryon density region. Figure 4.3 shows the measured dN/dy of ${}^{3}_{\Lambda}$H as a function of collision energy in central (0–10%) Au+Au collisions at mid-rapidity ($|y| < 0.5$). The data at $\sqrt{s_{NN}}$ = 2.76 TeV is taken from ALICE experiment [85]. In this figure, the yield increases sharply as $\sqrt{s_{\mathrm{NN}}}$ decreases from 27 GeV to 4.5 GeV and appears to reach a maximum in the range of $\sqrt{s_{\mathrm{NN}}}$ = 3–4 GeV. At energies below this peak, the yield shows signs of plateau or a mild decrease. This behavior can be attributed to two competing effects. As $\sqrt{s_{\mathrm{NN}}}$ decreases, increasing baryon density enhances hypernucleus formation via coalescence, while stronger strangeness canonical suppression at lower energies reduces the available Λ yield, resulting in a peak around 3–4 GeV where the enhancement dominates.

To interpret the data, the results are compared to predictions from two theoretical

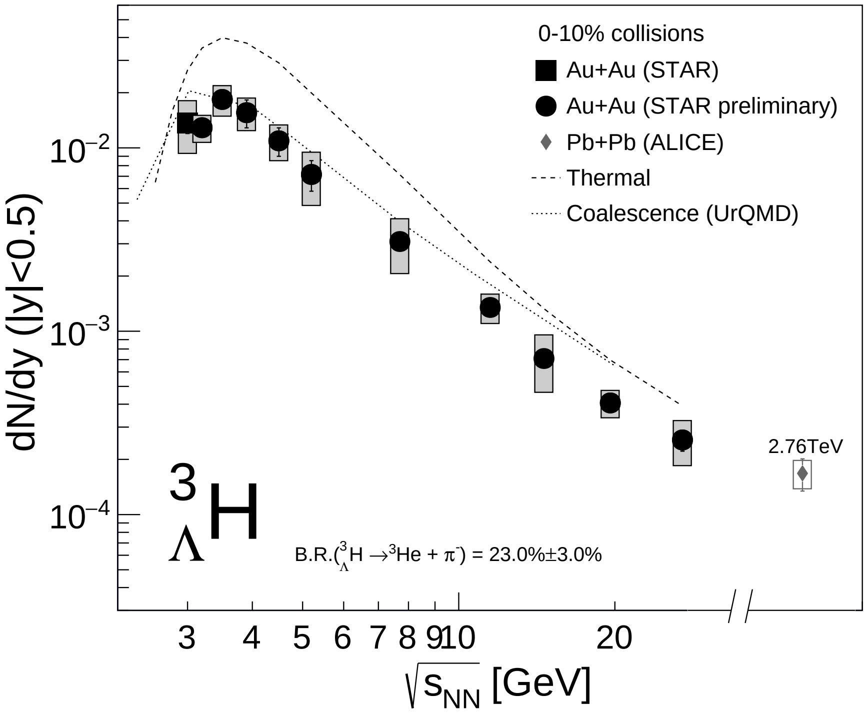

Figure 4.3 Energy dependence of mid-rapidity yields (dN/dy) of ${}^{3}_{\Lambda}$H in central (0–10%) Au+Au collisions. The boxes represent systematic uncertainties and the vertical lines represent statistical uncertainties. The measured data are compared with model predictions from Thermal-FIST (dashed line) and UrQMD with a coalescence afterburner (dotted lines) [97].

frameworks:

- **UrQMD+Coalescence [97]**: This calculation is based on freeze-out distributions provided by the UrQMD transport model. An instantaneous coalescence afterburner is applied to describe the formation of hypertriton from nucleons and hyperons that are close in phase space after freeze-out. This approach reproduces the experimental data well in the energy range from 3 to 10 GeV.
- **Thermal-FIST model [97, 99]**: The thermal model uses chemical freeze-out parameters, such as temperature and baryon chemical potential, obtained from light hadron yields. It assumes that hypernuclei are produced in statistical equilibrium under these freeze-out conditions. While it reproduces the overall trend, it overestimates the yields by about a factor of 2 at low collision energies, which suggests that hypernuclei may do not freeze out at the same time as light hadrons.

The experimental results provide evidence that hypertriton is formed via a coalescence mechanism in the high baryon density region of heavy-ion collisions. The thermal model appears insufficient to fully describe hypertriton production, indicating that hypertriton likely decouples from the medium at a different time compared to light hadrons.

4.4 Centrality Dependence of ${}^{3}_{\Lambda}$H Production

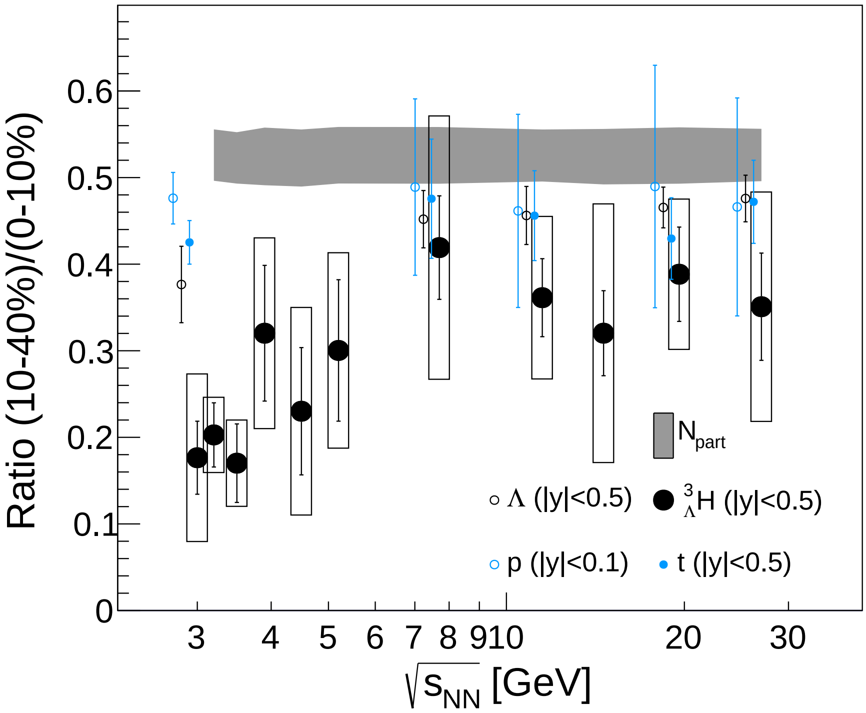

Figure 4.4 Mid-central-to-central (10–40%)/(0–10%) yield ratios of ${}^{3}_{\Lambda}$H, Λ, triton, and proton, as a function of collision energy. For ${}^{3}_{\Lambda}$H, the boxes represent systematic uncertainties and the vertical lines represent statistical uncertainties. The shaded band represents the ratio expected from participant scaling (N_{part}).

Figure 4.4 shows the mid-central-to-central yield ratio (10–40%)/(0–10%) of ${}^{3}_{\Lambda}$H as a function of collision energy, compared with similar ratios for protons, tritons, and Λ. The horizontal band represents the expectation based on participant scaling (N_{part}). At low collision energies ($\sqrt{s_{NN}} < 7.7$ GeV), the yield of ${}^{3}_{\Lambda}$H appears to decrease more steeply in peripheral collisions than that of other hadrons. This deviation from N_{part} scaling, and the relatively stronger suppression observed in ${}^{3}_{\Lambda}$H production, may be associated with differences in formation conditions for hypernuclei. However, further data and model studies are required to draw firm conclusions.

Chapter 5 Summary and Outlook

5.1 Summary

In this thesis, we present a comprehensive study of light hypernuclei—${}^{3}_{\Lambda}\mathrm{H}$, ${}^{4}_{\Lambda}\mathrm{H}$, and ${}^{4}_{\Lambda}\mathrm{He}$—produced in heavy-ion collisions at RHIC. Precision measurements of their lifetimes, production are carried out using data taken from the STAR experiment, particularly from the BES-II fixed-target mode at low collision energies ($\sqrt{s_{NN}}$ = 3.0–7.2 GeV). These studies contribute crucial insight into the inner structure, and the production dynamics of hypernucei in the baryon-rich environments produced by the violent heavy-ion collisions.

The lifetime study is based on the reconstruction of hypernuclei via their mesonic decay channels. The ${}^{3}_{\Lambda}\mathrm{H}$ and ${}^{4}_{\Lambda}\mathrm{H}$ hypernuclei are reconstructed through their two-body decays: ${}^{3}_{\Lambda}\mathrm{H} \to {}^{3}\mathrm{He} + \pi^{-}$ and ${}^{4}_{\Lambda}\mathrm{H} \to {}^{4}\mathrm{He} + \pi^{-}$, respectively. The lifetimes of ${}^{3}_{\Lambda}\mathrm{H}$ and ${}^{4}_{\Lambda}\mathrm{H}$ measured at $\sqrt{s_{NN}} = 7.2$ GeV are $\tau({}^{3}_{\Lambda}\mathrm{H}) = 219.4 \pm 19.8$ (stat.) $\pm$ 18.6 (syst.) ps and $\tau({}^{4}_{\Lambda}\mathrm{H}) = 217.0 \pm 16.0$ (stat.) $\pm$ 16.0 (syst.) ps, respectively. The weighted averages of lifetimes measured at $\sqrt{s_{NN}} = 7.2$ and 3.0 GeV are $\tau({}^{3}_{\Lambda}\mathrm{H}) = 221 \pm 15$ (stat.) $\pm$ 19 (syst.) ps and $\tau({}^{4}_{\Lambda}\mathrm{H}) = 218 \pm 6$ (stat.) $\pm$ 13 (syst.) ps, respectively, representing the most precise values at the time they published [88]. Both ${}^{3}_{\Lambda}\mathrm{H}$ and ${}^{4}_{\Lambda}\mathrm{H}$ results are systematically shorter than the free Λ lifetime by approximately 1.8σ and 3σ, respectively. The global averaged lifetimes of ${}^{3}_{\Lambda}\mathrm{H}$ and ${}^{4}_{\Lambda}\mathrm{H}$, obtained from all available experimental data, further support this systematic reduction relative to the free Λ lifetime. However, the most recent ALICE measurement [90] supports a ${}^{3}_{\Lambda}\mathrm{H}$ lifetime that is closer to the free Λ lifetime. This discrepancy highlights a tension between the STAR and ALICE measurements. To resolve this inconsistency, further high-precision measurements from STAR are necessary.

The ${}^{4}_{\Lambda}\mathrm{He}$ hypernucleus, reconstructed via the three-body decay channel ${}^{4}_{\Lambda}\mathrm{He} \to d + p + \pi^{-}$, was measured at $\sqrt{s_{NN}}$ = 3.0, 3.2, and 3.5 GeV. The combined lifetime measurement yields $\tau({}^{4}_{\Lambda}\mathrm{He}) = 214 \pm 10$ (stat.) $\pm$ 10 (syst.) ps, which is the most precision lifetime measurement for this hypernucleus to date. Similar to ${}^{4}_{\Lambda}\mathrm{H}$, the measured lifetime of ${}^{4}_{\Lambda}\mathrm{He}$ is also shorter than the free Λ lifetime by approximately 3σ. This result provides valuable constraints on theoretical models of hypernuclear decay, including the underlying hyperon–nucleon interaction and the internal structure of the hypernucleus. The precise lifetime measurements of ${}^{4}_{\Lambda}\mathrm{He}$ and ${}^{4}_{\Lambda}\mathrm{H}$ not only provide tighter constraints on theoretical models of hypernuclei, but also highlight the potential of precision lifetime measurements as a probe for testing isospin symmetry in mirror hypernuclei.

In this thesis, we also present a detailed analysis of ${}^{3}_{\Lambda}\mathrm{H}$ production at $\sqrt{s_{NN}}$ = 3.2 GeV in Au+Au collisions. The study includes differential p_T spectra, integrated yield dN/dy , and $\langle p_T \rangle$ measurements for two centrality classes: central (0–10%) and mid-central (10–40%). These measurements provide key observables for probing the production mechanism and freeze-out behavior of hypernuclei in high density region. The ${}^{3}_{\Lambda}\mathrm{H}$ yield result at 3.2 GeV is further combined with measurements at other beam energies to investigate the energy dependence of hypertriton production. The dN/dy values exhibit a pronounced maximum around $\sqrt{s_{NN}} \sim$ 3–4 GeV, highlighting the interplay between baryon density enhancement and strangeness suppression at low energies. Thermal model calculations, which assume that hypernuclei freeze out along with other light hadrons, significantly overestimate the measured yields at low energies. In contrast, the data are well described by transport models with a coalescence afterburner, where hypernuclei are formed from nearby nucleons and hyperons in phase space after freeze-out. These observations support the scenario in which ${}^{3}_{\Lambda}\mathrm{H}$ production is dominated by coalescence rather than thermal production. It also suggests that the ${}^{3}_{\Lambda}\mathrm{H}$ yield is not in equilibrium and fixed at chemical freeze-out simultaneously with other light hadrons.

Additionally, the $\langle p_T \rangle$ of ${}^{3}_{\Lambda}\mathrm{H}$, measured at $\sqrt{s_{NN}}$ = 3.2 GeV and presented together with results from other energies, is systematically lower than the predictions from blast-wave fits to light hadron spectra. This suppression suggests that hypertriton may do not follow same collective expansion as light hadrons, indicating a different decoupling time from the system. Such behavior may be explained within the coalescence picture, given the hypertriton's large size [191].

In summary, the lifetime measurements presented in this thesis suggest that light hypernuclei have systematically shorter lifetimes than the free Λ. These precision measurement of hypernuclei lifetimes provide essential constraints for theoretical models of hypernuclear. The production measurements of ${}^{3}_{\Lambda}\mathrm{H}$, including its energy dependence of dN/dy and $\langle p_T \rangle$, indicate that hypertriton do not decouple from the medium at hadron freeze-out. The experimental measurements support the coalescence as the dominate mechanism of hypertriton formation in the high baryon density region.

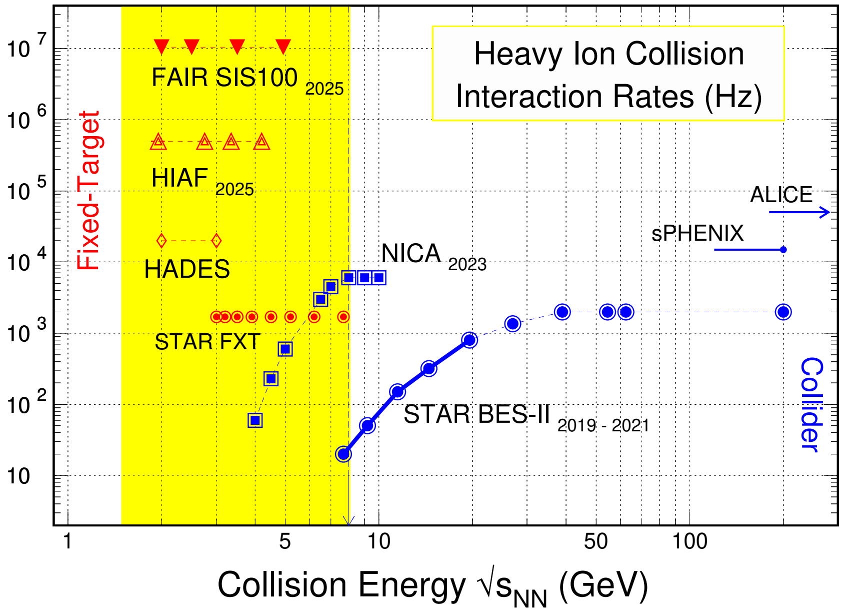

Figure 5.1 Interaction rates for current and upcoming heavy-ion experiments. Fixed-target programs at STAR, HADES, FAIR-CBM, and HIAF cover the high baryon density region at low energies with increasing luminosity and improved detector capabilities. This picture is taken from Ref. [192].

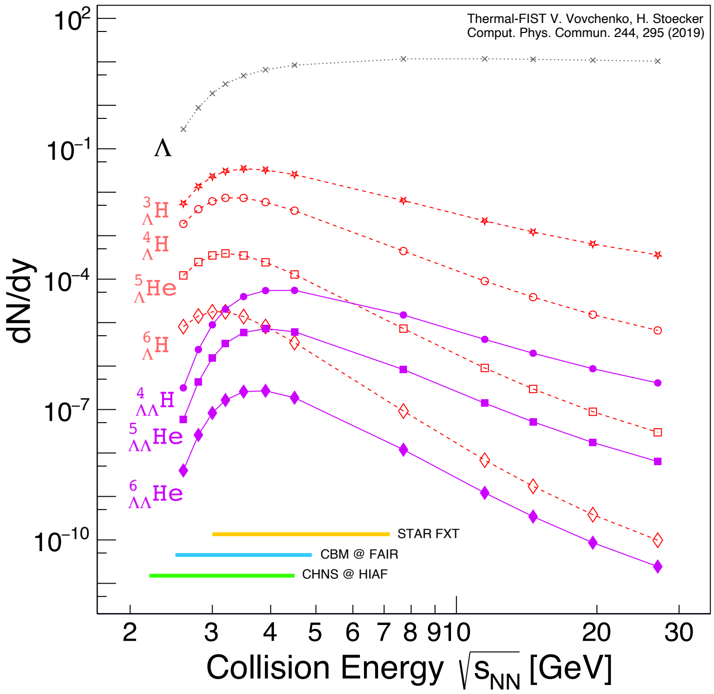

Figure 5.2 Thermal model predictions of mid-rapidity yields (dN/dy) for various hypernuclei as a function of collision energy [99]. Projected experimental sensitivities from STAR FXT, CBM@FAIR, and CHNS@HIAF are indicated.

5.2 Outlook

Hypernuclear research is entering a new era of precision, fueled by high-statistics datasets from a series of heavy-ion collision experiments conducted at low collision energies, as illustrated in Figure 5.1. These experiments provide access to the high baryon density region of the QCD phase diagram, where the production of hypernuclei is expected to be enhanced (see Figure 5.2).

There is significant potential for the discovery of previously unobserved hypernuclei in heavy-ion collisions. These include medium-to-heavy hypernuclei with mass numbers $A \geq 5$, anti-hypernuclei, as well as multi-strange systems such as Ξ hypernuclei. In particular, the search for double-Λ hypernuclei—such as ${}^{4}_{\Lambda\Lambda}$H, ${}^{5}_{\Lambda\Lambda}$H, ${}^{5}_{\Lambda\Lambda}$He, and ${}^{6}_{\Lambda\Lambda}$He—is one of the major goals for upcoming experiments. These double-Λ systems are essential for constraining the hyperon–hyperon(Y–Y) interaction and provide critical input for resolving the hyperon puzzle in neutron star matter.

Such studies are part of a broader effort to extend the nuclear chart into the strangeness sector, mapping out the properties and existence limits of strange nuclear systems. Ongoing and future experiments at various facilities play a key role in this endeavor. At RHIC, the STAR FXT program offers unique access to high baryon density conditions and enables systematic studies of hypernuclei at low energies. Complementarily, the collider-mode data at $\sqrt{s_{NN}} = 200$ GeV, with an enormous dataset of approximately 20 billion events, also facilitates precise measurements of hypernuclei in the low baryon density regime.

The Compressed Baryonic Matter (CBM) experiment at FAIR and the China HyperNuclear Spectrometer (CHNS) experiment at the High Intensity heavy-ion Accelerator Facility (HIAF) are designed to operate at high interaction rates with advanced detector technologies. These capabilities make them ideally suited for the study of the search for new hypernuclei and high-precision hypernuclear spectroscopy. These programs are expected to explore previously inaccessible regions of the hypernuclear chart and provide critical insights into Y–N and Y–Y interactions, as well as the internal structure of hypernuclei. A dramatic expansion of the hypernuclear chart is expected.

With enhanced detector capabilities and high interaction rates at facilities such as RHIC, HADES, FAIR, and HIAF at low collision energies, future experiments are well-positioned to explore hypernuclear production in high baryon density environments and to push the boundaries of our understanding of hypernuclear matter. Together, these global experimental programs will significantly deepen our understanding of hypernuclear structure, production mechanisms, and their role in dense QCD matter—bridging nuclear physics, astrophysics, and fundamental strong-interaction theory.

Bibliography

[1] Wikipedia contributors. Standard Model of elementary particles[EB/OL]. 2024. https://commons.wikimedia.org/wiki/File:Standard_Model_of_Elementary_Particles.svg.

[2] AAD G, et al. Observation of a new particle in the search for the Standard Model Higgs boson with the ATLAS detector at the LHC[J/OL]. Phys. Lett. B, 2012, 716: 1-29. DOI: 10.1016/j.physletb.2012.08.020.

[3] CHATRCHYAN S, et al. Observation of a new boson at a mass of 125 GeV with the CMS experiment at the LHC[J/OL]. Phys. Lett. B, 2012, 716: 30-61. DOI: 10.1016/j.physletb.2012.08.021.

[4] HIGGS P W. Broken symmetries and the masses of gauge bosons[J/OL]. Phys. Rev. Lett., 1964, 13: 508-509. DOI: 10.1103/PhysRevLett.13.508.

[5] ENGLERT F, BROUT R. Broken symmetry and the mass of gauge vector mesons[J/OL]. Phys. Rev. Lett., 1964, 13: 321-323. DOI: 10.1103/PhysRevLett.13.321.

[6] GURALNIK G S, HAGEN C R, KIBBLE T W B. Global conservation laws and massless particles[J/OL]. Phys. Rev. Lett., 1964, 13: 585-587. DOI: 10.1103/PhysRevLett.13.585.

[7] MARCIANO W J, PAGELS H. Quantum Chromodynamics: a review[J/OL]. Phys. Rept., 1978, 36: 137. DOI: 10.1016/0370-1573(78)90208-9.

[8] HAN M Y, NAMBU Y. Three triplet model with double SU(3) symmetry[J/OL]. Phys. Rev., 1965, 139: B1006-B1010. DOI: 10.1103/PhysRev.139.B1006.

[9] BJORKEN J D. Asymptotic sum rules at infinite momentum[J/OL]. Phys. Rev., 1969, 179: 1547-1553. DOI: 10.1103/PhysRev.179.1547.

[10] POLITZER H D. Reliable perturbative results for strong interactions?[J/OL]. Phys. Rev. Lett., 1973, 30: 1346-1349. DOI: 10.1103/PhysRevLett.30.1346.

[11] GROSS D J, WILCZEK F. Ultraviolet behavior of nonabelian gauge theories[J/OL]. Phys. Rev. Lett., 1973, 30: 1343-1346. DOI: 10.1103/PhysRevLett.30.1343.

[12] GROSS D J, WILCZEK F. Asymptotically free gauge theories. I[J/OL]. Phys. Rev. D, 1973, 8: 3633-3652. DOI: 10.1103/PhysRevD.8.3633.

[13] GROSS D J, WILCZEK F. Asymptotically free gauge theories. II[J/OL]. Phys. Rev. D, 1974, 9: 980-993. DOI: 10.1103/PhysRevD.9.980.

[14] WILSON K G. Confinement of quarks[J/OL]. Phys. Rev. D, 1974, 10: 2445-2459. DOI: 10.1103/PhysRevD.10.2445.

[15] NAVAS S, AMSLER C, GUTSCHE T, et al. Review of particle physics[J/OL]. Phys. Rev. D, 2024, 110: 030001. DOI: 10.1103/PhysRevD.110.030001.

[16] BETHKE S. Experimental tests of asymptotic freedom[J/OL]. Prog. Part. Nucl. Phys., 2007, 58: 351-386. DOI: 10.1016/j.ppnp.2006.06.001.

[17] COLLINS J C, PERRY M J. Superdense matter: neutrons or asymptotically free quarks?[J/OL]. Phys. Rev. Lett., 1975, 34: 1353-1356. DOI: 10.1103/PhysRevLett.34.1353.

[18] KARSCH F. The phase transition to the quark gluon plasma: recent results from lattice calculations[J/OL]. Nucl. Phys. A, 1995, 590: 367C-382C. DOI: 10.1016/0375-9474(95)00248-Y.

[19] STEPHANOV M A. QCD phase diagram and the critical point[J/OL]. Prog. Theor. Phys. Suppl., 2004, 153: 139-156. DOI: 10.1143/PTPS.153.139.

[20] AOKI Y, ENDRŐDI G, FODOR Z, et al. The order of the quantum chromodynamics transition predicted by the standard model of particle physics[J/OL]. Nature, 2006, 443(7112): 675-678. DOI: 10.1038/nature05120.

[21] FUKUSHIMA K, HATSUDA T. The phase diagram of dense QCD[J/OL]. Rept. Prog. Phys., 2011, 74: 014001. DOI: 10.1088/0034-4885/74/1/014001.

[22] BAZAVOV A, BHATTACHARYA T, CHENG M, et al. Chiral and deconfinement aspects of the QCD transition[J/OL]. Phys. Rev. D, 2012, 85: 054503. DOI: 10.1103/PhysRevD.85.054503.

[23] BELLWIED R, BORSANYI S, FODOR Z, et al. The QCD phase diagram from analytic continuation[J/OL]. Phys. Lett. B, 2015, 751: 559-564. DOI: 10.1016/j.physletb.2015.11.011.

[24] BORSANYI S, FODOR Z, GUENTHER J N, et al. QCD crossover at finite chemical potential from lattice simulations[J/OL]. Phys. Rev. Lett., 2020, 125: 052001. DOI: 10.1103/PhysRevLett.125.052001.

[25] SWEGER Z. Recent results and future prospects from the STAR Beam Energy Scan program [A]. 2023. arXiv: 2305.07139.

[26] Particle Data Group. The history of the universe[EB/OL]. 2015. https://particleadventure.org/history-universe.html.

[27] AOKI Y, FODOR Z, KATZ S D, et al. The QCD transition temperature: results with physical masses in the continuum limit[J/OL]. Phys. Lett. B, 2006, 643: 46-54. DOI: 10.1016/j.physletb.2006.10.021.

[28] AOKI Y, BORSANYI S, DURR S, et al. The QCD transition temperature: results with physical masses in the continuum limit II.[J/OL]. JHEP, 2009, 06: 088. DOI: 10.1088/1126-6708/2009/06/088.

[29] BORSANYI S, FODOR Z, HOELBLING C, et al. Is there still any T_c mystery in lattice QCD? Results with physical masses in the continuum limit III[J/OL]. JHEP, 2010, 09: 073.

DOI: 10.1007/JHEP09(2010)073.

[30] BAZAVOV A, et al. The chiral and deconfinement aspects of the QCD transition[J/OL]. Phys. Rev. D, 2012, 85: 054503. DOI: 10.1103/PhysRevD.85.054503.

[31] GAVAI R V, GUPTA S. Pressure and nonlinear susceptibilities in QCD at finite chemical potentials[J/OL]. Phys. Rev. D, 2003, 68: 034506. DOI: 10.1103/PhysRevD.68.034506.

[32] EJIRI S. Existence of the critical point in finite density lattice QCD[J/OL]. Phys. Rev. D, 2008, 77: 014508. DOI: 10.1103/PhysRevD.77.014508.

[33] FODOR Z, KATZ S D. Critical point of QCD at finite T and μ, lattice results for physical quark masses[J/OL]. JHEP, 2004, 04: 050. DOI: 10.1088/1126-6708/2004/04/050.

[34] SUMOWIDAGDO S. Experimental study of matter under the influence non-abelian gauge theory[J/OL]. J. Phys. Conf. Ser., 2017, 856(1): 012002. DOI: 10.1088/1742-6596/856/1/012002.

[35] MILLER M L, REYGERS K, SANDERS S J, et al. Glauber modeling in high energy nuclear collisions[J/OL]. Ann. Rev. Nucl. Part. Sci., 2007, 57: 205-243. DOI: 10.1146/annurev.nucl.57.090506.123020.

[36] CAINES H. What's interesting about strangeness production? An overview of recent results [J/OL]. J. Phys. G, 2005, 31: S101-S118. DOI: 10.1088/0954-3899/31/4/013.

[37] SAITO T R, et al. New directions in hypernuclear physics[J/OL]. Nature Rev. Phys., 2021, 3(12): 803-813. DOI: 10.1038/s42254-021-00371-w.

[38] MAINZ H I. Hypernuclear chart[EB/OL]. https://www.hi-mainz.de/research/research-sections/specf-spectroscopy-flavour/specf-hyp/hyper-database.

[39] BOTTA E, BRESSANI T, GARBARINO G. Strangeness nuclear physics: a critical review on selected topics[J/OL]. Eur. Phys. J. A, 2012, 48: 41. DOI: 10.1140/epja/i2012-12041-6.

[40] DAVIS D H. 50 years of hypernuclear physics. I. The early experiments[J/OL]. Nucl. Phys. A, 2005, 754: 3-13. DOI: 10.1016/j.nuclphysa.2005.01.002.

[41] DALITZ R H. 50 years of hypernuclear physics. II. The later years[J/OL]. Nucl. Phys. A, 2005, 754: 14-24. DOI: 10.1016/j.nuclphysa.2005.01.016.

[42] CHATTERJEE D, VIDAÑA I. Do hyperons exist in the interior of neutron stars?[J/OL]. Eur. Phys. J. A, 2016, 52(2): 29. DOI: 10.1140/epja/i2016-16029-x.

[43] LONARDONI D, LOVATO A, GANDOLFI S, et al. Hyperon puzzle: hints from quantum Monte Carlo calculations[J/OL]. Phys. Rev. Lett., 2015, 114: 092301. DOI: 10.1103/PhysRevLett.114.092301.

[44] ANTONIADIS J, FREIRE P C C, WEX N, et al. A massive pulsar in a compact relativistic binary[J/OL]. Science, 2013, 340(6131): 1233232. DOI: 10.1126/science.1233232.

[45] DANYSZ M, AND J P. Delayed disintegration of a heavy nuclear fragment: I[J/OL]. The

London, Edinburgh, and Dublin Philosophical Magazine and Journal of Science, 1953, 44 (350): 348-350. DOI: 10.1080/14786440308520318.

[46] TIDMAN D, DAVIS G, HERZ A, et al. Delayed disintegration of a heavy nuclear fragment: II [J/OL]. The London, Edinburgh, and Dublin Philosophical Magazine and Journal of Science, 1953, 44(350): 350-352. DOI: 10.1080/14786440308520319.

[47] BHOWMIK B, et al. The interaction and decay of K^- mesons in photographic emulsion: Part I. general characteristics of K^--interactions and analysis of events in which a charged π-meson is emitted[J/OL]. Nuovo Cim., 1959, 13(4): 690-729. DOI: 10.1007/BF02726361.

[48] BHOWMIK B, EVANS D, FALLA D, et al. The interaction of K^--mesons with photographic emulsion nuclei: Part II. the emission of hyperons from K^--interactions at rest[J/OL]. Nuovo Cim., 1959, 14(2): 315-364. DOI: 10.1007/BF02728320.

[49] EVANS D, HASSAN F, NAGPAUL K K, et al. The interaction and decay of K^--mesons in photographic emulsion: Part III[J/OL]. Nuovo Cim., 1960, 15(6): 873-898. DOI: 10.1007/BF02860193.

[50] PHILLIPS R E, SCHNEPS J. Lifetimes of light hyperfragments. ii[J/OL]. Phys. Rev., 1969, 180: 1307-1318. DOI: 10.1103/PhysRev.180.1307.

[51] BOHM G, et al. On the lifetime of the ${}^{3}_{\Lambda}$H hypernucleus[J/OL]. Nucl. Phys. B, 1970, 16: 46-52. DOI: 10.1016/0550-3213(70)90335-4.

[52] PREM R J, STEINBERG P H. Lifetimes of hypernuclei, ${}^{3}_{\Lambda}$H, ${}^{4}_{\Lambda}$H, ${}^{5}_{\Lambda}$H[J/OL]. Phys. Rev., 1964, 136: B1803-B1806. DOI: 10.1103/PhysRev.136.B1803.

[53] KEYES G, DERRICK M, FIELDS T, et al. New measurement of the ${}^{3}_{\Lambda}$H lifetime[J/OL]. Phys. Rev. Lett., 1968, 20: 819-821. DOI: 10.1103/PhysRevLett.20.819.

[54] KEYES G, DERRICK M, FIELDS T, et al. Properties of ${}^{3}_{\Lambda}$H[J/OL]. Phys. Rev. D, 1970, 1: 66-77. DOI: 10.1103/PhysRevD.1.66.

[55] KEYES G, SACTON J, WICKENS J H, et al. A measurement of the lifetime of the ${}^{3}_{\Lambda}$H hypernucleus[J/OL]. Nucl. Phys. B, 1973, 67: 269-283. DOI: 10.1016/0550-3213(73)90197-1.

[56] DANYSZ M, GARBOWSKA K, PNIEWSKI J, et al. Observation of a double hyperfragment [J/OL]. Phys. Rev. Lett., 1963, 11: 29-32. DOI: 10.1103/PhysRevLett.11.29.

[57] DANYSZ M, et al. The identification of a double hyperfragment[J/OL]. Nucl. Phys., 1963, 49: 121-132. DOI: 10.1016/0029-5582(63)90080-4.

[58] KILIAN K. The $(K^-\pi^-)$ reaction at CERN[J/OL]. AIP Conf. Proc., 1979, 54: 666-679. DOI: 10.1063/1.32012.

[59] BERTINI R, et al. Hypernuclei with Σ particles[J/OL]. Phys. Lett. B, 1980, 90: 375-378. DOI: 10.1016/0370-2693(80)90952-1.

[60] BERTINI R, et al. Hypernuclear production in the (K^-, π^-) reaction[J/OL]. Nucl. Phys. A, 1981, 360: 315-330. DOI: 10.1016/0375-9474(81)90149-4.

[61] KUBOTA K, HAYANO R S, ISHIKAWA T, et al. Search for neutron-rich Λ hypernuclei in the $(K^-_{stopped}, \pi^+)$ reaction[J/OL]. Nucl. Phys. A, 1996, 602: 327-333. DOI: 10.1016/0375-9474(96)00083-8.

[62] FUKUDA T, et al. Cascade hypernuclei in the (K^-, K^+) reaction on ^{12}C[J/OL]. Phys. Rev. C, 1998, 58: 1306-1309. DOI: 10.1103/PhysRevC.58.1306.

[63] MOTOBA T, BANDO H, WUNSCH R, et al. Hypernuclear production by the (π^+, K^+) reaction[J/OL]. Phys. Rev. C, 1988, 38: 1322-1334. DOI: 10.1103/PhysRevC.38.1322.

[64] SUGIMURA H, et al. Search for $^6_\Lambda$H hypernucleus by the ^{6}Li(π^-, K^+) reaction at $p_{\pi^-} = 1.2$ GeV/c[J/OL]. Phys. Lett. B, 2014, 729: 39-44. DOI: 10.1016/j.physletb.2013.12.062.

[65] EKAWA H, et al. Observation of a Be double-Lambda hypernucleus in the J-PARC E07 experiment[J/OL]. PTEP, 2019, 2019(2): 021D02. DOI: 10.1093/ptep/pty149.

[66] YOSHIMOTO M, et al. First observation of a nuclear s-state of a Ξ hypernucleus, $^{15}_{\Xi}$C[J/OL]. PTEP, 2021, 2021(7): 073D02. DOI: 10.1093/ptep/ptab073.

[67] AKAISHI T, et al. Precise lifetime measurement of $^4_\Lambda$H hypernucleus using in-flight ^{4}He$(K^-, \pi^0)^4_\Lambda$H reaction[J/OL]. Phys. Lett. B, 2023, 845: 138128. DOI: 10.1016/j.physletb.2023.138128.

[68] BRAUN-MUNZINGER P, STACHEL J. Production of strange clusters and strange matter in nucleus-nucleus collisions at the AGS[J/OL]. J. Phys. G, 1995, 21: L17-L20. DOI: 10.1088/0954-3899/21/3/002.

[69] ANDRONIC A, BRAUN-MUNZINGER P, STACHEL J, et al. Production of light nuclei, hypernuclei and their antiparticles in relativistic nuclear collisions[J/OL]. Phys. Lett. B, 2011, 697: 203-207. DOI: 10.1016/j.physletb.2011.01.053.

[70] ABELEV B I, et al. Observation of an antimatter hypernucleus[J/OL]. Science, 2010, 328: 58-62. DOI: 10.1126/science.1183980.

[71] ABDULHAMID M, et al. Observation of the antimatter hypernucleus $^4_{\bar{\Lambda}}\overline{\mathrm{H}}$[J/OL]. Nature, 2024, 632(8027): 1026-1031. DOI: 10.1038/s41586-024-07823-0.

[72] ACHARYA S, et al. Measurement of the lifetime and Λ separation energy of $^3_\Lambda$H[J/OL]. Phys. Rev. Lett., 2023, 131(10): 102302. DOI: 10.1103/PhysRevLett.131.102302.

[73] SUN K J, LIU D N, ZHENG Y P, et al. Deciphering hypertriton and anti-hypertriton spins from their global polarizations in heavy-ion collisions[J/OL]. Phys. Rev. Lett., 2025, 134(2): 022301. DOI: 10.1103/PhysRevLett.134.022301.

[74] GAL A, GARCILAZO H. Towards resolving the $^3_\Lambda$H lifetime puzzle[J/OL]. Phys. Lett. B, 2019, 791: 48-53. DOI: 10.1016/j.physletb.2019.02.014.

[75] HILDENBRAND F, HAMMER H W. Three-body hypernuclei in pionless effective field theory[J/OL]. Phys. Rev. C, 2019, 100: 034002. DOI: 10.1103/PhysRevC.100.034002.

[76] BEDJIDIAN M, FILIPKOWSKI A, GROSSIORD J Y, et al. Observation of a gamma transition in the ${}^{4}_{\Lambda}$H hypernucleus[J/OL]. Phys. Lett. B, 1976, 62: 467-470. DOI: 10.1016/0370-2693(76)90686-9.

[77] YAMAMOTO T O, et al. Observation of spin-dependent charge symmetry breaking in ΛN interaction: Gamma-ray spectroscopy of ${}^{4}_{\Lambda}$He[J/OL]. Phys. Rev. Lett., 2015, 115(22): 222501. DOI: 10.1103/PhysRevLett.115.222501.

[78] ABDALLAH M, et al. Measurement of ${}^{4}_{\Lambda}$H and ${}^{4}_{\Lambda}$He binding energy in Au+Au collisions at $\sqrt{s_{NN}}$ = 3 GeV[J/OL]. Phys. Lett. B, 2022, 834: 137449. DOI: 10.1016/j.physletb.2022.137449.

[79] GAZDA D, GAL A. Ab initio calculations of charge symmetry breaking in the $A = 4$ hypernuclei[J/OL]. Phys. Rev. Lett., 2016, 116: 122501. DOI: 10.1103/PhysRevLett.116.122501.

[80] HILDENBRAND F, HAMMER H W. Lifetime of the hypertriton[J/OL]. Phys. Rev. C, 2020, 102: 064002. DOI: 10.1103/PhysRevC.102.064002.

[81] PÉREZ-OBIOL A, GAZDA D, FRIEDMAN E, et al. Revisiting the hypertriton lifetime puzzle[J/OL]. Phys. Lett. B, 2020, 811: 135916. DOI: 10.1016/j.physletb.2020.135916.

[82] RAYET M, DALITZ R H. Lifetime of ${}^{3}_{\Lambda}$H[J/OL]. Nuovo Cim. A, 1966, 46: 786-794. DOI: 10.1007/BF02857527.

[83] ZYLA P A, et al. Review of particle physics[J/OL]. PTEP, 2020, 2020(8): 083C01. DOI: 10.1093/ptep/ptaa104.

[84] RAPPOLD C, et al. Hypernuclear spectroscopy of products from ^{6}Li projectiles on a carbon target at 2 AGeV[J/OL]. Nucl. Phys. A, 2013, 913: 170-184. DOI: 10.1016/j.nuclphysa.2013.05.019.

[85] ADAM J, et al. ${}^{3}_{\Lambda}$H and ${}^{3}_{\bar{\Lambda}}\overline{\mathrm{H}}$ production in Pb-Pb collisions at $\sqrt{s_{\mathrm{NN}}} = 2.76$ TeV[J/OL]. Phys. Lett. B, 2016, 754: 360-372. DOI: 10.1016/j.physletb.2016.01.040.

[86] ADAMCZYK L, et al. Measurement of the ${}^{3}_{\Lambda}$H lifetime in Au+Au collisions at the BNL Relativistic Heavy Ion Collider[J/OL]. Phys. Rev. C, 2018, 97(5): 054909. DOI: 10.1103/PhysRevC.97.054909.

[87] ACHARYA S, et al. ${}^{3}_{\Lambda}$H and ${}^{3}_{\bar{\Lambda}}\overline{\mathrm{H}}$ lifetime measurement in Pb-Pb collisions at $\sqrt{s_{\mathrm{NN}}} = 5.02$ TeV via two-body decay[J/OL]. Phys. Lett. B, 2019, 797: 134905. DOI: 10.1016/j.physletb.2019.134905.

[88] ABDALLAH M, et al. Measurements of ${}^{3}_{\Lambda}$H and ${}^{4}_{\Lambda}$H lifetimes and yields in Au+Au collisions in the high baryon density region[J/OL]. Phys. Rev. Lett., 2022, 128(20): 202301. DOI:

10.1103/PhysRevLett.128.202301.

[89] CONGLETON J G. A simple model of the hypertriton[J/OL]. J. Phys. G, 1992, 18: 339-357. DOI: 10.1088/0954-3899/18/2/015.

[90] KAMADA H, GOLAK J, MIYAGAWA K, et al. π mesonic decay of the hypertriton[J/OL]. Phys. Rev. C, 1998, 57: 1595-1603. DOI: 10.1103/PhysRevC.57.1595.

[91] JURIC M, et al. A new determination of the binding-energy values of the light hypernuclei (A≤15)[J/OL]. Nucl. Phys. B, 1973, 52: 1-30. DOI: 10.1016/0550-3213(73)90084-9.

[92] STOKS V G J, KLOMP R A M, TERHEGGEN C P F, et al. Construction of high quality n n potential models[J/OL]. Phys. Rev. C, 1994, 49: 2950-2962. DOI: 10.1103/PhysRevC.49.2950.

[93] MAESSEN P M M, RIJKEN T A, DE SWART J J. Soft core baryon baryon one boson exchange models. 2. hyperon - nucleon potential[J/OL]. Phys. Rev. C, 1989, 40: 2226-2245. DOI: 10.1103/PhysRevC.40.2226.

[94] BOTTA E, BRESSANI T, BUFALINO S, et al. Status and perspectives of experimental studies on hypernuclear weak decays[J/OL]. Riv. Nuovo Cim., 2015, 38(9): 387-448. DOI: 10.1393/ncr/i2015-10116-x.

[95] ITONAGA K, MOTOBA T. Hypernuclear weak decays[J/OL]. Prog. Theor. Phys. Suppl., 2010, 185: 252-298. DOI: 10.1143/PTPS.185.252.

[96] MATTIELLO R, SORGE H, STÖCKER H, et al. Nuclear clusters as a probe for expansion flow in heavy ion reactions at (10–15)A GeV[J/OL]. Phys. Rev. C, 1997, 55: 1443-1454. DOI: 10.1103/PhysRevC.55.1443.

[97] REICHERT T, STEINHEIMER J, VOVCHENKO V, et al. Energy dependence of light hypernuclei production in heavy-ion collisions from a coalescence and statistical-thermal model perspective[J/OL]. Phys. Rev. C, 2023, 107: 014912. DOI: 10.1103/PhysRevC.107.014912.

[98] DÖNIGUS B. Selected highlights of the production of light (anti-)(hyper-)nuclei in ultra-relativistic heavy-ion collisions[J/OL]. Eur. Phys. J. A, 2020, 56(11): 280. DOI: 10.1140/epja/s10050-020-00275-w.

[99] VOVCHENKO V, STOECKER H. Thermal-FIST: A package for heavy-ion collisions and hadronic equation of state[J/OL]. Comput. Phys. Commun., 2019, 244: 295-310. DOI: 10.1016/j.cpc.2019.06.024.

[100] ZHANG S, CHEN J H, CRAWFORD H, et al. Searching for onset of deconfinement via hypernuclei and baryon-strangeness correlations[J/OL]. Phys. Lett. B, 2010, 684: 224-227. DOI: 10.1016/j.physletb.2010.01.034.

[101] LIN Z W, KO C M, LI B A, et al. Multiphase transport model for relativistic heavy ion collisions[J/OL]. Phys. Rev. C, 2005, 72: 064901. DOI: 10.1103/PhysRevC.72.064901.

[102] VOVCHENKO V, DÖNIGUS B, KARDAN B, et al. Feeddown contributions from unstable nuclei in relativistic heavy-ion collisions[J/OL]. Phys. Lett. B, 2020: 135746. DOI: 10.1016/j.physletb.2020.135746.

[103] STAR Collaboration. Studying the phase diagram of QCD matter at RHIC[J/OL]. STAR Note, 2014, SN0598. https://drupal.star.bnl.gov/STAR/starnotes/public/sn0598.

[104] Brookhaven National Laboratory. RHIC complex[EB/OL]. 2024. https://www.bnl.gov/newsroom/news.php?a=221190.

[105] HARRISON M, PEGGS S G, ROSER T. The RHIC accelerator[J/OL]. Ann. Rev. Nucl. Part. Sci., 2002, 52: 425-469. DOI: 10.1146/annurev.nucl.52.050102.090650.

[106] HAHN H, et al. The RHIC design overview[J/OL]. Nucl. Instrum. Meth. A, 2003, 499: 245-263. DOI: 10.1016/S0168-9002(02)01938-1.

[107] HARRISON M, LUDLAM T, OZAKI S. RHIC project overview[J/OL]. Nucl. Instrum. Meth. A, 2003, 499: 235-244. DOI: 10.1016/S0168-9002(02)01937-X.

[108] LUDLAM T W. RHIC and quark matter: a proposed heavy ion collider at Brookhaven National Laboratory[R/OL]. Brookhaven National Lab., Upton, NY (USA), 1984. https://www.osti.gov/servlets/purl/6191838-ADIaVd/.

[109] OZAKI S. RHIC project[R/OL]. Brookhaven National Lab., Upton, NY (USA), 1991. https://www.osti.gov/servlets/purl/5660785.

[110] BUNCE G, SAITO N, SOFFER J, et al. Prospects for spin physics at RHIC[J/OL]. Ann. Rev. Nucl. Part. Sci., 2000, 50: 525-575. DOI: 10.1146/annurev.nucl.50.1.525.

[111] ADAM J, et al. Charge-dependent pair correlations relative to a third particle in p + Au and d+ Au collisions at RHIC[J/OL]. Phys. Lett. B, 2019, 798: 134975. DOI: 10.1016/j.physletb.2019.134975.

[112] NOVITZKY N. Small collision systems at RHIC[J/OL]. EPJ Web Conf., 2018, 171: 11002. DOI: 10.1051/epjconf/201817111002.

[113] ALVER B, et al. Elliptic flow and initial eccentricity in Cu+Cu and Au+Au collisions at RHIC[J/OL]. J. Phys. G, 2007, 34: S887-892. DOI: 10.1088/0954-3899/34/8/S119.

[114] DASGUPTA P, CHATTERJEE R, SRIVASTAVA D K. Directed flow of photons in Cu+Au collisions at RHIC[J/OL]. J. Phys. G, 2020, 47(8): 085101. DOI: 10.1088/1361-6471/ab920e.

[115] KHARZEEV D E, LIAO J, SHI S. Implications of the isobar-run results for the chiral magnetic effect in heavy-ion collisions[J/OL]. Phys. Rev. C, 2022, 106(5): L051903. DOI: 10.1103/PhysRevC.106.L051903.

[116] ADAMCZYK L, et al. Azimuthal anisotropy in U+U and Au+Au collisions at RHIC[J/OL]. Phys. Rev. Lett., 2015, 115(22): 222301. DOI: 10.1103/PhysRevLett.115.222301.

[117] LOMNITZ M R. Measurement of D-meson azimuthal anisotropy in Au+Au 200 GeV collisions at RHIC[J/OL]. Nucl. Phys. A, 2016, 956: 256-259. DOI: 10.1016/j.nuclphysa.2016.04.027.

[118] ADAM J, et al. Measurements of W and Z/γ^* cross sections and their ratios in p+p collisions at RHIC[J/OL]. Phys. Rev. D, 2021, 103(1): 012001. DOI: 10.1103/PhysRevD.103.012001.

[119] ALESSI J G, BEEBE E N, GOULD O, et al. High performance EBIS for RHIC[J/OL]. Conf. Proc. C, 2007, 070625: 3782. DOI: 10.1109/PAC.2007.4440116.

[120] ALESSI J G, et al. The Brookhaven National Laboratory electron beam ion source for RHIC [J/OL]. Rev. Sci. Instrum., 2010, 81: 02A509. DOI: 10.1063/1.3292937.

[121] Brookhaven National Laboratory. A new pre-injector system for RHIC[Z].

[122] WILLEKE F. Electron Ion Collider conceptual design report 2021[EB/OL]. 2021. DOI: 10.2172/1765663.

[123] HARRIS J W. Physics of the STAR experiment at RHIC[M/OL]. Boston, MA: Springer US, 1998: 127-136. DOI: 10.1007/978-1-4757-9089-4_14.

[124] ACKERMANN K H, et al. STAR detector overview[J/OL]. Nucl. Instrum. Meth. A, 2003, 499: 624-632. DOI: 10.1016/S0168-9002(02)01960-5.

[125] STAR experiment. STAR detector 3D view with MTD and EPD[EB/OL]. https://www.star.bnl.gov/protected/heavy/aschmah/STAR_3D/STAR_V19_MTD_EPD.jpg.

[126] ANDERSON M, et al. The Star Time Projection Chamber: a unique tool for studying high multiplicity events at RHIC[J/OL]. Nucl. Instrum. Meth. A, 2003, 499: 659-678. DOI: 10.1016/S0168-9002(02)01964-2.

[127] STAR Collaboration. Technical design report for the iTPC upgrade[J/OL]. STAR Note, 2015, SN0644. https://drupal.star.bnl.gov/STAR/starnotes/public/sn0644.

[128] STAR Collaboration. Proposal for a large area time of flight system for STAR[J/OL]. STAR Note, 2004, SN0621. https://drupal.star.bnl.gov/STAR/starnotes/public/sn0621.

[129] LLOPE W J. The large-area time-of-flight upgrade for STAR[J/OL]. Nucl. Instrum. Meth. B, 2005, 241: 306-310. DOI: 10.1016/j.nimb.2005.07.089.

[130] BEDDO M, et al. The STAR barrel electromagnetic calorimeter[J/OL]. Nucl. Instrum. Meth. A, 2003, 499: 725-739. DOI: 10.1016/S0168-9002(02)01970-8.

[131] BERGSMA F, et al. The STAR detector magnet subsystem[J/OL]. Nucl. Instrum. Meth. A, 2003, 499: 633-639. DOI: 10.1016/S0168-9002(02)01961-7.

[132] RUAN L, et al. Perspectives of a midrapidity dimuon program at RHIC: a novel and compact muon telescope detector[J/OL]. J. Phys. G, 2009, 36: 095001. DOI: 10.1088/0954-3899/36/9/095001.

[133] ALLGOWER C E, et al. The STAR endcap electromagnetic calorimeter[J/OL]. Nucl. In-

strum. Meth. A, 2003, 499: 740-750. DOI: 10.1016/S0168-9002(02)01971-X.

[134] Physics program for the STAR/CBM eTOF upgrade[A]. 2016. arXiv: 1609.05102.

[135] LLOPE W J, et al. The STAR Vertex Position Detector[J/OL]. Nucl. Instrum. Meth. A, 2014, 759: 23-28. DOI: 10.1016/j.nima.2014.04.080.

[136] ADLER C, DENISOV A, GARCIA E, et al. The RHIC zero degree calorimeter[J/OL]. Nucl. Instrum. Meth. A, 2001, 470: 488-499. DOI: 10.1016/S0168-9002(01)00627-1.

[137] SCHMAH A, REED R, LISA M. An Event Plane Detector for STAR[J/OL]. STAR Note, 2017, SN0666. https://drupal.star.bnl.gov/STAR/starnotes/public/sn0666.

[138] ADAMS J, et al. The STAR Event Plane Detector[J/OL]. Nucl. Instrum. Meth. A, 2020, 968: 163970. DOI: 10.1016/j.nima.2020.163970.

[139] WHITTEN C A. The beam−beam counter: a local polarimeter at STAR[J/OL]. AIP Conf. Proc., 2008, 980(1): 390-396. DOI: 10.1063/1.2888113.

[140] LEBEDEV A. A laser calibration system for the STAR TPC[J/OL]. Nucl. Instrum. Meth. A, 2002, 478: 163-165. DOI: 10.1016/S0168-9002(01)01747-8.

[141] ABELE J, et al. The laser system for the STAR time projection chamber[J/OL]. Nucl. Instrum. Meth. A, 2003, 499: 692-702. DOI: 10.1016/S0168-9002(02)01966-6.

[142] BICHSEL H. Energy loss in thin layers of argon[J/OL]. STAR Note, 2003, SN0418. https://drupal.star.bnl.gov/STAR/starnotes/public/sn0418.

[143] BICHSEL H. Ionization energy loss: Straggling functions, the most probable loss, and the bethe-bloch formula[J/OL]. STAR Note, 2003, SN0439. https://drupal.star.bnl.gov/STAR/starnotes/public/sn0439.

[144] BICHSEL H. A method to improve tracking and particle identification in TPCs and silicon detectors[J/OL]. Nucl. Instrum. Meth. A, 2006, 562: 154-197. DOI: 10.1016/j.nima.2006.03.009.

[145] ABDALLAH M S, et al. Light nuclei collectivity from $\sqrt{s_{NN}} = 3$ GeV Au+Au collisions at RHIC[J/OL]. Phys. Lett. B, 2022, 827: 136941. DOI: 10.1016/j.physletb.2022.136941.

[146] YANG Y. The STAR detector upgrades for the BES II and beyond physics program[J/OL]. Nucl. Phys. A, 2021, 1005: 121758. DOI: 10.1016/j.nuclphysa.2020.121758.

[147] LLOPE W J. Multigap RPCs in the STAR experiment at RHIC[J/OL]. Nucl. Instrum. Meth. A, 2012, 661: S110-S113. DOI: 10.1016/j.nima.2010.07.086.

[148] AGGARWAL M M, et al. An experimental exploration of the qcd phase diagram: The search for the critical point and the onset of de-confinement[A]. 2010. arXiv: 1007.2613.

[149] ADAMCZYK L, et al. Beam-energy dependence of charge separation along the magnetic field in Au+Au collisions at RHIC[J/OL]. Phys. Rev. Lett., 2014, 113: 052302. DOI: 10.1103/PhysRevLett.113.052302.

[150] ADAMCZYK L, et al. Observation of an energy-dependent difference in elliptic flow between particles and antiparticles in relativistic heavy ion collisions[J/OL]. Phys. Rev. Lett., 2013, 110(14): 142301. DOI: 10.1103/PhysRevLett.110.142301.

[151] ADAMCZYK L, et al. Beam-energy dependence of the directed flow of protons, antiprotons, and pions in Au+Au collisions[J/OL]. Phys. Rev. Lett., 2014, 112(16): 162301. DOI: 10.1103/PhysRevLett.112.162301.

[152] ADAMCZYK L, et al. Energy dependence of moments of net-proton multiplicity distributions at RHIC[J/OL]. Phys. Rev. Lett., 2014, 112: 032302. DOI: 10.1103/PhysRevLett.112.032302.

[153] Brookhaven National Laboratory. RHIC run overview[EB/OL]. 2025[2025-03-31]. https://www.rhichome.bnl.gov/RHIC/Runs/.

[154] YANG Q. The STAR BES-II and forward rapidity physics and upgrades[J/OL]. Nucl. Phys. A, 2019, 982: 951-954. DOI: 10.1016/j.nuclphysa.2018.10.029.

[155] XIAO B, et al. Design and test of 704 MHz and 2.1 GHz normal conducting cavities for low energy RHIC electron cooler[J/OL]. Phys. Rev. Accel. Beams, 2019, 22(3): 030101. DOI: 10.1103/PhysRevAccelBeams.22.030101.

[156] LIU C, et al. Gold-gold luminosity increase in RHIC for a beam energy scan with colliding beam energies extending below the nominal injection energy[J/OL]. Phys. Rev. Accel. Beams, 2022, 25(5): 051001. DOI: 10.1103/PhysRevAccelBeams.25.051001.

[157] ARSLANDOK M, et al. Hot QCD white paper[A]. 2023. arXiv: 2303.17254.

[158] MEEHAN K C. Fixed target collisions at STAR[J/OL]. Nucl. Phys. A, 2016, 956: 878-881. DOI: 10.1016/j.nuclphysa.2016.04.016.

[159] BIESER F S, et al. The STAR trigger[J/OL]. Nucl. Instrum. Meth. A, 2003, 499: 766-777. DOI: 10.1016/S0168-9002(02)01974-5.

[160] JUDD E G, et al. The evolution of the STAR trigger system[J/OL]. Nucl. Instrum. Meth. A, 2018, 902: 228-237. DOI: 10.1016/j.nima.2018.03.070.

[161] STAR Collaboration. Run-by-run QA for 3.0 GeV 2018 production[EB/OL]. https://drupal.star.bnl.gov/STAR/system/files/Kimelman_3GeV_run_by_run_QA_badRuns.pdf.

[162] STAR Collaboration. Centrality determination for 3.2 GeV 2019 production[EB/OL]. https://drupal.star.bnl.gov/STAR/system/files/Centrality_Determination_for_3_2_GeV_2019_Production_0.pdf.

[163] STAR Collaboration. Centrality determination for 3.5 GeV 2020 production[EB/OL]. https://drupal.star.bnl.gov/STAR/system/files/Centrality_Determination_for_3_5_GeV_2020_Production.pdf.

[164] STAR Collaboration. FXT centrality study[EB/OL]. https://drupal.star.bnl.gov/STAR/syste

m/files/Centrality_BES_FXT.pdf.

[165] ZYZAK M. Online selection of short-lived particles on many-core computer architectures in the CBM experiment at FAIR[D]. Universitätsbibliothek Johann Christian Senckenberg, 2016: 165.

[166] JU X Y, et al. Applying the Kalman filter particle method to strange and open charm hadron reconstruction in the STAR experiment[J/OL]. Nucl. Sci. Tech., 2023, 34(10): 158. DOI: 10.1007/s41365-023-01320-1.

[167] HOECKER A, SPECKMAYER P, STELZER J, et al. TMVA - toolkit for multivariate data analysis[A]. 2009. arXiv: physics/0703039.

[168] ADAMCZYK L, et al. Bulk properties of the medium produced in relativistic heavy-ion collisions from the beam energy scan program[J/OL]. Phys. Rev. C, 2017, 96(4): 044904. DOI: 10.1103/PhysRevC.96.044904.

[169] ADAM J, et al. Strange hadron production in Au+Au collisions at $\sqrt{s_{\mathrm{NN}}}$ = 7.7, 11.5, 19.6, 27, and 39 GeV[J/OL]. Phys. Rev. C, 2020, 102(3): 034909. DOI: 10.1103/PhysRevC.102.034909.

[170] OUTA H. Exotic bound states of light hypernuclei[J/OL]. Hyperfine Interact., 1996, 103: 227-235. https://api.semanticscholar.org/CorpusID:102381118.

[171] PARKER J D, et al. Weak decays of ${}^{4}_{\Lambda}$He[J/OL]. Phys. Rev. C, 2007, 76: 035501. DOI: 10.1103/PhysRevC.75.035501.

[172] BARLOW R. Systematic errors: Facts and fictions[A]. 2002: 134-144. arXiv: hep-ex/0207026.

[173] XU Y. Measurement of hypertriton lifetime at STAR[J/OL]. JPS Conf. Proc., 2017, 17: 021005. DOI: 10.7566/JPSCP.17.021005.

[174] COHEN J. Weak non-mesonic decays of Λ hypernuclei[J/OL]. Prog. Part. Nucl. Phys., 1990, 25: 139-234. DOI: 10.1016/0146-6410(90)90031-X.

[175] GAZDA D, PÉREZ-OBIOL A, FRIEDMAN E, et al. Hypertriton lifetime[J/OL]. Phys. Rev. C, 2024, 109(2): 024001. DOI: 10.1103/PhysRevC.109.024001.

[176] ECKERT P, et al. Systematic treatment of hypernuclear data and application to the hypertriton [J/OL]. Rev. Mex. Fis. Suppl., 2022, 3(3): 0308069. DOI: 10.31349/SuplRevMexFis.3.0308069.

[177] ABDALLAH M S, et al. Probing strangeness canonical ensemble with K^{-}, $\phi(1020)$ and Ξ^{-} production in Au+Au collisions at $\sqrt{s_{NN}}$=3 GeV[J/OL]. Phys. Lett. B, 2022, 831: 137152. DOI: 10.1016/j.physletb.2022.137152.

[178] SCHNEDERMANN E, SOLLFRANK J, HEINZ U W. Thermal phenomenology of hadrons from 200A/GeV S+S collisions[J/OL]. Phys. Rev. C, 1993, 48: 2462-2475. DOI: 10.1103/

PhysRevC.48.2462.

[179] STAR Collaboration. Measurements of ${}^{3}_{\Lambda}$H and ${}^{4}_{\Lambda}$H lifetimes and yields in Au+Au collisions in the high baryon density region[J/OL]. STAR Note, 2021, SN0774. https://drupal.star.bnl.gov/STAR/starnotes/private/psn0774.

[180] TROGOLO S. (Anti-)(hyper-)nuclei production in Pb-Pb collisions with ALICE at the Large Hadron Collider[A]. 2019. arXiv: 1912.09707.

[181] SPIES S. Production of strange mesons, hyperons and hypernuclei in Ag+Ag collisions at $\sqrt{s_{NN}}$ = 2.55 GeV measured with HADES[EB/OL]. 2022. https://indico.cern.ch/event/895086/contributions/4705479/attachments/2422487/4148164/SimonSpies_HADESHypernuclei.pdf.

[182] OUTA H, YAMAZAKI T, AOKI M, et al. Mesonic weak decay of ${}^{4}_{\Lambda}$H and ${}^{4}_{\Lambda}$He[J/OL]. Nucl. Phys. A, 1995, 585: 109C-112C. DOI: 10.1016/0375-9474(94)00552-X.

[183] AVRAMENKO S A, et al. A Study of the production and lifetime of the lightest relativistic hypernuclei[J/OL]. Nucl. Phys. A, 1992, 547: 95C-100C. DOI: 10.1016/0375-9474(92)90714-U.

[184] KANG Y W, KWAK N, SCHNEPS J, et al. Lifetimes of light hyperfragments[J/OL]. Phys. Rev., 1965, 139: B401-B406. DOI: 10.1103/PhysRev.139.B401.

[185] CRAYTON N, et al. Determination of the ${}^{4}_{\Lambda}$H lifetime[EB/OL]. 1962: 460-462. https://inspirehep.net/files/c0925dacbfe5c8c22e9c0bf5df5a4922.

[186] PARKER J D, ATHANAS M J, BARNES P D, et al. Publisher's note: Weak decays of ${}^{4}_{\Lambda}$He [Phys. Rev. C 76, 035501 (2007)][J/OL]. Phys. Rev. C, 2007, 76: 039904. DOI: 10.1103/PhysRevC.76.039904.

[187] OUTA H, AOKI M, HAYANO R S, et al. Mesonic and non-mesonic decay widths of ${}^{4}_{\Lambda}$H and ${}^{4}_{\Lambda}$He[J/OL]. Nucl. Phys. A, 1998, 639: 251-260. DOI: 10.1016/S0375-9474(98)00281-4.

[188] GAL A. Recent progress on few-body hypernuclei[J/OL]. EPJ Web Conf., 2022, 259: 08002. DOI: 10.1051/epjconf/202225908002.

[189] ABDULHAMID M, et al. Production of protons and light nuclei in Au+Au collisions at $\sqrt{s_{NN}}$= 3 GeV with the STAR detector[J/OL]. Phys. Rev. C, 2024, 110(5): 054911. DOI: 10.1103/PhysRevC.110.054911.

[190] AHLE L, et al. Proton and deuteron production in Au + Au reactions at 11.6A GeV/c[J/OL]. Phys. Rev. C, 1999, 60: 064901. DOI: 10.1103/PhysRevC.60.064901.

[191] LIU D N, KO C M, MA Y G, et al. Softening of the hypertriton transverse momentum spectrum in heavy-ion collisions[J/OL]. Phys. Lett. B, 2024, 855: 138855. DOI: 10.1016/j.physletb.2024.138855.

[192] MOHANTY B, XU N. QCD critical point and high baryon density matter[A]. 2021. arXiv:

2101.09210.

Acknowledgements

As I reach the conclusion of my Ph.D. journey at the University of Science and Technology of China (USTC), I find myself reflecting on the countless individuals whose guidance, support, and encouragement have made this dissertation possible. Over these years, I have been fortunate to receive help from many remarkable mentors, colleagues, friends, and family members. To all of them, I express my deepest and most sincere gratitude.

First and foremost, I would like to express my heartfelt thanks to my advisor, Prof. Dr. Yifei Zhang, for his unwavering support and guidance since my master's studies. His profound expertise, scientific vision, and dedication to nurturing young researchers have shaped my approach to research and helped me grow into an independent scientist.

I am also deeply grateful to Prof. Dr. ShinIchi Esumi, who mentored me during my exchange period at the University of Tsukuba. His insightful feedback, patient discussions, and detailed suggestions significantly improved my analysis and enriched my understanding of the field. My sincere thanks also go to Prof. Dr. Takafumi Niida and other staffs in Tsukuba for their constructive comments and support during this period. I would like to acknowledge Moe Isshiki and Kosuke Okubo for their help both academically and in daily life during my stay in Japan. I am also grateful to the China Scholarship Council (CSC) for providing financial support for my research abroad.

I would also like to express my sincere appreciation to Prof. Dr. Nu Xu, Prof. Dr. Xin Dong, Dr. Yue-hang Leung, Dr. Yuanjing Ji, and Prof. Dr. Guannan Xie, whose valuable input and discussions through the STAR collaboration have significantly enhanced the quality of my research and broadened my academic perspective. Their advice was particularly helpful for my study and provided important guidance on the hypernuclei study, which constituted the core of my Ph.D. work.

I would also like to thank Prof. Dr. Zebo Tang, Prof. Dr. Wangmei Zha, Prof. Dr. Cheng Li, Prof. Dr. Ming Shao, and Prof. Dr. Yongjie Sun for their valuable guidance during group meetings and collaborative discussions. I am especially grateful to Dr. Zhen Liu, Dr. Xiaolong Chen, and Dr. Shenghui Zhang for their support during the early stages of my research. I have also been fortunate to work alongside many wonderful colleagues and friends, including Jian Zhou, Yang Li, Ziyang Li, Xinyue Ju, Kaifeng Shen, Xin Wu, Yan Wang, Fengyi Zhao, Chenlu Hu, Yingjie Zhou, Dongsheng Li, Yulou Yan, Fan Si, and other USTCers, whose collaboration and friendship brought both inspiration and joy to this journey.

I gratefully acknowledge all members of the STAR Collaboration for providing the platform and data essential to my research. The weekly meetings and discussions sharpened my analytical thinking and problem-solving skills. My appreciation also goes to the RHIC operation team for their tremendous efforts in delivering high-quality data.

Finally, I am profoundly grateful to USTC, my academic home for the past seven years. It has provided me with an inspiring environment, rigorous training, and lasting friendships. The experiences and memories I have gained here will always hold a special place in my heart.

A very special thanks goes to my parents, whose unconditional love, support, and sacrifices have carried me through all stages of life. Their belief in me has been my greatest source of strength and motivation.

To everyone who has walked beside me on this journey—thank you.

Publications

Publications

1. **Xiujun Li** (Principal Author) *et al.* [STAR], “Measurements of ${}^{3}_{\Lambda}$H and ${}^{4}_{\Lambda}$H lifetimes and yields in Au+Au collisions in the high baryon density region”, Phys. Rev. Lett. **128**, no.20, 202301 (2022)
2. **Xiujun Li** (Principal Author) *et al.* [STAR], “Elliptic flow of heavy-flavor decay electrons in Au+Au collisions at $\sqrt{s_{NN}}$ = 27 and 54.4 GeV at RHIC”, Phys. Lett. B **844**, 138071 (2023)
3. **Xiujun Li**, Fan Si, Zebang Fu and Yifei Zhang, “Temperature fluctuation and the specific heat in Au+Au collisions at collision energies from 5 to 200 GeV”, Nucl. Phys. Rev. **36**, no.4, 395-399 (2019)
4. **Xiujun Li**, “Collision energy dependence of hypertriton production in Au+Au collisions at RHIC”, EPJ Web Conf. **316**, 06009 (2025) (SQM 2024)

STAR Analysis Note

1. Xiujun Li, “Measurements of ${}^{3}_{\Lambda}$H and ${}^{4}_{\Lambda}$H lifetimes and yields in Au+Au collisions in the high baryon density region”, PSN0774.
2. Xiujun Li, “Hypertriton production in Au+Au collisions at $\sqrt{s_{NN}}$ = 3.2 GeV”

Prepare to publish

1. “Collision energy dependence of ${}^{3}_{\Lambda}$H production in Au+Au collisions at RHIC” (Principal Author), Target journal: Phys. Rev. Lett.
2. “Hyper-nuclei ${}^{4}_{\Lambda}$He production in $\sqrt{s_{NN}}$ = 3 GeV Au+Au collisions at RHIC” (Principal Author), Target journal: Chin. Phys. C

Presentations

1. Xiujun Li, “Collision Energy Dependence of Hypertriton Production in Au+Au Collisions from the STAR experiment”, STAR Regional Meeting, Oct. 10–15, 2024, Chongqing, China (talk)
2. Xiujun Li, “Collision Energy Dependence of Hypertriton Production in Au+Au Collisions at RHIC”, SQM 2024, Jun. 3–7, 2024, Strasbourg, France (talk)

3. Xiujun Li, "Measurement of ${}^{4}_{\Lambda}$He lifetime in Au+Au collisions from STAR fixed target mode experiment", SQM 2024, Jun. 3–7, 2024, Strasbourg, France (poster)
4. Xiujun Li, "Lifetime measurements of light hypernuclei in Au+Au Collisions from STAR experiment", Quark Matter 2023, Sep. 3–9, 2023, Houston, USA (poster)
5. Xiujun Li, "Measurements of light hypernuclei properties and production yields in Au+Au collisions from the STAR experiment", J-PARC HI workshop, Oct. 27–28, 2023, Tokai, Japan (talk)
6. Xiujun Li, "Recent light hypernuclei measurements from STAR experiment", 2nd Workshop on Hadron Interactions, Hyper-Nuclei and Exotic Hadron productions at High-Energy Experiments, May 22, 2023, Tokyo, Japan (talk)
7. Xiujun Li, "Hypernuclei measurements at RHIC-STAR", WHBM 2023, Apr. 29–30, 2023, Tsukuba, Japan (talk)
8. Xiujun Li, "Measurements of light hypernuclei properties and production yields in Au+Au collisions from the STAR experiment", ATHIC 2023, Apr. 24–27, 2023, Hiroshima, Japan (talk)
9. Xiujun Li, "Measurements of light hypernuclei production and properties in Au+Au collisions from STAR experiment", CPOD 2022, Nov. 28–Dec. 2, 2022, online (talk)
10. Xiujun Li, "Lifetime measurements of light hypernuclei in Au+Au collisions from STAR experiment", SQM 2022, Jun. 13–17, 2022, Busan, Korea (+ online) (poster)
11. Xiujun Li, "Lifetime measurements of light hypernuclei in Au+Au Collisions from STAR experiment", Quark Matter 2022, Apr. 4–10, 2022, Kraków, Poland (+ online) (poster)
12. Xiujun Li, "Recent hypernuclei measurements from BES program", 2022 RHIC AGS Annual Users's Meeting (AUM 2022), Jun. 7–10, 2022, online (talk)
13. Xiujun Li, "Lifetime measurements of ${}^{3}_{\Lambda}$H and ${}^{4}_{\Lambda}$H in Au+Au Collisions at $\sqrt{s_{NN}}$ = 7.2 GeV from STAR fixed target mode experiment", CPPC 2021, Aug. 16–19, 2021, Qingdao, China (+ online) (poster)
14. Xiujun Li, "Lifetime measurements of ${}^{3}_{\Lambda}$H and ${}^{4}_{\Lambda}$H in Au+Au Collisions at $\sqrt{s_{NN}}$ = 7.2 GeV from STAR fixed target mode experiment", QPT 2021, Jul. 26–30, 2021, Guiyang, China (talk)
15. Xiujun Li, "Temperature fluctuation and the specific heat in Au+Au collisions at $\sqrt{s_{NN}}$ = 7.7–200 GeV from STAR", Quark Matter 2019, Nov. 4–9, 2019,

Wuhan, China (poster)

16. Xiujun Li, “Temperature fluctuation and the specific heat in Au+Au collisions at $\sqrt{s_{NN}} = 7.7$–200 GeV”, CNPC 2019, Oct. 8–12, 2019, Wuhan, China (poster)